

Doctoral theses at NTNU, 2022:42

Alberto Dallolio

# Design and Experimental Validation of a Control Architecture for a Wave-Propelled USV

From system design to ocean studies

ISBN 978-82-326-6895-3 (printed ver.)  
ISBN 978-82-326-5709-4 (electronic ver.)  
ISSN 1503-8181 (printed ver.)  
ISSN 2703-8084 (electronic ver.)

Doctoral theses at NTNU, 2022:42

**NTNU**  
Norwegian University of  
Science and Technology  
Thesis for the degree of  
Philosophiae Doctor  
Faculty of Information Technology  
and Electrical Engineering  
Department of Engineering Cybernetics



Alberto Dallolio

# Design and Experimental Validation of a Control Architecture for a Wave- Propelled USV

From system design to ocean studies

Thesis for the degree of Philosophiae Doctor

Trondheim, February 2022

Norwegian University of Science and Technology  
Faculty of Information Technology  
and Electrical Engineering  
Department of Engineering Cybernetics



Norwegian University of  
Science and Technology



**NTNU**

Norwegian University of Science and Technology

Thesis for the degree of Philosophiae Doctor

Faculty of Information Technology  
and Electrical Engineering  
Department of Engineering Cybernetics

© Alberto Dallolio

ISBN 978-82-326-6895-3 (printed ver.)  
ISBN 978-82-326-5709-4 (electronic ver.)  
ISSN 1503-8181 (printed ver.)  
ISSN 2703-8084 (electronic ver.)

ITK-report: 2022-3-W

Doctoral theses at NTNU, 2022:42



Printed by Skipnes Kommunikasjon AS



*Pe' mmare nu' nce stanno taverne,  
dicette Pulecenella.  
– Voices of Naples*



# Summary

In a time of unprecedented anthropogenic pressures on the oceans, preserving the health of underwater ecosystems is of the uttermost importance. Since the beginning of human exploration of the oceans, ship-based ocean monitoring methodologies have dominated the stage, providing the ability to gather isolated point measurements mostly biased by poor scalability and continuity in space and time. The advent of robotic platforms has revolutionized ocean observation practices, enabling measurements on scales logistically and technologically impossible using traditional techniques.

Wave-propelled unmanned surface vehicles (USVs) constitute a very unique class of marine robots that, unlike common platforms, are not constrained by onboard energy limitations since their propulsion is entirely due to waves. This makes them capable of performing long-duration operations and, therefore, of observing oceanographic phenomena at more appropriate spatio-temporal scales. The glaring advantages that, from a scientific point of view, come along with this class of USVs are however hindered by numerous navigation and control challenges. As their propulsion and heading rely on the environment, stable course-over-ground (COG) control can be a challenging task when environmental forces and forward propulsion are in the same order of magnitude. Moreover, navigation performances are likely to deteriorate when hostile sea conditions arise, to a point in which maneuverability is reduced and, eventually, controlling the vehicle is no longer possible.

The principal contribution of this thesis relates to the design of a navigation control system that robustly governs the course of the commercially available, wave-propelled vehicle AutoNaut, when the environment generates drift forces acting on its body. In particular, the control design relies on extensive analysis of the nonlinearities appearing in the USV's steering dynamics model, mainly caused by the low speed relative to water and to ground observed when environmental drift forces and the force due to wave propulsion are in the same order of magnitude. Additional contributions of this work are related to i) the design, implementation

## *Summary*

---

and experimental validation of the hardware and software onboard architectures, and ii) showcasing two applications in which the proposed system is employed in ocean studies.

# Contents

<b>Summary</b>	<b>iii</b>
<b>Contents</b>	<b>v</b>
<b>Preface</b>	<b>ix</b>
<b>Glossary</b>	<b>xi</b>
<b>1 Introduction &amp; motivation</b>	<b>1</b>
1.1 Ocean observation: from manned to unmanned . . . . .	1
1.2 Robotic marine platforms for ocean observation . . . . .	3
1.3 Long-endurance unmanned surface vehicles . . . . .	7
1.4 Thesis contributions and outline . . . . .	14
<b>2 USV background: <i>An introduction to guidance, navigation and control</i></b>	<b>17</b>
2.1 Major architectural elements . . . . .	18
2.2 Common guidance & navigation approaches . . . . .	19
2.3 Control of unmanned surface vehicles . . . . .	24
<b>3 Onboard system architecture</b>	<b>29</b>
3.1 Main system requirements . . . . .	29
3.2 Architecture overview . . . . .	33
3.3 Energy harvesting, storage & distribution . . . . .	35
3.4 System monitoring & fallback autopilot . . . . .	37
3.5 Advanced navigation & collision avoidance . . . . .	41
3.6 Scientific instrumentation . . . . .	44
3.7 Communication links . . . . .	45
3.8 A near real-time environmental monitoring system . . . . .	52
3.9 Power system validation . . . . .	56
<b>4 Course control system: <i>Design and experimental validation</i></b>	<b>59</b>

4.1	Theory . . . . .	60
4.2	Experimental results and discussion . . . . .	72
4.3	Discussion . . . . .	83
<b>5</b>	<b>Gain-scheduled steering control</b>	<b>85</b>
5.1	Gain scheduling principles . . . . .	86
5.2	Three-state quasi-linear model frequency analysis . . . . .	88
5.3	Simulation results . . . . .	98
5.4	Field experiments . . . . .	103
5.5	Discussion . . . . .	112
<b>6</b>	<b>Estimation of the wave encounter frequency: <i>Wave-filtered steering control</i></b>	<b>115</b>
6.1	Wave filtering of the rudder control . . . . .	116
6.2	Wave encounter frequency estimation . . . . .	117
6.3	Heave dynamic model . . . . .	118
6.4	Switching-gain WEF estimation . . . . .	119
6.5	Offline experimental validation . . . . .	122
6.6	Wave-filtered steering control . . . . .	125
6.7	Discussion . . . . .	129
<b>7</b>	<b>Anti-Collision and anti-grounding system: <i>Design and experimental validation of a ENC-based approach</i></b>	<b>133</b>
7.1	MPC strategy for anti-collision & anti-grounding . . . . .	135
7.2	Environmental factors for collision avoidance scenarios . . . . .	137
7.3	Risk factors & collision costs . . . . .	139
7.4	Scenario definitions . . . . .	143
7.5	Hydrographic data extraction & transformation . . . . .	144
7.6	Architecture design . . . . .	147
7.7	Results . . . . .	149
7.8	Discussion . . . . .	168
<b>8</b>	<b>Long-endurance operations in harsh weather conditions: <i>Challenges and lessons learned</i></b>	<b>171</b>
8.1	Cooperative monitoring of HABs . . . . .	172
8.2	Risk assessment & mitigation . . . . .	174
8.3	Case study . . . . .	181
8.4	Discussion . . . . .	191
<b>9</b>	<b>Persistent observation of mesoscale oceanographic phenomena: <i>Modelling and simulations of a satellite-USV system</i></b>	<b>195</b>

9.1	Introduction . . . . .	195
9.2	Motivation . . . . .	196
9.3	System & scenario description . . . . .	197
9.4	Methods . . . . .	208
9.5	Results . . . . .	211
9.6	Discussion . . . . .	216
<b>10</b>	<b>A persistent sea-going platform for robotic fish telemetry: <i>Technical solutions and proof-of-concept</i></b>	<b>221</b>
10.1	Methods . . . . .	223
10.2	Results . . . . .	231
10.3	Discussion . . . . .	241
<b>11</b>	<b>Conclusions</b>	<b>247</b>
11.1	Summary of the main contributions . . . . .	248
11.2	Future works . . . . .	251
	<b>Appendices</b>	<b>255</b>
	<b>A</b>	<b>257</b>
	<b>References</b>	<b>263</b>





# Preface

This thesis is submitted in partial fulfilment of the requirements for the degree of Philosophiae Doctor (PhD) at the Norwegian University of Science and Technology (NTNU). This work was carried out at the Centre for Autonomous Marine Operations and Systems (AMOS) at the Department of Engineering Cybernetics, with the supervision of Tor Arne Johansen and Jo Arve Alfredsen. This work was supported by the Research Council of Norway (RCN) through the MASSIVE project (grant no. 270959).

## Acknowledgements

I would like to thank my supervisor Tor Arne Johansen, Professor at Department of Engineering Cybernetics, for his outstanding guidance, support and sharing of knowledge that walked me through these three years.

I would also like to thank my co-supervisor Jo Arve Alfredsen and Thor Inge Fossen, Associate Professor and Professor at Department of Engineering Cybernetics respectively, for their valuable contributions, both practical and theoretical, in the development of this thesis.

Some words are also dedicated to Pedro De La Torre, an all-round marine engineer with great practical skills, who helped me the most during each field campaign. Pedro taught me the seamanship and the basis to conduct safe (and dangerous) marine operations.

I have had a great time working with my colleagues at the Department of Engineering Cybernetics. In particular, I have appreciated the discussions with Artur Piotr Zolich, the original mind behind my project; with João Fortuna and Frederik Stendahl Leira, who helped me considerably in the hardware and software development; with Henning Øveraas, who joined the project in the final months of my PhD.

In parts of my study I have worked closely with the MSc students I have been co-supervising. Particularly Thea Kristine Bergh has been involved in work closely related to the material published in this thesis.

Peter Alexander Bailey Knutsen, Åsmund Stavdahl, Glenn Angell, Stefano Bertelli and Terje Haugen are acknowledged for their precious contributions to the mechanical design and production of the USV's equipment and parts, and for important support for logistics during field experiments. The LSTS team from the University of Porto is also acknowledged for their essential support they provided me on the software development and the important sharing of field experience. The SmallSat Lab team is finally thanked for the precious interactions and multiple discussions.

Finally, writing this thesis would never been possible without the support of my girlfriend Cindy, my mother Enrica and my sister Marta.

# Glossary

**API** Application Programming Interface.

**COG** Course-over-ground.

**DOF** Degrees Of Freedom.

**ENC** Electronic Navigational Chart.

**GNC** Guidance, Navigation and Control.

**GNSS** Global Navigation Satellite System.

**GPS** Global Positioning System.

**HAB** Harmful Algae Bloom.

**IMU** Inertial Measurement Unit.

**LOS** Line-Of-Sight.

**NTNU** Norwegian University of Science and Technology.

**SOG** Speed-over-ground.

**USV/ASV** Unmanned/Autonomous Surface Vehicle.

**UTC** Universal Time Coordinated Orbit.



# Chapter 1

## Introduction & motivation

With the emphasis on the ocean as the primary sink for greenhouse gases, ocean science has become critical to the understanding of climate changes. The warming of the planet driven by anthropogenic causes represents a profound threat to biodiversity. Monitoring environmental changes is of extreme urgency and to do so by moving towards sustainable and persistent ocean observation [1].

### 1.1 Ocean observation: from manned to unmanned

Despite our reliance on the ocean, less than 20% of the realm is explored [2]. Throughout history, humans have studied and navigated the seas and the oceans for centuries, starting with rudimentary instrumentation and improving their techniques decade by decade. What is nowadays called “modern oceanography” appeared as a scientific field in the late 19th century with the Challenger expedition in 1872-1876, which traveled nearly 70,000 nautical miles and sampled all oceans except the Arctic [3]. The Arctic was instead the main interest of the Norwegian scientist Fridtjof Nansen, who became known for the “Fram Expedition” [4] (see Figure 1.1) and his valuable discoveries in the fields oceanography, magnetism, and meteorology. Engineers and oceanographers have always strived to improve the scientific instrumentation needed to study the ocean. Efforts towards technological improvements were mostly driven by the fact that oceanographic exploration needed both to discover what was still unknown but also to reduce the cost of experiments. The understanding of climatic processes and their evolution builds on the observation of physical interactions in the ocean, which require continuous measuring of water and its constituents over time. Traditional ocean observation methods still are (for the most part) ship-based and involve exhausting information collection methods such as manual water sampling and vertical profiling using various instruments. The employment of different manual techniques successfully



Figure 1.1: *Fram* in Antarctica, 1910-1912.

led to large-scale monitoring of water properties such as salinity, temperature, and density, associated with the dominant ocean currents [5]. An inherent limitation, typical of ship-based observations, was the lack of resolution in time and space which prevented oceanographers to monitor and understand a number of important physical processes and their variability.

The glaring gap created by the lack of synoptic observations started to be bridged in the early 70s, when the first floaters and buoys (drifters) dedicated to ocean studies increased the spatio-temporal resolution and confirmed the necessity to abandon traditional observation methodologies in order to capture the variability of oceanographic processes. A first moored array was designed to reconstruct mesoscale phenomena<sup>1</sup> [6]. In those years, it became clear that the information collected with the adopted methods was not sufficient to reconstruct the observed phenomena. In other words, part of the information was lost when making observations.

Technologies improved quickly and in the late 70s the first ocean-observing satellite (SeaSat) was launched. Oceanography complemented with space science was revolutionary and put ocean studies under a different light, since it allowed some

---

<sup>1</sup>Phenomena occurring at scales from  $\sim 50 - 500$  km, and  $\sim 10 - 100$  days.

of the physical processes to be properly sampled and analysed with adequate resolution despite electromagnetic waves cannot penetrate the water column. Satellite-based remote sensing became available and the first sea surface temperature (SST) reconstructions were produced [7] with radiometers.

In parallel, the first ocean models were being developed and proved to be useful tools to fill in the gaps in the observations [8, 9]. Soon it was discovered the benefit of complementing observations with ocean models in what is nowadays called “data assimilation” [10–12].

The advent of more capable technological tools in the field of marine robotics enhanced data collection at large scales which was impossible to achieve through traditional ocean observation techniques. Traditional methodologies were not discarded, but could instead be complemented with the newer technologies. Coordinated robotic sampling programs were launched with the objective of studying the variability of physical oceanographic phenomena combining multiple source of in-situ information [13]. Nowadays, coordinated robotic exploration and observation is a consolidated field and the benefits are already proved in a number of applications [14–17].

## 1.2 Robotic marine platforms for ocean observation

The ability to monitor the oceans has improved significantly in the past decades. The combination of different remote sensing techniques and robotic platforms with high resolution ocean models has put oceanographic studies under a different light, where increased presence in-situ and information fusion at different spatio-temporal scales is becoming more feasible (see Figure 1.2).

To date, the primary platform to conduct oceanographic surveys is still the ship and studies indicate that its role cannot be completely replaced by the new, current tools [18]. Despite that, new methodologies based on technological advances in the field of marine robotics and remote sensing are increasingly being used to support data gathering tools. Unlike traditional methodologies, which in most cases involve the use of a single platform operating at fixed spatio-temporal scales, new approaches to ocean studies are rather centered on heterogeneity, i.e., multiple assets sampling diverse environments and providing information at different scales (see Figure 1.2).

Mainly, this is motivated by the fact that oceanographic phenomena happen at different spatio-temporal scales (see Figure 1.3) and, the single platform, is not capable alone to characterize the full dynamics of the observed phenomenon.

Figure 1.4 from [20] shows spatial and temporal scales of the most common marine and aerial systems employed in ocean studies. Small satellites and gliders operate at scales that mostly overlap in space and time and can as such enable



## 1. Introduction & motivation

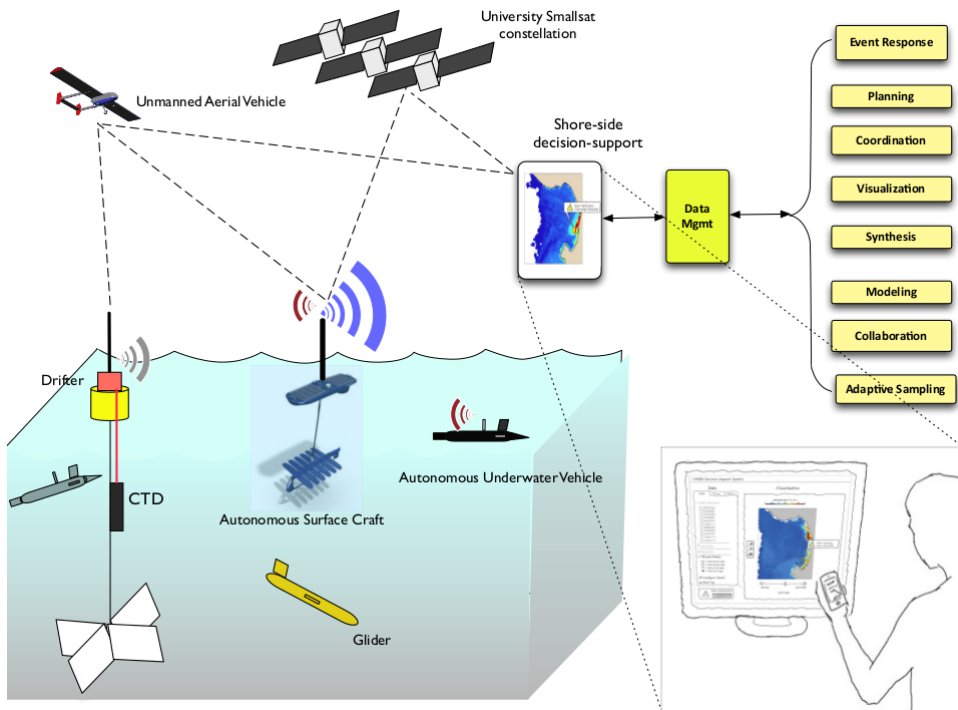


Figure 1.2: Conceptual view of a multi-platform, multi-scale field experiment involving ships, drifters, AUVs, gliders, satellite, and aerial drones. To be achieved, a synoptic understanding of the ocean requires a joint effort between a range of marine data sources. Figure credit: Kanna Rajan.

synoptic measurements of the same phenomena. The cooperation of both systems indicates coverage of phenomena in the range of 100 meters to 1000 kilometers in space, while from hours up to one year in time. Ship-based ocean observation also involves similar scales and points to well-consolidated methods ocean studies have relied on in the last decades. However, these involve higher operational cost and risk (for example, personnel costs, humans exposed to harsh environments), cause substantial release of  $CO_2$ , disturb the boundary layer significantly and, most importantly, they cannot scale across space and time and are therefore not suitable for the study of slow-changing oceanographic phenomena. Combining multiple different autonomous agents in a heterogeneous ocean sampling network has been demonstrated to increase the amount of information and, therefore the observation quality of physical phenomena beyond what each platform can achieve individually [16, 17].

Each platform has a specific coverage capability and resolution, which has to be

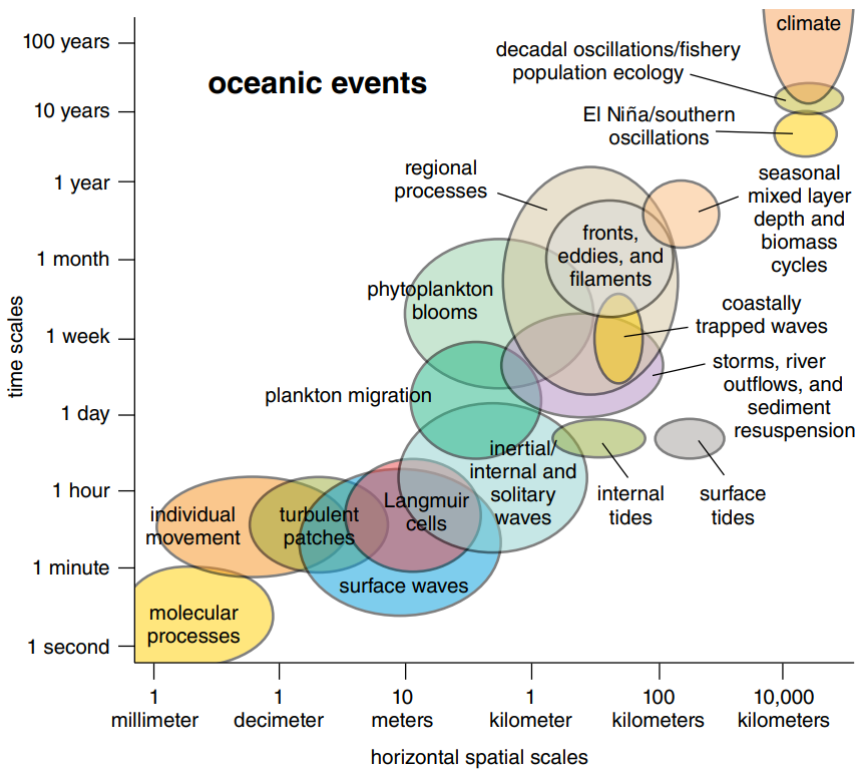


Figure 1.3: An illustration of the spatio-temporal extent of the most observed oceanographic processes. Figure credit: [19].

considered when planning and coordinating oceanographic surveys. As can be deduced from Figure 1.3 and Figure 1.4, mission planning is dictated by the resolution and the inherent dynamics of the ocean process being studied. This can span over several orders of magnitude from the millimetric observation of phytoplankton species, to mesoscale studies of algal blooms. Capturing the process at an adequate resolution is thus often only possible employing multiple sources. The unification of ocean models, remote sensing resources, different robotic nodes, and ship-based sampling is of primary importance in order to address this.

Mesoscale variability can be best analysed with semi-autonomous mobile platforms equipped with a suite of scientific payloads that can sample chlorophyll and biomass concentration, temperature, salinity, vertical current structure, sea surface height, turbulence etc. To date, oceanic exploration and monitoring of the upper water column, driven by scientific hypothesis and by means of robotic platforms, has already been demonstrated, e.g. [21, 22].

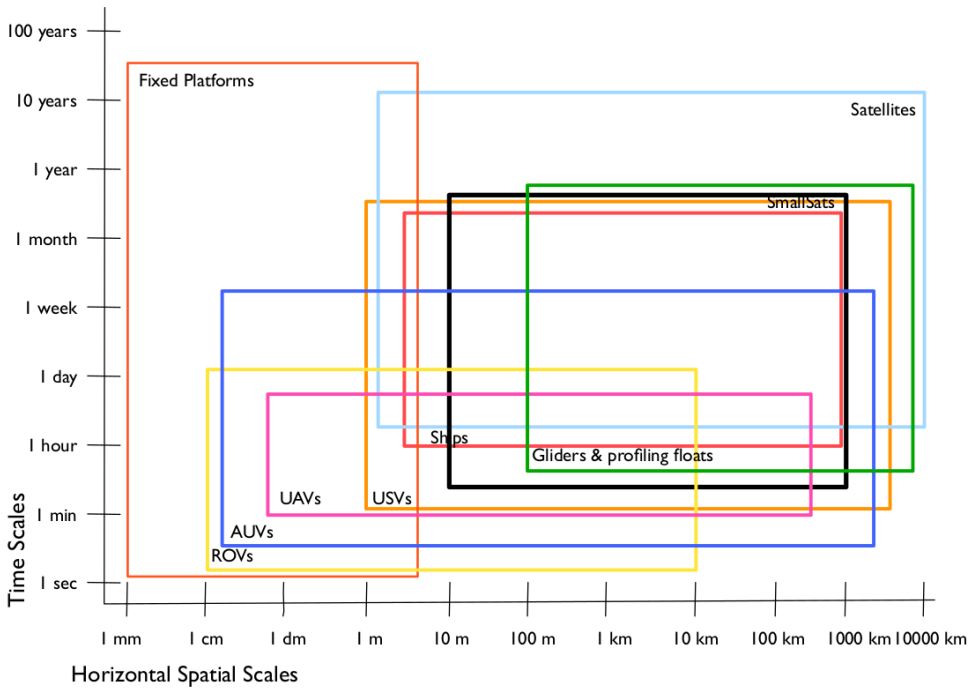
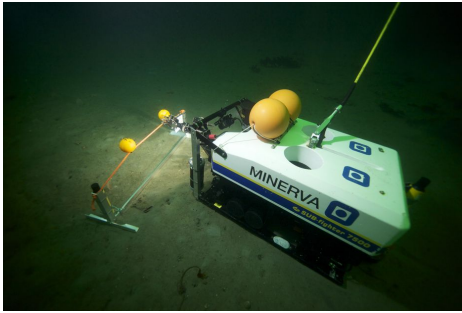


Figure 1.4: Temporal and spatial scales of marine systems. Figure modified from [20].

There exist three major categories of marine robots used in ocean studies: autonomous underwater vehicles (AUVs), autonomous or unmanned surface vehicles (ASVs/USVs), and remotely operated vehicles (ROVs) (see Figure 1.5). While ROVs need ship support for power and control AUVs and ASVs are equipped with onboard power (either from batteries or from an engine), data storage, and navigation units. To date, most of the AUVs and ASVs are equipped with active propulsion systems that make use of engines or electrical batteries to drive propellers and control their speed and heading as intended. This limits their endurance and therefore the time duration of scientific missions they can accomplish, which are bounded by the energy available onboard. As a consequence, human presence in the surroundings of these platforms is needed to retrieve them once unable to continue the mission.

Passive types of propulsion include instead buoyancy (glider AUVs), wavefoil (wave energy USVs), and currents (drifter USVs). Passive propulsion systems naturally involves less maneuverability and lower speeds compared to active propulsion systems, but can sustain longer operations as energy is harvested from the environment, as described in the following section.



(a) Minerva ROV, NTNU.



(b) Jetyak ASV, NTNU



(c) Harald LAUV, NTNU



(d) Otter ASV, Maritime Robotics

Figure 1.5: Main categories of marine robotic vehicles: remotely operated vehicles (ROVs), autonomous surface vehicles (ASVs), and autonomous underwater vehicles (AUVs).

### 1.3 Long-endurance unmanned surface vehicles

The lack of autonomous mobile platforms recording data continuously over long periods of time and in different areas of the globe, suggests the necessity to develop technologies that allow a persistent and sustainable presence at sea.

Oceans are populated with measurement buoys (drifters) that continuously sample their surrounding environment and transmit collected data to shore for further analysis and processing [23]. The network created by remote sensing buoys is however constrained by fixed position, short sensor range, lagrangian motion or limited payload energy.

Unlike common marine vehicles, surface or underwater gliders are designed to operate at sea for extended periods of time (i.e., weeks and months). The control of such robotic systems is, however, a challenging task due to the unpredictability of the environment that most of the time governs their behavior. This has a significant impact on the goal-driven intents associated to scientific missions, i.e., the onboard autonomy will require careful balancing between the value of informa-

tion related to the observed phenomenon and the ability to be at the right place at the right time. Moreover, communication challenges such as the limited bandwidth of satellite links influence the ability to provide valuable data to shore.

Several types of long-endurance, green-energy powered surface vehicles are nowadays available on the market, e.g., the Liquid Robotics Wave Glider [24], the Offshore Sensing SailBuoy [21], the AutoNaut [25], the Saildrone [26] or the L3 Technologies C-Enduro [27]. All show different architectural approaches, and find utility in various types of applications. Depending on their size and capacity, these platforms can be equipped with a wide-range sensor suite [28] that samples both near-surface atmospheric parameters (such as wind speed, pressure, temperature) [29] and features of the upper water column (for example, water salinity and temperature, sea currents, oxygen concentration) [30]. From ecological and biological perspectives, such systems are able to quantify natural phenomena related to animal primary productivity (by collecting chlorophyll and dissolved organic matter concentration), to assess the health of the ecosystem [31] (such as algal blooms, toxins concentration) or to study fish behavior and migrations via acoustic hydrophones [32], for example.

The benefits of employing these platforms in remote sensing applications have been presented in a number of works. In [33], for example, a Wave Glider is used to persistently collect chlorophyll-a data for several months and validate satellite measurements. This work demonstrates that in-situ measurements provided by long-endurance marine systems can be used, in combination with satellite observations, to provide a better understanding of the natural phenomena and climate changes of the planet. The Wave Glider was also used to validate winds measured by satellites in orbit [34] that use microwave sensors to observe the sea surface backscatter.

In [35], a harmful algal bloom (HAB) detection system is proposed using existing satellites (MODIS Aqua and Terra, NASA) and gives some indications on how predictions of HAB can be carried out. The 2021 IOCCG report [36] provides more examples of HAB warning systems and how the data can be collected.

Enhanced endurance and bigger payloads come, however, with a number of challenges related to the maneuverability and operational capabilities of such platforms, as described in Chapter 4 of this thesis.

Among the surface vehicles whose propulsion is controlled by the environment we find two main categories: wind-powered (or wind-propelled) USVs (e.g., the Saildrone [26] and the SailBuoy[21]) and wave-powered (or wave-propelled) USVs (e.g., the Wave Glider [24] and the AutoNaut [25]). Unlike motored marine robots, wave-propelled and wind-propelled vehicles cannot directly control their speed, but rely instead on the forces exerted by the environment to navigate as intended.

Given the strong influence that environmental drift forces have on the navigation capabilities of such vehicles, it is chosen to investigate and design a course-over-ground (COG) control system for a wave-propelled USV. The reason for this is that, in order to perform scientific surveys the USV needs to be able to navigate according to an intended behaviour and to reach the designated locations. When the vehicle is subject to significant drift, heading control would not steer the USV towards the target location and crab angles would be observed.

The following three sections describe respectively the USV used in this research, the AutoNaut, and two ocean studies applications in which the developed system is employed.

#### 1.3.1 The AutoNaut USV

The AutoNaut is a wave-propelled surface vehicle whose heading, course-over-ground (COG) and speed are influenced by the environmental forces due to winds, waves and surface currents. The AutoNaut is a commercially available platform [25] equipped with a patented, passive propulsion system, and manufactured by the British AutoNaut Ltd company.

Two pairs of spring-loaded submerged hydrofoils are connected at the bow and stern by two vertical struts (see Figure 1.6). When a surface wave lifts the bow or the stern of the vehicle, the corresponding strut lifts the foils, which are subsequently pulled back by the spring generating a forward thrust. This self-propelling mechanism limits the speed achieved by the vessel during operations up to 3-4 knots. However, the platform is equipped with a small thruster that can be actuated by the collision avoidance algorithm to enable sharper maneuvers or whenever surface waves are too small to produce acceptable propulsion. The heading of the vessel is controlled by means of a rudder commanded by the navigation control unit, and can turn up to  $\pm 45^\circ$  relative to its centered position.

The hull is divided into two main water-tight compartments, where batteries, computers and some sensors are hosted. However, most of the sensors needed for navigation and environmental data collection are placed on the keel or on the deck, as described in Chapter 3.

The manufacturer usually sells the platform equipped with third-party hardware and software for command, control and communication functionalities. The AutoNaut was purchased by the Department of Engineering Cybernetics (NTNU), in 2017, with the only scientific instrumentation physically installed. The whole hardware and software architecture is designed at NTNU [28] and documented in this thesis. Two applications to ocean studies in which the AutoNaut was involved are introduced in the following sections.

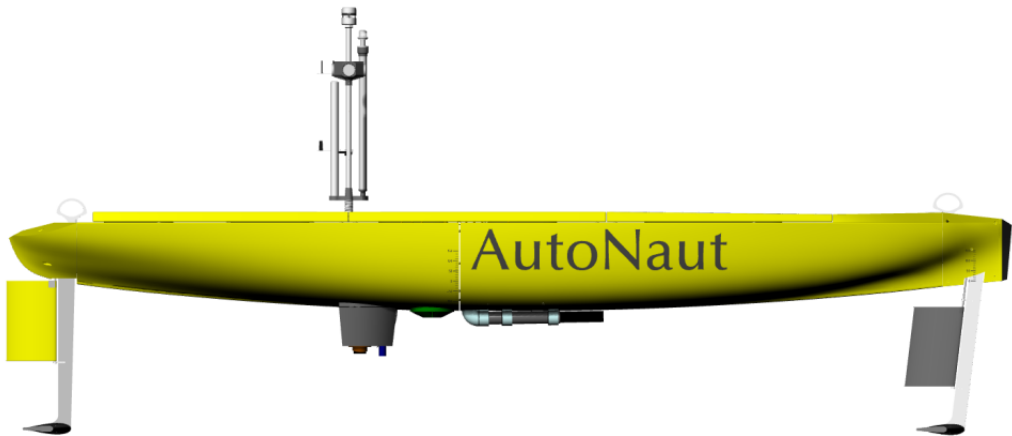


Figure 1.6: Side view of the NTNU AutoNaut and its main components: passive bow and aft hydrofoils, submerged scientific payload, mast sensors and antennas, rudder.

### 1.3.2 Persistent observation of harmful algal blooms

The frequency of HABs is increasing in step with increased human activity and eutrophication and, depending on the type of bloom, in some cases with the increased temperature of the oceans [36, p. 17]. HABs occur in oceans and lakes and can be highly toxic to aquatic and non-aquatic life, causing harmful effects by anoxia (oxygen depletion). These effects reduce the water quality and leads to significant recreational, economic, and ecological impacts [36]. Because the blooms typically occur in dynamic and optically complex water systems, space-based remote sensing systems are desired to provide radiometry services multiple times a day [37]. Accordingly, the International Ocean-Colour Coordinating Group (IOCCG) states that “it is necessary to take a multi-layered approach to HAB studies, amalgamating information from multiple satellites, multiple sensors, and multiple adjunctive data sources to form a multidimensional understanding of the nature and dynamics of HAB” [36, p. 11]. While global environmental changes happen at large temporal and spatial scale, the study of phenomena evolving at smaller scales can provide valuable insights and enhance our understanding of the global, slow-changing dynamics of our planet.

The mesoscale variability ( $< 1000 \text{ km}^2$ ) can be best observed with mobile platforms that can sample a wide range of properties such as chlorophyll-a concentration, oxygen concentration, biomass, anthropogenic runoffs, temperature, salinity, vertical current structure, seafloor topography, and turbulence. Unmanned vehi-



cles (such as UUV, USV, UAV) are flexible assets that can individually observe and acquire data from various target areas [1]. However, no single platform is ideal for full coverage of oceanographic mesoscale phenomena [36]. Furthermore, to gain useful insights based on observations from different assets, they should be coordinated to observe the same patch of the ocean near-simultaneously, within time scales that fit the observed phenomena, i.e., synoptic observations [38]. The physical and operational diversity across such mobile platforms may result in complementary spatial and temporal sampling capabilities.

As mentioned earlier, combining multiple different autonomous agents in a heterogeneous ocean sampling network has been demonstrated to increase the amount of information and, therefore the observation quality of physical phenomena beyond what each platform can achieve individually. Some works show the possibility to utilize such platforms to validate satellites measurements [33, 34]. Nevertheless, the current state of the art lacks detailed modeling of marine operations in which the science-driven objectives for unmanned assets are based on processed data from small satellites.

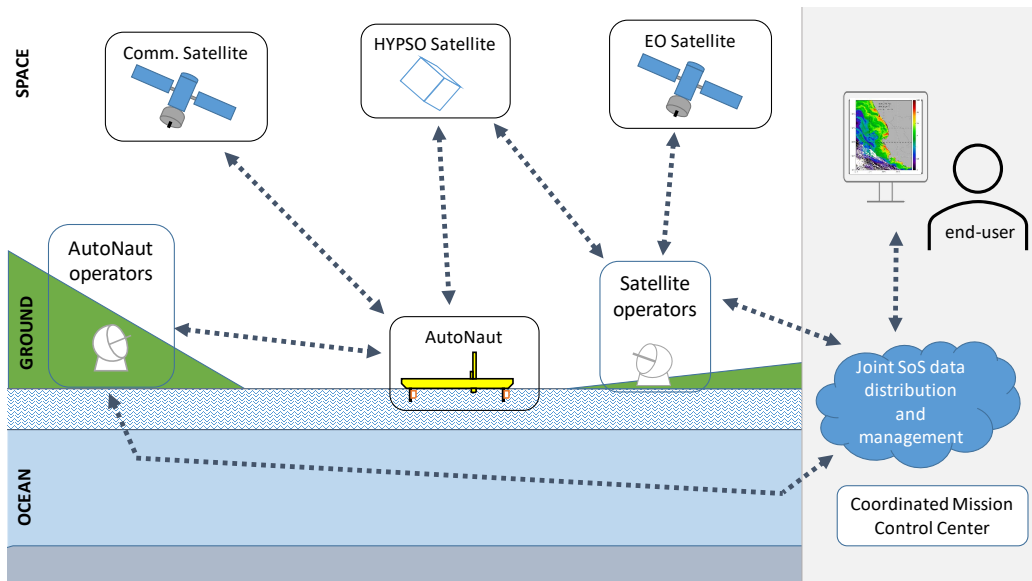


Figure 1.7: Persistent monitoring of mesoscale oceanographic phenomena: the proposed system architecture.



In this thesis, Chapter 9 is based on the manuscript [39], and describes a satellite-USV system for persistent observation of mesoscale oceanographic phenomena. Figure 1.7 shows different models of the proposed concepts. The proposed models rely on satellite imagery, which is used to detect and classify the occurrence of a natural phenomenon in the ocean, e.g., a front or an algal bloom. The raw or processed information is communicated to land or directly to the USV. In the first two cases, further processing of the received data is used to confirm the event and to generate a mission plan that is communicated to the USV. In the third case, the USV's onboard software synthesizes autonomously the mission plan according to the information received from space. Benefits and limitations of three scenarios are compared and discussed, according to theoretical considerations, simulation and experimental results.

### 1.3.3 Acoustic fish telemetry

Fish movement and migration are essential mechanisms for the productivity and health of ocean ecosystems and, consequently, for the sustenance and livelihoods of people and communities around the world [40]. Fish migrations regularly manifest themselves as remarkable natural phenomena that probably have intrigued humans at all times, and the quest to understand them has developed into an area of vigorous scientific inquiry [41–43]. In a time of unprecedented anthropogenic pressures on the oceans [44], knowledge on how fish move and distribute over different scales of space and time, how they interact with their biophysical environment, and how this affects their reproduction and survival is of crucial interest and plays an essential role in developing and implementing well-advised ocean management and conservation strategies [45, 46]. Central to research in this area is our ability to make observations of fish movement of sufficient quality and quantity on relevant temporal and spatial scales. However, the opacity, inaccessibility, and the sheer vastness of the ocean render the pursuit of such observations a far from trivial task.

Driven by rapid technological advances in microelectronics and sensor technology, acoustic fish telemetry has developed over the recent decades into a viable approach for acquiring remote observation of the behaviour of free-ranging fish in the marine environment [47–49]. When attached to or implanted into a fish, an acoustic transmitter tag enables remote underwater detection of a fish' presence and identity at ranges typically  $< 1$  km using a matching acoustic receiver. Detection range depends on the tag's power output and carrier frequency, receiver sensitivity and the intrinsic properties of the acoustic channel, while its operating life ranges from days to years depending on transmitter power level, signal modulation and battery capacity [50]. The growing availability of miniature low-power

microelectronic sensors and their integration into tags has further paved the way for acoustic sensor transmitters that allow remote sensing of physiological (e.g., heart rate, respiration and tailbeat frequency) and ambient physical variables (e.g., temperature, salinity and water depth) pertaining to the fish, providing physiological and environmental context for a plausible eco-physiological interpretation of fish movements [51].

Successive detections of a tagged fish at different receiver locations make it possible to establish a chronological account of a fish' movement pattern. Depending on the configuration of the receiver system, a single transmission may also permit fine-scale localisation of the fish in two or three dimensions [52]. The acoustic receiver thus comprises the inseparable and essential second half of a telemetry system as its performance and placement, together with the transmitter and the channel characteristics, jointly determine the probability of making detections. Although active (mobile) tracking of fish is regularly used and serves as a viable option in many scenarios [53], the advent of cost-effective automatic monitoring receivers has made it feasible to deploy entire systems of moored receivers (often referred to as passive acoustic telemetry) that enable continuous year-round monitoring of aquatic habitats over a wide span of geographical scopes [48]. Such stationary receiver systems are typically organised as clusters of transects [54, 55] or arrays [56–58], or in less regular structures, e.g., focusing on monitoring of specific landmarks or bottlenecks where the fish are expected to dwell or pass [59].

Apart from the information obtained from being non-present, acoustic transmitters residing beyond the detection range of receivers for prolonged periods of time are obviously of limited value. The data yield, and ultimately the scientific outcome of telemetry studies, is thus inherently linked to receiver-side design parameters, such as the number of receivers used, how they are distributed in space and time, as well as their technical performance (e.g., sensitivity, bandwidth, operational life). The number of receivers that can be deployed in a passive telemetry system is usually subject to practical and economic constraints and can not scale cost-effectively with the size of the target area to make complete coverage a realistic option in many studies. Optimal placement and configuration of receiver transects and arrays with respect to detection probability have been investigated and established [58, 60, 61]. However, the risk of low detection rates and location biases in movement data will necessarily increase with a decreasing ratio of receivers to the size of the sample area.

The Chapter 10 is based on the manuscript [62], submitted to the *Frontiers in Marine Science* journal, in which it is experimentally demonstrated that the AutoNaut can enhance the capacity of acoustic detections of acoustic receiver arrays,

typically employed to study the migration patterns of tagged fish.

### 1.4 Thesis contributions and outline

The unique structural characteristics of the AutoNaut USV make it an interesting platform to study from control and autonomous navigation perspectives. Depending on the sea state, navigation performances may deteriorate and eventually the destination might not be reached at all (see Chapter 4 and Chapter 5). Moreover, the long-endurance unmanned vehicle demands high levels of autonomy with quite limited backup solutions available. To minimize the risk of collision and grounding, loss of maneuverability, and situations that might damage the USV or endanger other people, risk-aware autonomous navigation must be ensured. The overall main research question of this thesis is the design, development, practical integration and experimental validation of an autonomous marine robotic platform whose objective is to operate remotely and persistently, and provide oceanography and marine biology communities a deeper insight into the evolution of natural phenomena in the ocean.

In this large scope, relevant contributions are presented and belong to different scientific domains, e.g., hardware/software design and integration, control theory, oceanography and animal biotelemetry.

The thesis is therefore split in two parts, whose principal respective contributions are related to i) the design and validation of an onboard control and communication system for the AutoNaut USV and ii) testing and validating the proposed architecture within different research applications.

In the first part of this thesis (**Part I**), the design and validation of the proposed system are supported with extensive experimental results achieved in Norwegian fjords and Atlantic ocean. This work aims at showing the operational challenges and limitations related to the autonomy of the AutoNaut. Despite the modeling and control design presented in this thesis is unique for the considered wave-propelled USV, theoretical considerations are also relevant to similar marine robots that transform environmental forces into propulsion.

In the second part of this thesis instead (**Part II**), the performances of the developed system are evaluated and the benefits of employing the AutoNaut in different ocean research studies are discussed.

This thesis complements several publications and is organized as follows.

#### **Part I**

Chapter 2 of the thesis introduces the reader to USVs, describing the general components, and common guidance, navigation and control techniques implemented

onboard.

Chapter 3 of the thesis presents a detailed overview the designed control and communication architecture implemented onboard the AutoNaut (**Paper A**). Chapter 4 delves into the design and validation of the course control system implemented and tested on the USV (**Paper B**). The presented course control architecture is supported with theoretical considerations including a detail mathematical model, and with practical experiments to confirm the hypotheses.

Chapter 5 extends the considerations of the previous chapter, in which it is indicated that gain-scheduling based on the measurements of the sea current velocity and of the USV's speed-over-ground (SOG) is a viable option to achieve stable navigation in situations of low maneuverability (**Paper C**). Again, theoretical studies are supported with field results.

In Chapter 6, a nonlinear observer for the estimation of the wave encounter frequency (WEF) is tested (**Paper D**). Knowledge of the WEF is important for two reasons: it improves the USV's perception and situational awareness of the environment; it is employed in wave filtering techniques used to remove wave-induced components from the rudder command signal. Experimental results validate the method.

Chapter 7 discusses the importance of anti-grounding and anti-collision for a wave-propelled USV. This chapter evaluates the benefits of using a scenario-based model predictive control (SB-MPC) algorithm to avoid static and dynamics obstacles at sea (**Paper E**). Once again, theoretical investigations are supported with simulations and experimental results.

In the last chapter of the first part of the thesis (Chapter 8), the challenges and lessons learned from operational experience gathered in the field are presented and discussed (**Paper F**).

## **Part II**

The second part of this thesis includes two use cases that see the AutoNaut USV employed in ocean studies. Long-endurance capabilities make the AutoNaut a suitable platform for the persistent observation of mesoscale oceanographic phenomena (**Paper G**). In this work, the system is modeled with a System-of-Systems (SoS) approach coupled with operational simulations. As described in the introduction of this thesis, the use of long-endurance USVs together with remote sensing assets is shown to be a benefit in ocean studies. In the first use case, the modelling of a satellite-USV system for the study of mesoscale oceanographic phenomena is presented.

In addition to being capable of extended operations, the AutoNaut USV is also silent since no active propulsion is generally employed. This make the wave-propelled vehicle suitable to study fish migration in fjords and their outlets, given the reduced acoustic disturbance at the boundary layer. In Chapter 10 it is described how the AutoNaut can be used to enhance the detection capacity in acoustic re-

ceiver arrays, widely employed in fish migration studies (**Paper H**). Finally, the author has actively contributed to the articles [63] and [64], despite these are not presented in this thesis.

### 1.4.1 Contributions

The list below contains all the articles, co-authored by the author of this thesis, that are either accepted for publication or submitted for review

- **Paper A:** A. Dallolio, B. Agdal, A. Zolich, J. A. Alfredsen and T. A. Johansen, "Long-Endurance Green Energy Autonomous Surface Vehicle Control Architecture," OCEANS 2019 MTS/IEEE SEATTLE, 2019.
- **Paper B:** A. Dallolio, H. Øveraas, J.A. Alfredsen, T.I. Fossen, T.A. Johansen, "Design and Validation of a Course Control System for a Wave-Propelled Unmanned Surface Vehicle". Field Robotics, August 2021.
- **Paper C:** A. Dallolio, H. Øveraas, T.A. Johansen. "Gain-Scheduled Steering Control for a Wave-Propelled Unmanned Surface Vehicle". Ocean Engineering, (submitted in October 2021).
- **Paper D:** A. Dallolio, J. A. Alfredsen, T. I. Fossen, and T. A. Johansen, "Experimental Validation of a Nonlinear Wave Encounter Frequency Estimator Onboard a Wave-Propelled USV," IFAC-PapersOnLine, vol. 54, no. 16, pp. 188–194, 2021, 13th IFAC Conference on Control Applications in Marine Systems, Robotics, and Vehicles CAMS 2021.
- **Paper E:** A. Dallolio, T. K. Bergh, P. De La Torre, H. Øveraas, T.A. Johansen, "ENC-based Anti-Grounding and Anti-Collision System for a Wave-Propelled USV", OCEANS 2022, Chennai, India (accepted).
- **Paper F:** Henning Øveraas, Alberto Dallolio, Pedro R. De La Torre, Tor A. Johansen. Field Report: Long-Endurance Operation of Wave-Propelled and Solar-Powered Autonomous Surface Vehicle in Harsh Weather. Field Robotics (submitted).
- **Paper G:** Dallolio A, Quintana-Diaz G, Honoré-Livermore E, Garrett JL, Birke-land R, Johansen TA. "A Satellite-USV System for Persistent Observation of Mesoscale Oceanographic Phenomena". Remote Sensing. 2021; 13(16):3229.
- **Paper H:** A. Dallolio, H. B. Bjerck, H. A. Urke, and J. A. Alfredsen, "A persistent sea-going platform for robotic fish telemetry using a wave-propelled USV: technical solution and proof-of-concept," Frontiers in Marine Science (submitted), 2021.

## Chapter 2

# USV background

### *An introduction to guidance, navigation and control*

With the advent of more compact, effective, and affordable navigation equipment, as well as more powerful and reliable wireless communication systems [65], the employment of USVs has increased in a number of applications related to the ocean. Nowadays, unmanned surface platforms can be customized in a cost-effective way for a wide range of applications spanning from scientific research to resource exploration (e.g., oil and gas industry), to military uses and other applications. Over the past decades, numerous universities, research institutions and military apparatuses have begun developing unmanned surface platforms tailored for the specific application [66]. Current technological development remains immature and most of the existing USVs are bounded to be experimental platforms with limited autonomy, endurance and payloads [67]. Most of them still require extensive human intervention (e.g., remote control) and proximity to shore or to support ships to complete the designed missions successfully. Despite the fact that USVs are starting to populate commercial markets, the majority of industrial-level platforms are still employed in military and research applications. Despite this, only semi-autonomous rather than fully-autonomous USVs have normally been used, due to the numerous challenges faced by the latter, such as limited onboard autonomy. Reliable and autonomous guidance, navigation and control (GNC) functionalities for all different operating conditions and environments are still core issues addressed by researchers in the field. This includes sensor, actuator and communication failures.

## 2.1 Major architectural elements

Depending on specific application, USVs may be equipped differently depending on their functionalities. However, the following basic elements are typically included in most of the platforms:

- *Hull and its elements*: hulls can be grouped in monohulls and multihulls. Whereas monohulls can be rigid, inflatable hulls or kayak-like hulls, multihulls can be either catamarans or trimarans. Variations in hull design depend on the application. For example, inflatable hulls are typically employed in military applications because of their endurance and payload capacity. Kayak-like and catamaran-like designs are popular because they are easy to manufacture, modify and equip. Catamarans and trimarans instead, are often preferred due to their greater navigation stability, decreasing the risk of capsizing in rough weather.
- *Propulsion and power system*: most commonly, speed and heading/course control of most existing USVs are provided by means of propeller and rudder, respectively. Catamarans-like USVs are commonly steered by differential thrust by means of two independent motors attached to each hull. Since USVs are typically not equipped with an additional side thruster, they can be considered under-actuated robots. In other words, the number of DOF of motion is greater than the available actuators. This makes the safe and precise control of under-actuated USVs a significant challenge. Despite that, the literature presents several methods to control such systems [68–70]. Fully- and over-actuated vehicles are instead relatively easier to operate than under-actuated ones, but come with comparatively higher costs [71].
- *GNC unit*: as the most vital component onboard a USV, GNC modules are generally constituted by computers, sensors and software, which together are responsible for managing the entire system. Diverse sensors and hardware components can be interfaced to the GNC unit, and combine navigation and control with data collection. Alternatively, one could decouple the scientific instrumentation from the sensors related to navigation and control [28].
- *Communication systems*: communication systems can include wireless communication (e.g., cellular network, satellite, VHF radio, etc) with a ground control station and other vehicles to achieve collaborative tasks, but may also include onboard wired/wireless communication with onboard sensors, actuators, and other hardware/software equipment.
- *Navigation instrumentation*: includes all the sensors and hardware components that are needed in order to control the USV, e.g., global positioning system (GPS), automatic identification system (AIS), inertial measurement

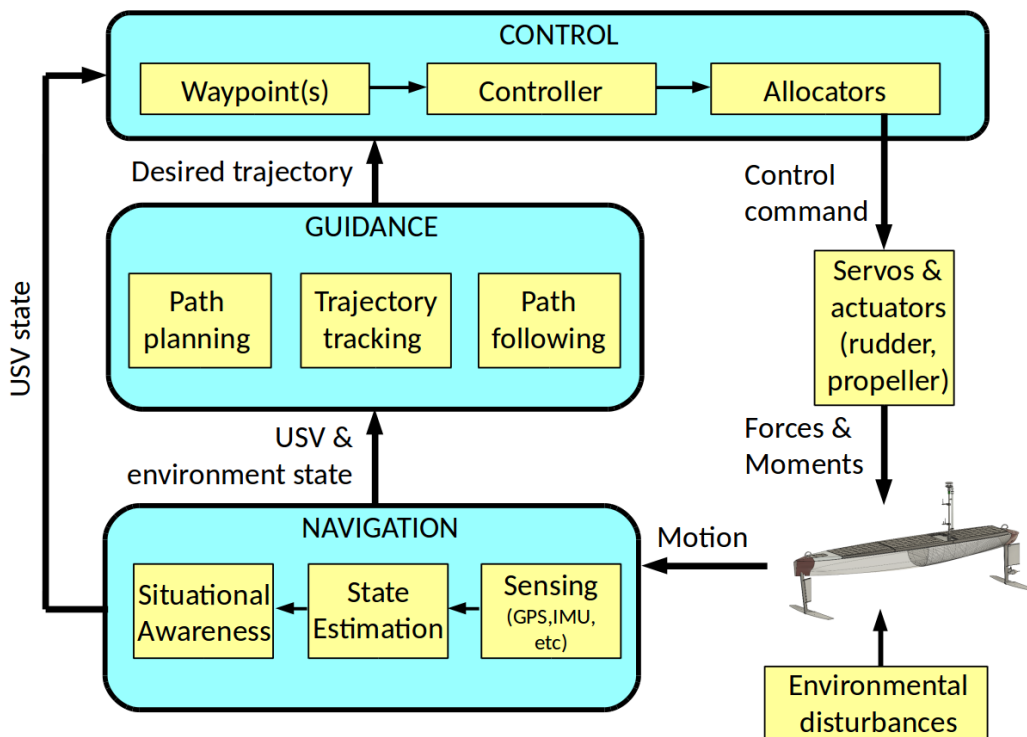


Figure 2.1: General architecture of a USV's GNC system.

unit (IMU), compass, sonar, laser detection and ranging (LIDAR), radar, camera, etc.

- *Scientific payload*: the scientific payload is the ensemble of sensors that collect data and serve the dedicated scientific purpose. Currently, USVs can be customized with wide-range payloads that target a variety of properties both related to the upper water column but also to the oceanic atmospheric environment.

## 2.2 Common guidance & navigation approaches

The fundamental elements needed to operate autonomously surface vehicles are typically the guidance, navigation, and control subsystems (see Figure 2.1) [72]. These subsystems interact with each other and are responsible for different functionalities core of the vehicle's autonomy. To achieve robust and reliable navigation performances, the three units need to be tuned accordingly to avoid that degraded performances of a single subsystem have an impact on the whole control system.



In general, the *guidance system* is responsible for continuously generating and updating smooth and feasible path or trajectory commands that are forwarded to the control subsystem and according to the information received by the navigation subsystem. The *navigation system* is responsible for the estimation of the current (and future) USV's and environment states<sup>1</sup>. This is usually achieved by using the knowledge of the previous (and current) states. Both the vehicle's and the environment's states can be estimated from the measurements provided by the onboard sensors. Finally, the *control system* computes the proper control command that has to be communicated to servos and actuators. Computation of the correct control command can be based on the knowledge of the USV's response to certain inputs, i.e., on the knowledge of the specific forces and moments that will be exerted on it and knowledge of its resulting state. As indicated in Figure 2.1, the motion of the vehicle is the combination of two types of forces and moments: those caused by the onboard steering system and those caused by the environment, that acts as a disturbance.

### 2.2.1 Common guidance techniques

The guidance system is an essential component for increasing the navigation autonomy of the USV. According to the control literature, the different motion control scenarios are typically classified as *path planning*, *trajectory tracking* or *path following* scenarios. Tracking control systems can be further designed for *target tracking* and *path tracking*. For example, a target-tracking system tracks the motion of a stationary or moving target whose trajectory can be observed. Some examples of target-tracking guidance systems are *line-of-sight* (LOS), *constant bearing* (CB) and *pure pursuit* (PP) guidance [72].

*Trajectory tracking* guidance systems are designed for tracking a smooth time-varying trajectory  $y_d(t) \in \mathbb{R}^m$ , where the desired speed and acceleration are obtained from time-differentiation of  $y_d(t)$ .

Whereas a trajectory describes the motion of a moving object through space, as a function of time, a path involves spatial rather than temporal constraints. In other words, *path following* is the task of following a predefined path independent of time. A commonly adopted path following method is again LOS guidance, where a vector (the *LOS vector*) from the USV to the next waypoint or a point on the path between two way points can be used for both course and heading control.

---

<sup>1</sup>The vehicle's state collects physical information that describe its motion such as position, orientation, direction of motion, speed, and acceleration; the environment's state quantifies instead all the disturbances affecting the vehicle's navigation, e.g., currents, winds, waves.

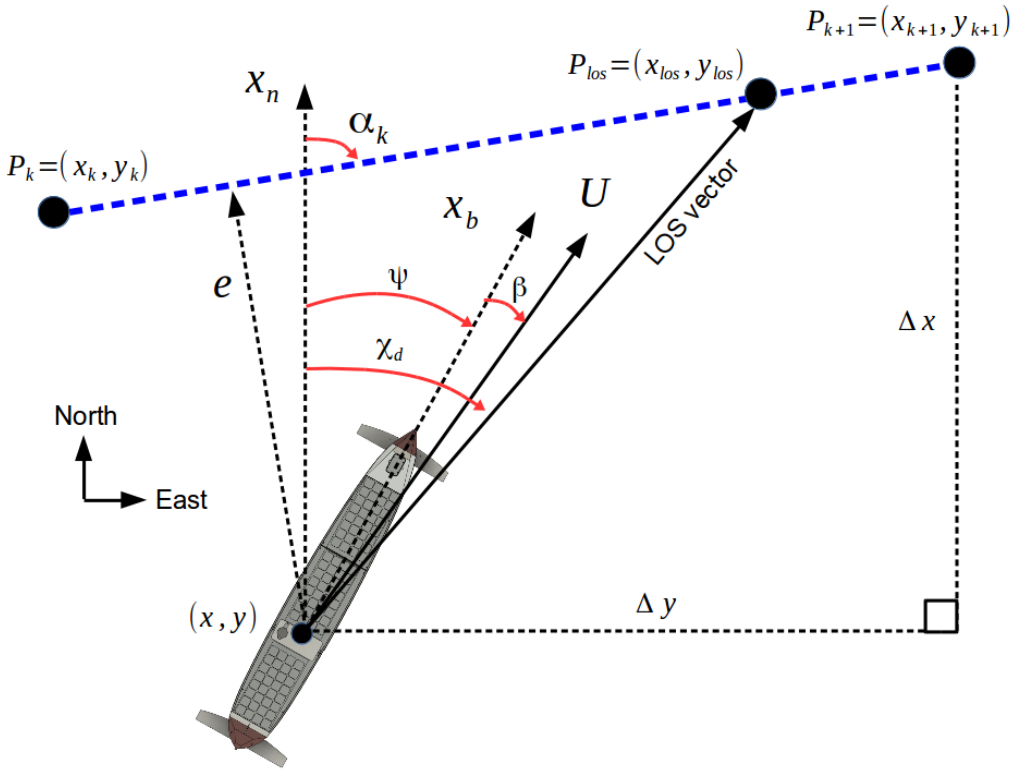


Figure 2.2: LOS guidance where the desired course angle  $\chi_d$  is chosen to point towards the LOS intersection point  $P_{los} = (x_{los}, y_{los})$ .

### Path following of straight-line paths: LOS steering laws

The most employed technique in path following is line-of-sight (LOS), a successful guidance method that is widely employed in guidance techniques of missiles and marine vehicles. Its application to USVs has been successfully demonstrated in a number of works [73–77].

According to [78], two different guidance principles can be used to steer along the LOS vector: *enclosure-based steering* and *lookahead-based steering*.

Figure 2.2 shows the geometrical representation of a LOS steering system. In the 2-D horizontal plane, the cross-track error  $e$  and the speed of the USV are defined as

$$e(t) = -[x(t) - x_k] \sin(\alpha_k) + [y(t) - y_k] \cos(\alpha_k) \quad (2.1)$$

and

$$U(t) := \|v(t)\| = \sqrt{\dot{x}(t)^2 + \dot{y}(t)^2} \geq 0, \quad (2.2)$$

respectively.

The enclosure-based strategy for driving the cross-track error  $e$  to zero is then to direct the velocity vector  $U$  towards the intersection point  $P_{los}$ . This can be achieved by directly assigning  $\chi_d$  as shown in Figure 2.2. The desired course angle is therefore computed as

$$\chi_d(t) = \text{atan2}(y_{los} - y(t), x_{los} - x(t)), \quad (2.3)$$

where  $\text{atan2}(\cdot, \cdot)$  is the four-quadrant version of  $\arctan(y/x) \in [-\pi/2, \pi/2]$ .

The lookahead-based steering method is slightly more complex and the desired course computation is split in two parts:  $\chi_d = \chi_p + \chi_r(e)$ , where  $\chi_p = \alpha_k$  is the path-tangential angle (see Figure 2.2), while  $\chi_r := \arctan(-e/\Delta)$  is a velocity-path relative angle as described in [79].

In this research, a LOS *enclosure-based steering law* is employed to control the course/heading of the AutoNaut USV, as described in Chapter 4.

### Path planning methods

Path planning is a critical part in the development of the USV's control system, and its main objective is to determine optimal trajectories to guide the vehicle. It can be defined as the problem of finding a route between two positions, assuming that the route should be collision-free, physically feasible according to spatial constraints, and possibly satisfy certain optimization criteria with respect to, for example, space and time, energy consumption, operational risk, and others. Also, while trajectory planning involves geometric paths endowed with temporal properties, path planning is typically defined within purely geometric spaces.

In the literature, path planning is commonly categorized as *global path planning* and *local path planning* [80]. Global path planning aims at finding a safe path between the initial and the goal states considering known obstacles and assuming that a complete model of the environment is available. Local path planning, instead, aims at generating a feasible path which is safe with respect to the dynamic obstacles in its vicinity. This is achieved by using the information acquired with onboard sensors, which make the USV situational aware of the surrounding environment.

The literature presents a wide variety of path planning algorithms. According to [81], for example, path planning algorithms can be based on a *classical*, *advanced* or *hybrid* approach.

The classical approach consists of two steps being the environment modelling and the search of the optimal path. Algorithms based on this approach are most commonly used for global offline path planning with static obstacles, where there is usually no need for path re-planning or local collision avoidance.

On the contrary, algorithms based on the advanced approach are commonly used

to deal with dynamic obstacles, path re-planning and local collision avoidance in real-time. Most commonly, these algorithms do not need prior modelling of the environment. Some examples are machine learning algorithms and potential field methods.

Finally, algorithms based on hybrid approaches result from a combination of classical and advanced methods. These algorithms combine several path planning algorithms to ensure safe and feasible navigation both globally and locally.

### 2.2.2 Navigation systems

The safe and efficient control of USV heavily depends on an appropriate navigation system showing sensing, state estimation, environment perception, and situational awareness capabilities.

Appropriate sensing capabilities are a required to improve the navigation performances of vehicles at sea. The raw measurements are processed and transmitted to the navigation computer which uses a state estimator capable of noise filtering, prediction and reconstruction of unmeasured states [72]. In general, the position, orientation and speed of the vehicle are provided by the global navigation satellite systems (GNSS) and compass systems. Knowledge of body accelerations and angular rates can be obtained with IMUs. Determination of its full state requires, therefore, reconstruction based on measured information. Critical to this matter are the state estimation techniques, which reconstruct the current state of the vehicle. Most common state estimation methods are based on conventional GNSS/IMU approaches and, performance specifications often require that such systems provide high-resolution estimates. Unfortunately, these can be very imprecise in many applications due to several reasons as environmental noise, accumulative errors resulting from measurement drift, model uncertainties and sensor faults.

The most common state estimation techniques achieved with GNSSs and IMUs involve *state observers* (or state estimators) [72, 82], which are systems providing an estimate of the internal state of a given system, from measurements of its inputs and outputs. In many applications of control theory, knowing the state of a system is necessary to control it and make it stable. This is motivated by the fact that in most practical cases, the physical state of the system cannot be determined by direct observation. The literature is rich of examples of linear and nonlinear observers employed to estimate, for example, the position and velocity of a surface vehicle [83]. The Kalman Filter (KF) [84] and its variations (e.g., EKF, UKF) are commonly used to reconstruct part of the system's state [85]. Some examples are found in [86], where the position and velocity are estimated using an EKF on the basis of both GNSS and compass measurements, and in [87], where an adaptive UKF is proposed for the state estimation without *a priori* knowledge of the noise distribution.

In addition to conventional state estimation methods, active ranging sensors (LIDAR, radar and sonar) and vision-based approaches can be employed for the estimation of the USV state. Estimation based on these sensors find their utmost utility when GNSS systems loose signal (sensor jamming).

## 2.3 Control of unmanned surface vehicles

With the considerable improvements in the field of control theory, state-of-the-art control techniques are continually being designed and implemented to enhance navigation performances in the marine robotics research community [72, 88]. Modern control systems are based on a variety of design techniques such as PID control, nonlinear control theory, linear quadratic optimal control,  $H_\infty$  control, neural networks, fuzzy systems, etc. In order to design and implement the control system of a USV, one has to deal with three major topics: USV modelling, design and embedded systems development.

The design of an effective controller can hardly be achieved without a model of the system to be controlled. The model not only finds utility to control the system in the field, but also to simulation studies. Modelling the vehicle dynamics require prior investigation of a mathematical model and of its parameters. In general, a physical USV model consists of its kinematics and kinetics [72].

Since USVs are not subject to requirements of cargo stability or passenger comfort, their primary control objective is to follow an intended path. This means that the general 6-DOF model can be simplified to consider only the dynamics in surge, sway and yaw, while the dynamics associated with the motion in roll, pitch, and heave are typically neglected to keep the model rather simple as described in [72].

### 2.3.1 Kinematic modelling

The general kinematic model [72] in planar motion and without disturbances can then be expressed as:

$$\dot{\eta} = R(\psi)\mathbf{v}, \quad (2.4)$$

where  $\eta = [x, y, \psi]^T$  is the vector of position and heading in the earth-fixed reference frame,  $\mathbf{v} = [u, v, r]^T$  is the vector of associated linear and yaw velocities in the BODY-fixed reference frame, and  $R(\psi)$  is the rotation matrix between the earth-fixed and the BODY-fixed frames. The pair  $(x, y)$  and  $\psi$  represent the position and orientation (yaw/heading angle) of the vehicle in the earth-fixed frame, while  $u$ ,  $v$  and  $r$  represent the linear surge and sway velocities, and the angular yaw velocity in the BODY-fixed frame, respectively. Due to the presence of disturbances at sea (winds, waves, and currents) and the rapid turning of vehicles capable of high surge speeds, the so-called *sideslip* phenomenon may also occur [89]. As explained

in [72], this phenomenon is commonly described by the variables  $\beta = \arcsin(\frac{u}{U})$  (named *crab angle*) where  $U = \sqrt{u^2 + v^2}$ .

### 2.3.2 Dynamic modelling

In addition to the kinematic models, dynamic models have also been extensively investigated. The reason for this is mainly that kinematic models alone do not provide enough information to model the USV motion, in particular when there are environmental forces, propulsion and steering forces and the sideslip is significant [90].

In order to facilitate the design of USV controllers, the following assumptions are commonly made:

1. the vehicle's masses are uniformly distributed;
2. the vehicle moves in the horizontal plane;
3. the center of the BODY-fixed coordinate system coincides with the center of gravity (CG);
4. both the CG and the center of buoyancy (CB) lie on the vertical axis;
5. the USV is symmetric on both its port and starboard sides;
6. longitudinal (surge) and lateral (sway-yaw) dynamics are decoupled.

Based on these assumptions, the widely used dynamic model can then be obtained [72]:

$$M\dot{\boldsymbol{v}} + C(\boldsymbol{v})\boldsymbol{v} + D(\boldsymbol{v})\boldsymbol{v} + g(\boldsymbol{\eta}) = \boldsymbol{\tau}, \quad (2.5)$$

where  $M = M_{RB} + M_A$  is the system inertia matrix (including added mass  $M_A$ ),  $C(\boldsymbol{v})$  is the Coriolis and centripetal matrix (including added mass  $C_A$ ),  $D(\boldsymbol{v})$  is the hydrodynamic damping matrix,  $g(\boldsymbol{\eta})$  expresses the restoring forces and moments due to gravitation and buoyancy, and  $\boldsymbol{\tau} = \boldsymbol{\tau}_C + \boldsymbol{\tau}_E$  is the vector that contains the forces and moments generated by the propulsion and steering system and acting on the USV ( $\boldsymbol{\tau}_C$ ) and the forces and moments  $\boldsymbol{\tau}_E$  caused by the environment (winds, waves and currents).

### 2.3.3 Model simplification

Although accurate models that represent the inherent physics of the systems dynamics are normally required, complete and detailed models are hard to derive, especially if the system is nonlinear. This means that some common model simplifications and reductions are inevitable in order to favor the controller design. The need to simplify the model is due to the many practical challenges that include, for example, modelling of hydrodynamic forces and moments. A complete numerical model for a USV is usually difficult, expensive and time-consuming to establish

experimentally due to the need for specific equipment and facilities (e.g., basins). Some of the most common model simplifications are:

1. *Added mass and gravity*: when these coincide,  $M_A = M_A^T$  and  $C_A(\boldsymbol{\nu}) = -C_A(\boldsymbol{\nu})^T$  [91];
2. *Low or constant surge speed*: in some cases the surge speed is assumed to be close to zero or small and constant. This involves that the whole  $C(\boldsymbol{\nu})$  matrix and the off-diagonal elements of  $M$  and  $D(\boldsymbol{\nu})$  are negligible because small enough;
3. *Fore/aft symmetry*: this assumption allows to discard the off-diagonal entries of  $M$  and  $D(\boldsymbol{\nu})$  can be neglected;
4. *Calm sea*: under this assumption the environmental disturbances ( $\tau_E$ ) disappear and one can assume that the hydrodynamic coefficients are time-invariant, resulting in the matrices  $M$ ,  $C(\boldsymbol{\nu})$  and  $D(\boldsymbol{\nu})$  all being constant.

### 2.3.4 Course control: motored vs. wave-propelled vehicles

The COG (conventionally named  $\chi$ ) is the actual direction of velocity of a vehicle, between two locations, with respect to the surface of the Earth. The heading (typically called  $\psi$ ) is the direction in which a vehicle is pointing at any given moment, with respect to the North. Many navigation systems provide both measurements. While the first is obtained by computing the bearing between two successive locations, the second is computed by a compass. Intuitively, the COG of a vehicle is *undefined* when its speed is zero. The same does not hold for the heading, which is always defined no matter the speed of the USV. Depending on the accuracy of the GNSS system, the precision of the speed-over-ground (SOG) measurement might differ. Since the computation of the COG relies on the velocity-over-ground, it is known that COG measurement is affected by noise when the speed approaches zero. More precisely, in most navigation systems the noise is inversely proportional to the SOG, i.e., the noise grows high as the speed decreases.

Controlling the COG is usually not a big deal for motored vehicles, since the propulsion system is capable of imposing a thrust force that overcomes the drift forces (wind, waves, current) caused by the environment. Moreover, if not during turns, the difference between the heading and the COG tends to be small and, at the control level, classical linear control theory can be applied to cope with it.

The same does not apply to vehicles whose propulsion relies on environmental forces, since their propulsion forces are usually in the same order of magnitude of that of the disturbances (winds and currents). Vehicles of this kind tend to move slowly, meaning that the COG measurement might become unreliable. For vehicles propelled by environmental forces, if the course and heading are controlled

by a rudder, their speed relative to the water flow is a critical parameter. When the speed relative to water is very low, the rudder is not able of applying a force to the water mass, it becomes ineffective, and the heading of the vehicle cannot be controlled. It is therefore important that the relative speed does not drop significantly, so that the rudder remains effective. The same analogy can be extended to sailboats, whose sail is hardly able to govern the navigation if the vehicle moves at the same speed as the wind.

For vehicles that have a large variation in speed, the nonlinear effects of speed are often handled using gain-scheduled control. Autonomous underwater vehicles, may use heading control rather than course control since accurate heading measurements are more easily available under water than accurate course-over-ground measurements, as described in [72].

Course-keeping autopilots are usually designed using classical linear control theory, based on basic models such as the classical Nomoto model [92], that neglects the effect of environmental forces and simply relies on integral action to counteract them [72]. Since environmental forces and propulsion forces are in the same order of magnitude, the impact that the former have on the steering dynamics of these vehicles cannot be neglected while modelling their dynamics. Furthermore, the simple, well-known Nomoto model cannot accurately describe the nonlinearities introduced by currents and winds.

When considering the research field of control of autonomous surface vehicles, one may observe that the literature lacks detailed mathematical analyses of how control systems onboard the aforementioned platforms can cope with environmental forces that are in the same order of magnitude as their propulsion capabilities. One of the objectives of this thesis is therefore to describe the dynamic modeling and course control of wave-propelled USVs taking into account the relevant effects of ocean current and other environmental forces that may lead to very low speed-over-ground. When removing this assumption, one must consider singularities at zero ground speed that are generally not considered in the course-keeping control of marine vehicles with motorized propulsion, since these can avoid such conditions. The proposed models (see Chapter 4 and Chapter 5) give insight into the changes in steering dynamics as a function of changing environmental conditions, which is exploited in the control design to handle singular situations that occur when the speed-over-ground approaches zero.





## Chapter 3

# Onboard system architecture

This chapter is inspired by the conference article [28] and it describes the hardware and software architecture of a green-energy wave-propelled USV which relies on solar energy for powering its scientific payload and support both navigation, control and communication. This system is specifically developed for the commercially available AutoNaut<sup>1</sup> (see Figure 3.1), chosen for its simplicity of operation and innovative propulsion system. Unlike common robotic platforms, this system is less constrained by energy limitation with respect to both propulsion and payload, ensuring long-duration missions without physical human intervention.

This chapter presents a communication and control system architecture, entirely developed in academic environment at NTNU, that is designed to meet the requirements of robustness, endurance and redundancy required to successfully accomplish long-duration operations in the open ocean. The described architectural choices revolve around the unique self-powering nature of the vehicle, that is both capable of transforming the energy induced by surface sea waves into forward propulsion but also of harvesting the energy captured by solar panels. The proposed solution is modular and scalable, and it relies on off-the-shelf components to target science-driven mission profiles.

### 3.1 Main system requirements

The main end-user application of the proposed system is research activities conducted both in the Arctic and Atlantic waters, and in Norwegian coastal waters. The harshness of these regions and research applications result in a set of requirements that the presented system architecture aims to fulfill.

Research missions in the Arctic waters face different challenges. The use of classic research vessels usually implies significant constraints, such as limited num-

---

<sup>1</sup><https://www.autonautusv.com/>



Figure 3.1: The NTNU AutoNaut during operations in Nordfjord (Central Norway).

ber of onboard researchers, tight schedules due to high cost of operation, or non-negligible travel time to the point of interest. Moreover, human factors as crew fatigue and sea-sickness can have a significant impact on missions results and therefore cannot be neglected.

Two types of mission profiles are defined for the considered autonomous vehicle.

#### 3.1.1 Long-duration ocean operations

This mission profile envisions the USV being deployed using a research vessel (R/V) in the ocean, where it should operate continuously for weeks continuously. The vehicle needs to be able to collect scientific data with re-configurable intervals, assuming that communication is reduced to a global-coverage satellite network. As the access to the vehicle is limited, the control system robustness is a key feature. Large volumes of sensor data can be accessed primarily using a local short-range radio, such as WiFi, e.g., from a R/V or UAV.

### 3.1.2 Short-duration fjord operations

In this mission profile, instead, the vehicle is deployed from the shore (using a slip or pier crane), and performs single or multi-day missions in the fjord. This mission profile serves coastal research and supports vehicle development and testing. The vehicle is typically within the coverage of a high-speed cellular network. Access to the vehicle is possible, although may require additional assets. Quick access to both vehicle and sensor data is a key characteristics of this type of operation.

### 3.1.3 Design requirements

Based on the described mission profiles, the design requirements of the vehicle are defined as follows:

- *Deployment and recovery*: the vehicle should support deployment from a slip or by crane. Deployment should not require significant effort or put users at risk. The sea-bottom depth during launch should be as low as possible. The vehicle should also be tow-able using a support boat.
- *Robustness*: the system needs to be robust enough to avoid maintenance for several weeks. Mechanically that can be achieved by a sturdy design and a limited number of moving parts. Electronically, the system should be based on industrial grade components, including cables and connectors. Control-wise, the system should provide a well defined fallback system with redundant communication channels.
- *Energy management*: the energy management system should be able to plan and monitor energy consumption, as well as to harvest energy. The low-level system should allow to schedule when selected components are turned on and off.
- *Communication*: three categories of communication links need to be covered. A near-real-time, low bandwidth, global coverage link to report health status and location of the vehicle, and an emergency manual control. A real-time, low bandwidth, long-range control of the vehicle, and detailed vehicle status and telemetry. A real-time, high bandwidth, short-range data link to collect sensors data. The mission scenario should define which links are active. Therefore, faster links with lower range should be able to cover functions of the slower, long-range links.
- *Autonomy and control*: the vehicle needs to be able to execute maneuvers, and its predicted trajectory needs to be computed taking into account environmental conditions such as sea currents or winds. The system needs to be able to handle current and future developments in control algorithms and autonomy. The control system should be inter-operable with the fleet of

Sensor	Information
Nortek Signature500 ADCP (1)	Current profiles up to 60m.
Seabird CTD SBE49 (2)	Conductivity, temperature and pressure.
ThelmaBiotel TBLive (3)	Acoustic tracking of tagged fishes.
Aanderaa Oxygen Optode 4835 (4)	Oxygen concentration and % saturation.
WET Labs ECO Puck Triplet-w (5)	Chlorophyll-a and FDOM and turbidity.
ECO PAR (6)	Photosynthetically Active Radiation.
Airmar 200WX Weather Station (7)	Wind, temperature and pressure.

Table 3.1: Onboard scientific payload

unmanned vehicles used at NTNU [93, 94], supporting a fully autonomous tasks allocation and multi-type, multi-vehicle cooperation in the future. The vehicle should also support manual control, especially for launch and recovery.

- *Modularity and scalability*: the control and sensors systems should not limit each others development and upgrades. The system should be modular, and each segment should support independent upgrades. Finally, the platform should be able to accommodate additional scientific sensors in the future.

#### 3.1.4 The scientific payload

In order to accomplish missions with the described mission profiles, the AutoNaut is equipped with a scientific payload that targets the environmental parameters of interest. The sensors suite is described in Table 3.1. Except for the weather station (Airmar 220WX) which is connected to the vehicle mast and for and the ECO PAR which is connected to the deck, all sensors are placed on the submerged keel (see Figure 3.2). The sensors were chosen in order to target a wide range of ocean phenomena that can be measured at the boundary layer (upper water column). For example, primary productivity dynamics can be analysed by quantifying the amount of chlorophyll-a, dissolved organic matter and turbidity (WET Labs ECO Puck Triplet-w). The inherent processes related to photosynthesis can be best understood is by complementing such information with salinity and temperature readings (Seabird CTD SBE49), and with oxygen concentration measurements (Aanderaa Oxygen Optode 4835).

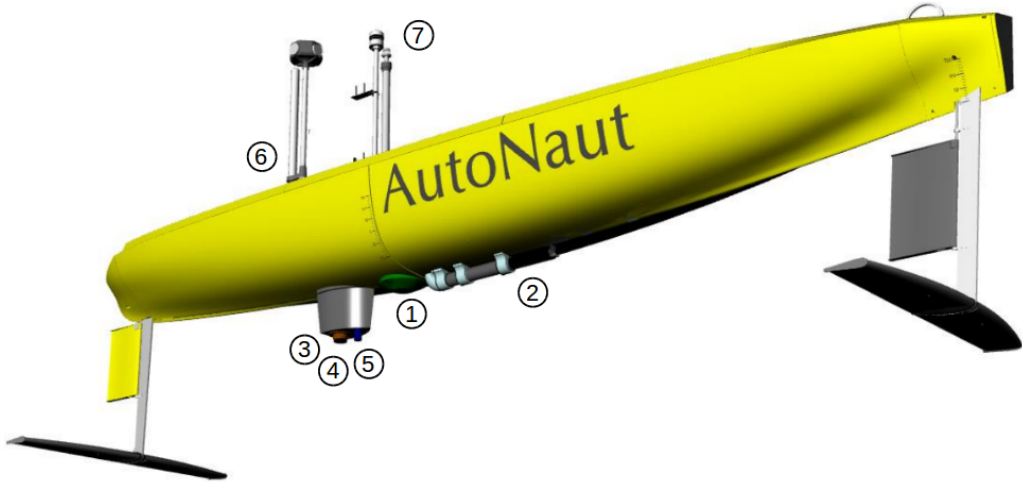


Figure 3.2: View from below of the AutoNaut: the passive propulsion system and the scientific payload. Numbers indicate the sensors listed in Table 3.1.

The sensors can be used separately, to study a specific independent process, or together, to observe a phenomenon whose consequences are found in multiple physical properties of the surface water. For example, monitoring the appearance and growth of harmful algal blooms (HAB) is best achieved by merging chlorophyll-a concentration with the photosynthetically active radiation from the sun (ECO PAR), as described in Chapter 8 and Chapter 9.

## 3.2 Architecture overview

The proposed architecture, which is publicly available and documented<sup>2</sup>, equips the vehicle with autonomous communication and navigation control capabilities. This section discusses the design choices that have been made in order to provide the vehicle with reliable navigation, control and communication tools. The table 3.2 lists all the sensors and hardware units involved in the navigation, communication, power management and onboard computation. The reader is invited to refer to Table 3.1 for the onboard scientific instrumentation.

In the presented control and communication architecture, a layered subdivision of computation efforts and mission responsibilities provides a high degree of robustness and redundancy (see Figure 3.3).

*Level 1* unit is the lowest-level component of the system, which also provides a fallback mechanism in case of failure of the higher-level units. It monitors the

<sup>2</sup><http://autonaut.itk.ntnu.no/doku.php>

### 3. Onboard system architecture

---

Unit name	Information/purpose
<b>Navigation units</b>	
Vector V104 GPS	Time, SOG, COG, location and others.
Raymarine Class B AIS650	Marine traffic.
Airmar 220WX station	GNSS and wind information.
ADIS16485 IMU	Triaxial gyroscope and accelerometer data.
HMR3000 Digital Compass	Heading, pitch and roll outputs.
Echomax radar	Active radar reflector.
<b>Communication units</b>	
OWL VHF	Long-range, low bandwidth radio transceiver.
MikroTik 4G/LTE Modem	4G/LTE Modem onboard the vehicle.
RockBLOCK+ Iridium	Satellite communication.
<b>Power management units</b>	
Solbian SP 104	Solar panels.
Victron BlueSolar MPPT	Battery charge controller.
DRA1-MPDCD3-B	Solid state relay.
861SSR115-DD	Solid state relay.
<b>Computational units</b>	
Campbell Scientific CR6 Datalogger	<i>Level 1</i> : system monitoring, power distribution, fallback communication and autopilot.
BeagleBone Black	<i>Level 2</i> : advanced navigation, collision avoidance and system monitoring.
TS-7970	<i>Level 3</i> : scientific payload control unit.

Table 3.2: List of hardware components onboard. Colors indicate if the units are interfaced to *Level 1* (black), *Level 2* (blue) or *Level 3* (red).

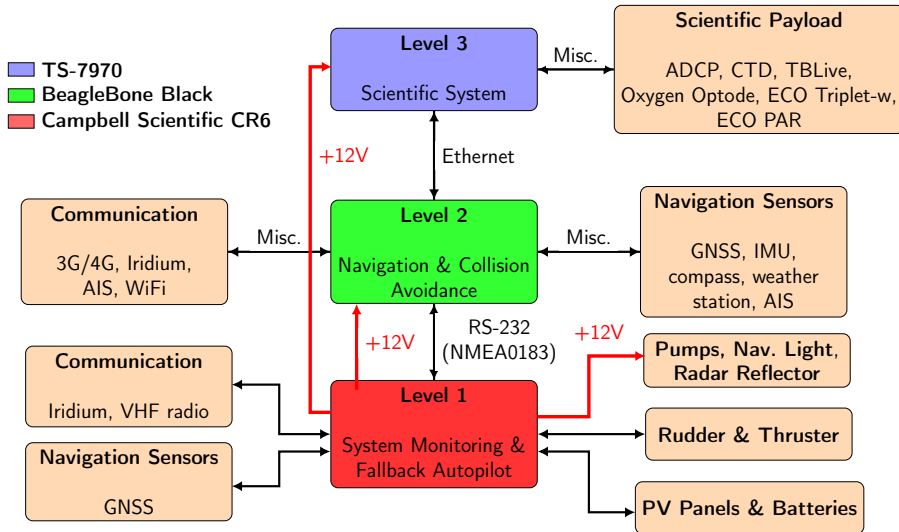


Figure 3.3: Onboard system architecture.

hardware and health status of the vehicle, autonomously commands fallback maneuvers, and manages power harvesting, storage and distribution. *Level 2* provides the vehicle with advanced navigation capabilities, including a course-keeping autopilot and an automatic identification system (AIS)-based collision avoidance algorithm. *Level 3* controls the scientific payload, handling data collection from the sensors, data storage and transmission to shore, depending on the mission profile. The *Level 3* runs as a slave CPU, controlled by *Level 2*. Because of the slow-moving nature of the vehicle, *Level 3* is mostly in stand-by mode during navigation towards the mission area in order to limit power consumption. The multi-layered approach decreases the interdependencies of the design and facilitates easy integration of new functionalities. Also, it enables graceful degradation in low energy situations. As the only energy source for the onboard electronics is solar panels, situations where energy must be conserved might arise. In such cases *Level 3* (and *Level 2* in the worst-case scenario) can be turned off without losing safety-critical functions.

### 3.3 Energy harvesting, storage & distribution

The USV's deck is covered with three Solbian SP 104 solar panels whose maximum output power rating is 104W each. The onboard battery bank is made of four 12V 70Ah Lead Gel batteries, wired in parallel as most of the components require around 12V. In order to control the power produced by the panels, two Maximum Power Point Tracking (MPPT) [95] controllers are chosen. These have



### 3. Onboard system architecture

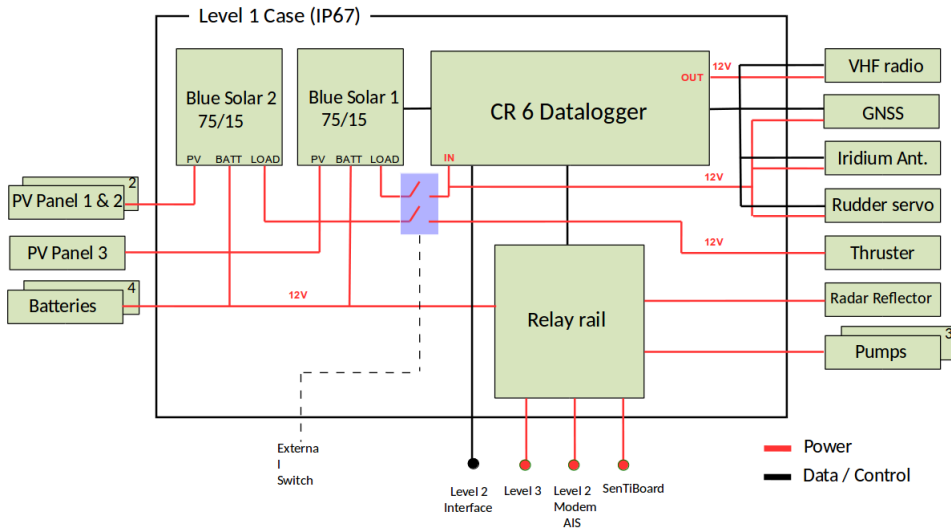


Figure 3.4: Simplified *Level 1* hardware architecture.

built-in inverters and can step the voltage up or down prior to supplying the batteries. This is required as the solar panel output varies with the observed load impedance. Two step-down MPPT controllers is used in the power system. The panel which is furthest from the mast is connected to one controller because it is unlikely that the internal bypass diodes are activated due to shading, meaning that the panel output always will be higher than the required input voltage for the controller. The panels near the mast which are likely subject to partial shading, are connected in series to another step-down MPPT controller. The charger's input will thus always be higher than the minimum voltage requirement, even if both arrays in one panel are bypassed. The chosen controller are the Victron BlueSolar MPPT 75/15.

Figure 3.4 provides an overview of the structural design of the power management system implemented into *Level 1* unit housing. An external toggle switch allows to disconnect the load power line that provides power to all components. This means that when a mission is completed and the user turns off the computers and sensors, the batteries can still be recharged by the solar panels through the controllers. Figure 3.4 also shows how the power is distributed to the whole system. The CR6 Campbell Scientific Datalogger, GPS, Iridium and rudder / servo are directly connected to the load port of BlueSolar 1, through the switch. However, they are controlled by the CR6. *Level 2*, *Level 3*, AIS transceiver, 4G/LTE Modem, SentiBoard timing unit, radar reflector and pumps are instead powered through solid state relays that are digitally controlled by CR6's GPIOs. The OWL VHF radio is the only component being directly powered by a 12V output port of the CR6. His-

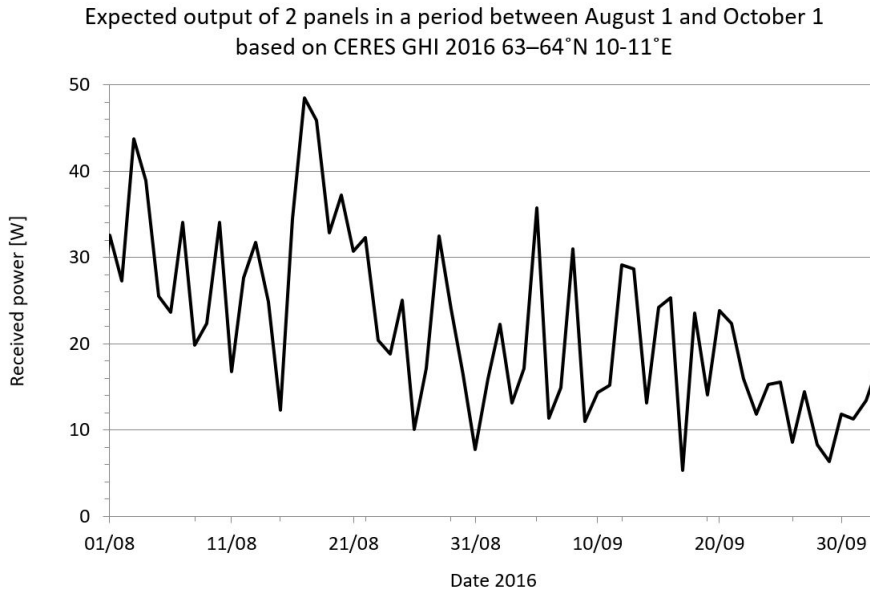


Figure 3.5: Expected power on two solar panels through a period between August and September in Trondheim, based on historic data.

toric data for solar radiation during fall in Trondheim (Central Norway), reduced by the solar panel efficiency factor, gives an insight about the expected amount of energy the panels should produce (see Figure 3.5). An estimate of the power consumption of the vehicle was defined according to datasheets of onboard sensors, considering the expected time of use for each device mentioned in tables 3.1 and 3.2. *Level 1* and *Level 2* are estimated to consume approximately 20W, assuming 14V system voltage (fully charged lead-acid batteries), while the maximum average current consumption is estimated to be around 1.4A. The consumption of *Level 3* depends on sampling frequency of the scientific payload. Based on sampling routine, the average constant power requirement for *Level 3* is estimated to reach 21W.

Further discussion, together with a validation of the power system are presented in Section 3.9.

### 3.4 System monitoring & fallback autopilot

*Level 1* subsystem is responsible for monitoring the health status of the whole system. This unit observes the operation of all sensors and subsystems and is able to identify anomalies. These can be related to powering issues, e.g., sudden decrease

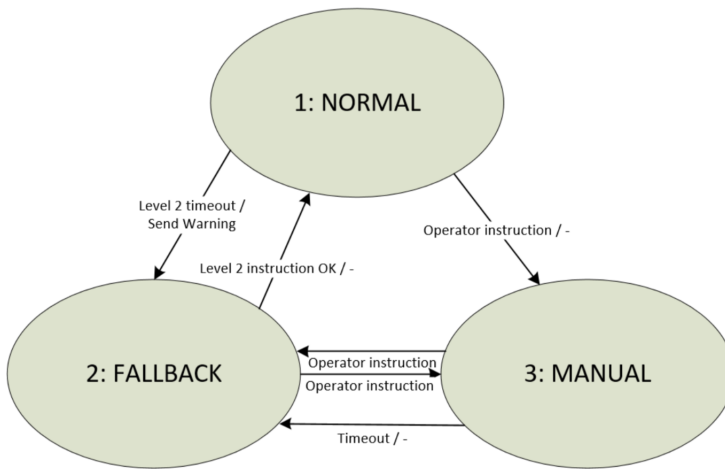


Figure 3.6: *Level 1* state diagram.

of supplied current or increase of consumed energy, or to communication issues. In case an anomaly is detected, a dedicated routine will try to provide a solution for it (e.g., restarting) and will open a communication link to notify the operators about the failure. During development of the system, it was sought to keep complexity as low as possible while still meeting the system requirements listed in Table 3.3, as described in [96].

#### 3.4.1 Behavioural design

*Level 1* works as a state machine, switching operation mode when a failure is detected or when the operators need to manually control the vehicle (see Figure 3.6). The transition from *normal* or *fallback* to *manual* only takes place if the operator sends a dedicated command to the system. If the connection is lost between the remote operator and the USV when in *manual* mode, the USV will enter *fallback* mode. Also, *fallback* state will be entered automatically if *Level 1* does not receive commands from *Level 2*. Note that a warning will be sent to the operator, over Iridium, in the event of this transition. The transition from *fallback* to *normal* is also automatic and occurs as soon as *Level 1* receives a valid command from *Level 2*. During normal operations, *Level 1* periodically receives rudder (and, if needed, thruster) commands from the heading controller running on *Level 2*. Communication happens according to NMEA0183 protocol at RS-232 voltage levels. The communication standard was chosen because of low power consumption, low bandwidth requirement and human-readable formats. If the CR6 computer does not receive a verified control signal from the *Level 2* computer within a user-

System requirement description	Subsystem requirements
Onboard power	Battery and load power monitoring PV panel power monitoring Disabling device power
Error handling	Device error/failure monitoring <i>Level 2</i> failure monitoring <i>Level 3</i> failure monitoring Leak detection Bilge pumps control
Operation mode control	Remote control interface protocol Manual control mode <i>Level 2</i> control mode Fallback autopilot mode
Manual control	Remote control interface protocol Rudder angle control Thruster control Disabling power for devices
Remote data & communication	Iridium communication link VHF radio communication link 4G/LTE communication link Transmit system Energy parameters Transmit position, COG and SOG Transmit leak and error status

Table 3.3: List of *Level 1* requirements.

defined amount of time, it will assume that *Level 2* has failed and therefore switch to *fallback* state (see Figure 3.7). When the system enters fallback mode, three

### 3. Onboard system architecture

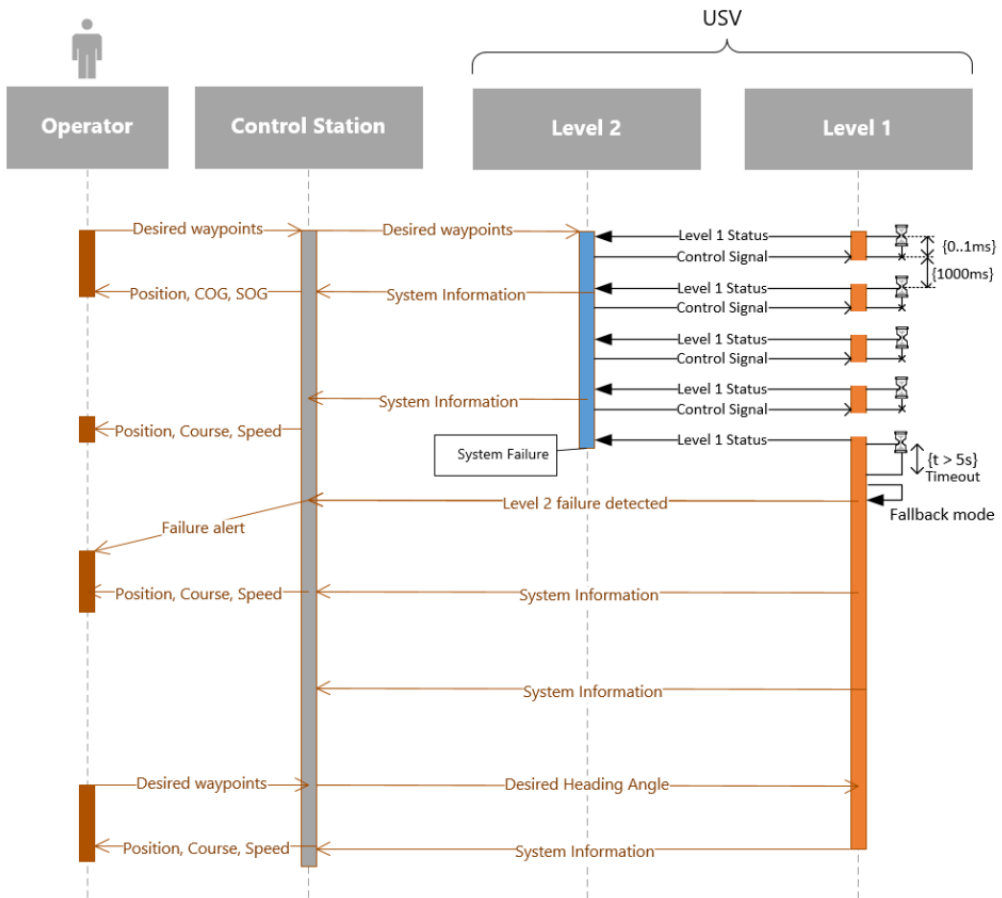


Figure 3.7: *Level 1* system fallback implementation.

different operating modes can be selected depending on the circumstances:

- *Fallback mode 0*: sets the rudder angle to  $0^\circ$  and thruster to 0 RPM.
- *Fallback mode 1*: sets the rudder angle to  $45^\circ$  and the thruster to 0 RPM.
- *Fallback mode 2*: activates a course-keeping autopilot that reads the course over ground (COG) measurement from the GPS and computes the rudder angle that makes the vehicle keep a desired course.

However, *Level 1* periodically checks for messages received from the operators over VHF radio or Iridium. If a message is received by the onboard transceiver, the state machine automatically switches to *manual*, as shown in Figure 3.6, prioritizing the operator's directives. Manual control is needed, for example, to directly maneuver

the vehicle inside the harbor.

As already anticipated, *Level 1* also monitors the battery voltage, solar cell power and load power. It obtains navigation data from GPS and checks for leaks. For leak detection, the onboard bilge pumps are used. Since the motors are inductive loads, the current will change based on their resistance. Pumps are periodically activated, and based on the increase in current, the system is able to detect if water is being pumped.

#### 3.4.2 Software implementation

The choice of Campbell Scientific CR6 computer to fulfill the requirements proposed for *Level 1* is due to its proven reliability in long-term monitoring experiments in harsh environments<sup>3,4</sup>. The Campbell Scientific CR6 has a Renesas RX63N processor with a clock rate of 100 MHz and has sixteen general I/O pins and dedicated hardware for supporting numerous communication protocols<sup>5</sup>. The CR6 was also chosen due to the need of multiple I/O ports and a fast CPU. All the functionalities of *Level 1* described so far are implemented by means of the PC400 Datalogger Support Software and CR Basic Editor. To support communication over VHF Radio and provide a human-readable GUI for operators onshore, a Java application was developed. Figure 3.10 shows how the operator is able of manually command the rudder and thruster of the vehicle. Sensors and other units can be manually turned on and off and the fallback behaviour can be chosen and communicated to the vehicle.

### 3.5 Advanced navigation & collision avoidance

The *Level 2* subsystem implements advanced navigation and collision avoidance capabilities. It is powered through a dedicated solid state relay in the *Level 1* casing that provides 12V. This voltage is then regulated to match the input requirements for some of the components of *Level 2* that work at 5V (see Figure 3.8). The embedded computer chosen for this subsystem is a BeagleBone Black, provided with a 1GHz ARM-based CPU and two 46 pin headers that enable communication with a wide range of sensors and other hardware components. During normal operations, *Level 2* acquires navigation data from the global navigation satellite system (GNSS) system, compass and inertial measurement unit (IMU). Information about the environment, that is useful to tune navigation parameters, is instead obtained from the weather station and the Acoustic Doppler Current Profiler (ADCP). The

---

<sup>3</sup><https://www.campbellsci.com/greenland-ecosystem-monitoring>

<sup>4</sup><https://www.campbellsci.com/costa-rica-buoy>

<sup>5</sup><https://s.campbellsci.com/documents/au/manuals/cr6.pdf>

### 3. Onboard system architecture

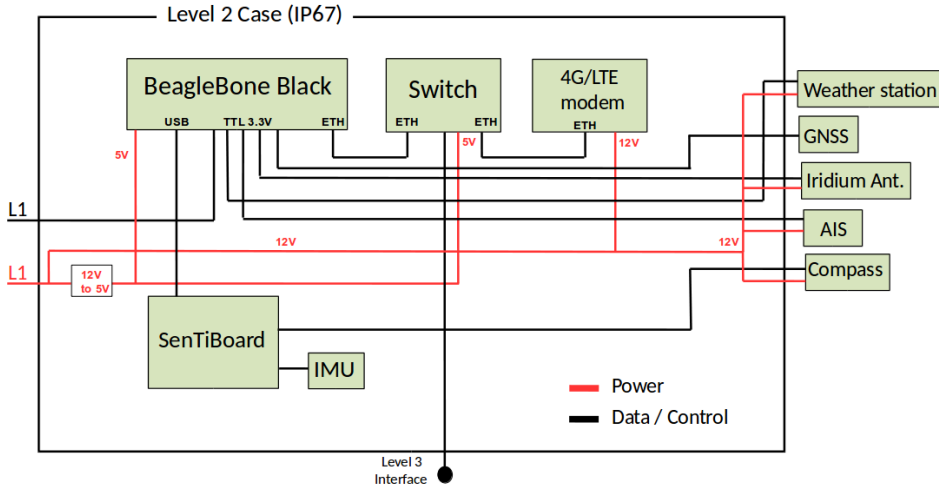
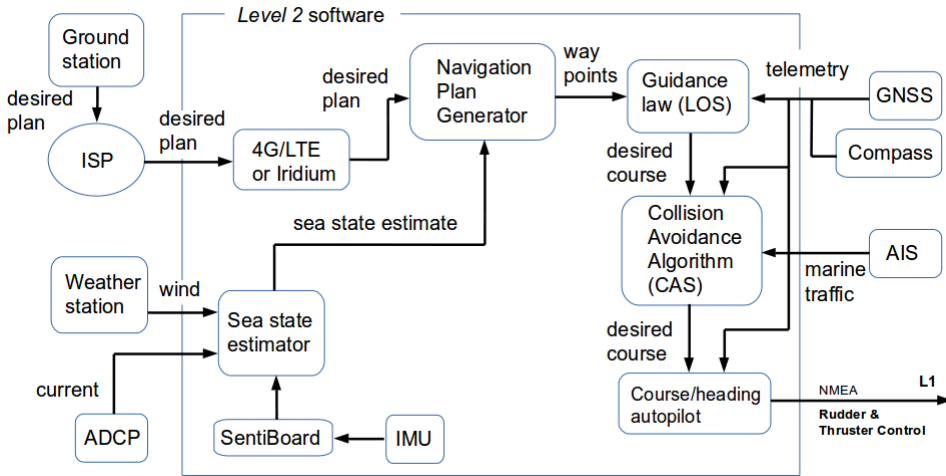


Figure 3.8: Simplified *Level 2* hardware architecture.

sensors depicted in Figure 3.8 are used to determine both the current state of the vehicle (heading, COG, SOG, location) and the state of the sea (waves amplitude, frequency and direction, wind speed and direction). A high-level autopilot is implemented in order to govern the course and the speed of the vehicle by observing the waves' direction and height. Plans can be defined by the operator onshore and dispatched over 4G/LTE or Iridium to the onboard unit (see Figure 3.9). A typical mission plan can be made of a single way point or of a more complex sequence of way points, e.g., a survey plan of an area. When the vehicle operates in remote areas, communication is sporadic and onshore operators may not have the same situational awareness of the environment as the vehicle. In this case, a mission plan dispatched from shore may be a list of high-level goals including target areas and specific data to be collected and sent to shore. An onboard decision-making system supports the generation of the navigation plan, based on in-situ measurements and sea-state estimation.

As described in Chapter 6, a sea state estimator might merge the environmental data from the weather station (wind speed and direction), from the ADCP (current speed and direction), and from the IMU (heave acceleration) and compute an estimate of the current state of the environment. In Chapter 6 specifically, the heave motion measured by the GNSS system is used to estimate the encounter frequency of waves.

Once the plan is refined onboard the vehicle, the desired course is computed according to the chosen navigation law. *Line-of-sight* is preferred, due to its simple implementation. A PI course controller reads the current course provided by the GPS and computes the rudder angle that allows the vehicle to keep the desired

Figure 3.9: *Level 2* software architecture.

course to the target way point, as described in detail in Chapter 4.

### 3.5.1 Software implementation

The software employed in this subsystem is an open-source toolchain developed by the Underwater System and Technology Laboratory (LSTS). The toolchain supports networked vehicles systems constituted by human operators, heterogeneous autonomous vehicles and sensors [97]. The software toolchain is primarily composed of the onshore mission control software Neptus [98], the onboard software Dune, and IMC, a communication protocol [99]. The toolchain also uses its own operating system (GLUED), a minimal Linux distribution targeted at embedded systems. Operators onshore have complete control over the mission through Neptus and are able to customize the mission plan visually as shown in Figure 3.10. The collision avoidance algorithm involves a continuous monitoring of the area in which the vehicle is navigating. A monitoring radius around the vehicle is defined and navigation data of nearby vehicles equipped with AIS, are provided by the transceiver. For the USV to obey the rules-of-traffic when encountering other vehicles and execute the correct and predictable actions in hazardous situations, the algorithm needs to be COLREGS compliant. Based on the information provided by the onboard AIS transceiver, the algorithm searches for COLREGS compliant and collision-free trajectories through a series of predictive simulations with a finite set of offsets to the nominal course. The offset associated with the lowest cost, while producing a collision-free and COLREGS compliant trajectory, is selected as the new modified course reference, and is passed on to the autopilot. When the orig-



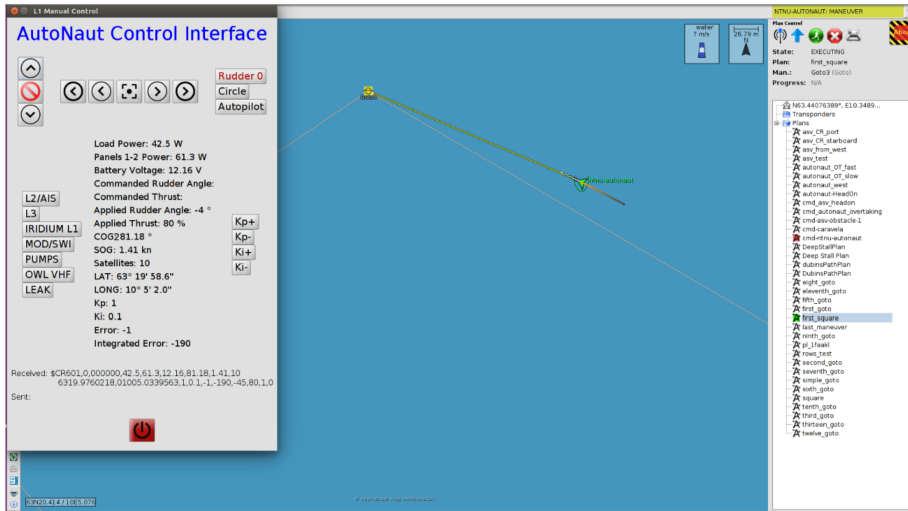


Figure 3.10: Neptune onshore mission control center.

inal desired trajectory no longer contains any potential collision, the USV would return to the desired nominal path and proceed towards the target destination. If no obstacle is present in the vicinity of the vehicle, no deviation is applied to desired course and speed. The algorithm, presented in Chapter 7, is described in detail in [100], [101] and [102].

## 3.6 Scientific instrumentation

The *Level 3* subsystem is responsible for controlling the scientific payload (see Table 3.1) according to the mission plan. During navigation to the survey site, this unit is meant to be turned off in order to save energy. When the target area is reached, *Level 2* communicates to *Level 1* the need to turn on the scientific unit (see Figure 3.3). A plan that involves commanding the scientific payload is either manually built by the operators and dispatched to *Level 2* over 4G/LTE or Iridium, or autonomously synthesized onboard the vehicle. Plans involving the control of the scientific payload are created in *Level 2*, where decision-making techniques deduce mission plans while reasoning on resources, time constraints, environment changes and operational risk. This functionality will support the mission execution when the vehicle is exploring remote areas and communication to shore happens to be sporadic and expensive.

The master-slave relation between *Level 2* (master) and *Level 3* (slave) further explained with the following routine example.

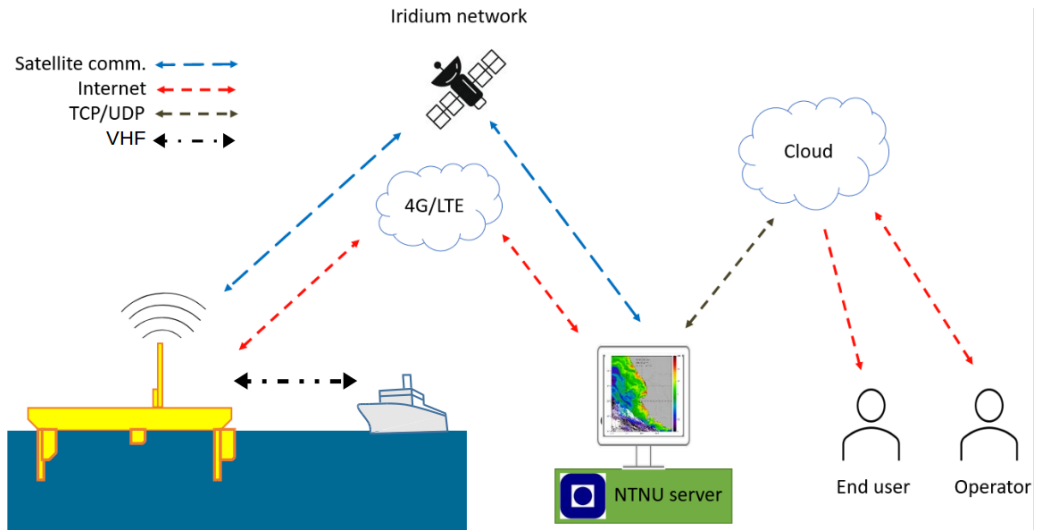


Figure 3.11: Communication overview.

1. based on the chosen navigation law, the master autopilot computes rudder commands that allow the vehicle to reach the area of interest described by the operator plan - the slave unit is turned off.
2. once the target area is reached, the slave is turned on and a plan is communicated by the master to the slave.
3. the slave executes the plan and locally stores data sampled by the sensors.
4. data are then compressed, packed and transferred to the master.
5. the master communicates the outcome of the mission to the operator, transmits the data to shore and turns off the scientific subsystem.

## 3.7 Communication links

The vehicle is equipped with three different communication links. Depending on the mission type and location, the operator can communicate with the onboard computers over 4G/LTE, Iridium or VHF radio (see Figure 3.11). Both *Level 1* and *Level 2* have access to separate Iridium transceivers.

### 3.7.1 4G/LTE communication

Communication over Internet allows operators onshore to have a full live stream of the mission. Onboard the vehicle a 4G/LTE modem connects to Internet through a dedicated antenna on the mast. Every five minutes a programmed routine in the

### 3. Onboard system architecture

modem reports the modem's internet protocol (IP) to a dynamic domain name system (DNS) remote service. The modem is configured to implement port forwarding and network address translation (NAT) routines, enabling communication between operators and the BeagleBone Black (and the TS-7970) in both directions, through the router itself (see Figure 3.12). The local network is therefore always accessible via the same URL, no matter the IP provided by the internet service provider (ISP). An ethernet switch allows the inclusion of *Level 3* in the local network (see Figure 3.8). The operators are able to closely observe and control *Level 2* and *Level 3* via the Secure Shell (SSH) protocol.

As discussed in Section 3.5.1, the communication protocol (IMC) allows different nodes to share the same message formatting. In order to enable a full transmission of the messages payload from one node (or client) to another (in this case, the operators and the vehicle), a dedicated proxy is used. The *IMCProxy* is a software written in Java that bridges IMC networks over Internet, as described below. This is achieved through a centralized proxy server based at NTNU that receives IMC messages and forwards them to other connected nodes (see Figure 3.11 and Figure 3.12). For operations in fjords and coastal waters, where signal coverage is good, this communication link is preferred due to its flexibility.

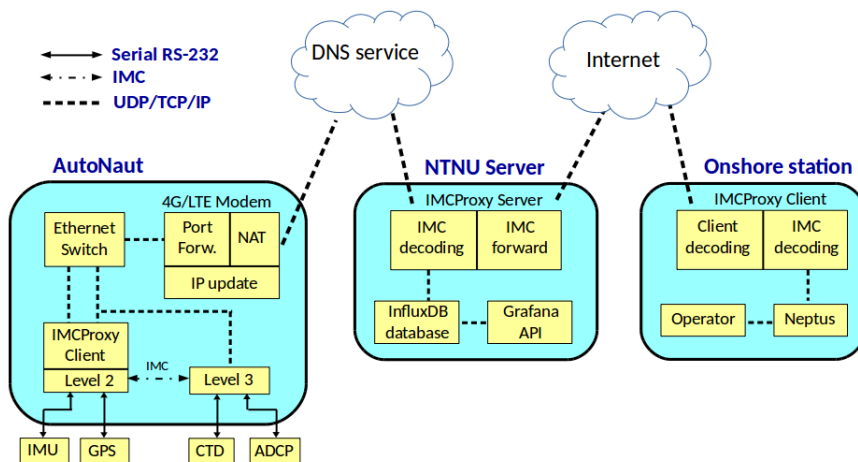


Figure 3.12: Overview of the communication process that allows the operators to send and retrieve data from the vehicle. This architecture was built not only to enable data retrieval, but also to support direct intervention on the hardware and software, mission update and monitoring functionalities.

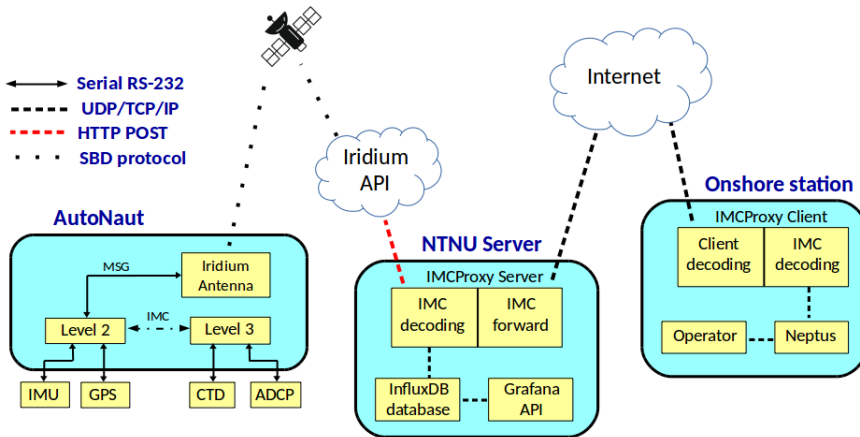


Figure 3.13: Overview of the satellite communication process between the USV and the operators.

### 3.7.2 Iridium communication

The vehicle is equipped with two separate Iridium Rockblock+ units that host an Iridium 9602 transceiver, an antenna and a voltage regulator. The Rockblock+ antennas communicate with Iridium satellites using the short burst data (SBD) protocol, an efficient network protocol designed for shorter sized data messages. As shown in Figure 3.3, both *Level 1* and *Level 2* can send a receive messages over satellite. Moreover, also *Level 3* can send a message via *Level 2* (see Figure 3.13). Despite it involves less operational flexibility and higher costs, this communication link is used when 4G/LTE coverage is absent.

*Level 1* periodically sends a message reporting the overall state of the system: time and location, power settings, battery voltage, consumed and produced power. The operator is therefore able to communicate changes in the power settings of the vehicle and restart sensors and components.

The Rockblock+ unit connected to *Level 2* is instead used to communicate new or modified plans to the onboard software (DUNE). The vehicle acknowledges the reception of the plan and later its outcome. This solution has a limited bandwidth and is therefore only suitable for simple control monitoring or tracking applications. The maximum package sizes are 340 bytes for sending and 270 bytes for receiving. Although the latency is typically a few seconds, it may increase to up to a minute or more depending on the remoteness of the area and the available satellites.

#### Iridium remote control: list of commands & USV replies

Several functionalities were implemented to improve the flexibility and the quality of the satellite communication link. Moreover, most of them are publicly available<sup>6</sup>. The implementation of such functionalities translates to programming of high-level functions running on the DUNE software in *Level 2*. As described in the previous paragraph, the SBD protocol is quite limited in bandwidth and, for this reason, the designed messages need to be concise and optimized as much as possible.

The first message that was designed enables the operators to turn on, turn off and restart the main hardware components of the system, i.e., *Level 2*, *Level 3*, Iridium, 4G/LTE modem, bilge pumps and VHF radio. For example, the command `on vhf` turns on the VHF radio, intuitively. More hardware units can be manipulated via one single message, e.g., `cr6 011011` indicates that *Level 2* is ON, *Level 3* is OFF, Iridium is OFF, 4G/LTE modem is ON, pumps are OFF, VHF is OFF.

Table 3.4 shows the IDs of the hardware units and scientific sensors.

#### Navigation commands

- `info`: retrieve information about plan being executed.  
Replies:
  1. *Vehicle is ready*: the vehicle is ready to execute its first plan.
  2. *Initializing <planID>*.: the vehicle is in calibration mode, starting a plan with ID `<planID>`.
  3. *Executing <planID> / <manID>*. *ETA: <eta in seconds> (<progress>%)*  
: the vehicle is currently executing the maneuver `<manID>` of a plan with ID `<planID>`; the estimated time of arrival (ETA) and percentage of mission completion are following.
  4. *Finished <planID>*: the vehicle has finished executing a plan successfully.
  5. *Failed to exec <planID>*: *<reason>*: the vehicle has failed to execute its plan and the reason is communicated.
- `abort`: this command aborts the execution of any ongoing plan and receives no arguments.
- `start <planID>`: commands the execution of a plan already in the Plan Database of the vehicle.
- `force <planID>`: commands the execution of a plan ignoring any errors.

---

<sup>6</sup><http://autonaut.itk.ntnu.no/doku.php?id=iridium>

Hardware units	
Unit name	Hardware ID
<i>Level 2</i>	l2
<i>Level 3</i>	l3
Iridium	iridium
4G/LTE modem	modem
Bilge pumps	pumps
OWL VHF radio	vhf
Payload units	
Unit name	Sensor ID
Oxygen Optode 4835	opt
Seabird SBE49	ctd
ECO Puck	eco
TBLive	tbl
Nortek500 ADCP	adcp
Eco PAR	par

Table 3.4: List of sensors and hardware units, and their abbreviation.

- `resume <planID> <GoToNUM>`: commands the execution of a plan, starting from a specific maneuver ID. It will generate a new plan that has the given maneuver ID as the starting maneuver and then will proceed to execute it.
- `go lat=<latitude>;lon=<longitude>`: commands the vehicle to navigate to a given waypoint (using a Goto maneuver).

### Hardware commands

- `cr6 relays`: where *relays* is the string of booleans that enables/disables the solid-state relays.
- `on <hardwareID>`: turns on a sensor with ID `<hardwareID>`.
- `off <hardwareID>`: turns off a sensor with ID `<hardwareID>`.

#### Payload commands

Payload commands can trigger data collection from one or multiple sensors. Sensors can be started, stopped or triggered periodically.

- `sensor <sensorID> <on/off> <samp_duration> <samp_interval>`: where `<sensorID>` is the sensor ID; `<on/off>` determines if the sensor has to be turned ON or OFF; `<samp_duration>` determines the duration (seconds) of the sampling period; `<samp_interval>` indicates the seconds between two consecutive samplings (sensor is turned OFF between them).

Replies:

1. *L3 is OFF, turn on first.*: if the payload computer is OFF.
2. *<sensorID> is already ON.*: if the sensor to be turned ON is already ON.
3. *<sensorID> is already OFF.*: if the sensor to be turned OFF is already OFF.
4. *<sensorID> <action>*.: where `<action>` indicate what is actually being commanded; for example, if the sensor is OFF and I turn it ON, `<actions>` will be *sensorID is turning on*.

Some examples: `sensor ctd 0 60 120` turns ON the CTD at regular intervals of 120s and collect CTD data for 60s; `sensor opt 0 0 0` will turn ON the Optode 4835 and sample indefinitely; `sensor eco 1 0 0` will turn OFF the ECO Puck Triplet indefinitely.

#### USV reports

The onboard software is programmed to periodically transmit a report to the operators via satellite. The report is encoded in a ASCII text message that summarizes the status of the mission, the health of the system or some specific information related to the hardware (e.g., what is ON and what is OFF). Periodical reports are automatically received and decoded by the server at NTNU (see Figure 3.13) and the information they contained is immediately available to operators and scientists in Grafana. An example is:

(R) 13:29:16/63.872886,8.640461/b:127/c:78/s:0.00/sat:8/pp:15/cp:17/s:M/001011. The message starts with the report ID (R), meaning this message contains a report. Then, in order, it contains: UTC time, USV location, battery voltage, course over ground, speed over ground, visible satellites, power produced by solar panels, power consumed by the system, status (M for maneuvering, S for service, E for error) and finally the relays (i.e., what is ON and what is OFF).

Furthermore, to enhance mission flexibility, the operators can query the USV at any time, asking detailed information concerning the its navigation or about the data being collected by the sensors. For example:

- `navstat`: queries navigation statistics.

Example reply: (NAV) 2020-06-23 13:28:06/63.8728 8.6404/C:69/dC:-20/r:-57/th:0/S:0.0/aws:0.7/awd:118. The message starts with the navigation ID (NAV). Then, in order, it contains: UTC date and time, USV location, course over ground, desire course over ground, rudder angle, thruster actuation, speed over ground, absolute wind speed, absolute wind direction.

- `ctd report`: queries a report of the last CTD measurements.

Example reply: (CTD) 2020/06/23 09:37:49/63.8728 8.6404/S:0.29/C:0.04/T:15.80/SS:1471/D:0.05/P:1340. The message starts with the sensor ID (CTD). Then, in order, it contains: UTC date/time, USV location, salinity (PSU), conductivity (S/m), water temperature (degrees Celsius), sound speed (m/s), depth (m), pressure (hPa).

The reports from scientific sensors can be transmitted also when the sensor is momentarily OFF because it is sampling periodically or when the sensor is permanently OFF. In the first case, the ID of the reply will be (CTD-P), where P stands for “periodical”. In the second case instead, the reply will start with (CTD-L), where L stands for “last”. In this case, the software keeps in memory the values of the last received information, the USV location and more importantly the date and time of when the measurement occurred. This helps scientists and oceanographers to have a better insight of the observed natural phenomena.

### 3.7.3 VHF radio communication

Onboard the vehicle, an OWL VHF<sup>7</sup> radio transceiver allows efficient point-to-point communication between the operators and *Level 1*. It supports a large variety of modulation types and encoding, that can be configured through a serial port. A Java GUI (see Figure 3.10) enables manual control and direct monitoring of the vehicle, over VHF. During a mission, this link is turned off in order to save energy. It is however turned on when manual control of the vehicle is needed. An automatic routine enables the radio whenever a fault is detected. The radio transmits the location and power settings, allowing the operators to find the vehicle and manually control it to shore.

A passive duplexer allows the OWL VHF radio to share one antenna with the AIS. Unlike an active splitter, the duplexer has a passive notch filter in each port that

<sup>7</sup><http://skagmoelectronics.com/>



attenuates the frequency used by the other port. This means that both radios can always transmit without hearing each other and everything is sent out on the antenna. The filters are tuned to specific frequencies, so the radios cannot change frequency. The selected cut-off frequency of the AIS port is 162MHz (center of AIS frequencies 161,975MHz and 162,025MHz) and 155,9MHz for the VHF radio.

## 3.8 A near real-time environmental monitoring system

This section describes how the information carried by each communication link presented above is conveyed to a centralized hub (NTNU server) responsible for compressing, storing and displaying it. The designed system is composed of three subsystems as described in Figure 3.11: the data transmission unit onboard the USV, a server at NTNU, and USV's operators (end-users).

### 3.8.1 The role of IMCProxy

The data transmission system onboard the USV is constituted of the 4G/LTE and Iridium modems that transmit data when requested by the operators onshore or by the onboard software. The transmission of IMC messages between the USV and the onshore station is relayed by the NTNU server, as shown in Figure 3.15 and Figure 3.13, independently of the employed communication link. Compression and transmission of the IMC payload is handled by the IMCProxy for all the three components (USV, NTNU server, onshore station). Onboard the USV and in the operators computers, a client is running, whereas at NTNU the server side of the proxy is implemented.

IMC networks are implemented in a way that they are able to automatically discover and connect to each other by listening to broadcasted announce and discovery messages. When using IMC over the UDP protocol, these broadcasted messages are often not routed to other networks, and thus they are limited to the local network. In solutions where traffic across different networks is necessary, a proxy solution is necessary to bridge two (or multiple) networks. The IMCProxy has been created for this purpose, and it is based on a WebSocket<sup>8</sup> server/client architecture written in Java<sup>9</sup>, where the server (NTNU server) has a separate connection for each connected client (the USV and the operators). The proxy server receives all IMC messages from connected clients, and relays them to all the other connected clients, as shown in Figure 3.14.

---

<sup>8</sup>A computer communication protocol, providing full-duplex communication channels over a single TCP connection

<sup>9</sup><https://github.com/adallolio/imcproxy>

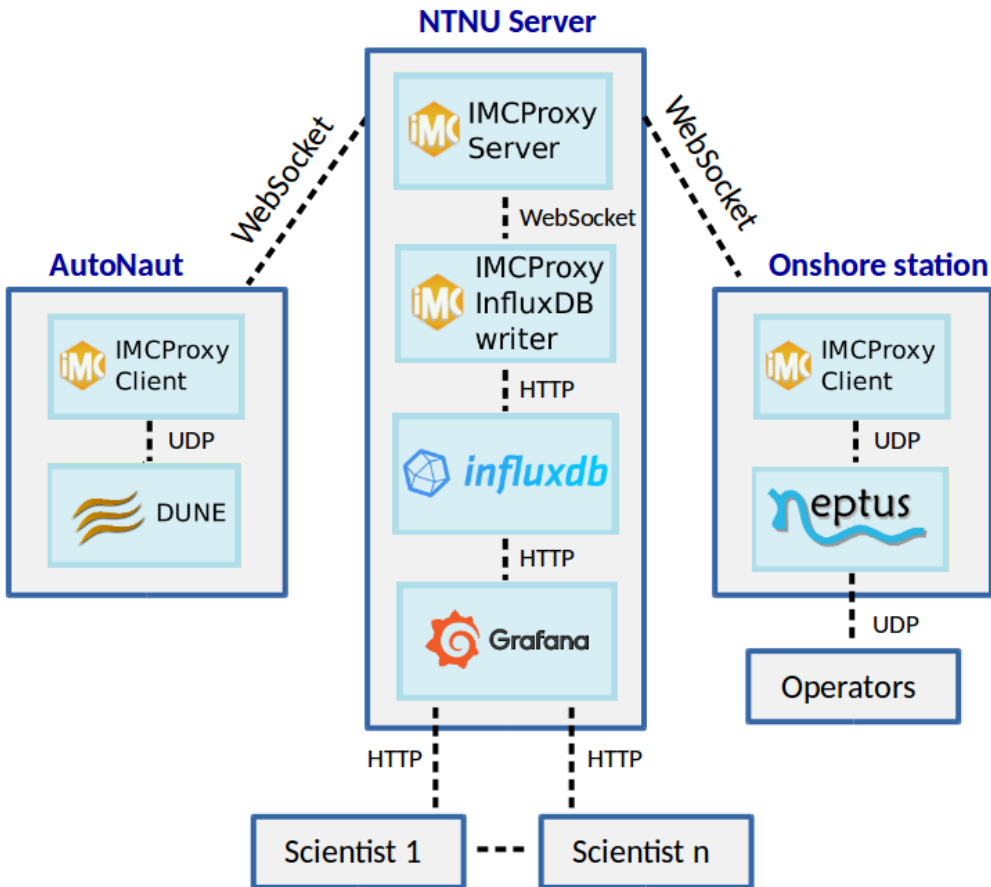


Figure 3.14: The implemented software architecture that enables: real-time control, and mission monitoring from the operators and near real-time mission observation from the involved scientists.

### 3.8.2 Relational database

Databases are used to store large amounts of data in a way that balances searching performance and overhead storage. A Database Management System (DBMS) is used to create a database, by defining its structure, filling it with data, and storing them based on some predefined data-structure. After creation, an application program can access the DBMS to manipulate the data, or run queries to receive the indexed data. An important aspect is that the DBMS allows multiple-users to access the database simultaneously in a way that maintains the database in an atomic state [103].

In a relational database, the content is defined by tables having attributes stored in tuples. Each single row of the table is a tuple that contains related data. The structure description of such a database includes the datatype of the attributes. For each database, there exist a key that uniquely identifies every tuple. To be able to efficiently search a database on keys, auxiliary data structures called indexes are used. How these are implemented varies between database systems. Most commonly, hash-tables or binary-heap implementations are used. For some types of data (e.g., spatial or time-varying data), specialized indexes exist. The method to access the data stored in a database is based on queries that precisely describe the desired portion of the data to be retrieved. For this purpose, multiple languages have been invented and, a desirable characteristic of such languages is that they do not depend on the underlying data structure. The Structured Querying Language (SQL) is a standard language for relational DBMSs, that provides a high-level declarative way of querying [103]. SQLite is a light-weight DBMS that stores its database in a single self-contained file [104]. This makes it widely employed in a number of applications, and also serves as a base for a lot of file formats<sup>10</sup>. Unlike many other DBMSes, no server is required to use SQLite since everything is implemented in a single library written in the C programming language. Both DUNE and Neptus use SQLite to store information, e.g., the vehicle's mission plans. This means that the library is already integrated in both software packages.

#### 3.8.3 InfluxDB: a Time-Series Database Management System

A Time-Series Database Management System (TSDBMS), is a DBMS optimized for time-stamped data<sup>11</sup>. The primary key of a TSDBMS is always a measure of time. InfluxDB is open-source and has been optimized for storing time series through associated pairs of time(s) and value(s). The values are further divided into tags and fields. While tags are automatically indexed, fields are not being indexed at all and, choosing between them is a part of the database design. This choice depends on which queries will be performed most frequently.

In the application developed and presented in this thesis, the data are received by the NTNU server, which compresses and stores them in a InfluxDB database. In particular, InfluxDB is used for storing converted IMC messages (see Figure 3.14). Accessing InfluxDB is done through a SQL based language called InfluxQL<sup>12</sup>, or through a HTTP-based API. In this work, the Grafana API is used for accessing and displaying the data from the database.

To ingest the IMC messages into the database, a simple Java application has been

---

<sup>10</sup><https://www.sqlite.org/about.html>

<sup>11</sup><https://www.influxdata.com/time-series-database/>

<sup>12</sup>[https://docs.influxdata.com/influxdb/v1.8/query\\_language/](https://docs.influxdata.com/influxdb/v1.8/query_language/)

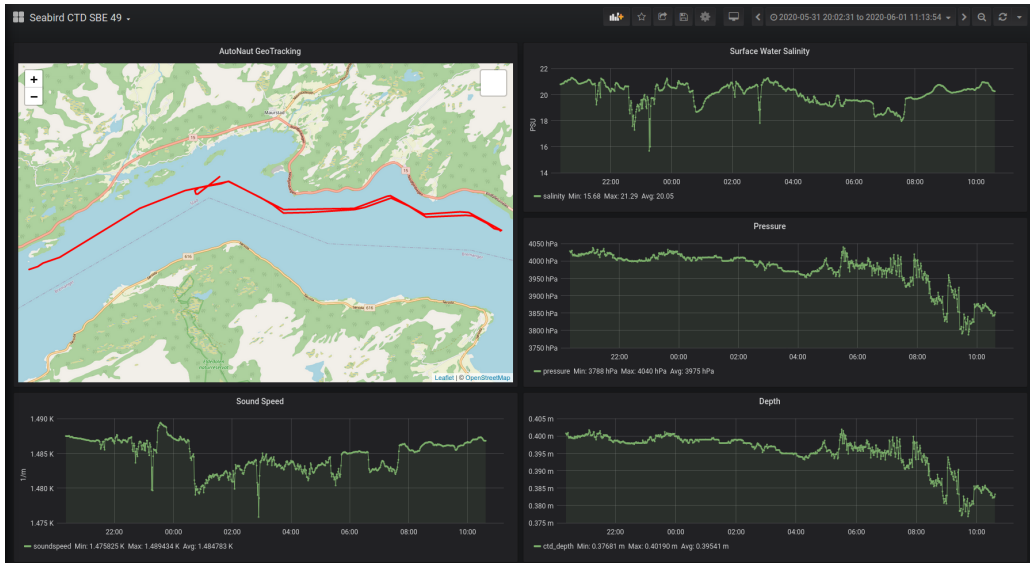


Figure 3.15: An example of CTD measurements displayed in real-time in the Grafana API, during a mission in Nordfjord (Central Norway) in May 2020.

developed<sup>13</sup> based on the original version from LSTS. This new implementation allows to store data in the database and at the same time relay them to the connected IMC clients. Moreover, since one of the requirements was to make the system independent of the communication link, a software program was developed<sup>14</sup> to re-direct satellite messages from the Iridium API to the server, where they are decoded and inserted into a dedicated table of the database. This allows the NTNU server to collect, store and display without any loss all the information transmitted from the USV.

### 3.8.4 Real-time data querying and display

The server runs an API named Grafana<sup>15</sup>, which queries the database and displays them (see Figure 3.14 and 3.15). Grafana is a multi-platform open source analytics and interactive visualization web application that lets users create multiple dashboards containing data visualizations<sup>16</sup>. The time range, visualizations and appearance is entirely defined by the user, and is configured in the web interface. Grafana supports multiple data sources (e.g., Prometheus, MySQL, InfluxDB and

<sup>13</sup><https://github.com/adalolloio/imcproxy>

<sup>14</sup><https://github.com/adalolloio/iridium-to-influxDB>

<sup>15</sup><https://grafana.com/>

<sup>16</sup>A live demo: <https://play.grafana.org/>

PostgreSQL) that can be queried through an online interface. The result can then be presented in diverse visualizations such as graphs, maps, gauges, tables etc. Since the interface is open source, custom visualizations can also be implemented. Moreover, queried data can be exported in CSV or JSON format. Once the dashboards are configured, users can browse through the data without any knowledge of the underlying database or querying happening in the background.

In this work, the data flow is continuous. This means that once the AutoNaut is turned on and the a communication channel is up and running (either 4G/LTE or satellite), data are transmitted from the USV to the server at NTNU. The data are automatically stored in the InfluxDB and Grafana is set to constantly query, automatically, the database. Grafana dashboards can be set to refresh the query at periodical intervals between 5 seconds and one day. This means that the minimum data delay is 5 seconds, which is considered not crucial since the majority of users is made of oceanographers and marine biologists. On the contrary, this allows precise data time-stamping and georeferencing, since multiple samples collected by the USV can be analysed in time and space (i.e., associating them with the current or past vehicle's locations) An example is shown in Figure 3.15, which shows CTD data transmitted by the USV while operating in a Norwegian fjord in May 2020. This system is primarily needed to scientists and oceanographers at NTNU (and not only), who can observe in near real-time the progress of a mission and the data collected by the USV on the sea. In the course of the last two years, this tool has proved to be useful and important to support mission planning from shore, during the execution of the mission itself.

## 3.9 Power system validation

The initial architecture has been validated through several field trials in the Trondheimsfjord (Trondheim, Norway). The missions conducted initially aimed at testing the correct functioning of *Level 1* and *Level 2* subsystem. This involved monitoring of the onboard energy balance of the vehicle, manual control and basic autonomous way point navigation. Implicitly, all three communication links were successfully tested. The proper functioning of *Level 3* was validated months later, since its practical assembly happened once the basic functionalities of the USV were operational.

Since advanced navigation functionalities are discussed in the next chapters, here it is presented a validation of the designed power system. The validation of the power system makes use of a 24-hours long dataset acquired on September 7, 2019 in Trondheim. Figure 3.16 shows that the power harvested by two solar panels properly fits within the margins defined by historic data (see Figure 3.5). Figure 3.17 shows a 24-hours system run. It can be observed that measured cur-

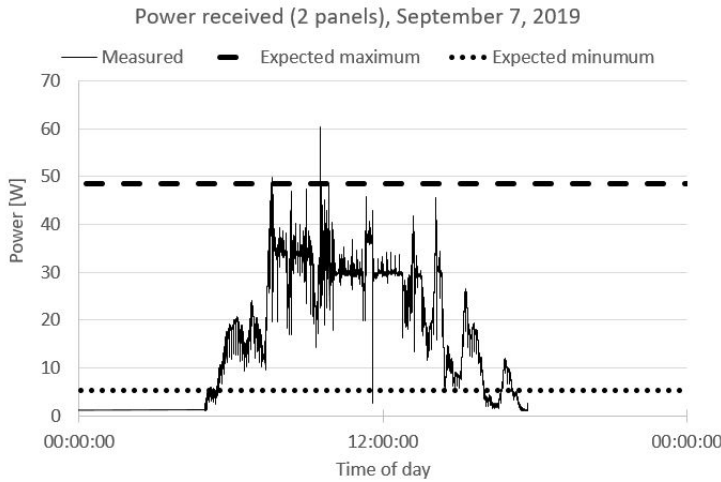


Figure 3.16: Power generated by two solar panels on September 7, 2019 in Trondheim.

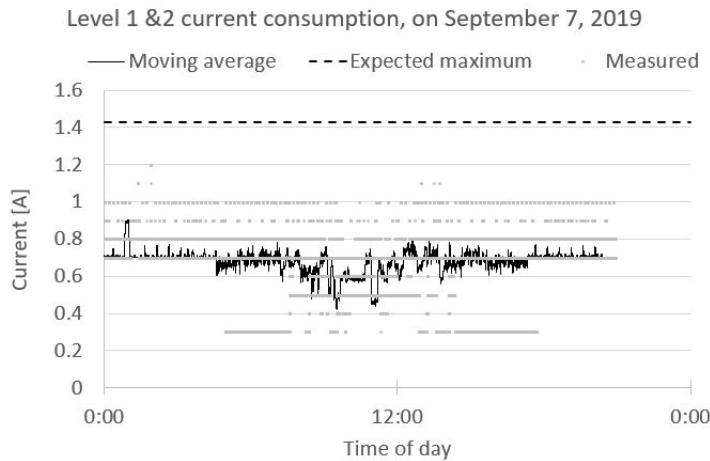


Figure 3.17: Current consumption by *Level 1* and *Level 2* on September 7, 2019

rent consumption of *Level 1* and *Level 2* is below the estimated value of 1.4A, based on maximum consumption of the whole system as mentioned in Section 3.3. Graphs showing the expected remaining onboard energy for Trondheim and Svalbard (Norway) areas, where the vehicle is expected to operate mostly, are presented in Figure 3.18 and Figure 3.19. Graphs are based on expected power consumption of all three subsystems, and the historic data of solar irradiance in these regions. The graphs give an insight about the remaining energy stored in

### 3. Onboard system architecture

---

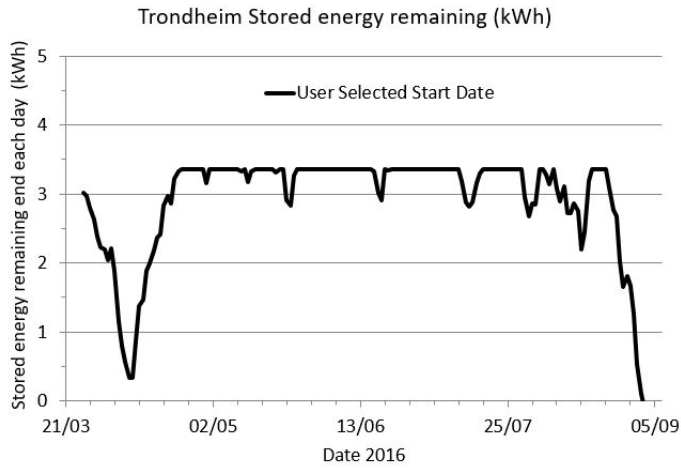


Figure 3.18: Expected onboard stored energy based on data from 2016 in Trondheim.

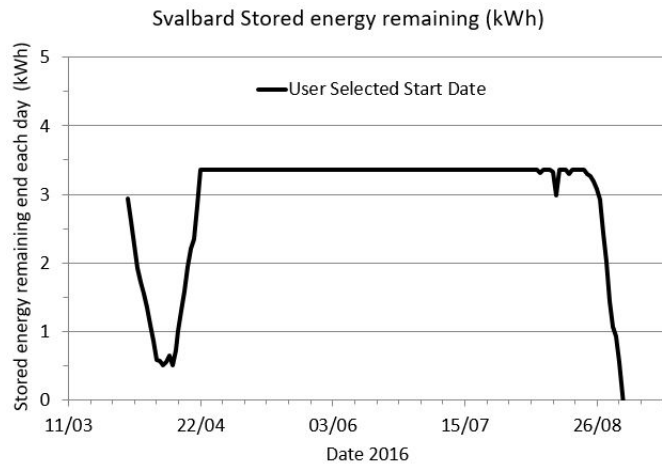


Figure 3.19: Expected onboard-stored energy based on data from 2016 in Svalbard (Norway).

the onboard battery bank of the vehicle during a long-term mission. By evaluating both the power produced by solar panels and that consumed by the system, including *Level 1* and *Level 2*, the graphs show a higher energy efficiency than the estimated values.

# Chapter 4

## Course control system

### *Design and experimental validation*

This chapter is inspired by the journal article [105].

For the AutoNaut, stable COG control can be a challenge whenever the forces exerted by the environment predominate on its steering and propulsion forces, and prevent them from achieving an intended behavior. The maneuverability limitations due to adverse environmental forces cannot be addressed with common navigation and control techniques, which rely on the ability of motored propulsion to firmly govern the behavior of the vehicle. The design of course-keeping autopilots usually refers to classical linear control theory, based on basic models such as the classical Nomoto model [92] that neglects the effect of environmental forces and simply relies on integral action [72]. Course control of a different wave-propelled USV using linear control theory is addressed in [106]. That work is however developed for the Wave Glider [22], a multi-body unmanned platform that is significantly different from the one considered in this thesis since the propulsion and steering force generating underwater body is tethered (i.e., not rigidly attached) to the surface hull. Despite being focused on modeling the speed, [107] and [108] show relevant modeling approaches for the Wave Glider.

The literature lacks detailed mathematical analyses of how control systems on-board wave-propelled vehicles can cope with environmental forces that are in the same order of magnitude as their propulsion capabilities. This chapter describes the dynamic modeling and course control system for the AutoNaut, taking into account the relevant effects of ocean current and other environmental forces that may lead to very low speed-over-ground (SOG). When removing this assumption, we must consider singularities at zero ground speed that are generally not considered in the course-keeping control of marine vehicles with motorized propulsion



and that can therefore avoid these conditions. The models give insight into the changes in steering dynamics as a function of changing environmental conditions, which is exploited in the control design to handle singular situations that occur when the SOG approaches zero. Although the singularity as zero ground speed invalidates the common assumption of linearity of the course-keeping model, it is shown that classical control design principles based on robust linear course and heading control can still be applied by switching to heading control at low ground speed.

In this research, the derived dynamic models are used to design a model-based control system. The dynamic properties and limitation of the wave-propelled USV are incorporated into the design process to obtain robust performance.

## 4.1 Theory

This section includes an overview of the path-following control architecture, a detailed presentation of the nonlinear model and an extensive investigation of its nonlinearities achieved with a frequency domain analysis.

### 4.1.1 Control architecture

As described in Section 2.2.1 of Chapter 2, LOS-based methods are widely employed in path following systems onboard USVs.

Different principles for path following can be applied depending on whether the velocity measurements is available or not. Figure 4.1 depicts the path-following control architecture designed for the AutoNaut USV. As shown in the previous chapter, the *enclosure-based steering law* can be applied and the desired course  $\chi_d$  can be computed as

$$\chi_d(t) = \text{atan2}(y_{los} - y(t), x_{los} - x(t)), \quad (4.1)$$

such that the BODY x-axis of the craft points in the direction of the LOS intersection point  $P_{los}$  (see Figure 2.2). In this approach, the crab angle  $\beta$  is assumed to be unknown and the control objective is  $\chi \rightarrow \chi_d$ . Consequently, a course autopilot of PI type is

$$\tau = -K_p \chi_e - K_i \int_0^t \chi_e(\tau) d\tau, \quad (4.2)$$

where  $\chi_e$  is the course error,  $K_p$  and  $K_i$  are the proportional and integral gains respectively. Similarly, equations 4.1 and 4.2 can be formulated for the control objective  $\psi \rightarrow \psi_d$ , as indicated in Figure 4.1.

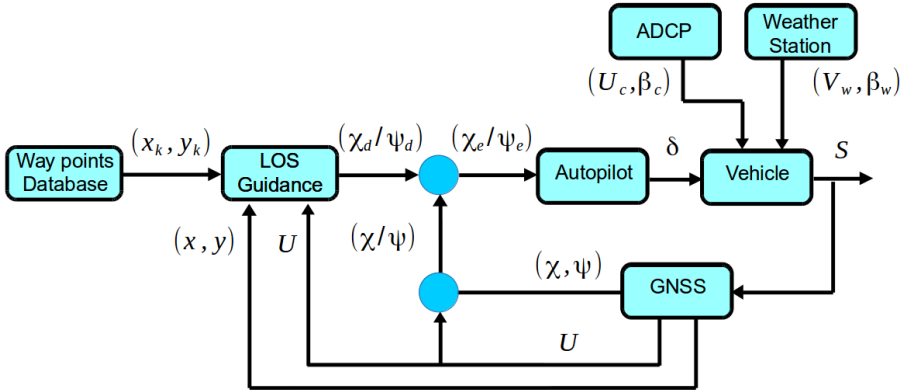


Figure 4.1: Path-following control architecture: the LOS guidance system computes a desired course/heading to the target location  $P_k = (x_k, y_k)$ , based on the vehicle position  $(x, y)$  obtained from the measured USV's state  $S$ ; rudder and course/heading control is achieved by measuring the current course ( $\chi$ ) or heading ( $\psi$ ), selected based on the measured ground speed ( $U$ ).

Figure 4.1 also shows the course/heading switching mechanism based on the measured SOG ( $U$ ). Further details and motivations for this implementation are provided in Section 4.1.3 and 4.2.2.

#### 4.1.2 Nonlinear dynamic model

The USV's speed relative to its surrounding water is mainly determined by surface currents, waves, and wind direction and speed. Speed drops are commonly observed when currents from starboard or port side prevent the vehicle from gliding on top of the waves or when strong winds and surface currents oppose to the vehicle's forward motion. Forces applied to the vehicle's sides also influence course-keeping performances, resulting in low controllability situations when the magnitude of environmental forces exceeds that generated by the propulsion system. In order to understand the control problem and the vehicle's inherent performance limitations, both a mathematical model analysis and field experiments are used. Typically, the speed over ground (SOG) achieved by a wave-propelled USV is in the range of 0-3 knots depending on the sea state and the ocean currents and wind. This implies that the vehicle's speed is of the same order of magnitude as the ocean currents, which must therefore be considered in the model and the course control algorithm. The common approach of relying on integral action to deal with the ocean current and second-order wave forces by viewing them as a slowly time-varying disturbance may still be highly useful and necessary, but the nonlinearities

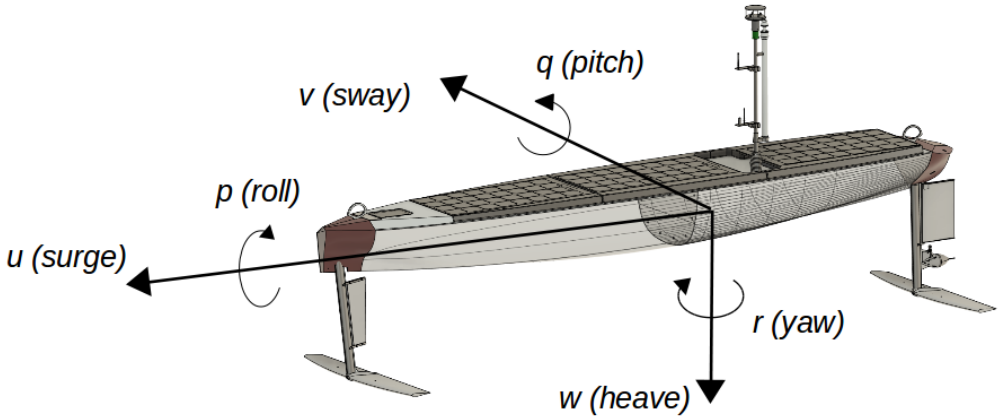


Figure 4.2: AutoNaut's 3D model with BODY-fixed reference frame. Vertical struts at the vehicle's bow and aft end with symmetrical spring-loaded hydrofoils, main source of its propulsion.

and couplings in the USV dynamics should also be addressed.

Consider the 3-degrees of freedom rigid body and hydrodynamic vehicle model (see Figure 4.2) for the horizontal plane [72]

$$M \dot{\mathbf{v}}_r + C(\mathbf{v}_r) \mathbf{v}_r + D(\mathbf{v}_r) \mathbf{v}_r = \boldsymbol{\tau}, \quad (4.3)$$

where  $M = M_A + M_{RB}$  accounts for rigid body and hydrodynamic added mass,  $C(\mathbf{v}_r) = C_A(\mathbf{v}_r) + C_{RB}(\mathbf{v}_r)$  accounts for Coriolis and centripetal terms, and  $D(\mathbf{v}_r)$  includes damping terms. In this representation  $\mathbf{v}_r$  is the velocity vector of the vehicle relative to the ocean current. The vector  $\boldsymbol{\tau}$  contains forces in surge and sway, and the corresponding yaw moment, generated by winds, waves, steering and propulsion mechanisms. Expanding the matrices in Equation 4.3 we obtain

$$M = \begin{pmatrix} m + A_{11} & 0 & 0 \\ 0 & m + A_{22} & 0 \\ 0 & 0 & J_z + A_{66} \end{pmatrix}, \quad (4.4)$$

$$C(\mathbf{v}_r) = \begin{pmatrix} 0 & -mr & -A_{22}v_r \\ mr & 0 & A_{11}u_r \\ A_{22}v_r & -A_{11}u_r & 0 \end{pmatrix} \quad (4.5)$$

and

$$D = \begin{pmatrix} D_{11} & 0 & 0 \\ 0 & D_{22} & 0 \\ 0 & 0 & D_{66} \end{pmatrix}. \quad (4.6)$$

The following notation was used:

- $m$  is the rigid-body vehicle mass;
- $r = \dot{\psi}$  is the yaw angular rate, where the yaw (heading) angle is denoted by  $\psi$ ;
- $u$  and  $v$  are the longitudinal and lateral components of the speed over ground (SOG), respectively, decomposed in the vehicle's BODY coordinate frame, such that  $SOG = U = \sqrt{u^2 + v^2}$
- $u_c$  and  $v_c$  are the longitudinal and lateral components of the ocean current velocity vector, respectively, decomposed in the vehicle's BODY coordinate frame. The current is assumed to be irrotational such that  $r_c = 0$ ;
- $u_r = u - u_c$  and  $v_r = v - v_c$  are the longitudinal and lateral components of the relative velocity, respectively, decomposed in the vehicle's BODY coordinate frame;  $\mathbf{v}_r = [u_r, v_r, r]^T$
- $J_z$  is the moment of inertia about the vertical axis;
- $A_{ij}$  are hydrodynamic added mass and moment of inertia coefficients;
- $D_{ij}$  are linear hydrodynamic damping coefficients;
- $F_X$  and  $F_Y$  are the longitudinal and lateral steering and propulsion forces acting on the vehicle body, respectively, and  $\tau_Z$  is the corresponding moment about the vertical axis acting on the vehicle body;  $\boldsymbol{\tau} = [F_X, F_Y, \tau_Z]^T$ .

The damping can be modeled using linear skin friction, quadratic surge resistance, and cross-flow drag in sway and yaw, see [72] for details. Since the USV's ground speed is low, the quadratic damping in surge and the cross-flow drag can be linearized. The off-diagonal damping terms are set to zero since they are negligible at low speed. In fact, the linear coupling terms will be less than 5 % of its diagonal counterparts if the method of [109] is applied. The parameters of the system matrices  $M$ ,  $C$  and  $D$  for the AutoNaut are presented in Appendix A.1.1.

By assuming that the ocean current is stationary and irrotational in the inertial coordinate system, a rotation with the vehicle's yaw angle should be used to define  $(u_c, v_c)$ . Note that since the vector  $(u_c, v_c)$  is decomposed in the BODY frame, we have that  $\dot{u}_c = v_c r$  and  $\dot{v}_c = -u_c r$ . Moreover,  $U_r = \sqrt{u_r^2 + v_r^2}$  is the USV's velocity relative to the water flow.

The course angle  $\chi = \psi + \beta$  depends on the crab angle  $\beta = \arctan(v/u) = \arcsin(v/U)$ . Hence, the course angle dynamics can be expressed as

$$\begin{aligned}\dot{\chi} &= r + \frac{1}{1 + \frac{v^2}{u^2}} \frac{d}{dt} \left( \frac{v}{u} \right) \\ &= r + \frac{1}{U^2} (\dot{v}u - \dot{u}v).\end{aligned}\quad (4.7)$$

The expressions for  $\dot{u}$  and  $\dot{v}$  can be obtained from the vehicle's dynamics given by Equation 4.3:

$$\dot{u} = r v_c + \frac{m + A_{22}}{m + A_{11}} v_r r - \frac{D_{11}}{m + A_{11}} u_r + \frac{1}{m + A_{11}} (F_X + F_{Xw}), \quad (4.8)$$

$$\dot{v} = -r u_c - \frac{m + A_{11}}{m + A_{22}} u_r r - \frac{D_{22}}{m + A_{22}} v_r + \frac{1}{m + A_{22}} (F_Y + F_{Yw}), \quad (4.9)$$

$$\dot{r} = -\frac{D_{66}}{J_z + A_{66}} r - \frac{A_{22} - A_{11}}{J_z + A_{66}} u_r v_r + \frac{1}{J_z + A_{66}} (\tau_Z + N_{Zw}), \quad (4.10)$$

where we define  $F_X$ ,  $F_Y$  and  $\tau_Z$  as

$$F_X := F_{prop} + F_{XR}, \quad (4.11)$$

$$F_Y := F_{YR}, \quad (4.12)$$

$$\tau_Z := N_{ZR}. \quad (4.13)$$

Here we assume that the propulsion force generated by the submerged hydrofoils mechanism only affects the surge dynamics.  $F_{XR}$ ,  $F_{YR}$  and  $N_{ZR}$  are respectively longitudinal and lateral horizontal forces, and yaw moment, generated by the rudder.  $F_{Xw}$ ,  $F_{Yw}$  and  $N_{Zw}$  are longitudinal and lateral horizontal forces, and yaw moment, generated by the wind. While the steering model is discussed in the next section, we refer to Appendix A.1.2 for the wind model. Moreover, we refer to Appendix sections A.3 and A.2 for the definition of wind and sea current relative directions and their transformation from Earth-fixed to BODY frame and viceversa.

In this chapter it is shown that a model of the longitudinal propulsion force generated by the submerged foils is not necessary for the design of a course-keeping autopilot that instead uses the longitudinal speed as a time-varying known (measured) variable.

### Steering model

The steering model captures the dynamics of the rudder forces and moments given by  $F_{XR}$ ,  $F_{YR}$  and  $N_{ZR}$ . The rudder normal force is expressed as [110]

$$F_N = \frac{1}{2} \rho U_r^2 A_R C_N \sin(\alpha_R), \quad (4.14)$$

where  $A_R$  is the rudder area,  $U_r$  is the total relative speed as defined earlier, and

$$\alpha_R = \delta - \tan^{-1} \left( \frac{v_r}{u_r} \right) \quad (4.15)$$

is the relative angle between rudder and current (in BODY frame) angles. According to [111],  $C_N$  can be computed by

$$C_N = \frac{6.13\Lambda}{\Lambda + 2.25}, \quad (4.16)$$

where  $\Lambda = b^2/A_R$  is the rudder aspect ratio, where  $b$  is the rudder height and  $A_R$  is the rudder area. The rudder normal force  $F_N$  contributes to forces in surge and sway as

$$F_{XR} = -(1 - t_R)F_N \sin(\delta) \quad (4.17)$$

$$F_{YR} = -(1 + a_H)F_N \cos(\delta) \quad (4.18)$$

and to the yaw moment as

$$N_{ZR} = -(x_R + a_H x_H)F_N \cos(\delta), \quad (4.19)$$

where  $x_R$  is the longitudinal coordinate of the rudder position (approximately  $-0.5L_{pp}$ , where  $L_{pp}$  is the length between perpendiculars of the vehicle). The coefficient for additional drag  $t_R$  can be approximated according to [112]

$$1 - t_R = 0.28C_B + 0.55, \quad (4.20)$$

where  $C_B$  is the USV block coefficient. The coefficients  $a_H$  and  $x_H$  can be chosen according to [110]. The numerical values associated to the presented rudder model are presented in Table A.2 of Appendix A.1.

### Simplified quasi-linear model

Assume the surge velocity  $u$  is constant. This may be reasonable when following straight paths in open ocean, but has limitations during fast heading changes and when operating closer to shore where currents may change quickly. In this section we neglect the wind forces, for simplicity. In this case the course angle dynamics becomes

$$\begin{aligned} \dot{\chi} &= r + \frac{u}{U^2} \dot{v} \\ &= r + \frac{u}{U^2} \left( -ru_c - \frac{m + A_{11}}{m + A_{22}} u_r r - \frac{D_{22}}{m + A_{22}} v_r + \frac{1}{m + A_{22}} F_Y \right) \\ &= \gamma r + \frac{u}{U^2} \left( -\frac{D_{22}}{m + A_{22}} v_r + \frac{F_Y}{m + A_{22}} \right), \end{aligned} \quad (4.21)$$

where

$$\gamma = 1 - \frac{u}{U^2} u_c - \frac{u}{U^2} \frac{m + A_{11}}{m + A_{22}} u_r. \quad (4.22)$$

Combining this with the lateral vehicle dynamics leads to the third order quasi-linear system

$$\begin{pmatrix} \dot{\chi} \\ \dot{v} \\ \dot{r} \end{pmatrix} = \begin{pmatrix} 0 & -\frac{u}{U^2} \frac{D_{22}}{m+A_{22}} & \gamma \\ 0 & -\frac{D_{22}}{m+A_{22}} & -u_c - \frac{m+A_{11}}{m+A_{22}} u_r \\ 0 & 0 & -\frac{D_{66}}{J_z+A_{66}} \end{pmatrix} \begin{pmatrix} \chi \\ v \\ r \end{pmatrix} + \begin{pmatrix} \frac{u}{U^2} \frac{D_{22}}{m+A_{22}} \\ \frac{D_{22}}{m+A_{22}} \\ 0 \end{pmatrix} v_c - \begin{pmatrix} 0 \\ 0 \\ \frac{A_{22}-A_{11}}{J_z+A_{66}} \end{pmatrix} u_r v_r \quad (4.23)$$

$$+ \begin{pmatrix} \frac{u}{U^2} \frac{1}{m+A_{22}} & 0 \\ \frac{1}{m+A_{22}} & 0 \\ 0 & \frac{1}{J_z+A_{66}} \end{pmatrix} \begin{pmatrix} F_Y \\ \tau_Z \end{pmatrix}, \quad (4.24)$$

whose equivalent formulation is:

$$\begin{pmatrix} \dot{\chi} \\ \dot{v}_r \\ \dot{r} \end{pmatrix} = \begin{pmatrix} 0 & -\frac{u}{U^2} \frac{D_{22}}{m+A_{22}} & \gamma \\ 0 & -\frac{D_{22}}{m+A_{22}} & -\frac{m+A_{11}}{m+A_{22}} u_r \\ 0 & -\frac{A_{22}-A_{11}}{J_z+A_{66}} u_r & -\frac{D_{66}}{J_z+A_{66}} \end{pmatrix} \begin{pmatrix} \chi \\ v_r \\ r \end{pmatrix} + \begin{pmatrix} \frac{u}{U^2} \frac{1}{m+A_{22}} & 0 \\ \frac{1}{m+A_{22}} & 0 \\ 0 & \frac{1}{J_z+A_{66}} \end{pmatrix} \begin{pmatrix} F_{YR} \\ N_{ZR} \end{pmatrix}. \quad (4.25)$$

The normal force generated by the rudder, Equation 4.14, can be rewritten as

$$F_N = \frac{1}{2} \rho U_r A_R C_N (u_r \sin(\delta) - v_r \cos(\delta)). \quad (4.26)$$

We further assume the rudder angle is small and make the approximations  $\cos(\delta) \approx 1$  and  $\sin(\delta) \approx \delta$ . The lateral force and yaw moment given by equations 4.18 and

4.19 then become

$$F_{YR} \approx -\frac{1}{2}(1 + a_H)\rho U_r A_R C_N (u_r \delta - v_r), \quad (4.27)$$

$$N_{ZR} \approx -\frac{1}{2}(x_R + a_H x_H)\rho U_r A_R C_N (u_r \delta - v_r) \quad (4.28)$$

or equivalently

$$F_{YR} \approx \alpha_{YR} U_r (u_r \delta - v_r) \quad (4.29)$$

$$N_{ZR} \approx \alpha_{ZR} U_r (u_r \delta - v_r), \quad (4.30)$$

where  $\alpha_{YR} = -\frac{1}{2}(1 + a_H)\rho A_R C_N$  and  $\alpha_{ZR} = -\frac{1}{2}(x_R + a_H x_H)\rho A_R C_N$ . The simplified quasi-linear model corresponding to Equation 4.25 then becomes:

$$\begin{pmatrix} \dot{\chi} \\ \dot{v}_r \\ \dot{r} \end{pmatrix} = \begin{pmatrix} 0 & -\frac{u}{U^2} \frac{1}{m+A_{22}} (D_{22} + \alpha_{YR} U_r) & \gamma \\ 0 & -\frac{1}{m+A_{22}} (D_{22} + \alpha_{YR} U_r) & -\frac{m+A_{11}}{m+A_{22}} u_r \\ 0 & -\frac{1}{J_z+A_{66}} ((A_{22} - A_{11})u_r + \alpha_{ZR} U_r) & -\frac{D_{66}}{J_z+A_{66}} \end{pmatrix} \begin{pmatrix} \chi \\ v_r \\ r \end{pmatrix} + \begin{pmatrix} \frac{u}{U^2} \frac{\alpha_{YR} U_r u_r}{m+A_{22}} \\ \frac{\alpha_{YR} U_r u_r}{m+A_{22}} \\ \frac{\alpha_{ZR} U_r u_r}{J_z+A_{66}} \end{pmatrix} \delta. \quad (4.31)$$

In the forthcoming we denote the transfer function resulting from this model  $H_{ql}(s) = \frac{\chi}{\delta}(s)$ .

### 4.1.3 Model analysis and control

We consider in this section the case in which the lateral dynamics is eliminated from the model in Equation 4.31 by discarding the second row and column of the third-order state-space model and the effects of  $F_{YR}$ . Assume that  $u = u_c + u_{prop}$ , where  $u_{prop}$  is an equivalent constant speed due to wave propulsion only. This leads to a second-order system that can easily be shown to correspond to the well-known and widely employed Nomoto model [72] with a gain that depends on  $\gamma$ ,  $u_{prop}$  and  $U_r$ :

$$H_n(s) = \frac{\chi}{\delta}(s) = \frac{\gamma u_{prop} U_r K}{s(1 + Ts)}. \quad (4.32)$$

Consider first a nominal reference case where  $u_{prop} = 1$  m/s and  $u_c = v_c = 0$ . The transfer function  $H_{ql}(s)$  is shown in Figure 4.3. The figure also shows the transfer



#### 4. Course control system: Design and experimental validation

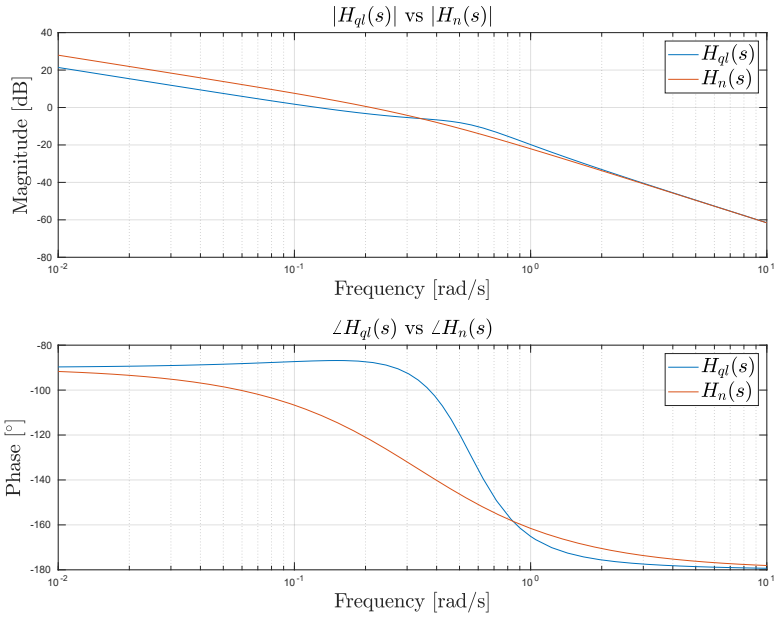


Figure 4.3: Transfer functions of quasi-linear third order model  $H_{ql}(s)$  (red) and Nomoto model  $H_n(s)$  (blue).

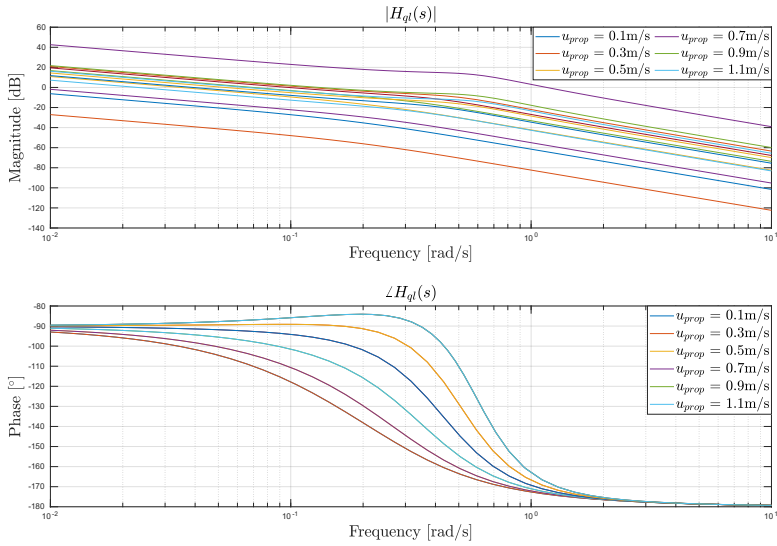


Figure 4.4: Transfer function  $H_{ql}(s)$  from  $\delta$  to  $\chi$  for third-order quasi-linear model when  $u_c \in [-1, 1]$  m/s and  $u_{prop} \in [0.1, 1.1]$  m/s.

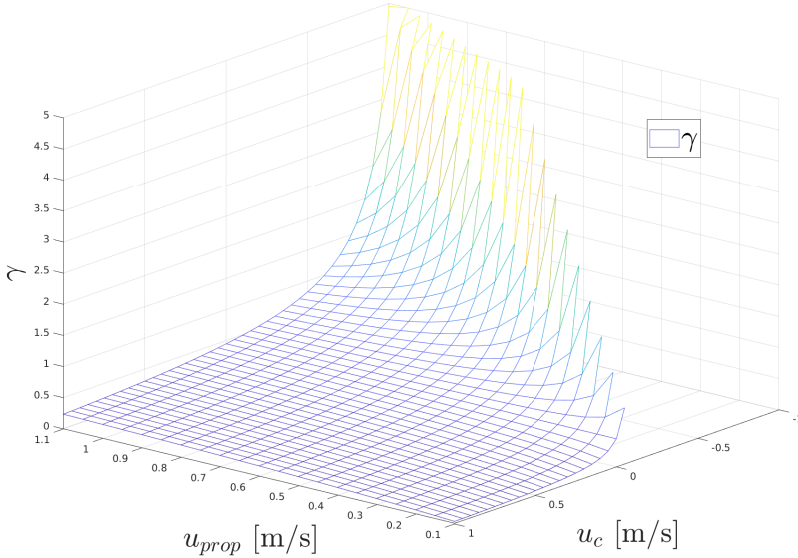


Figure 4.5: Example of  $\gamma$  as a function of  $u_{prop}$  and  $u_c$ .

function of the Nomoto model (Equation 4.32) for comparison. It can be seen that the high-frequency gain is the same, but there is a difference in the gain at lower frequencies between 0 and +8 dB, while the phase difference is up to  $40^\circ$ . In order to understand how the dynamics changes with variations in sea state ( $u_{prop}$ ) and current ( $u_c$ ), we assume  $v_c = 0$  and show the family of transfer functions  $H_{ql}(s)$  in Figure 4.4, where  $u_c \in [-1, 1]$  m/s and  $u_{prop} \in [0.1, 1.1]$  m/s. Due to the combined effects of order of magnitude variations in both  $u_r$  and  $U$ , we conclude by comparing Figure 4.4 with the nominal case in Figure 4.3 that one can expect gain variations between -50 dB and +20 dB compared to the nominal model. At the same time, the variations in phase up to  $60^\circ$  are observed. The cases with increased gain correspond to conditions where the ground speed  $U$  becomes very small, while cases with decreased gain correspond to situations where the propulsion speed  $u_{prop} = u_r$  is very small (e.g., due to the wave propulsion becoming ineffective in sea states with very small waves and/or waves from the side).

The main variations in dynamics are due to the parameter  $\gamma$  that influences the gain in the Nomoto model (4.32). We show how  $\gamma$  varies as a function of  $u_{prop}$  and  $u_c$  in Figure 4.5. Note that the parameter  $\gamma$  is infinite along the line  $u_c + u_{prop} = 0$ , which corresponds to the singularity  $U = 0$ . Figure 4.6 indicates that it is indeed the gain  $\gamma$  that is the main cause for the variations, where the normalized transfer function  $\frac{1}{\gamma}H_{ql}(s)$  is shown. For reference, Figure 4.7 plots  $H_{ql}(s)/H_n(s)$ , which

#### 4. Course control system: Design and experimental validation

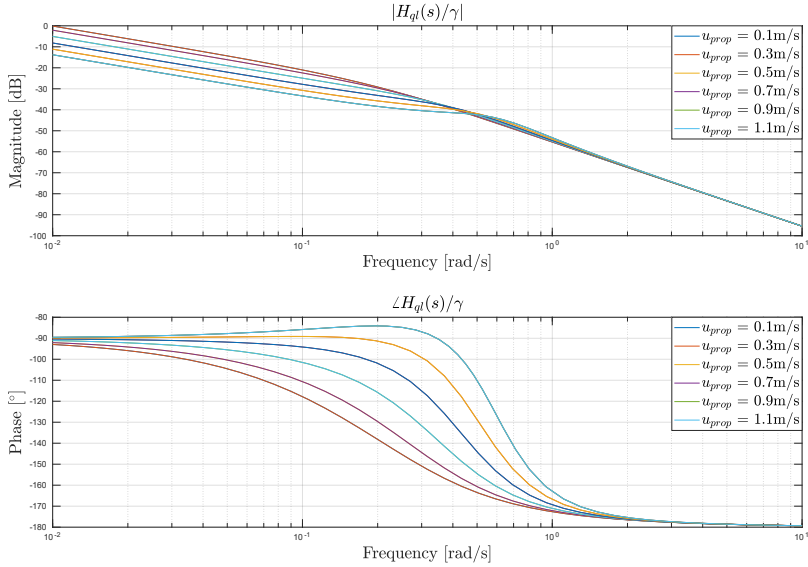


Figure 4.6: Normalized with  $\gamma$ : Transfer function  $H_{ql}(s)/\gamma$  for third-order quasi-linear model when  $u_c \in [-1, 1]$  m/s and  $u_{prop} \in [0.1, 1.1]$  m/s.

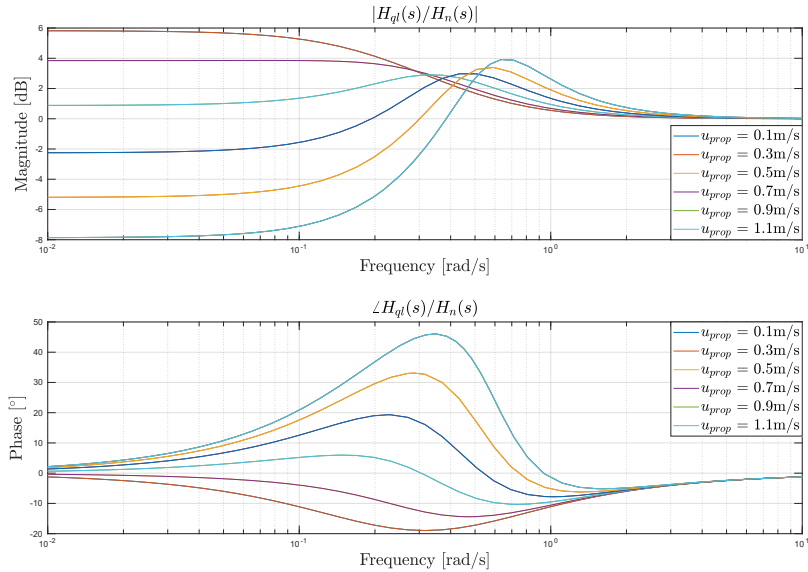


Figure 4.7: Ratio between the transfer functions of the quasi-linear third-order model and the Nomoto model with nonlinear gain  $H_{ql}(s)/H_n(s)$ , when  $u_c \in [-1, 1]$  m/s and  $u_{prop} \in [0.1, 1.1]$  m/s.

indicates that the Nomoto model with parameter-dependent gain is an accurate approximation at high frequencies, while its magnitude deviation is reduced by up to 14 dB at lower frequencies, and phase deviation still up to  $60^\circ$ .

This indicates that course-keeping control should consider the variations in the gain  $\gamma$ , and counteract the disturbances due to winds and current. The latter can be obtained by integral action, since the current, wind and propulsion speeds can be expected to be slowly time-varying variables.

Gain-scheduling based on  $\gamma$  is in principle an interesting approach as illustrated by the above mentioned analysis that shows that the main influence on the transfer function from rudder angle to course angle is captured by the scalar parameter  $\gamma$ . The linear control design approach that is the basis for gain-scheduled (quasi-linear) control is justified by the observation that the main nonlinearities are resulting from the slowly time-varying environmental parameters (winds, waves and current) as well as the course angle command. However, the prospects of a practical realization of a gain-scheduling strategy is limited by the following facts:

- The parameter  $\gamma$  depends on the ocean current, which may not be known. It should be kept in mind that although USVs could be equipped with an acoustic Doppler current profiler (ADCP), such an instrument is expensive, power hungry, and results may be inaccurate due to its proximity to the sea surface and the USV's pitching/rolling motions.
- Increasing the gain may not be very effective due to saturation of the rudder angle.
- There is a singularity with infinite  $\gamma$  when  $U$  goes to zero, which may be unavoidable due to the limited propulsion that makes the vehicle uncontrollable when the wind or current are too strong compared to the wave propulsion force.
- The course angle may not be reliably measured with the global navigation satellite system (GNSS) when  $U$  becomes close to zero, and is in fact undefined at the singular point  $U = 0$ .

It is therefore proposed a linear course controller that is robust over a range of environmental conditions, with a switch to a heading controller in case  $U$  becomes close to zero or the forward propulsion speed becomes negative. Due to the slowly time-varying nature of the quasi-linear model, a robust linear course controller should be designed with acceptable performance for any constant environmental parameters and course angle command for which  $U$  is sufficiently far from zero. In compliance with a preliminary analysis of the vehicle steering model [28], the implemented autopilot is a linear PI-controller, and its parameters are robustly tuned for  $U \geq 0.2$  m/s. This strategy is evaluated in field experiments as described in the next sections.

## 4.2 Experimental results and discussion

Sea trials are carried out in both the Trondheim fjord and off the coasts of Norway in the North Atlantic Ocean. Figure 4.1 depicts the USV's control architecture and shows how the GNSS is used to close the outer path control loop and the inner course control loop. The choice of controlling the course or the heading of the USV is based on measured currents (from ADCP or ocean models), winds (from weather station) and USV's ground speed. An example of how this logic is employed in the field is shown in Section 4.2.2. Autonomous path following is achieved via line-of-sight (LOS) guidance system that computes the desired course over ground that steers the vehicle towards the desired path [72].

### 4.2.1 Experimental control: basic results

In the following experiments (Section 4.2.1 and 4.2.1) basic control results obtained in fjord and ocean waters, respectively, are shown. In both experiments the USV course is controlled by a PI-controller with gains  $K_p = 1.25$  and  $K_i = 0.02$ , tuned experimentally.

#### Autonomous navigation in the Trondheim fjord

Fast and irregular waves are expected in fjords, where a reduced wind fetch generates short-crested waves whose amplitude and frequency are mainly dependent on the local wind speed. It is therefore expected that the vehicle's speed is affected by a combination of sea currents, waves and wind. The USV was commanded to follow a sequence of way points disposed in a way that the intended path would create a square and expose the vehicle to different angles relative to the aforementioned disturbances. The mission site is strongly affected by tidal currents with direction and intensity depending on the time of the day. At the time of the mission, low tide generated currents from South-East and the observed mean wave amplitude was approximately 1 meter. The effects of the current can be observed in Figure 4.8, where it is clear that the USV ground speed  $U$  is higher when it navigates North and West. Figure 4.8 also shows that the ground speed drops significantly when the vehicle turns into the wind and finds sea currents on its starboard side. In the fourth leg of the trajectory (i.e., from time  $t = 5500s$ ), the ground speed increases due to a combination of wind and current forces in the direction of the vehicle's heading. However, the USV's velocity remains quite high when it enters the last section of the mission. From this it is possible to conclude that surface currents have a greater impact than winds on the ground speed and that some forward propulsion is ensured as long as waves are present. From Figure 4.8 it can also be concluded that the chosen PI-controller shows a degree of robustness

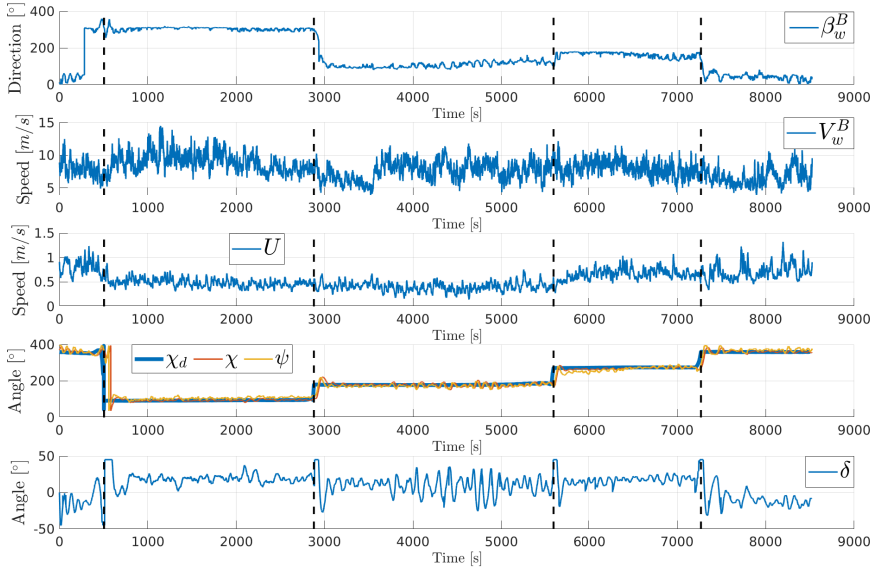


Figure 4.8: From the top: wind angle in USV's BODY frame ( $\beta_w^B$ ); wind speed relative to the USV ( $V_w^B$ ); vehicle ground speed ( $U$ ); desired course ( $\chi_d$ ) and measured course over ground ( $\chi$ ) and measured heading ( $\psi$ ); commanded rudder angle ( $\delta$ ). Black dashed lines indicate way point change.

that is good enough to steer the vehicle through the desired way points. The bottom graph shows the rudder angle commanded by the course autopilot where it is clear that the contribution of the integral action produces an average constant offset in the commanded rudder angle allowing the USV to keep the average course error within  $10^\circ$ . More wave-induced course and rudder oscillations are however observed in the third leg (from time  $t = 3000s$  to  $t = 5500s$ ), where the vehicle heads into the sea currents. The proportional action of the course controller allows indeed larger rudder oscillations meant to correct for the course error. This is in agreement with the linear analysis since the reduced ground speed leads to a higher gain  $\gamma$  in the response from rudder to course, which leads to less stability margins and more oscillations. The field-tested PI course controller proves itself capable of controlling the USV course when the forward propulsion due to waves exceeds the magnitude of environmental forces. Additionally, it is demonstrated that standard integral action is enough to compensate for environmental disturbances.

### Autonomous navigation in the North Atlantic Ocean

The same controller was tested in ocean waters, where more regular (i.e., constant in height and frequency over the considered time period) and higher waves are expected as a result of more constant and strong winds. As a consequence, the vehicle propulsion due to waves is also expected to be more regular, with variations in ground speed mainly due to wind and ocean current disturbances. The control architecture was tested along the Norwegian North Atlantic coasts, in a site located approximately 40km north of the Norwegian islands of Frøya and Hitra (mid-Norway). This area is known for quite intense coastal currents from South-West, as a result of the main North Atlantic Current (NAC) hitting the coasts of Norway (Norwegian Current) and continuing North/North-East. In this section it is discussed a portion of a 2-weeks mission which lasts for approximately one day. Figure 4.9 shows that the absolute wind direction varies significantly (variations up to  $120^\circ$ ) in the first hours of the mission, while it becomes more stable before the USV reaches the first way point and thereafter. The wind speed is very low in the first part of the mission, and keeps increasing steadily up to approximately 5 m/s in average in the first hours of June 16th. The wind speed increase is followed by an increase of the USV's ground speed that stabilizes around 0.75 m/s halfway between the first and second way point. Later during the same day it can be observed again a wind speed drop and increase, both somewhat correlated with the vehicle's ground speed. Figure 4.9 also compares measured heading ( $\psi$ ) and course over ground ( $\chi$ ) to the desired course ( $\chi_d$ ) between the way points. In the first leg of the mission it can be observed a course error always within  $10^\circ$  and an average positive rudder angle with oscillations of  $15^\circ$  mean amplitude, meaning that despite its lowest speed the wind is the main disturbance the integral action compensates for. The wind speed increase impacts the course control, that shows larger oscillations (with amplitude within  $20^\circ$ ) around the desired course due to a combined effect of enhanced ground speed and rudder oscillations (up to  $25^\circ$ ) observed after the second way point. Again, rudder oscillations of amplitude below  $15^\circ$  are commanded to compensate for first-order wave-induced vehicle motions, while larger oscillations are commanded to compensate for the wind gusts blowing on the USV port side and that have an immediate effect on the vehicle turning rate  $r$ . Moreover, the USV speed increases while moving North-East due to the additional speed provided by the ocean current that moves in the same direction. Overall, the course controller proves itself capable of rejecting the natural disturbances that act against its course-keeping capabilities.

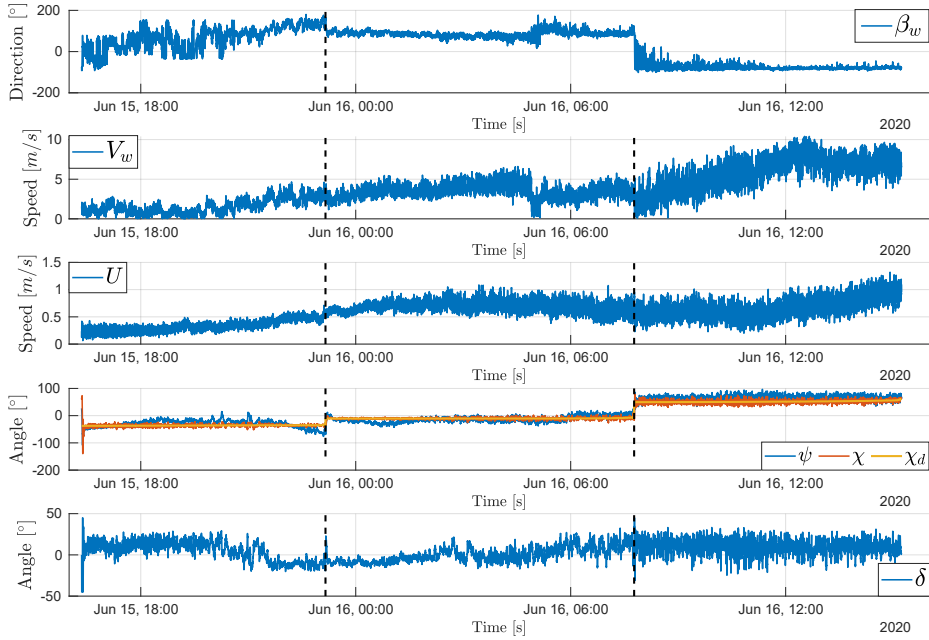


Figure 4.9: From the top: wind direction ( $\beta_w$ ) relative to North; wind speed relative to the vessel ( $V_w$ ); vehicle ground speed ( $U$ ); comparison between the measured heading ( $\psi$ ) and course ( $\chi$ ), and desired course ( $\chi_d$ ); commanded rudder angle ( $\delta$ ). Black dashed lines indicate way point change.

#### 4.2.2 Experimental control: adverse environmental disturbances

In this section, the limitations of this course control approach are discussed and situations in which the magnitude of environmental forces exceeds that of the propulsion system, leading to navigation instability, are shown. In most cases, loss of course controllability coincides with a loss of speed. The course over ground is defined only when the ground speed is greater than zero, when the latter drops significantly the course measurement provided by the GNSS system becomes unreliable. Most importantly however, if the ground speed drop coincides with a decrease of the USV's speed relative to water (i.e., when the current speed is low), the rudder becomes incapable of exerting a significant steering force. In such situations the closed-loop system (rudder to course) loses its performance as the commanded rudder angle does not generate a significant torque on the vehicle's yaw axis. This phenomenon is also observed when the environmental disturbance (e.g., wind or sea surface current) generates a force that balances the forward propulsion force produced by the submerged hydrofoils.

In this paragraph, two situations in which environmental forces prevent the vehi-



#### 4. Course control system: Design and experimental validation

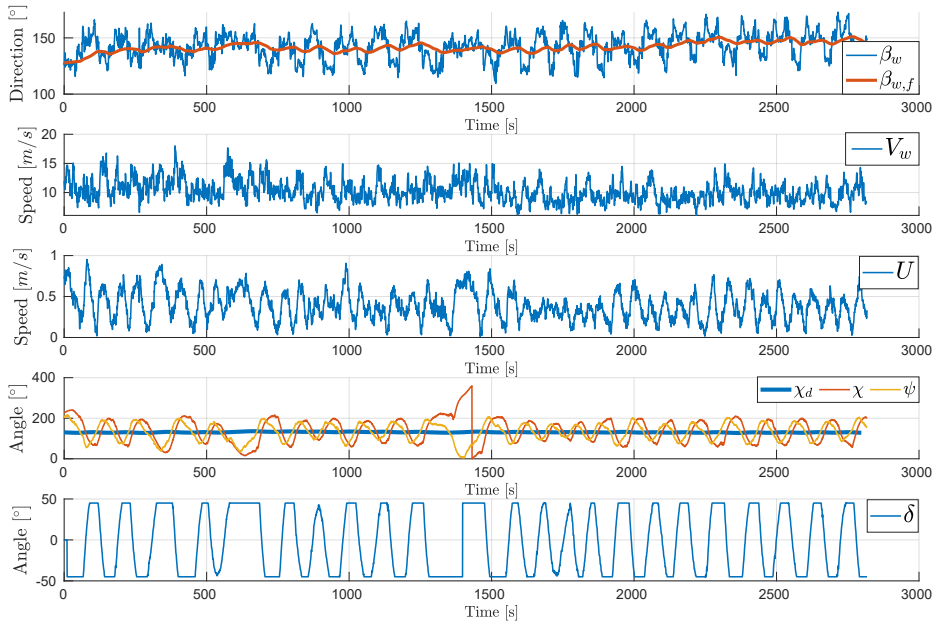


Figure 4.10: Top: wind direction ( $\beta_w$ ) and filtered wind direction ( $\beta_{w,f}$ ) relative to North; absolute wind speed ( $V_w$ ); measured ground speed ( $U$ ); comparison between the measured heading ( $\psi$ ) and course ( $\chi$ ), and desired course ( $\chi_d$ ); commanded rudder angle ( $\delta$ ).

cle to navigate in the intended direction, leading to large course oscillations and eventually total loss of control, are analysed.

#### Upwind control experiment

This field experiment took place in enclosed waters within the archipelago of Froan, which separates the coasts of mid-Norway from the North Atlantic Ocean. There the USV was commanded to navigated straight into the wind, which came from South-East with a speed between 10 and 12 m/s in average as shown in Figure 4.10. At the bottom of the figure it can observed the USV's speed over ground, that increases and decreases as the course oscillates around the desired course, which aligns with the wind direction. Figure 4.10 shows that the wind blows from an average direction  $\beta_{w,f} \approx 140^\circ$ , which coincides with the intended vehicle's course ( $\chi_d$ ) as observed in the fourth plot of Figure 4.10. The signal  $\beta_{w,f}$  is obtained after low-pass filtering  $\beta_w$  with a time constant  $t_f = 100s$ . From this we also notice that heading and course oscillations have a similar amplitude of approximately  $60^\circ$ . The last graph of Figure 4.10 clearly shows that the course controller introduced in Section 4.2.1 is not capable to keep course control with-

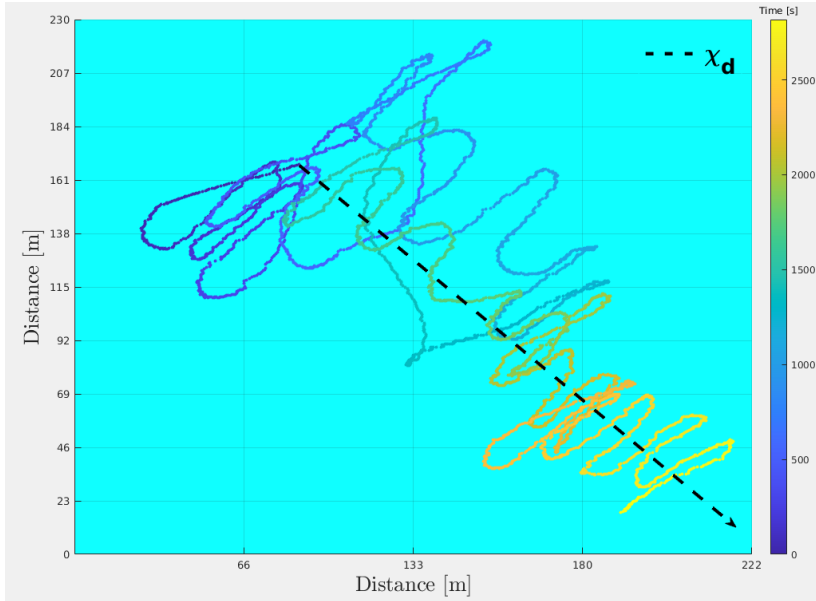


Figure 4.11: USV's track over time. The black dashed line indicates direction ( $\chi_d$ ) to the target location.

out significant course oscillations. This situation is observed, as expected, when the vehicle's speed over ground decreases towards zero as a result of the wind exerting a force on the USV that balances (or exceeds) its propulsion. This in turn makes the rudder ineffective and the integral error accumulates fast as the commanded rudder angles does not produce a yaw momentum on the vehicle and hence a course change. Moreover, at time  $t = 1600s$  the on-board software switches to a P controller with gain  $K_p = 1$ , as an attempt to reduce the amplitude of oscillations by removing integral effects, at the expenses of the USV's turn rate. Smaller oscillations are indeed observed until time  $t = 1800s$ , where the amplitude observed is the same as with the initial controller. This indicates, in addition, that the course is not controllable when the ground speed approaches zero. Figure 4.11 shows the track covered by the USV, characterized by numerous oscillations and a very inefficient navigation towards the desired location.

### Heading control switch experiment

This experiment took place in Frohavet, located North-East of the island Frøya and separated from the North Atlantic Ocean by the Froan archipelago. Frohavet is typically affected by full scale oceanic winds, whereas waves and sea currents show lower intensity thanks to the archipelago shielding. Since the effects of the

#### 4. Course control system: Design and experimental validation

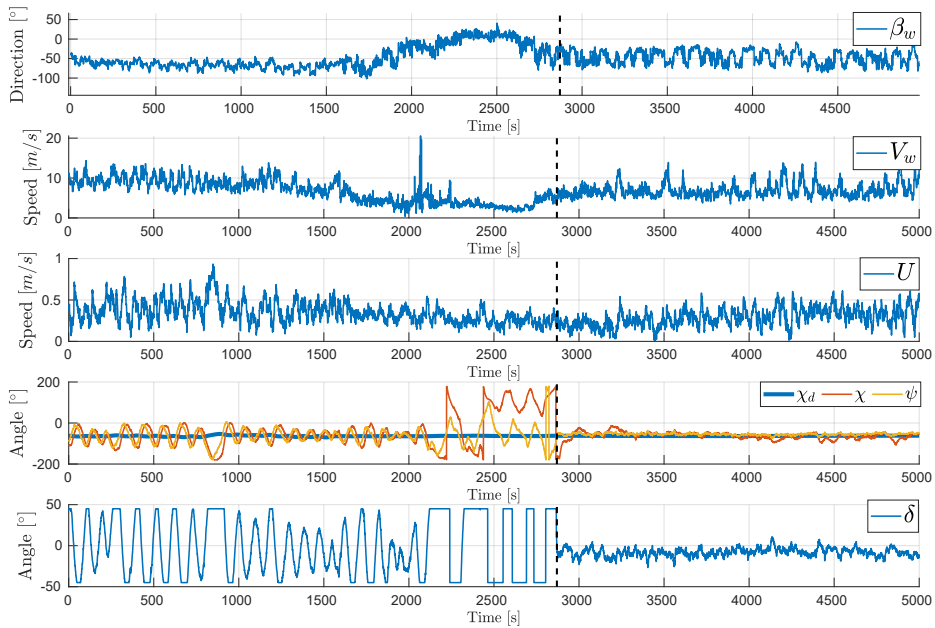


Figure 4.12: From the top: wind direction ( $\beta_w$ ) relative to North; absolute wind speed ( $V_w$ ); measured ground speed ( $U$ ); comparison between the measured heading ( $\psi$ ) and course ( $\chi$ ), and desired course ( $\chi_d$ ); commanded rudder angle ( $\delta$ ). The black dashed line indicates switch to heading control.

North Atlantic Current are filtered by the Froan islands, major currents components are due to tides.

In this example we show a situation in which with total loss of vehicle's controllability, caused by a combined action of wind and sea currents that cause a significant ground speed drop. In this experiment, the USV navigates towards a location North-West of its initial position with the same nominal PI gains of Section 4.2.1. Figure 4.12 shows that the vehicle is asked to head straight into the wind, which has initially an average speed of 9 m/s. The USV ground speed in the initial part of the considered period oscillates significantly (between 0.1 and 0.8 m/s), suggesting the presence of related course and heading oscillations. The wind speed decreases over time, causing a ground speed similar drop most likely due to the presence of smaller waves. Figure 4.12 shows in fact large course oscillations of approximately 60° amplitude from the very beginning. As the USV keeps moving with oscillatory course towards the desired location, the effect of tidal currents increases causing the speed over ground to drop even further (around 0.1 m/s). At time  $t = 2100$ s the current takes over the vehicle, which spins around and loses its course control stability. At time  $t = 2870$ s the on-board software switches from

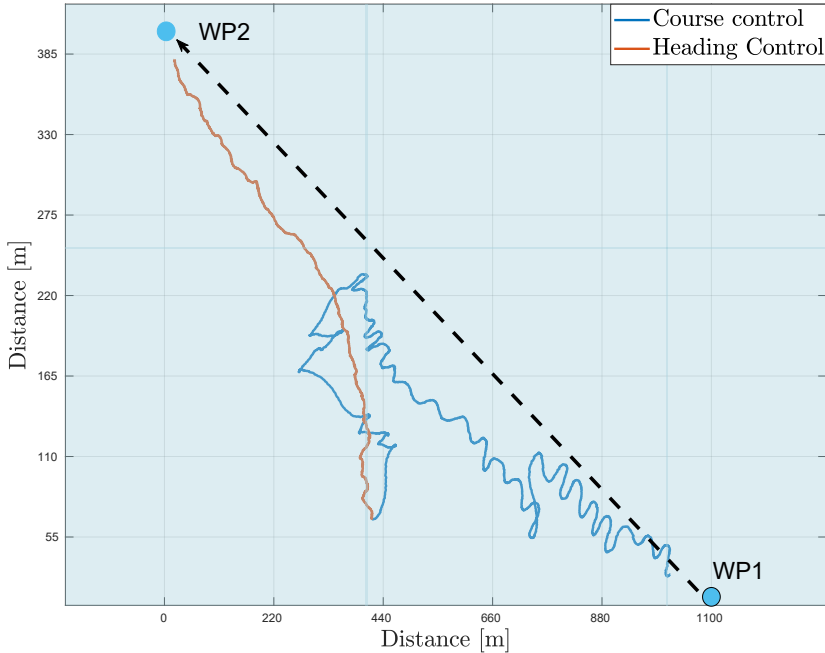


Figure 4.13: USV track over time: course over ground control (blue) and heading control (red). The black dashed line indicates the desired vessel path between the two way points.

course control to heading control, closing the control loop with the GNSS-provided measurement  $\psi$  instead of  $\chi$ . The heading control parameters are relaxed ( $K_p = 1$  and  $K_i = 0.01$ ) in order to produce a less aggressive steering control action. Immediate effects can be observed in the commanded rudder signal in Figure 4.12, whose oscillations and saturation are suppressed. As a consequence the vehicle's heading stabilizes around the desired reference (now a heading angle). Also the course over ground stabilizes with a larger error to the desired heading, indicating that the forces exerted on the USV by the environment are efficiently suppressed with integral action.

Figure 4.13 shows the complete track covered by the USV. It can be observed that when the autopilot tries to control the course over ground (blue curve), the USV oscillates around the desired path (black dashed line) connecting the two way points and eventually drifts away from it. When the autopilot switches to heading control (red curve) the USV's course becomes more stable as a result of oscillations suppression. Additionally, the vehicle navigates towards the desired location more efficiently.

### 4.2.3 Experimental model validation

In this section we present the validation of the full nonlinear model given by (4.7)-(4.10) and of the simplified quasi-linear model given by (4.31). As the quasi-linear model is valid on specific premises (i.e., straight line navigation) and is obtained by applying some assumptions to the full nonlinear model, we expect this model to perform worse than the full nonlinear model during turns. The validation is carried out using the data collected on-board the USV during sea-trials in the Trondheim fjord. Information on sea currents speed and direction, and waves (height and frequency) are instead obtained from the weather forecast service NorKyst-800<sup>1</sup>. For the purpose of model validation we use a constant propulsion force ( $F_{prop}$ ) in our simulations. The propulsion force is set such that the average surge velocity  $u$  in the simulation matches the average surge velocity of the USV during the sea trial. In reality, as the propulsion depends on waves, variations in propulsion force and USV's ground speed should be expected. As discussed in Section 4.1, sea currents have a large impact on the vehicle's course dynamics. The turning rate  $r$  (4.10) is indeed directly affected by currents as these modify both the Munk moment as well as the force that the rudder is able to exert on the water mass. The Munk moment has destabilizing effects due to quadratic velocity terms which can be positive and negative [72].

The validation consists in simulating the USV's dynamics with the same wind and sea current disturbances, and comparing the response of the simulated vehicle after step-wise changes in the desired course.

In the sea trials the rudder was controlled by the same PI-controller with gains mentioned in Section 4.2.1. In this validation we run both open- and closed-loop simulations. In the open-loop simulations the measured rudder angle from the sea trials is input to the model. In the closed-loop simulations the controller is included in the simulator to compute the rudder angle.

### Open-loop model validation

Figure 4.14 compares the measured course over ground ( $\chi$ ) to the courses simulated with full nonlinear model ( $\chi_{nml}$ ) and the quasi-linear model ( $\chi_{ql}$ ). It can be observed that the simulated courses resemble the measured USV's course. When the step in the desired course happens the course response of the nonlinear is nearly identical, while it shows some under-damping before stabilizing. The course of the quasi-linear model resembles closely the measured one during straight line navigation, while a larger overshoot is observed during the turn, confirming the premises that make this model valid. Figure 4.14 also compares the measured vehicle's states with the full nonlinear and quasi-linear models states. In the first

---

<sup>1</sup><https://imr.brage.unit.no/imr-xmlui/handle/11250/113865>

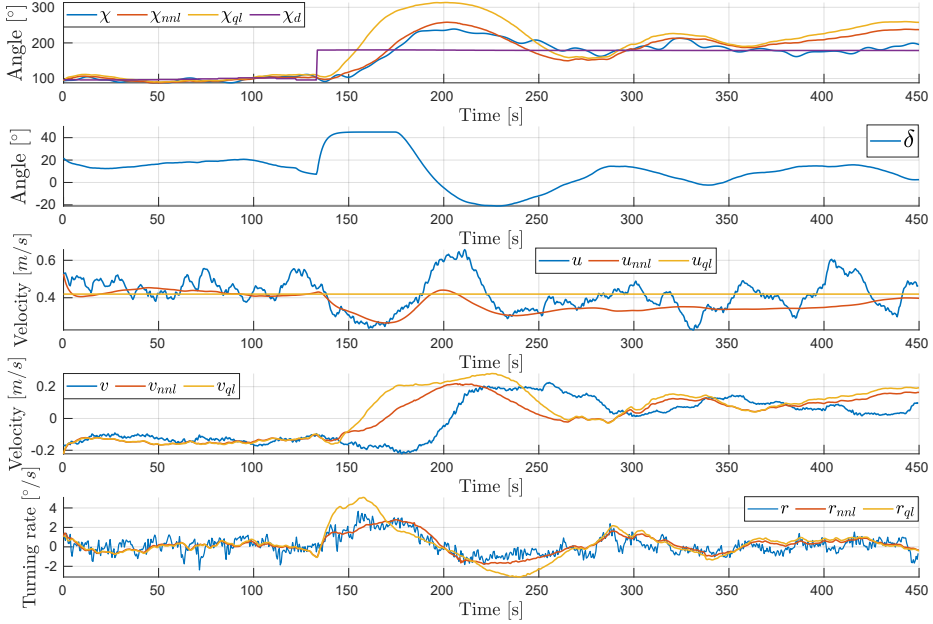


Figure 4.14: From the top: simulated courses from the full nonlinear and quasi-linear models ( $\chi_{nml}, \chi_{ql}$ ), measured ( $\chi$ ) and desired course over ground ( $\chi_d$ ); rudder signal ( $\delta$ ) used during the field test and fed to the models; full nonlinear model ( $u_{nml}, v_{nml}, r_{nml}$ ), quasi-linear model ( $u_{ql}, v_{ql}, r_{ql}$ ) and measured states ( $u, v, r$ ).

graph we notice that the surge velocity ( $u_{nml}$ ) varies less than the actual USV's speed due to the constant propulsion force simplification used in the model simulation. Moreover, given the assumptions made to derive the quasi-linear model, we have chosen a constant surge velocity  $u_{ql} = \bar{u}$ . Figure 4.14 shows that  $u$  increases rapidly at time  $t = 200s$ . At that point  $\dot{u}$  is large and positive, leading to a dampening effect on the course since  $v$  is positive (as seen by the last term in (4.7)). In the simulations however,  $\dot{u}$  is smaller and thus the dampening effect is smaller, resulting in the under-damped behaviour. In the quasi-linear model the dampening effect of  $\dot{u}$  is completely neglected, which explains the large overshoot. In the same figure it is also observed how waves impact the vehicle's turning rate  $r$ . A high-frequency component caused by first-order waves is present in the measured angular velocity  $r$ , while it is not present in the simulated one  $r_{sim}$ . An overshoot of  $r_{ql}$  is also observed, as a result of the higher USV surge speed  $u_{ql}$  when it enters the turn. Overall, the response of  $r$  clearly shows that the dominating dynamics are due to the rudder and that the employed models are able to capture them.

#### 4. Course control system: Design and experimental validation

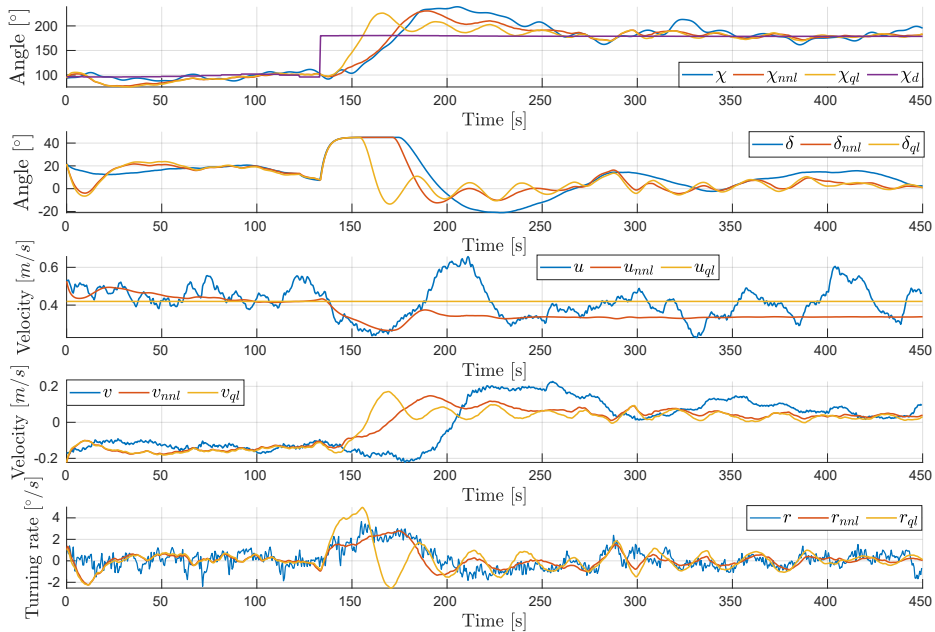


Figure 4.15: From the top: simulated courses from the full nonlinear and quasi-linear models ( $\chi_{nnl}, \chi_{ql}$ ), measured ( $\chi$ ) and desired course over ground ( $\chi_d$ ); rudder signals computed by the simulated autopilots and used as input to each model; full nonlinear model ( $u_{nnl}, v_{nnl}, r_{nnl}$ ), quasi-linear model ( $u_{ql}, v_{ql}, r_{ql}$ ) and measured states ( $u, v, r$ ).

#### Closed-loop model validation

In this section we analyse the models' stability when the vehicle is controlled by a fixed-gain PI-controller, using the same experimental data of the previous paragraph. This analysis is meant to confirm that the models are still valid when the controller is included in the control loop. The desired vehicle course ( $\chi_d$ ) computed by the LOS guidance during the sea trials is fed to the simulated control loop, for each model. Figure 4.15 shows the course response of the simulated models compared to the measured course ( $\chi$ ). It can be observed that the quasi-linear model has a faster course response. This is due to the quasi-linear model overestimating the surge velocity at the moment of turning, as seen in the same figure. This leads to a larger rudder force, seen as an overshoot in the turn rate  $r$  in Figure 4.15, and therefore a faster response. In comparison, the nonlinear model has a surge velocity closer to the measurement and both the course response and turn rate  $r$  closely resemble the true measured course during the turn.

When the assumptions of the quasi-linear model becomes invalid during the turn,

the gains of the controller are no longer suitable, resulting in oscillations in the course after the turn. The integrator in the controller starts at zero at the beginning of the sea trial and integrates the error. As the integrator state is not an available measurement, its value at any point during the sea trials is unknown. In the simulations we set the initial conditions of the integrator to zero, thus an error can be expected in the initial conditions, resulting in an error at the beginning of the closed-loop simulations. The simulated courses still clearly resemble the measured course, see Figure 4.15, proving the validity of the presented models.

## 4.3 Discussion

Nonlinear dynamic modeling of wave-propelled USV has been presented, taking into account the effects of ocean current that may lead to very low speed-over-ground. This includes zero and negative speed-over-ground that lead to singularities.

The models give insight into the changes in steering dynamics as a function of changing environmental conditions, which is exploited in the control design to handle singular situations that occur when the speed-over-ground approaches zero. Classical control design principles based on robust linear course control is used in normal conditions with a sufficiently large speed-over-ground, and with a switch to heading control in the singular conditions.

The presented numerical models highlight challenges and limitations of course-keeping control. This knowledge can be useful for high-level mission planning and decision-making purposes, e.g., a priori knowledge of wind and currents speed and direction might suggest that an alternative route would decrease the travel time to the destination.

In this context, a speed model is key and would provide useful knowledge used for mission planning and course control purposes. The investigation of a speed model for this unique wave-propelled USV is left as a future work.

The nonlinear model, the linearized model analysis, and the control design, are all validated using field experimental tests. The controller has been operational and tested at several sites both in the open ocean and coastal environments for about 7 weeks in total. Selected results have been presented to show the practical performance on the control system.

The model frequency analysis presented in Section 4.1.3 indicates that gain scheduling based on the variable  $\gamma$  is a viable approach to maintain a stable navigation when the singularity  $U = 0$  is approached. Gain scheduling relies however on accurate knowledge of the ocean current, which may not always be a reliable measurement due to uncertainty in the ADCP instrument and ocean models. For this reason we propose a solution in which control performances are kept and eventu-



ally improved using the heading measurement from GNSS, which is accurate and reliable at low ground speeds.

The next chapter investigates the control approach based on gain scheduling. Eventually, onboard wind and ocean current measurements will be used to adjust the controller's gains, in order to avoid deterioration of the control performances when the magnitude of environmental forces exceeds the USV's wave-induced propulsion.

## Chapter 5

# Gain-scheduled steering control

The previous chapter presents the model of the USV's dynamics and control solutions that allow stable course control in different sea states and environmental conditions. In that first investigation, it is identified the main source of model nonlinearity in a parameter named  $\gamma$  (see Equation 4.22), and it is anticipated that this variable can be employed in gain scheduling techniques of the course controller gains. When a controller is designed based on a linearized system, it is guaranteed to work optimally only in some neighbourhood of its equilibrium point. However, nonlinear systems may have multiple operating point depending on exogenous disturbances and hence the controller performances may deteriorate [113]. A solution to this is to extend the linearization approach to a range of operating points. This method is called *gain scheduling* and it finds its origins in works related to flight control systems [114]. In this work,  $\gamma$  is identified as the *scheduling variable*.

This chapter brings those assumptions to analysis and validation and it is based on the manuscript [115] submitted to the Ocean Engineering journal. In the first part, theoretical considerations are supported with an extensive model analysis in the frequency domain. The author presents two variations of the scheduling approach (with and without ocean current measurement) and demonstrates that the navigation performances are improved in both cases. Feasibility and limitations of both approaches are discussed and supported by simulation and experimental results. The first presented gain-scheduling method relies on the measurement of USV's speed relative to the ocean current provided by the ADCP, which can be affected by a number of factors as described in Sections 4.1.3 and 5.4. Additionally, when the vehicle moves slowly with respect to the Earth surface, the ground speed measurement provided by the GNSS is also deteriorated. The noise in both measurements will consequently appear in the computed ocean current, since  $U_c = U - U_r$ . More-

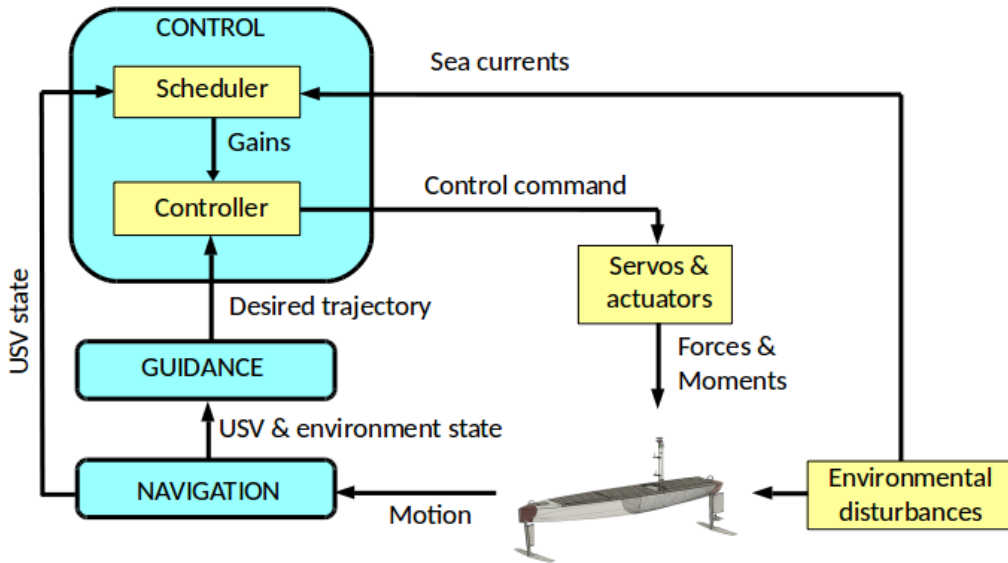


Figure 5.1: GNC with gain-scheduled controller.

over, the possibility of retrieving the current speed and direction from weather forecasts is hampered by their limited coverage and forecast update, and by the fact that the USV would necessarily require 4G/LTE coverage or connection to shore.

In the second part of this chapter, the practical implementation of a gain-scheduled course controller is presented. First, benefits and performances of the proposed approach are discussed with several simulations, in which different environmental disturbances are included. Finally, the controller is integrated in the USV’s onboard navigation software and tested experimentally in the Trondheim Fjord (Central Norway).

## 5.1 Gain scheduling principles

Gain scheduling is an approach to control of nonlinear systems that makes use of a family of linear controllers [113]. In fact, the single linear controller is meant to provide a satisfactory control performance for its specific operating point of the system. The operating points are characterized by a *scheduling variable*, that is used to adjust the controller gains based on the operating points. Figure 5.1 shows a typical GNC system with gain-scheduled controller. In this work, the scheduler computes  $\gamma$  (see Equation 4.22) and then adapts the proportional and integral

gains that are forwarded to the linear course controller that commands the rudder.

Since each linear controller can be tuned independently, one could see the gain scheduling method as a divide and conquer approach for controlling a nonlinear system where the advantage is that well established linear control theory can be used.

Gain scheduling is a common method which is applied today in a number of fields [116, 117]. The literature in the field of marine robotics shows several examples in which control strategies make use of gain scheduling. For example, [118] and [119] demonstrate that gain scheduling can be efficiently employed to tune a low-level heading controller and enhance navigation performances when a sailboat USV navigates into the wind. In [120] classical PID control with gain scheduling is used to adapt the speed of a motored USV. The design of a course control system that makes use of a gain-scheduled PID controller is discussed in [121], where the authors have initially identified offline the parameters of a classical Nomoto model [72]. Based on that, they have computed the optimal PID controller parameters using the pole-zero configuration method at different speeds.

In this work, the controller parameters are scheduled using  $\gamma$ , which is a slowly-varying variable since variations in the sea current and USV's ground speeds are slowly changing processes. The main contribution proposed in this chapter is the novel and practical gain scheduled control design that is shown, via model analysis and simulations and experimental results, to compensate for the main system nonlinearities when the USV operates at very low speed over ground. Such situations occur when the ocean current and/or wind forces are of the same magnitude as the wave-induced propulsion forces. Unlike other methods, the scheduling process is not a brute force assignment of the gains to pre-computed values, but results instead from the observation of the ocean current velocity and the vessel's velocity over ground. For this reason, the controller is more robust and is able to maintain course-keeping performances in a number of navigation scenarios including different currents, winds and waves.

## 5.2 Three-state quasi-linear model frequency analysis

As described in the previous chapter, the assumption of a constant surge velocity  $u$  leads to

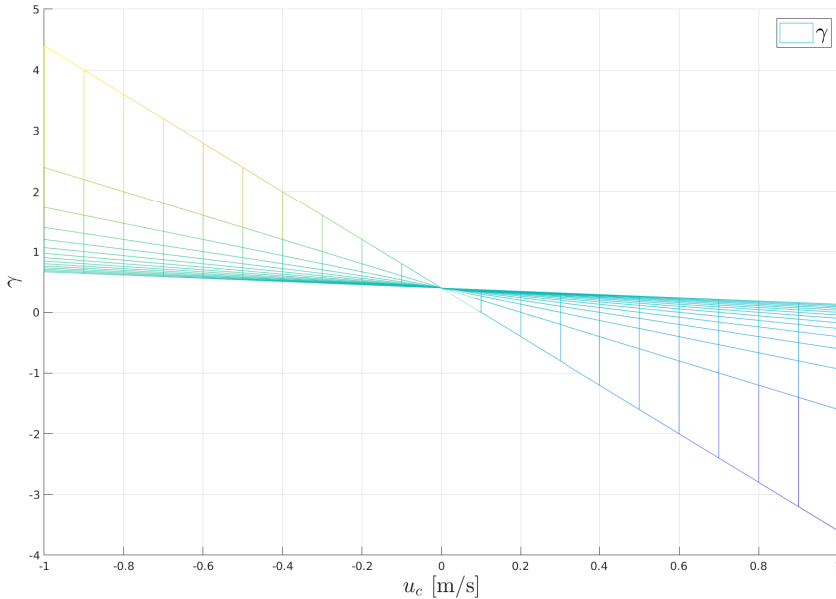
$$\begin{pmatrix} \dot{\chi} \\ \dot{v}_r \\ \dot{r} \end{pmatrix} = \begin{pmatrix} 0 & -\frac{u}{U^2} \frac{1}{m+A_{22}} (D_{22} + \alpha_{YR} U_r) & \gamma \\ 0 & -\frac{1}{m+A_{22}} (D_{22} + \alpha_{YR} U_r) & -\frac{m+A_{11}}{m+A_{22}} u_r \\ 0 & -\frac{1}{J_z+A_{66}} ((A_{22} - A_{11})u_r + \alpha_{ZR} U_r) & -\frac{D_{66}}{J_z+A_{66}} \end{pmatrix} \begin{pmatrix} \chi \\ v_r \\ r \end{pmatrix} + \begin{pmatrix} \frac{u}{U^2} \frac{\alpha_{YR} U_r u_r}{m+A_{22}} \\ \frac{\alpha_{YR} U_r u_r}{m+A_{22}} \\ \frac{\alpha_{ZR} U_r u_r}{J_z+A_{66}} \end{pmatrix} \delta, \quad (5.1)$$

where  $\alpha_{YR}$  and  $\alpha_{ZR}$  are constants obtained from a linearization of the steering model. Equation 5.1 allows us to isolate the main source of nonlinearity in the variable named  $\gamma$  (see Equation 4.22).

In the following section we use the three-state model of Equation 5.1 for gain-scheduled control design. We denote:  $H_{ql}(s) = \frac{\chi}{\delta}(s)$  the transfer function of the presented quasi-linear model;  $H_{ql}(s)/\gamma$  the normalized transfer function;  $C_{pi}(s)H_{ql}(s)$  and  $C_{gs}(s)H_{ql}(s)$  transfer functions of the open-loop systems with fixed-gains PI and gain-scheduled controllers, respectively;  $M_{pi}(s) = C_{pi}(s)H_{ql}(s)/(1 + C_{pi}(s)H_{ql}(s))$  and  $M_{gs}(s) = C_{gs}(s)H_{ql}(s)/(1 + C_{gs}(s)H_{ql}(s))$  the complementary sensitivity functions of the two closed-loop systems;  $N_{pi}(s) = 1/(1 + C_{pi}(s)H_{ql}(s))$  and  $N_{gs}(s) = 1/(1 + C_{gs}(s)H_{ql}(s))$  the corresponding sensitivity functions.

In Chapter 4 it is shown that the main variations in dynamics are due to the parameter  $\gamma$  that influences the gain in the simplified Nomoto model. The frequency analysis confirms that course-keeping control should therefore consider the variations in the gain  $\gamma$ , and use that knowledge to counteract the disturbances due to winds, waves and current. Much can be achieved with the integral action, since the current, wind and wave-driven propulsion speeds can be expected to be slowly time-varying variables. Moreover, while the integral action is well suited to handle additive disturbances, it is not sufficient to handle multiplicative disturbances (as the factor  $\gamma$ ). Gain scheduling based on  $\gamma$  is therefore an interesting approach, and the design of a gain-scheduled course controller is justified by the fact that the main nonlinearities are introduced by the slowly time-varying environmental parameters (winds, waves and current) as well as the course angle command.

Figure 5.2 shows the values of  $\gamma$  when considering a range of typical longitudinal AutoNaut's speed and ocean current values, e.g.,  $u \in [0, 1.5]$  m/s and  $u_c \in [-1, 1]$


 Figure 5.2: Nominal value  $\gamma^n = 0.4$ .

m/s. As discussed in our previous chapter, singularities are reached when the vehicle's ground speed drops towards zero in presence of ocean currents. Far from singularities,  $\gamma$  stabilizes around the nominal values  $\gamma^n = 0.4$ , which is the value that  $\gamma$  reaches when the current  $u_c$  is zero and when no lateral motion is observed (i.e.,  $U = u$ ), as shown in Figure 5.2. Further analysis reveals that  $\gamma$  becomes negative when  $u_c \geq u$ , i.e.,  $u_r \leq 0$ . From a control perspective this would lead to gain sign changes which means that the vehicle is “driving in reverse”, which is not a desirable situation. In the transition from positive to negative gain, there is a singular uncontrollable state when  $u_r = 0$  m/s, where the rudder has no effect.

In this analysis we therefore assume  $u_r > 0$  and hence  $\gamma > 0$ . This means that the analysis excludes situations in which  $u_c > u$  in the USV's BODY frame, i.e., when the vehicle is transported “in reverse” by a current and its speed is lower than that of the current itself. Figure 5.3 shows the frequency response (Bode plot) of the quasi-linear model for a set of different values of  $u_r$ . The relative longitudinal speed  $u_r$  is computed assuming a fixed longitudinal speed of the USV  $u = 0.8$  m/s and a varying current  $u_c \in [-0.7, 0.7]$  m/s in BODY frame. As  $u_r$  varies, the major differences are in the magnitude of the gain ( $\approx 85$  dB), although some phase variations are also observed. While increased gain is observed for high relative velocities, lower relative velocities reduce the system bandwidth to lower frequen-

## 5. Gain-scheduled steering control

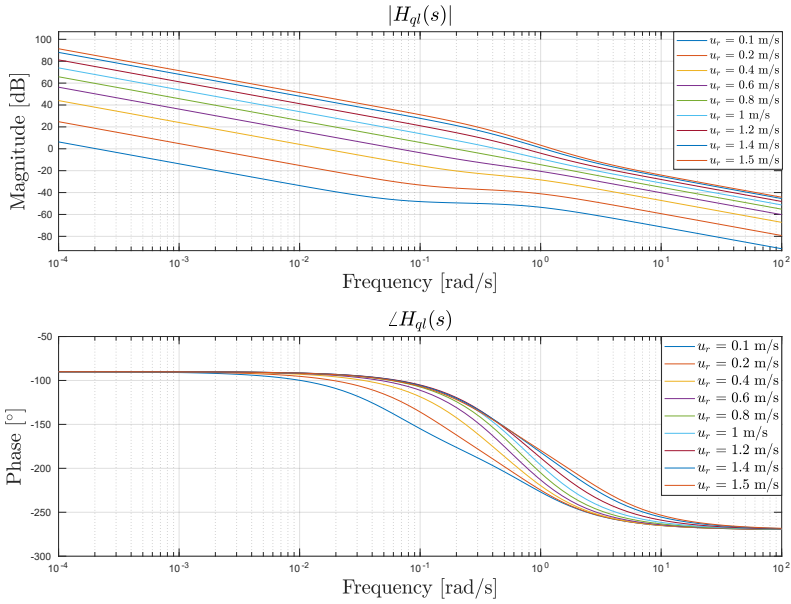


Figure 5.3: Magnitude (top) and phase (bottom) of  $H_{ql}$ .

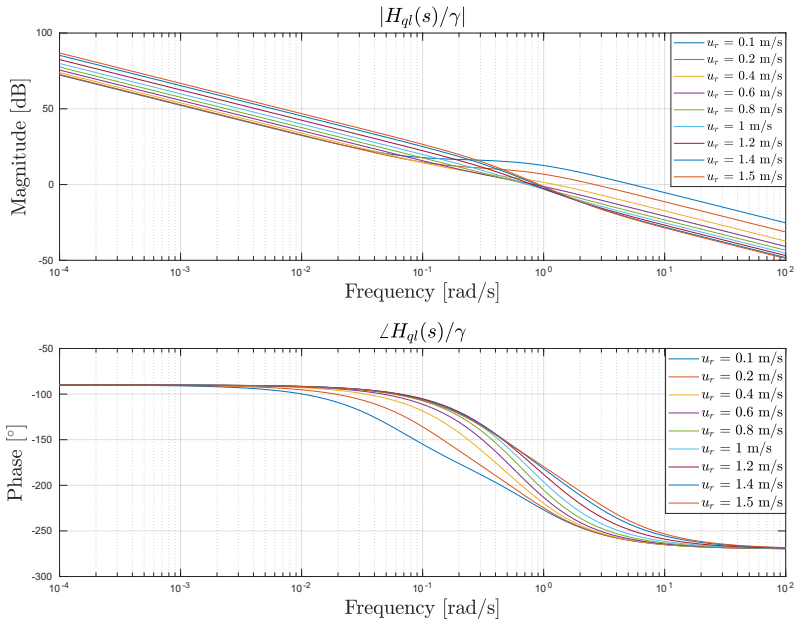


Figure 5.4: Magnitude (top) and phase (bottom) of  $H_{ql}/\gamma$ .

cies, i.e., at low  $u_r$  the rudder response is slower when trying to control the USV's course. In order to better evaluate the impact of  $\gamma$ , the quasi-linear system is normalized as shown in Figure 5.4. Since  $\gamma$  appears as a gain in the transfer function, no change in phase variations are expected. It can however be observed that gain variations are significantly reduced to  $\approx 15$  dB. Notably, the gain variations are smallest for  $0.1 \text{ rad/s} \leq \omega \leq 0.4 \text{ rad/s}$ , where the closed loop control bandwidth may be located. In fact, control design models should have smallest uncertainty in this frequency range since this will lead to best stability margins. This suggests that most of the model variation due to changes in  $u_r$  are captured by  $\gamma$ , and further suggests this variable may be suitable for gains scheduling. Based on this, it is proposed that the system can be controlled by a PI controller with a simple gain scheduling with the factor  $1/\gamma$ :

$$C_{gs}(s) = \frac{1}{\gamma} C_{pi}(s) = \frac{K_p}{\gamma} \left( 1 + \frac{1}{T_i s} \right), \quad (5.2)$$

where  $K_p$  is the proportional gain and  $T_i$  the integration time.

The linearized closed-loop stability properties can be investigated by analysing the phase and gain margins of the open-loop system. Figure 5.5 and 5.6 show the Bode plots of the open-loop transfer functions  $C_{pi}(s)H_{ql}(s)$  and  $C_{gs}(s)H_{ql}(s)$  respectively, where a lower bound on  $\gamma$  ( $\gamma \geq 0.05$ ) was used in order to avoid it becoming infinitely small (and hence the gains infinitely large). Figure 5.5 shows that when the fixed-gain linear controller is employed it is hard to find a set of gains which both achieve high control bandwidth and make the closed-loop systems stable for all values of  $u_r$  due to the large variation in the gain. The variation in the cross-over frequency is very large, i.e., when  $u_r$  is low the system is very slow and when it is high the system is very fast. The difference in cross-over frequency between the lowest and higher  $u_r$  spans almost four orders of magnitude, and at high values of  $u_r$  the system is unstable. Stability margins are also weak at low  $u_r$  values. Since the course dynamics acts as a pure integrator, including the integral action also in the controller would result in low phase margins unless the integral gain are chosen to be very small. Despite derivative action in the controller may improve the stability margins, this option is discarded for reasons described below.

Figure 5.6 shows that when the gain-scheduled controller is included in the open-loop the gain variations decrease and the bandwidth of the family of transfer functions narrows down mostly to the range between 0.01 rad/s and 1 rad/s. In other words, it is possible to find a combination of gains that make the closed-loop system stable for each value of the considered relative velocity.

Figures 5.7 and 5.8 show the Bode plots of the complementary sensitivity functions  $M_{pi}$  and  $M_{gs}$ , used to evaluate the systems' ability to track the reference. For low relative velocities the bandwidth is reduced (see Figure 5.7), meaning that the



## 5. Gain-scheduled steering control

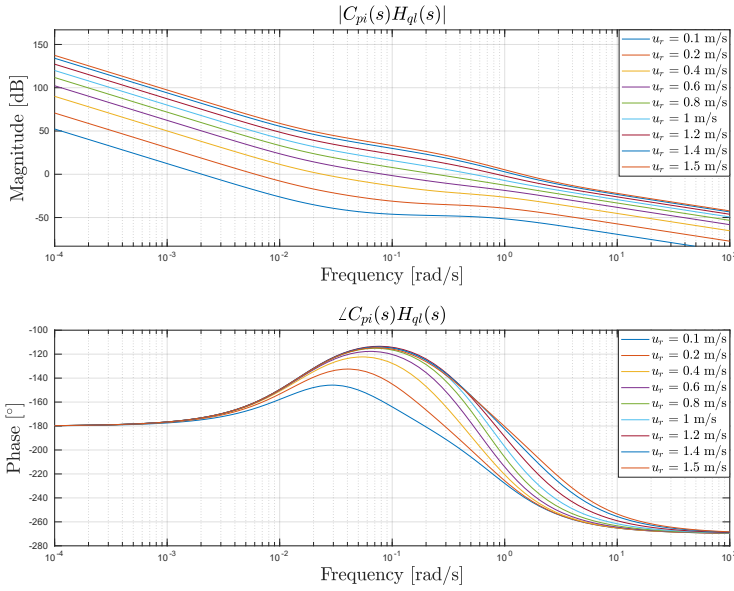


Figure 5.5: Magnitude (top) and phase (bottom) of the open-loop system  $C_{pi}H_{qi}$  (fixed-gain).

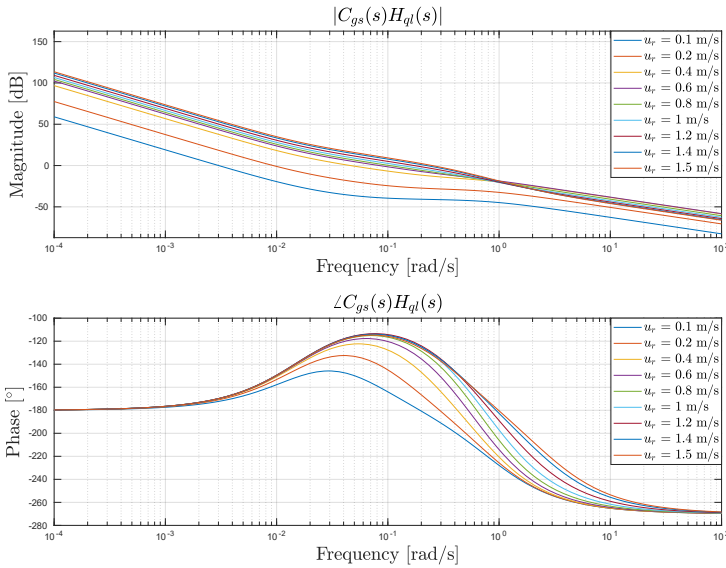


Figure 5.6: Magnitude (top) and phase (bottom) of the open-loop system  $C_{gs}H_{qi}$  (gain scheduling).

controller is only able to track course references of very low frequency. Also the gain-scheduled controller will have troubles tracking the course reference when the relative velocity is low, as the bandwidth is smaller than the expected frequencies of the course reference (see Figure 5.8). This may justify a different control strategy for very low relative velocities, e.g., heading control [105]. For the linear controller, the closed-loop system becomes unstable for high relative velocities ( $u_r \geq 1.2$  m/s), and explains the unusual phase of these systems. Figure 5.8 shows that, for large relative velocities, the gain-scheduled controller has significantly better tracking properties compared to the fixed-gain one.

Figures 5.9 and 5.10 show the Bode plots of the sensitivity functions  $N_{pi}$  and  $N_{gs}$ , which are used to evaluate the systems' ability to reject noise and disturbances. The magnitude of the sensitivity plots shows the frequencies that are rejected or amplified in the closed-loop system. It can be noticed that the magnitude peaks for some of the considered relative velocities with the PI controller are large (see Figure 5.9). The three largest peaks (up to 38 dB) correspond to the cases where the system is unstable, and any noise or disturbances with frequency corresponding to one of the peaks will be amplified by the closed-loop system. For the linear controller with fixed gains (see Figure 5.9) at  $u_r = 0.1$  m/s the peak is at 0.6 rad/s (period of approximately 10 seconds). This falls within typical frequencies of ocean waves and it is therefore important that the controller is robust enough to reject them from the closed-loop system. This technique is named *wave filtering* and the importance of attenuating wave-induced first-order oscillatory components in the rudder is more investigated in Chapter 6.

Figure 5.10 shows that when the gain-scheduled controller is employed the peaks are smaller, meaning that the closed-loop system will amplify the disturbances less. Moreover, the peaks are located around 0.4 rad/s, corresponding to a period of 15 seconds, which is larger than the most commonly encountered wave periods. This indicates that using derivative action in the controller, as discussed earlier, is not beneficial as the increased controller bandwidth would increase sensitivity to first-order wave disturbances.

### 5.2.1 Scheduling of the course controller gains

By selecting the gains according to  $\gamma$ , the control system will ensure stable course control when either the USV's ground speed ( $U$ ) or its longitudinal velocity relative to water ( $u_r$ ) become small. The controller gains are computed according to

$$K_p = \frac{\gamma^n}{\gamma} K_p^n \quad (5.3)$$

$$K_i = \frac{\gamma^n}{\gamma} K_i^n, \quad (5.4)$$

## 5. Gain-scheduled steering control

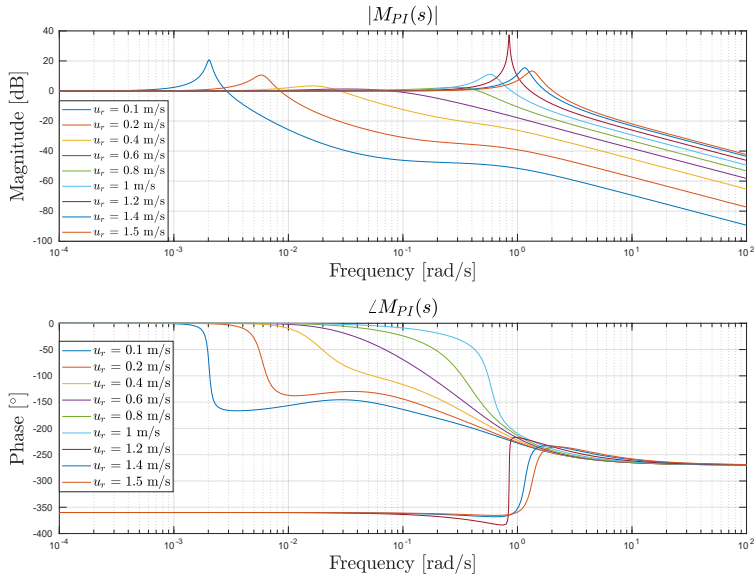


Figure 5.7: Magnitude (top) and phase (bottom) of the complementary sensitivity function  $M_{pi}$ .

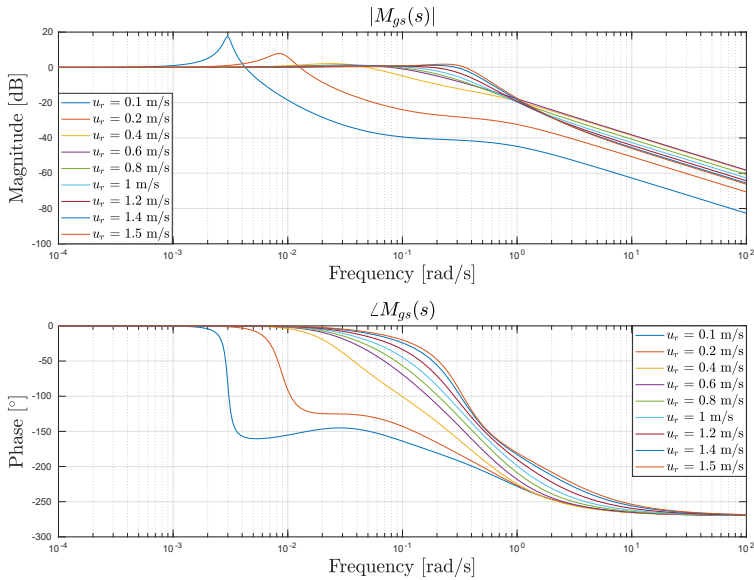


Figure 5.8: Magnitude (top) and phase (bottom) of the complementary sensitivity function  $M_{gs}$ .

## 5.2. Three-state quasi-linear model frequency analysis

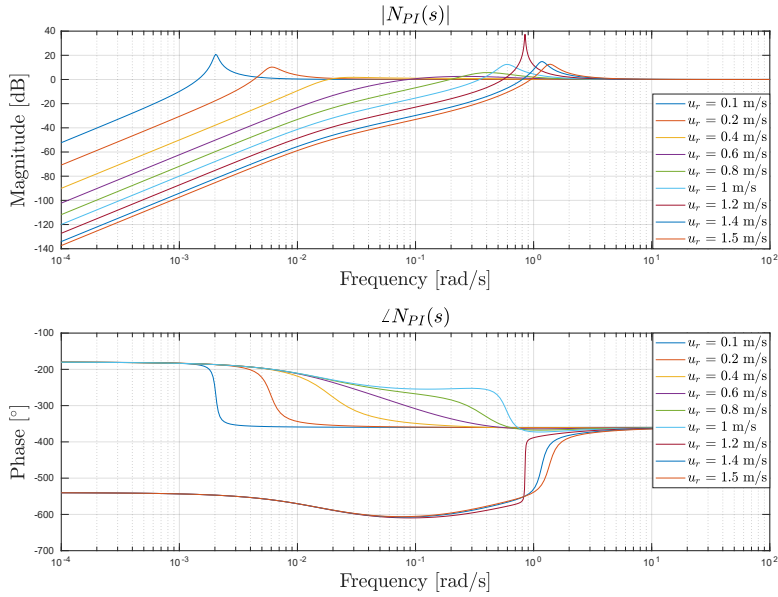


Figure 5.9: Magnitude (top) and phase (bottom) of the sensitivity function  $N_{PI}$ .

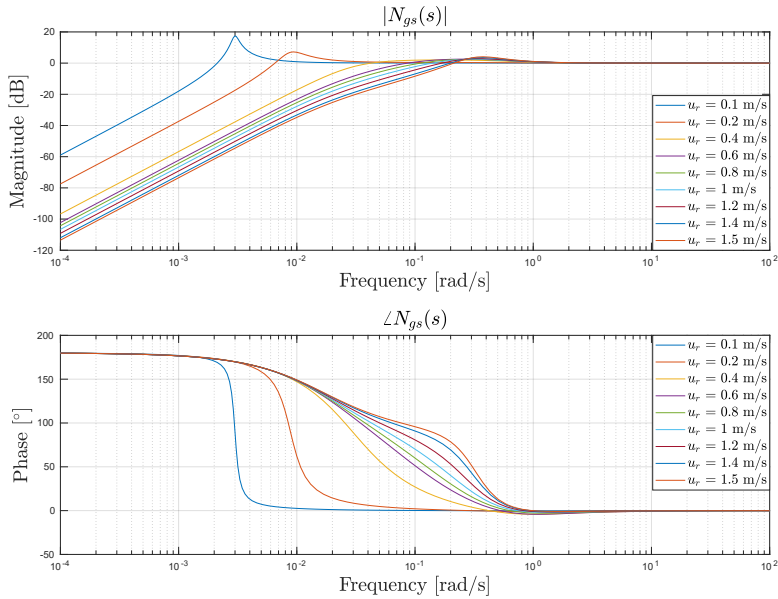


Figure 5.10: Magnitude (top) and phase (bottom) of the sensitivity function  $N_{gs}$ .

where  $\gamma^n$  is the nominal value and  $K_p^n$  and  $K_i^n$  are nominal gain values defined according to Chapter 4.

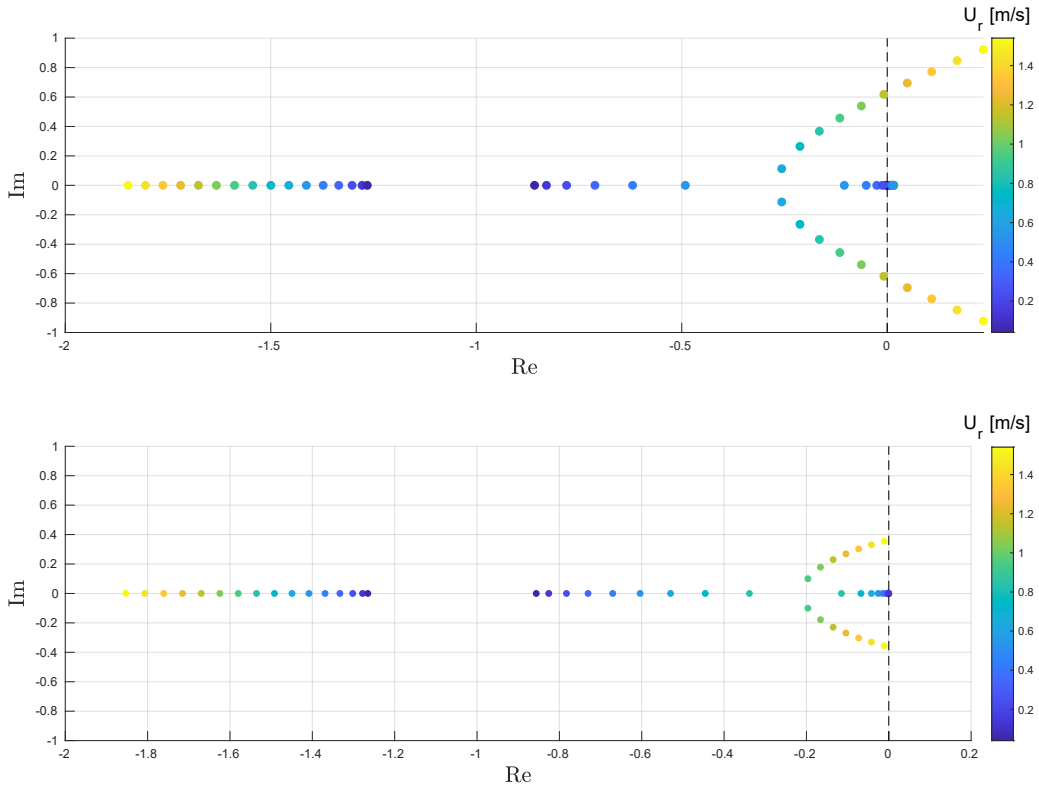


Figure 5.11: Closed-loop poles for the fixed-gain course controller (top); closed-loop poles for the gain-scheduled course controller (bottom).

As already discussed in the previous chapter, the practical realization of a gain-scheduling strategy is mostly hampered by physical limitations of the onboard ADCP instrument.

In the following two approaches in which  $\gamma$  is computed based on the available information are presented and discussed.

### ADCP-based gain scheduling

If the ADCP instrument is available, the longitudinal current  $u_c$  can be computed as described in the Appendix A.2. This means that we can compute  $\gamma$  according to Equation 4.22.

In this analysis we consider for simplicity that the current in the USV's BODY frame has no lateral component, i.e.,  $v_c = 0$  m/s and we compare the stability of two closed-loop systems: one controlled with a fixed-gain PI controller and the other with a gain-scheduled PI controller. The model used in this analysis is the

one in Equation 5.1, while the nominal controller gains are the same as in Chapter 4:  $K_p^n = 1.25$  and  $K_i^n = 0.02$ .

In this scenario, the USV travels at a ground speed  $U = u = 0.54$  m/s that corresponds to 1 knot, a typical speed for the AutoNaut. In this situation, we simulate and analyse the closed-loop stability when the vehicle is also affected by a current  $u_c \in [-1, 0.5]$  m/s. Figure 5.11 shows the poles of the closed-loop systems with respect to the relative speed  $U_r$ . In the first plot (top), we observe that the higher the relative speed, the more unstable the system is, meaning that the controller is not able to maintain stability in the system with the fixed gains. On the other hand, gain scheduling based on the parameter  $\gamma$  allows the closed-loop system to remain stable (poles in the left half-plane) even when the relative speed increases, as shown in the bottom graph.

Despite it is impossible to associate the poles to the system states  $(\chi, v_r, r)$ , the pole placement analysis indicates if the closed-loop system is stable or unstable with the employed PI controller. For the purpose of course-keeping, it is useful to confirm that the closed-loop system is stable with the chosen gains.

### SOG-based gain scheduling

The nonlinearities introduced by  $\gamma$  are mainly caused by of the vehicle's ground speed relative to the speed of ocean currents (i.e.,  $U_r$ ). In circumstances in which the sea current cannot be measured, the gains of the course controller can still be adapted assuming knowledge of the USV's ground speed  $U$  and longitudinal speed  $u$ :

$$\gamma_U \approx 1 - \frac{u^2}{U^2} \frac{m + A_{11}}{m + A_{22}}. \quad (5.5)$$

However, Equation 5.5 reduces to  $\gamma = 0.4$  when  $v = 0$  m/s. This means that in order to schedule the controller gains, the lateral velocity component is essential. We assume therefore that the current is not measured and that the USV's speed in the BODY frame is made of a longitudinal and lateral component. In this scenario, the USV travels with a ground speed  $U$  that varies from 0 m/s to 1 m/s and again to 0 m/s. Figure 5.12 shows the results of the pole placement analysis. It can be observed that when the USV's ground speed drops towards zero, the closed-loop system with the fixed-gain controller becomes unstable and the poles reach the right half-plane. Again, the gain-scheduled controller manages to keep the system stability.

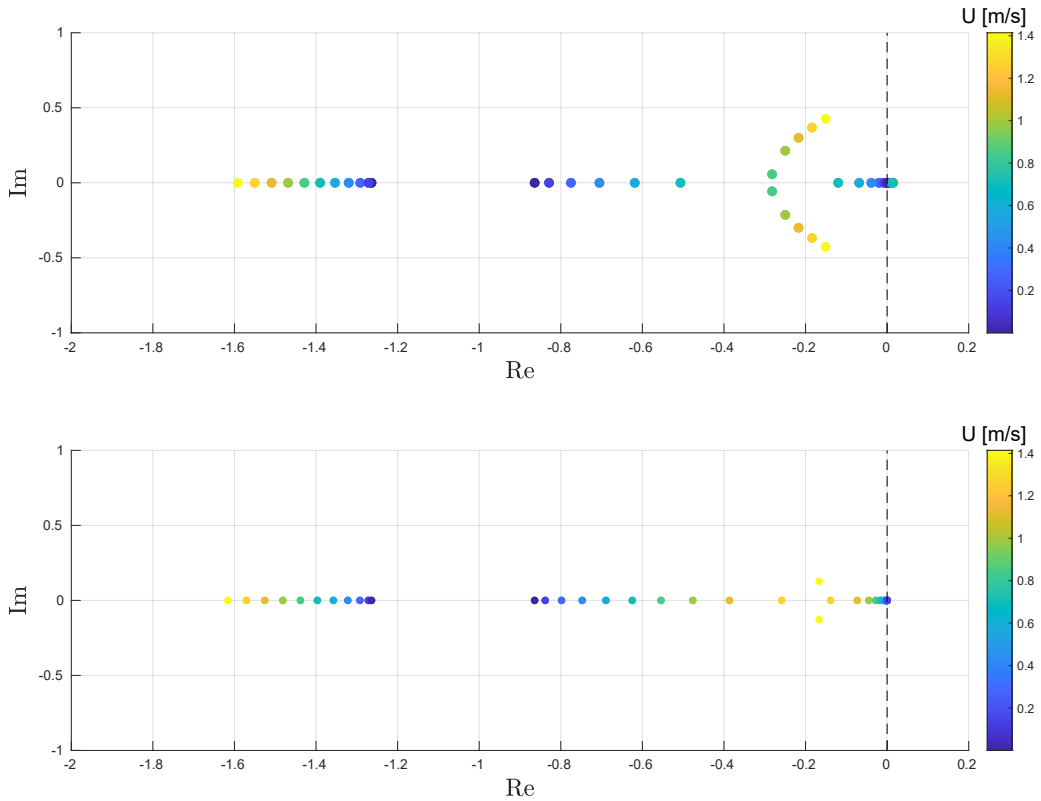


Figure 5.12: Closed-loop poles for the fixed-gain course controller (top); closed-loop poles for the gain-scheduled course controller (bottom).

### 5.3 Simulation results

The proposed gain scheduling technique is initially tested in simulation. The full nonlinear model of equations 4.7-4.10 is implemented in the MATLAB<sup>®</sup>/Simulink environment. Closed-loop simulations are achieved by simulating a line-of-sight (LOS) guidance system that computes desired vehicle courses from a list of way points. On the basis on the quasi-linear model of Equation 5.1, the response of two USVs with the same nonlinear dynamics but with different course controllers is compared. Whereas the course of one USV is controlled by a fixed-gain PI controller with nominal gains  $K_p^n$  and  $K_i^n$ , the gains of the other are computed according to Equation 5.4.

Table 5.1 contains the parameters that were used in the two simulations presented below.

Table 5.1: Simulation parameters

	Symbol	Value (Exp. 1)	Value (Exp. 2)
Initial location	$L^{init}$	(0,0) m	(0,0) m
Initial long. speed	$u^{init}$	0.35 m/s	0.2 m/s
Initial COG	$\chi^{init}$	0°	0°
Desired COG	$\chi_d$	0°	[0,90,180]°
WP location	WP	(0,75) m	[(0,75),(50,75),(50,0)] m
Current dir.	$\beta_c$	180°	-45°
Current speed	$U_c$	0.3 m/s	[0,0.3] m/s

### 5.3.1 Straight line navigation with environmental disturbance

In the first simulation the USV navigates North ( $\chi_d = 0^\circ$ ) with initial speed  $U = u^{init} = 0.35$  m/s. At time  $t = 400$  s a current from North to South appears (direction in Earth-fixed coordinates  $\beta_c = 180^\circ$ ) with total speed  $U_c = 0.3$  m/s. Figure 5.13 compares the desired ( $\chi_d$ ) and measured ( $\chi$ ) course over ground of the vehicle controlled with fixed (nominal) gains  $K_p^n = 1.25$  and  $K_i^n = 0.02$ . It can be observed that when the current hits the vehicle its ground speed decreases below 0.1 m/s (bottom plot). The USV's course is not initially affected by the sea currents, but as the ground speed keeps decreasing slowly and drops below 0.06 m/s oscillations appear. Figure 5.13 shows that course oscillations reach 60° of amplitude, therefore proving the inability of the controller to maintain a stable course control. The vehicle controlled with a gain-scheduled PI controller manages instead to keep a stable course despite the ocean current, as shown in Figure 5.14. This figure clearly indicates that adapting the gains according to the observed ocean current allows the USV to maintain the intended course and navigate more efficiently towards the desired location. Figure 5.15 also shows the adaptation of gains according to  $\gamma$ . The top graph compares the value of  $\gamma$  computed during the simulation to its nominal value  $\gamma^n = 0.4$ . Figure 5.15 also shows the relaxation of controller gains needed to cope with the speed drop. The last graph of the same figure compares the rudder angle commanded by the course-keeping autopilot of both vehicles. Whereas the fixed-gain controller commands large rudder efforts, reaching saturation, the rudder compensation commanded by the gain-scheduled controller are small enough to be considered negligible.



## 5. Gain-scheduled steering control

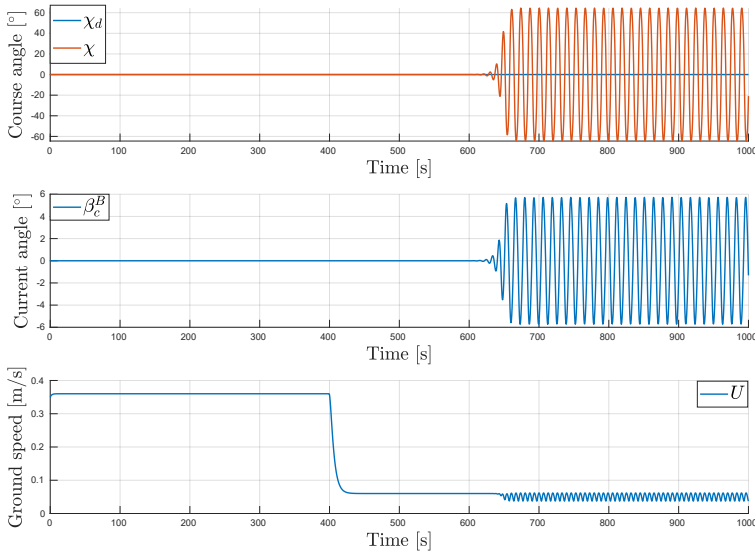


Figure 5.13: Desired ( $\chi_d$ ) and measured ( $\chi$ ) course over ground (top); ocean current direction ( $\beta_c^B$ ) in vehicle's BODY frame (middle); vehicle's ground speed ( $U$ , bottom).

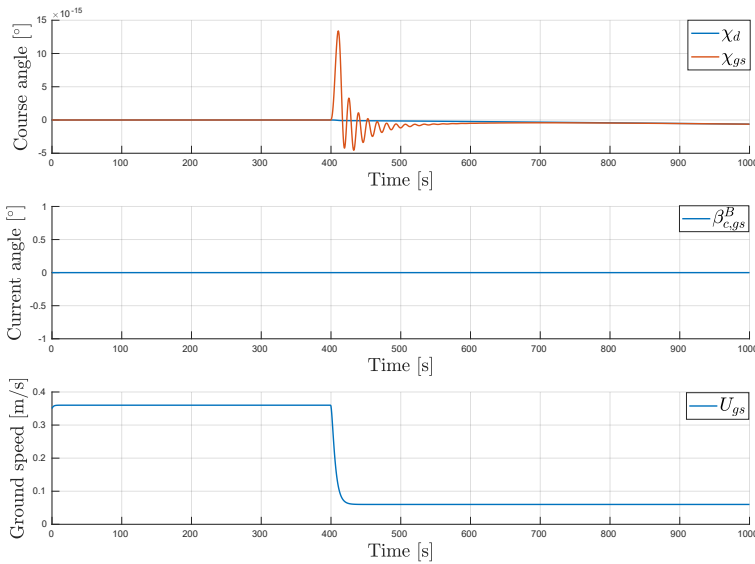


Figure 5.14: Desired ( $\chi_d$ ) and measured ( $\chi_{gs}$ ) course over ground (top); ocean current direction ( $\beta_{c,gs}^B$ ) in vehicle's BODY frame (middle); vehicle's ground speed ( $U_{gs}$ , bottom).

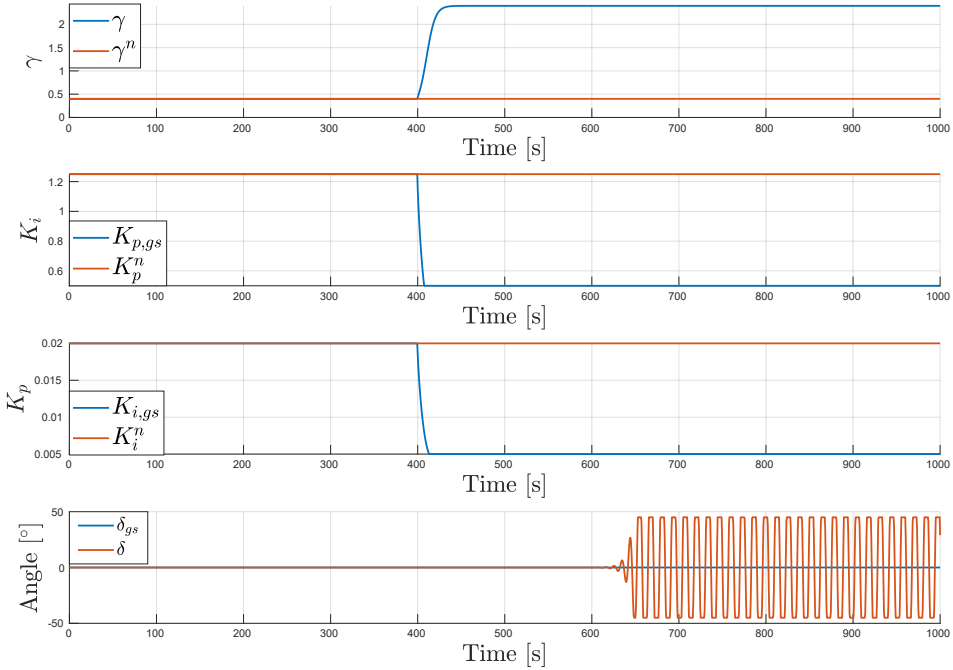


Figure 5.15:  $\gamma$  parameter for gain scheduling as compared to its nominal value ( $\gamma^n$ ); computed  $K_{p,gs}$  and  $K_{i,gs}$  gain as compared to their nominal values  $K_p^n$  and  $K_i^n$  (middle); comparison of the scheduled ( $\delta_{gs}$ ) and not ( $\delta$ ) rudder angles.

### 5.3.2 Way points navigation with environmental disturbance

This simulation compares the USVs responses during turns when the the difference between the initial speed of the vehicles and the ocean current velocity is increased. Table 5.1 shows the initial USV state, the location of the way points and the desired courses computed by the guidance system each time a way point is reached (Exp. 2 column). Both vehicles are initially moving North with ground speed  $U = u^{init} = 0.2$  m/s when at time  $t_1 = 300$  s a current directed towards North-West ( $\beta_c = -45^\circ$ ) appears with speed  $U_c = 0.3$  m/s. The current fades away at time  $t_2 = 1500$  s. Figures 5.16 and 5.17 show the steering response of both vehicles. Figure 5.16 shows that the USV controlled with fixed gains is not able to cope with the speed drop and its course starts oscillating around the desired one. In Figure 5.17 it can be noticed instead that the system controlled with gain scheduling robustly governs the course over ground, avoiding propagation of the rudder and course oscillations. The current appears while the vehicles navigate between the first and second way points (see Figure 5.19). While the course of the USV governed by fixed-gains controller starts oscillating and drifting North,

## 5. Gain-scheduled steering control

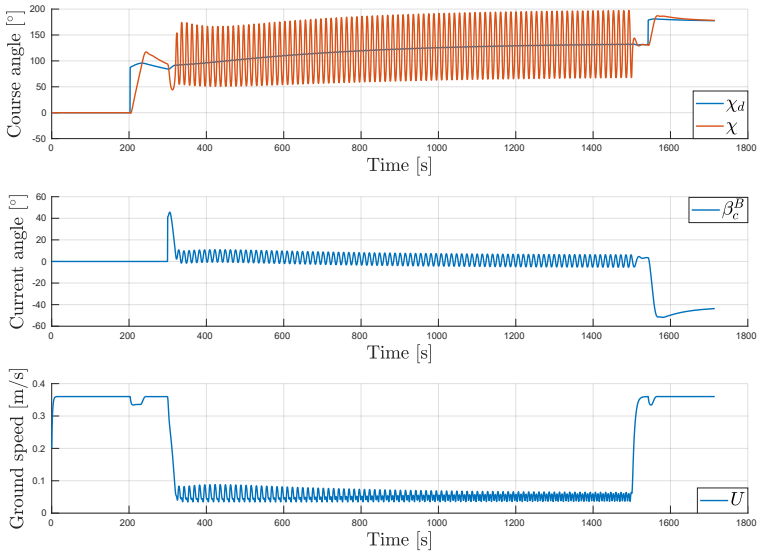


Figure 5.16: Desired ( $\chi_d$ ) and measured ( $\chi$ ) course over ground (top); ocean current direction ( $\beta_c^B$ ) in vehicle's BODY frame (middle); vehicle's ground speed ( $U$ , bottom).

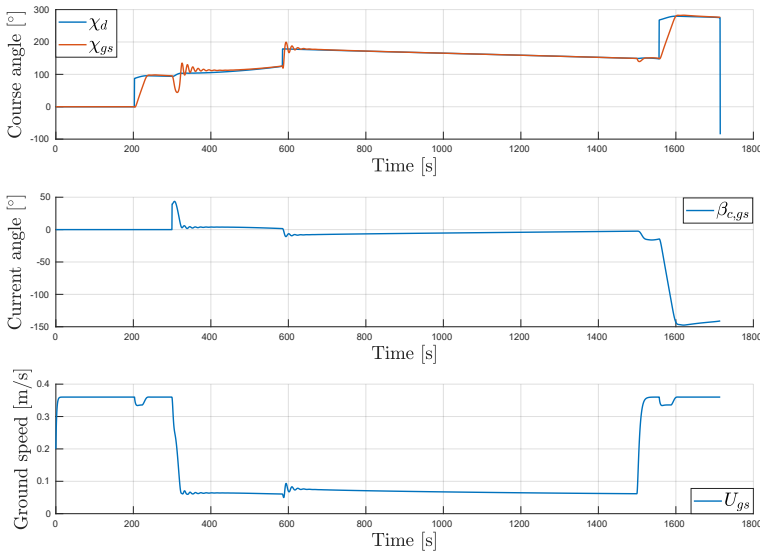


Figure 5.17: Desired ( $\chi_d$ ) and measured ( $\chi_{gs}$ ) course over ground (top); ocean current direction ( $\beta_{c,gs}^B$ ) in vehicle's BODY frame (middle); vehicle's ground speed ( $U_{gs}$ , bottom).

the vehicle with gain-scheduled course control efficiently reaches the second way point (WP 2) and then aims towards the third (WP 3). Some initial oscillations are observed when the current appears and when the way point is reached (see Figure 5.17). Figure 5.18 indicates that scheduling the gains based on the value of  $\gamma$  helps damping rudder and course oscillations. The impact of currents on the vehicles navigation is best observed in Figure 5.19, where it is clear that the ocean current transports both USVs North. The impact of drifting forces generated by the current on the USV navigation can be noticed while the system with gain-scheduled steering control navigates between WP 2 and WP 3. Finally, when the sea current disappears, both vehicles resume normal navigation with nominal gains. The simulation terminates when one vehicle reaches the initial location. The USV with gain-scheduled control navigates more efficiently, hence reaching the destination while the other is still far behind.

## 5.4 Field experiments

The USV is equipped with a Nortek Signature500 ADCP with four tilted beams that sample the water column as represented in Figure A.1 in Appendix A.2. The instrument measures current components in the beam frame (see Figure A.1) up to a depth of 60 meters. The ADCP is in general a very complex instrument, whose performances can vary significantly depending on the application. Factors such as bathymetry, flow turbulence and suspended matter may influence the stream velocity measurements and, to date, a rigorous assessment of ADCP measurement uncertainty is not yet available. The mean velocity spatial distribution is therefore subject to uncertainty associated with ping ADCP errors and the fact that instantaneous measurements both represent the mean velocity and turbulent velocity fluctuations. This means that instantaneous raw data are affected by variance due to both measurement error and real fluctuations and, therefore, instantaneous measurement may be a poor realization of the local mean velocity in some occasions [122]. The experimental results presented in this chapter are based on sea trials conducted in the Trondheim Fjord at outlet of the Nidelva river (see Figure 5.20). Tidal currents can be very strong in fjords, depending on their width, depth and other factors. As described in Chapter 4, there are situations in which the forces generated by the environment overcome the wave propulsion force. The area north of Munkholmen island is known for its strong currents, due to the steepness of the island shelf. For this reason, on the day of the mission it was decided to conduct the test close to the river outlet. The benefits of operating in this area are two. First, the vehicle can experience a constant current (river outflow) and hence it is easier to test the controller methodically. Secondly, we are able to assess the accuracy of the ADCP measurements, important for the gain scheduling procedure.

## 5. Gain-scheduled steering control

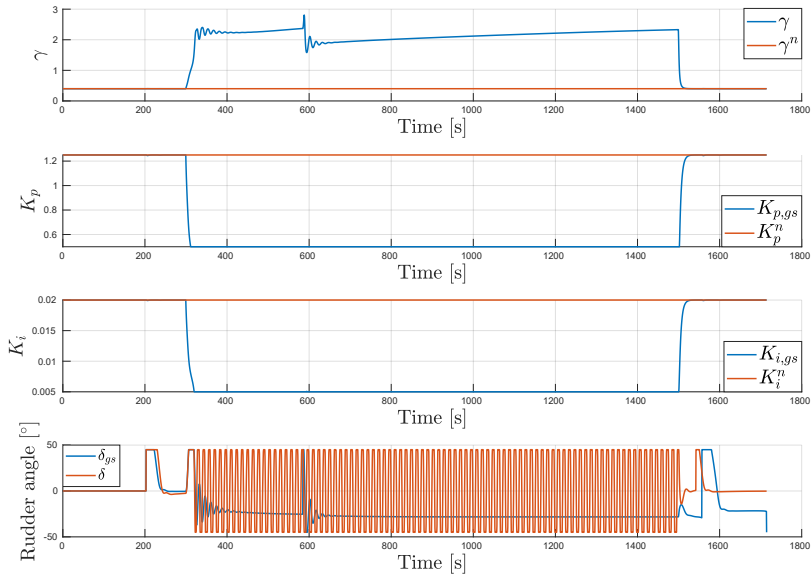


Figure 5.18:  $\gamma$  parameter for gain scheduling as compared to its nominal value ( $\gamma^n$ ); computed  $K_{p,gs}$  and  $K_{i,gs}$  gain as compared to their nominal values  $K_p^n$  and  $K_i^n$  (middle); comparison of the scheduled ( $\delta_{gs}$ ) and not ( $\delta$ ) rudder angles.

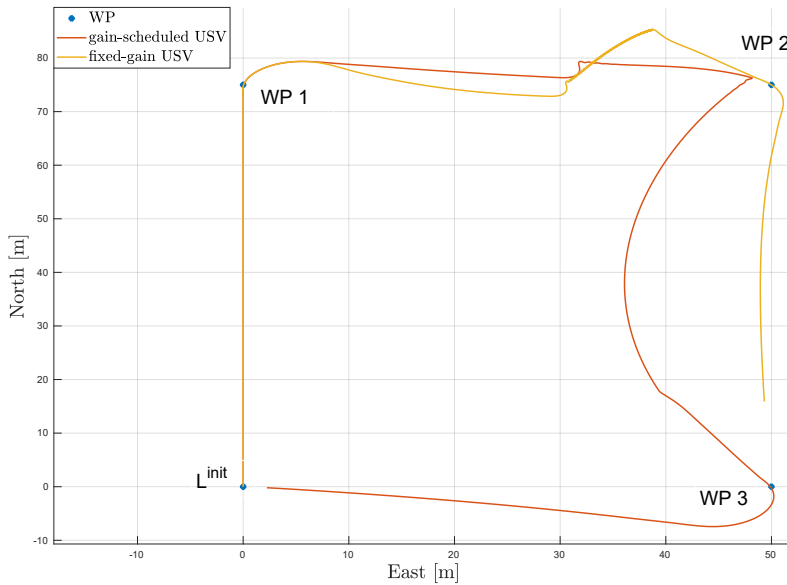


Figure 5.19: Vehicles' path.

Additionally, proximity to the deployment and recovery facilities is a benefit. Despite some techniques have been investigated in order to estimate the measurements uncertainty [123, 124], in this work we assume that the measured current shows a predominant velocity component that is the true velocity of the flow. The transducers are located approximately 40 centimeters below the waterline, so an additional half-meter as blanking distance<sup>1</sup> was chosen. Additionally, for the purpose of gain scheduling we avoid sampling the whole column and it was decided to set a 1-meter cell size. This means that the useful current measurements are performed in the range 90 to 190 centimeters depth. The instrument measures current velocities in each beam frame or an overall current velocity vector in its Cartesian (XYZ) frame, for each cell. The latter is then transformed to the USV BODY frame and eventually to Earth-fixed frame, as described in the Appendix A.2.

In the following, two scenarios are presented in which the gain-scheduled controller is tested and compared with the fixed-gains one. In the designed experiments, the USV was commanded to navigate autonomously from the fjords straight into the mouth of the river outlet (see Figure 5.20). So doing, the USV would experience a negative current in its longitudinal BODY frame component ( $u_c \leq 0$ ). Intuitively, the current would slow down the vehicle making the nominal course controller gains become ineffective. The current is measured by the ADCP and then post-processed by the onboard software, in order to extract i) its BODY frame components and ii) to compute the Earth-fixed components (see Appendix A.2), useful to provide the onshore operators with some situational awareness about the environment surrounding the USV.

#### 5.4.1 ADCP-based gain-scheduled steering control

In the first experiment the USV initially navigates in the surroundings of the river outlet (see Figure 5.20). Figure 5.21 shows the computed longitudinal current component  $u_c$  in the USV's BODY frame. It can be observed that when the USV moves away from the river mouth the perceived current is positive in the BODY frame, while it is negative when the vehicle heads towards the outlet. This confirms that the current moves outwards (North-East) as expected. Figure 5.22 shows the expected values  $\hat{\gamma}$  specific to this scenario and compares them with the values ( $\gamma$ ) computed during the sea trials. The expected values  $\hat{\gamma}$  are computed by iterating through a range of ground speed ( $U$ ) and heading ( $\psi$ ) values chosen in a way that simulate the USV moving from North to South towards the river mouth, i.e.,  $U \in [0.05, 0.7]$  m/s and  $\psi = \chi \in [150, 210]^\circ$ . Also, the computation of  $\hat{\gamma}$  depicted

<sup>1</sup>The blanking distance is the region immediately in front of the transducer where no measurements can be made while the transducers recover from the transmit pulse.

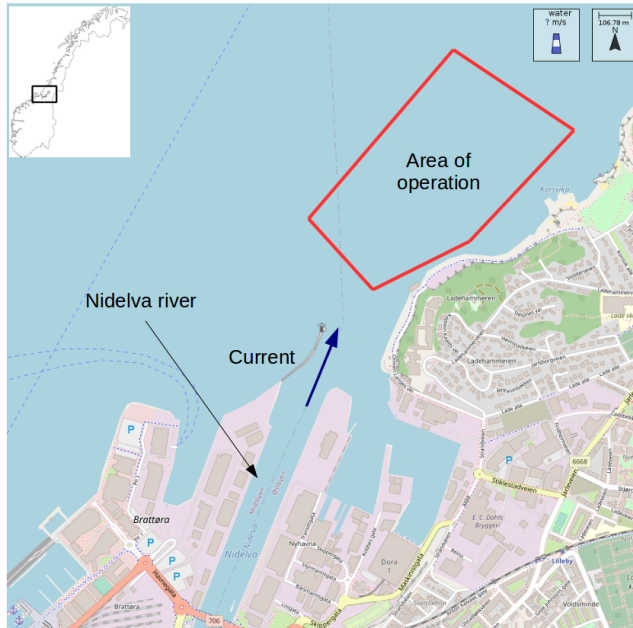


Figure 5.20: USV's operational area close to the mouth of the Nidelva river.

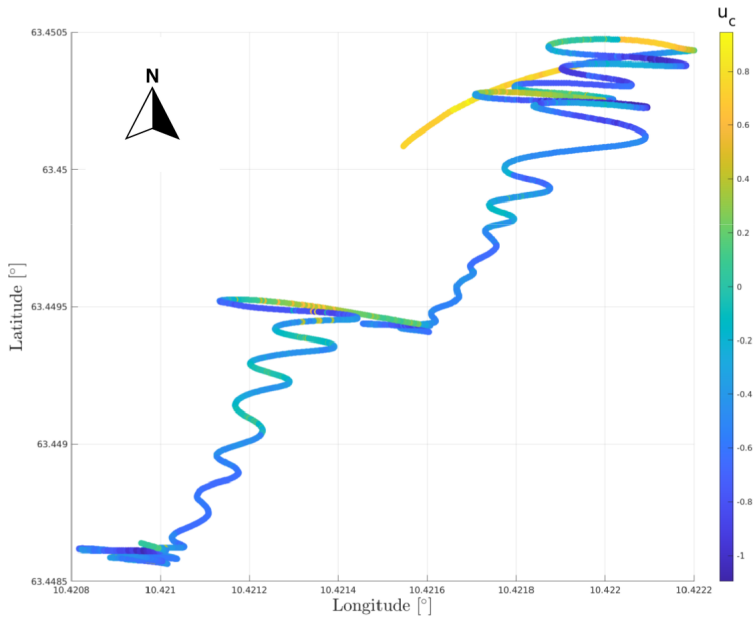


Figure 5.21: USV's track while collecting current measurements at the outlet of the Nidelva river.

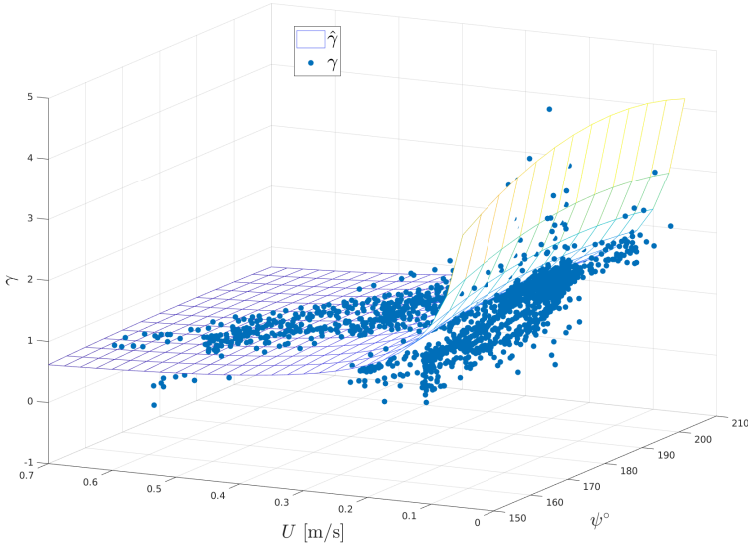


Figure 5.22: Expected values  $\hat{\gamma}$  and the values computed during the sea trials ( $\gamma$ ).

in Figure 5.22 assumes a sea current with constant Earth-fixed velocity  $U_c = 0.5$  m/s and direction  $\beta_c = 10^\circ$ , and that  $\chi = \psi$  for simplicity. With the presented information it is possible to compute the NED and BODY frame velocities of the USV, its velocities relative to the water flow and hence  $\hat{\gamma}$ . It can be observed that  $\gamma$  shows values similar to the expected ones when the USV's ground speed exceeds 0.2 m/s, i.e., the points are one the surface or very close to it. When the ground speed drops some error is observed, despite the trend of the spatial distribution of  $\gamma$  resembles that of the expected surface (e.g., increasing  $\gamma$  as  $U$  decreases). The error observed at low ground speeds can be due to two main reasons: the assumptions made on the current velocity and direction, and high sensitivity to noise that affects the ground speed  $U$  and course  $\chi$  measured by the onboard GNSS receiver when operating at low speeds. Moreover, it is important to notice that the values of  $\gamma$  computed during the sea trials will never match exactly the surface since the current measured by the ADCP is not constant. The authors have decided to simulate  $\gamma$  for an average, constant current velocity  $U_c = 0.5$  m/s and direction  $\beta_c = 10^\circ$  and, if one would iterate through more values of both would obtain a family of surfaces that would fit all the values computed during the sea trial. However, it is relevant to observe that the trend of  $\gamma$  resembles what is expected for the specific scenario.

The top graph of Figure 5.23 shows the measured velocities. It can be observed



## 5. Gain-scheduled steering control

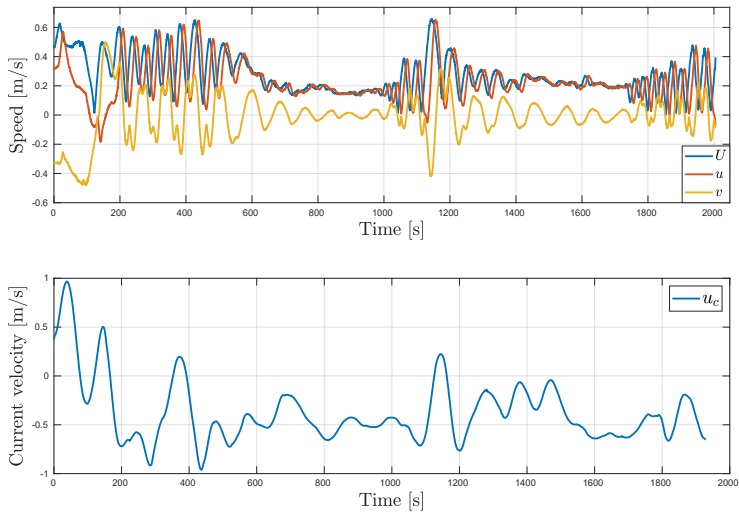


Figure 5.23: Measured ground speed  $U$  and its BODY frame components  $u$  and  $v$  (top); the longitudinal current component  $u_c$  in BODY frame (bottom).

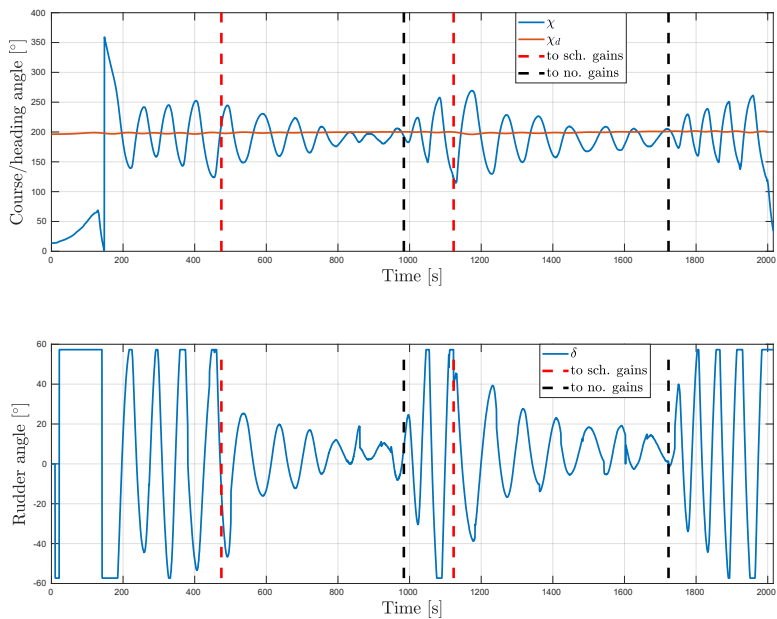


Figure 5.24: Measured ( $\chi$ ) and desired ( $\chi_d$ ) course over ground (top); the computed rudder angle ( $\delta$ ) (bottom). Dashed lines indicate switching to gain-scheduled (red) and nominal (black) course controller.

that when the USV navigates with the current, then  $U$  and  $u$  are similar and positive. A negative lateral speed  $v$  is observed and it is due to the vehicle's heading relative to the current which is hitting its starboard side. When the USV turns around and heads towards the Nidelva outlet the longitudinal current component in the BODY frame ( $u_c$ ) becomes negative and the vehicle's speed drops and oscillations are observed. This is where the nominal gains  $K_p^n = 1.25$  and  $K_i^n = 0.02$  become ineffective and the controller commands large rudder oscillations. The bottom graph of Figure 5.23 shows the value of  $u_c$  computed based on measurements during the experiment.

Figure 5.24 compares the measured course angle ( $\chi$ ) with the desired one ( $\chi_d$ ). It can be observed that large course oscillations are usually connected to large rudder angles (bottom). The red dashed lines indicate when the controller replaces the nominal gains with the scheduled ones. The reduction of the rudder efforts is clear when the scheduled gains are applied at time  $t = 474$  s and  $t = 1123$  s. As the rudder angle is reduced, an attenuation of the amplitude of course oscillations can be observed. Figure 5.24 clearly indicates that the nominal gains that have been employed extensively for controlling the USV in a number of missions (see Chapter 4) involve large rudder oscillations when a sea current is experienced in the same order of magnitude of the vehicle's speed. The gain scheduling approach based on ADCP data is capable of reducing the rudder effort and produce a more efficient navigation in the desired direction. The effects of gain scheduling of the rudder control signal can also be appreciated in the measured USV's pattern. The top graph of Figure 5.23 shows that when the gains are scheduled, the longitudinal speed ( $u$ ) and the ground ( $U$ ) speeds converge to the same values meaning no crab angle, while the lateral vehicle speed oscillates and eventually settles around 0 m/s. When the nominal gains are employed, however, larger course oscillations imply higher variation in the lateral speed as well.

Figure 5.25 shows the gains computed based on  $\gamma$ , as indicated in Equation 5.4. Periodically (every 2 minutes), an average  $\bar{\gamma}$  is computed and used to update the scheduled gains. A new computation of the gains does not indicate when the controller actually uses them: the choice of switching to nominal or scheduled gains (see Figure 5.24) is left to the operators for this initial experiment.

## 5.4.2 SOG-based gain-scheduled steering control

In this section we evaluate the performances of the gain scheduling approach when the knowledge of the sea current is not available. This implies that the computation of the scheduling variable (renamed  $\gamma_U$ ) is based only on the USV ground velocity, see Equation 5.5. The test area is the same as in the previous experiment. Again, the objective of the experiment is to quantify the benefits of gain-scheduled steering control when the USV's ground speed drops.

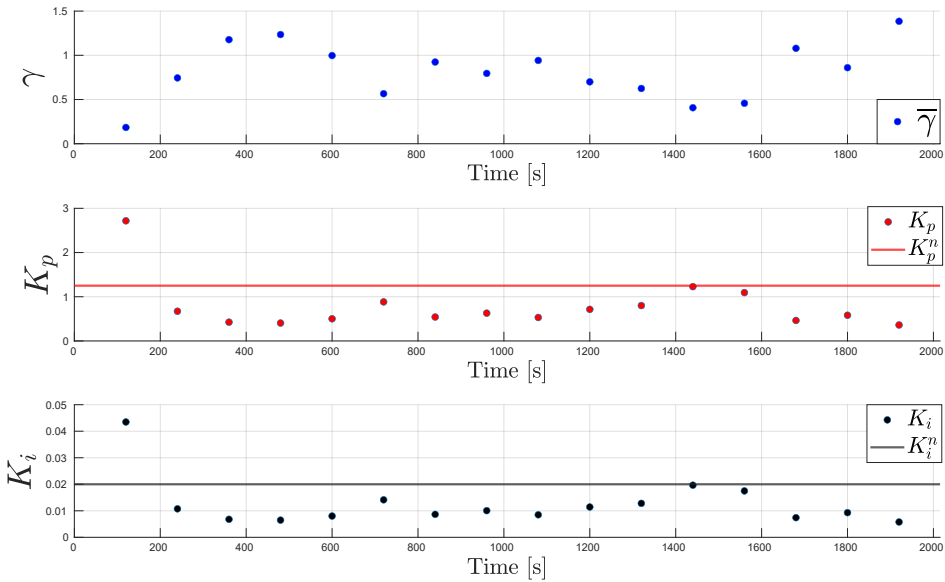


Figure 5.25: Average  $\bar{\gamma}$  (top); the nominal ( $K_p^n$ ) and scheduled ( $K_p$ ) proportional gain (middle); the nominal ( $K_i^n$ ) and scheduled ( $K_i$ ) integral gain (bottom).

Figure 5.26 compares the expected values  $\hat{\gamma}_U$  with those computed during the field experiment ( $\gamma_U$ ). Similarly to the previous experiment, the values computed during the mission are close to the expected surface, despite the surface itself has a different shape. This is due to the different equation that models the system nonlinearity  $\gamma_U$ . Again, expected values are computed by iterating through typical values of  $u$  and  $U$ .

The top graph of Figure 5.27 depicts the measured ground speed ( $U$ ) and the BODY frame longitudinal ( $u$ ) and lateral ( $v$ ) velocities. Right below, it shows the periodical average ( $\bar{\gamma}_U$ ) used to compute the scheduled gains. It can be observed that there are relatively large  $U$  oscillations measured until time  $t = 400$  s and from time  $t = 800$  s to the end of the mission. It can be noticed that such oscillations are partially followed by oscillations of  $u$  and  $v$ . Figure 5.27 also shows the proportional and integral gains that are computed using  $\bar{\gamma}_U$ .

Figure 5.28 compares the measured ( $\chi$ ) and desired ( $\chi_d$ ) course angles. Large course oscillations are caused by large rudder angles (bottom). The red dashed lines indicate when the controller replaces the nominal gains with the scheduled ones. The reduction of the rudder efforts is evident when the scheduled gains are applied at time  $t = 400$  s. As the rudder angle is reduced, an attenuation of the amplitude of course oscillations can be observed. Not only the course over ground

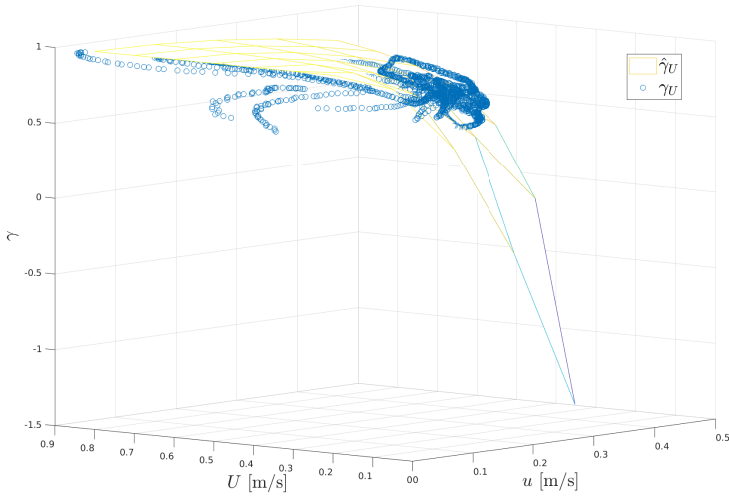


Figure 5.26: Expected values  $\hat{\gamma}_U$  and the values computed during the sea trials ( $\gamma_U$ ).

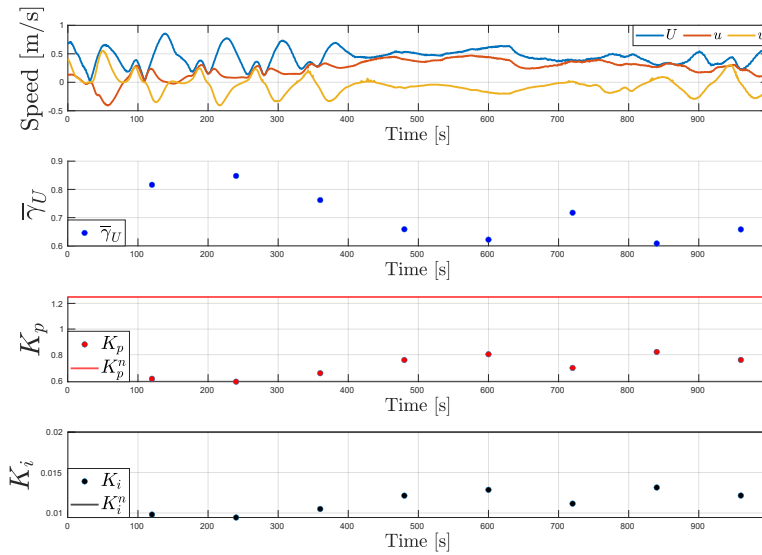


Figure 5.27: Measured ground speed  $U$  and its BODY frame components  $u$  and  $v$  (top), the average  $\bar{\gamma}_U$  (middle); the nominal ( $K_p^n$ ) and scheduled ( $K_p$ ) proportional gain (middle); the nominal ( $K_i^n$ ) and scheduled ( $K_i$ ) integral gain (bottom).

## 5. Gain-scheduled steering control

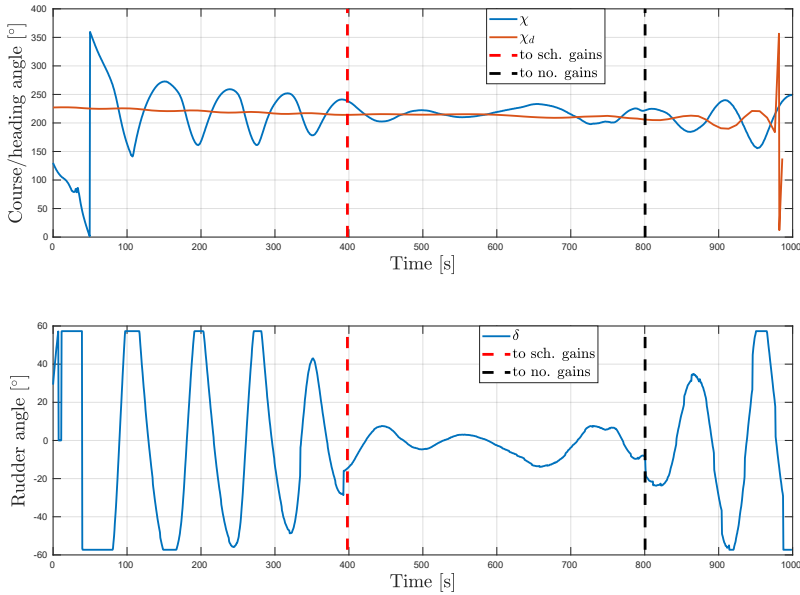


Figure 5.28: Measured ( $\chi$ ) and desired ( $\chi_d$ ) course over ground (top); the computed rudder angle ( $\delta$ ) (bottom). Dashed lines indicate switching to gain-scheduled (red) and nominal (black) course controller.

stabilizes, but also the speed over ground does (see Figure 5.27), increasing the navigation performance of the vehicle in the intended direction. The gains applied at time  $t = 400$  s are  $K_p = 0.55$  and  $K_i = 0.008$ . When the gain scheduling controller is deactivated and the nominal gains are restored at time  $t = 800$  s, large rudder oscillations are commanded and the course-keeping performances deteriorate.

### 5.5 Discussion

In this chapter the gain-scheduled steering system for the AutoNaut USV has been presented and discussed, taking into account the effects of ocean currents that may lead to very low speed relative to ground and to water.

A three-state quasi-linear model gives insight into the changes in steering dynamics as a function of changing environmental conditions, which is exploited in the control design to handle singular situations that occur when the USV's speed relative to the current approaches zero. Classical control design principles are applied based on a frequency analysis of the proposed model. The same analysis confirms that robust linear course control can be further investigated and achieved by im-

plementing a gain-scheduled course-keeping autopilot.

The presented gain scheduling approach is first studied theoretically using the pole placement technique, which supports the previous frequency analysis of the model and highlights the benefits of relaxing the controller gains. The analysis shows that the variable  $\gamma$  can be used to schedule the autopilot gains both when the sea current measurement is available and when it is not.

The proposed control system is initially studied with simulations, which reveal the benefits of scheduling the controller gains when the ocean currents appears in the same order of magnitude of the vehicle's speed.

The author has addressed the challenges and limitations related to the ADCP instrument, before experimental results are presented based on sea trials performed in the Trondheim Fjord (Central Norway). Experimental results demonstrate that the proposed gain scheduling approach enables a more efficient navigation of the vehicle, reducing the rudder efforts and the course oscillations. Furthermore, speed oscillations are suppressed and the average velocity of the USV increases when the scheduled gains are applied. This is observed both when the ocean current measurement is available and when it is not, proving the validity of both approaches.



## Chapter 6

# Estimation of the wave encounter frequency

### *Wave-filtered steering control*

This chapter is based on the conference article [125], which describes the experimental validation of a nonlinear wave encounter frequency (WEF) estimator.

Sea state estimation is of importance in marine operations. It provides information that can be used to increase mission safety and reduce operational risk, but also to enhance the seakeeping and autopilot system performance of marine crafts whose motion is determined by sea waves, ocean currents and winds. Estimation of the WEF can be used to forewarn incoming impetuous waves and rough environmental conditions.

For marine vehicles whose propulsion and course-keeping capabilities mainly rely on environmental forces, the estimation of the encounter frequency is relevant for two main reasons. First, it allows the vehicle to have in-situ situational awareness of the operational environment. Decision-making methods may benefit from estimates of the sea state and synthesize high-level mission plans that comply with the current condition of the environment. Moreover, by combining onboard estimates with metocean models it is possible to predict future sea states and eventually re-plan or modify the mission accordingly. Secondly, the estimated encounter frequency can be used as cut-off frequency in filters employed in wave filtering techniques for the rudder control command in a course-keeping controller [72].

When considering the nature of the AutoNaut's propulsion, it appears obvious that the onboard control system would benefit from the knowledge of the sea state, in order to adapt the mission parameters from a high-level perspective. For example, an estimation of the sea state might indicate that the current path cannot be pursued. Based on that, the decision-making unit might then modify the current



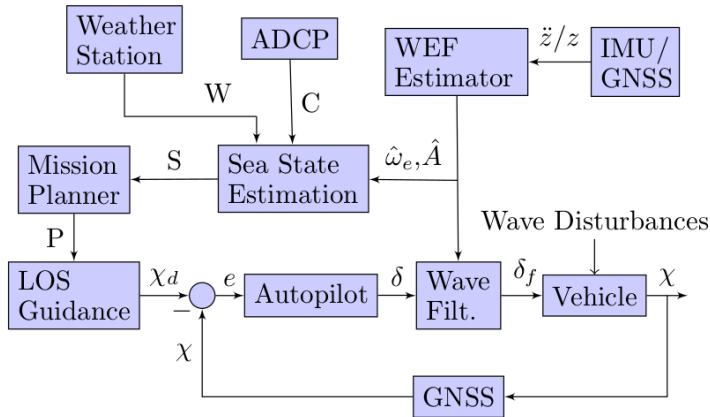


Figure 6.1: Knowledge of the WEF is important to enhance high-level mission planning and to perform wave filtering of the rudder command signal.

target locations in a way that makes the USV's navigation more effective with respect to wind, currents and waves.

Figure 6.1 suggests that, for example, sea currents ( $C$ ) and surface winds ( $W$ ) information can be merged, together with an estimate of the WEF ( $\hat{\omega}_e$ ) and amplitude ( $\hat{A}$ ), and used to estimate the current sea state ( $S$ ). Moreover, onboard decision-making entities can evaluate the feasibility of the current mission and eventually modify or re-plan the intended mission (e.g., desired course change) to comply with the environment.

Figure 6.1 also indicates that the same estimated wave information can be employed in the onboard guidance, navigation and control (GNC) system for wave filtering of the rudder command signal usually achieved with conventional low-pass, band-stop or notch filters. As discussed in [72] and in the next section, precise knowledge of the encounter frequency allows better tuning of these filters. The figure indicates that filters for this purpose are usually placed between the autopilot and the vehicle servo, producing a filtered version ( $\delta_f$ ) of the computed rudder angle ( $\delta$ ) that reduces wear of the servo mechanism.

## 6.1 Wave filtering of the rudder control

Wave filtering is one important issue to consider when designing ship control systems [126]. Environmental forces due to waves, wind and ocean currents are considered disturbances to the control system. These forces are conceptually separated into low-frequency (LF) and wave-frequency (WF) components. Waves produced

forces that are applied to the hull surface. These pressure-induced forces have an oscillatory component that depends linearly on the wave height. For this reason, these forces have the same frequency as that of the waves and are therefore referred to as wave-frequency forces [72]. Wave forces also have a component that depends nonlinearly on the wave height, and these present a wider frequency range.

In low and medium sea states, the oscillation frequencies of the linear wave forces do not normally affect the navigational performance of the USV. Hence, controlling only LF motion avoids correcting the motion for every single wave, which would result in unacceptable operational conditions. Course and heading control applications, for example, only require the control of LF motions.

It is important that only the slowly varying forces are counteracted by the steering system. In other words, the oscillatory motion due to the waves (first-order wave-induced forces) should be prevented from entering the feedback control loop. This is the purpose of *wave filtering* techniques [127].

This chapter refers to wave filtering as the reduction of wave-induced control forces, that are a combination of second-order slowly varying and zero-mean first-order oscillatory components. Whereas the former can be canceled by an integral action, the latter may be removed from the measured motion states using a band-stop (or similar) filter.

## 6.2 Wave encounter frequency estimation

Spectral analysis is a commonly adopted technique used to study irregular waves and approximate them to a series of sinusoidal components with different amplitude, frequency and phase. This operation is commonly achieved by the Fast Fourier Transform (FFT) algorithm, that applies the Discrete Fourier Transform (DFT) on a window moving over the signal. This makes the transformation itself affected by lag and the estimation of the time-varying WEF based on obsolete data. Rather than estimating the whole wave spectrum, the dominant frequency could be observed instead and used for wave filtering. In addition, more accurate techniques allow to estimate the direction of incoming waves [128, 129]. However, these are constrained by the same lag affecting FFT and require a dynamic model of the vehicle, which in this case is complicated to derive due to the wave-propulsion assembly.

The signal-based method employed in this work is based on [130], where it is demonstrated that roll and pitch angles can be used to estimate the WEF. This approach was further extended to include a variation of the estimation algorithm that employs the heave displacement measured onboard the vehicle [131]. The same work, where the observer is tested on a container ship whose model and

hydrodynamic coefficients can be found in [132], contains the only experimental data prior to the present manuscript.

This chapter describes the validation of the WEF estimator on data collected by the AutoNaut. The algorithm is validated with simulations and experimental results in both fjord and ocean waters, proving its ability to converge in different sea states. The originality of this research stands in the application of a WEF observer to a small (5 meters long) USV, which shows completely different wave response and motion than a large ship, and which is never demonstrated before. Moreover, this chapter presents the first closed-loop field experiments employing this observer in a course-control architecture.

### 6.3 Heave dynamic model

The heave motion of the USV can be modeled as a linear second-order system with sinusoidal forcing, [72],

$$\ddot{z} + 2\zeta\omega_n\dot{z} + \omega_n^2 z = \frac{F}{m - Z_{\dot{w}}} \sin(\omega t + \varepsilon) \quad (6.1)$$

where  $\omega$  is the modal (dominating) frequency of the waves,  $z$  is the heave position,  $\omega_n$  is the natural frequency,  $\zeta$  is relative damping ratio,  $F/(m - Z_{\dot{w}})$  is the wave force divided by mass (including hydrodynamic added mass  $Z_{\dot{w}}$ ) and  $\varepsilon$  is the oscillation phase. We only consider the steady-state solution

$$z = \frac{F}{(m - Z_{\dot{w}})Z_m\omega} \sin(\omega t + \varepsilon + \phi) \quad (6.2)$$

where  $Z_m$  is the impedance or linear response function and  $\phi$  is the phase angle relative to the driving force  $F$ . However, for a vehicle moving at ground speed  $U > 0$ , the Doppler Shift causes the wave angular frequency  $\omega$  to be modified as

$$\omega_e(U, \omega, \beta_{wa}) = \omega - kU \cos(\beta_{wa}) \quad (6.3)$$

where  $\omega_e$  is the *wave encounter frequency*,  $k$  is the wave number satisfying the deep water dispersion relation  $\omega^2 = kg$  in which  $g$  is the acceleration of gravity and  $\beta_{wa}$  is the wave encounter angle (zero for following seas). The wave number  $k$  relates to the wave length  $\lambda$  as  $k = 2\pi/\lambda$ . This implies that the solution (Equation 6.2) can be reformulated as

$$z = A \sin(\omega_e t + \epsilon) \quad (6.4)$$

where

$$A = \frac{F}{(m - Z_{\dot{w}})Z_m\omega_e}, \quad \epsilon = \varepsilon + \phi \quad (6.5)$$

are the amplitude and phase of the measured heave position, respectively.

## 6.4 Switching-gain WEF estimation

The estimation problem aims at estimating online the unknown frequency  $\omega_e$  of a measured time-varying signal  $z$  given by Equation 6.4, whose amplitude  $A$  and phase  $\epsilon$  are not known. The sinusoidal signal of Equation 6.4 can be represented by the linear differential equation

$$\ddot{z} = \psi z \quad (6.6)$$

where  $\psi := -\omega_e^2$  is the parameter to be estimated. As indicated in [133], the frequency  $\omega_e$  is estimated using the auxiliary filter

$$\begin{aligned} \dot{\zeta}_1 &= \zeta_2 \\ \dot{\zeta}_2 &= -2\omega_f \zeta_2 - \omega_f^2 \zeta_1 + \omega_f^2 z. \end{aligned} \quad (6.7)$$

The filter cut-off frequency  $\omega_f$  has to be chosen so that  $0 < \omega_e < \omega_f$ . The Laplace transformation of the linear system (Equation 6.7) leads to the transfer function

$$\zeta_1(s) = \frac{\omega_f^2}{(s + \omega_f)^2} z(s) \quad (6.8)$$

From Equation 6.6 it follows that  $s^2 z(s) = \psi z(s)$  and

$$z(s) = \frac{2\omega_f s + \omega_f^2 + \psi}{\omega_f^2} \zeta_1(s) \quad (6.9)$$

The time domain representation of Equation 6.9 is recognized as

$$z = \frac{1}{\omega_f^2} (2\omega_f \dot{\zeta}_2 + \omega_f^2 \zeta_1 + \psi \zeta_1). \quad (6.10)$$

The parameter update law for  $\psi$  presented in [134] makes use of the variable given by the auxiliary filter

$$z' := \dot{\zeta}_2 = -2\omega_f \zeta_2 - \omega_f^2 \zeta_1 + \omega_f^2 z \quad (6.11)$$

By denoting  $\hat{\psi}$  the parameter estimate and defining  $\hat{z}' = \zeta_1 \hat{\psi}$ , the parameter update law becomes

$$\dot{\hat{\psi}} = k_f \zeta_1 (\dot{\zeta}_2 - \zeta_1 \hat{\psi}), \quad (6.12)$$

where  $k_f$  is the adaptation gain obtained by low-pass filtering the gain switching mechanism as described in the next paragraph.

Global exponential stability of the equilibrium point of the estimator is proven in [131], where it is shown how the original fixed-gain estimation algorithm of [134] can be modified to include a gain adaptation algorithm, which depends on the estimated heave amplitude  $\hat{A}$ .

### 6.4.1 Switching-gain mechanism

According to [130], we choose the switching mechanism for the gain as

$$k(A) = \begin{cases} k_{init} & \text{if } t \leq t_{init} \\ k_{min} & \text{if } t > t_{init} \wedge A > A_0 \\ k_{max} & \text{if } t > t_{init} \wedge A \leq A_0 \end{cases} \quad (6.13)$$

where  $A$  is the signal amplitude,  $A_0$  is the amplitude used to switch gains, and  $t_{init}$  is the time duration in which the gain is in its initial value. The amplitude  $A$  of the measured signal cannot be directly computed. However, the amplitude can be estimated using the squared measurement

$$z^2 = \frac{A^2}{2}(1 - \cos(2\omega_e t + 2\epsilon)). \quad (6.14)$$

Consequently, by low-pass filtering the signal of Equation 6.14, the amplitude  $A^2/2$  of the squared measured signal  $z^2$  is obtained

$$\gamma = \frac{1}{Ts + 1} z^2, \quad (6.15)$$

where  $T > 0$  implies that the estimate of amplitude becomes

$$\hat{A} = \sqrt{2\gamma}. \quad (6.16)$$

The adaptation gain  $k_f(t)$  is obtained by low-pass filtering  $k(\hat{A})$  according to

$$T_f \dot{k}_f + k_f = k(\hat{A}), \quad (6.17)$$

where  $T_f > 0$  is recognized as the switching time constant and  $k(\hat{A}) \leq \max(k_{max}, k_{init})$ .

### 6.4.2 Preliminary considerations

In this work we assume that the wave amplitude is similar to the heave amplitude of the USV (unitary transfer function in heave). Hence we use the heave amplitude measured by the GPS placed at the bow, after a transformation to the vehicle's BODY frame (located in the CG). The homogeneous transformation does not affect the measured heave period of the USV, but it uses the knowledge of lever arm and Euler angles to compute the heave in BODY frame, which shows intuitively a lower amplitude. For the purpose of WEF estimation, the effects of sensor location and lever arms can be neglected since it is primarily the time between peaks that contains information. Alternatively, it is possible to estimate the USV heave displacement from the vertical acceleration ( $\ddot{z}$ ) measured by the IMU [135], as

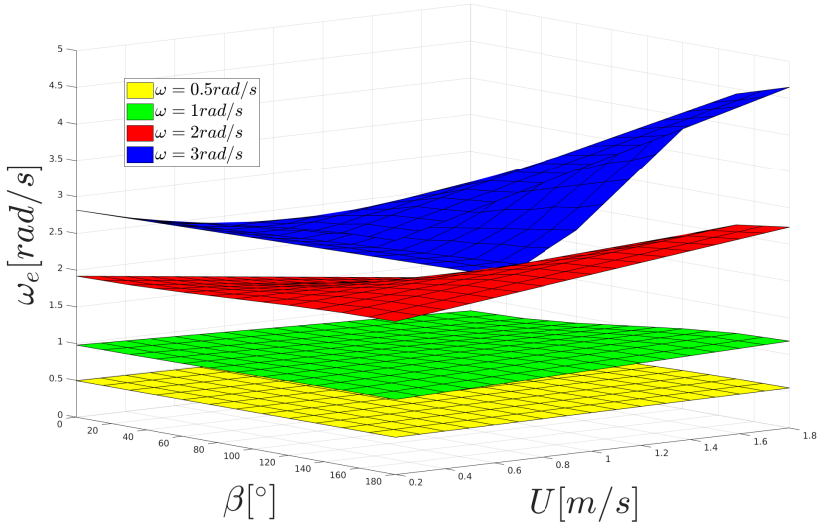


Figure 6.2: Expected WEF perceived by the USV based on varying ground speed  $U$ , encounter angle  $\beta_{wa}$  and wave frequency  $\omega$ .

indicated in Figure 6.1.

For wave periods in the interval  $5 < T_w < 20$  seconds, the modal frequency  $f$  of a wave spectrum will be in the range  $0.05 < f < 0.2$  Hz. Therefore, the wave circular frequency  $\omega = 2\pi f$  is in the range of  $0.3 < \omega < 1.3$  rad/s. Fast and irregular waves are expected in fjords, where a reduced wind fetch generates short-crested waves whose amplitude and frequency are mainly dependent on the local wind speed. Typical fjord waves show therefore spectra with higher dominant frequencies  $\omega > 1.3$  rad/s. Depending on the sea state, the measured speed over ground (SOG) of the USV may fluctuate between 0.5 and 2 knots (approximately 0.25 to 1 m/s). Figure 6.2 shows how the WEF, computed as in Equation 6.3, varies according to variations in waves encounter angle ( $\beta_{wa}$ ), vehicle ground speed ( $U$ ) and wave frequency ( $\omega$ ). As the wave direction and frequency are not directly measured, assumptions needs to be made according to weather forecasts.

The natural frequency of the USV heave motion is computed using standard methods from hydrostatics [72]. Assume that the added mass  $-Z_{\dot{w}} = m$ . Hence,

$$\omega_n = \sqrt{\frac{\rho g A_{wp}}{2m}}, \quad (6.18)$$

where  $A_{wp}$  is the waterplane area and  $\rho$  is the seawater average density  $1025 \text{ kg/m}^3$ . An estimate of  $\omega_n$  can be found by approximating the USV as a box for which

	Symbol	Value
Switching time constant	$T_f$	0.05 s
Switching time constant	$T_f$	0.05 s
Filter cut-off frequency	$\omega_f$	1.5 rad/s
Initial frequency	$\hat{\omega}_e^{init}$	0 rad/s
Switching amplitude	$A_0$	0.5 m
Initialization time	$t_{init}$	200 s
Adaptation gains (S1)	$k_f^{S1}$	10,5,25
Adaptation gains (S2)	$k_f^{S2}$	25,10,50

Table 6.1: Estimator parameters used in the Norwegian Sea experiment.

$A_{wp} = LB$  (length times beam). Furthermore, the mass  $m$  of a box-shaped USV is  $m = \rho LBT_{USV}$  where  $T_{USV}$  is the draught. Hence,

$$\omega_n \approx \sqrt{\frac{g}{2T_{USV}}}, \quad (6.19)$$

The vehicle draft  $T_{USV} = 0.3$  m (0.7 m including the submerged struts and hydrofoils) gives  $\omega_n = 4.1$  rad/s, which corresponds to a heave period of approximately 1.5 seconds. Hence, the natural frequency is far away from the WEF and resonance situations are avoided.

## 6.5 Offline experimental validation

The estimated encounter frequency is compared to the dominant frequency observed with spectral analysis (FFT). Moreover, we compute and compare the average frequency of heave peaks measured by the GPS. This does not indicate the dominant frequency of the asymmetric wave spectrum and therefore we expect the frequency  $\hat{\omega}_e$  estimated by the observer to be higher. Tables 6.1 and 6.2 contain the employed estimator parameters, where  $\hat{\omega}_e^{init}$  is the initial WEF.

### 6.5.1 Experimental validation in the Norwegian Sea

The estimation algorithm was first tested on data collected in the ocean, 40 km north-west of the island Frøya situated along the coasts of Central Norway. We

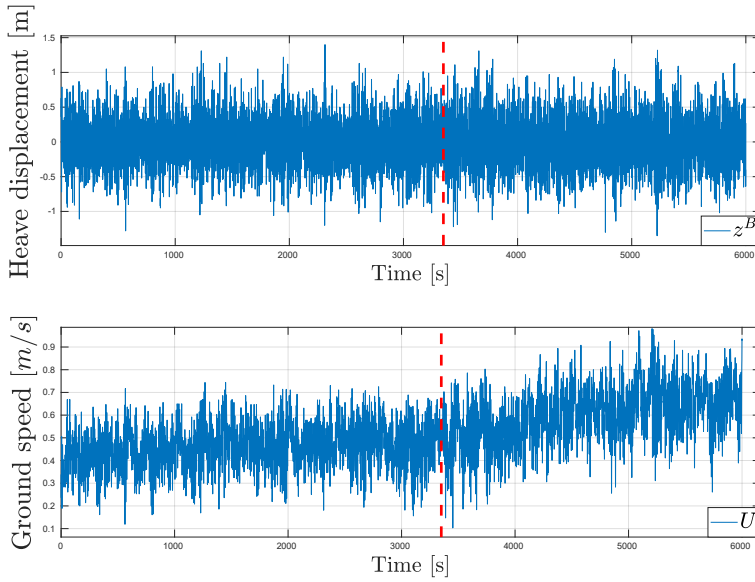


Figure 6.3: Top: heave displacement ( $z^B$ ). Bottom: USV ground speed ( $U$ ).

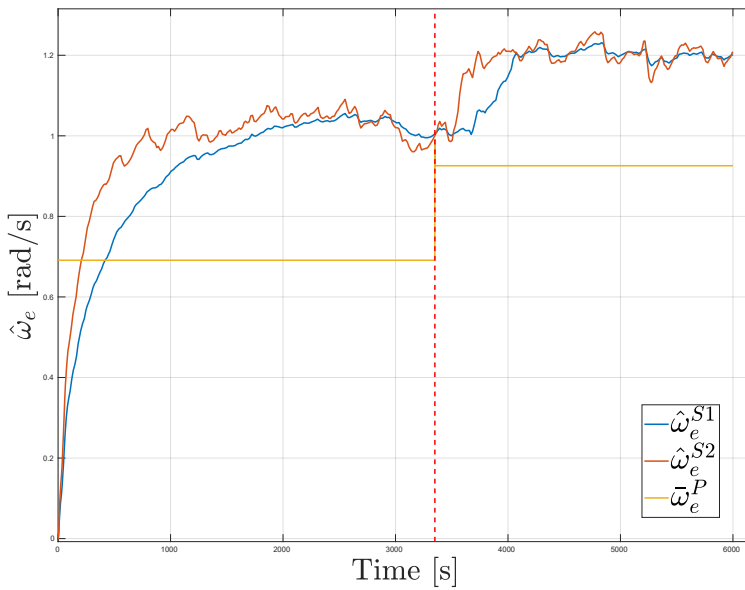


Figure 6.4: Estimated WEF with different gains sets ( $\hat{\omega}_e^{S1}$ ,  $\hat{\omega}_e^{S2}$ ), as compared to average frequency computed from heave peaks ( $\bar{\omega}_e^P$ ). The red dashed line indicates change in desired course.



	Symbol	Value
Switching time constant	$T_f$	0.05 s
Filter cut-off frequency	$\omega_f$	4 rad/s
Initial frequency	$\hat{\omega}_e^{init}$	2 rad/s
Switching amplitude	$A_0$	0.2 m
Initialization time	$t_{init}$	200 s

Table 6.2: Estimator parameters used in the Trondheim Fjord experiment.

focus on a 100 minutes long portion of the collected data in which there is an increase of USV ground speed from 0.4 m/s to 0.7 m/s on average. The red dashed line in Figure 6.3 indicates the separation before and after the speed increase. The estimator is run with parameters indicated in Table 6.1. Figure 6.4 shows the WEF ( $\hat{\omega}_e$ ) estimated with different sets of gains ( $S1, S2$ ) and same initial value ( $\hat{\omega}_e^{init}$ ) for the estimation. The estimation results are compared to the average frequencies ( $\bar{\omega}_e^P$ , yellow lines) obtained by computing local maxima of the heave signal ( $z^B$  in Figure 6.3), on both trajectory legs. Local maxima are data samples that are larger than its two neighboring samples. It can be noticed that the set of higher gains ( $S2$ ) allows the estimator to converge faster ( $\hat{\omega}_e^{S2}$ ) to approximately 1 rad/s and 1.2 rad/s and that the estimation trend resembles the average frequencies computed in each leg. Higher estimated values are however observed since the estimator extracts the peak in the spectrum. Ground truth is obtained with FFT spectral analysis (Figure 6.5), that reveals higher peaks around the estimated frequencies observed in Figure 6.7, and proves the ability of the observer to estimate dominant frequencies in both spectra.

### 6.5.2 Experimental validation in the Trondheim Fjord

Figure 6.6 shows the heave measurement collected while the USV executed autonomously a squared trajectory in Trondheimsfjord. The estimator was run with parameters indicated in Table 6.2 and same sets of gains of Table 6.1. Figure 6.7 shows the estimated WEF for both gain sets and compares it to the average frequency measured from the heave signal. Even if the convergence speed is increased by setting the initial frequency to 2 rad/s, it is observed that the amount of data collected in the first trajectory leg is not enough to achieve convergence. Again the use of a set of higher gains ( $S2$ ) leads to a faster convergence.

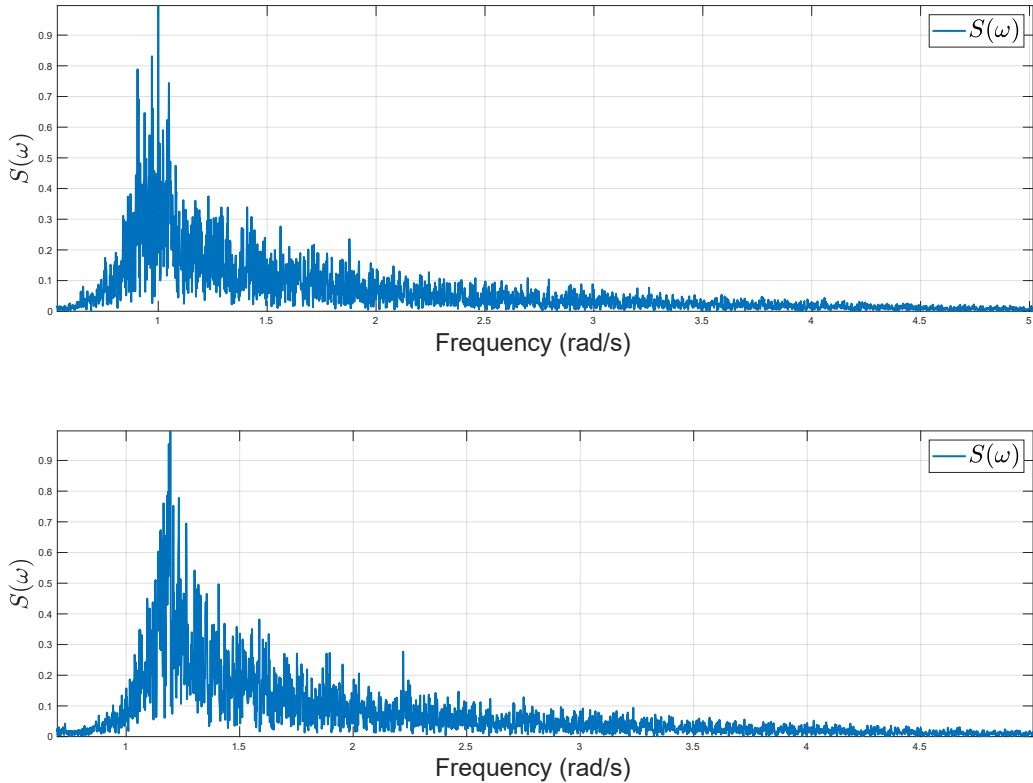


Figure 6.5: FFT indicates the range of frequencies present in the heave signal  $z^B$ . Top: before wind speed increase. Bottom: after wind speed increase.

FFT in Figure 6.8 shows richer spectra with frequencies in the range of 1.5 and 4 rad/s. It can be noticed that the frequencies at which the estimator converges (Figure 6.7) match, in each section of the trajectory, with the peaks observed in FFT spectral analysis. Moreover, wave spectra do not contain significant energy at lower frequencies, indicating predominance of irregular waves on swell components.

## 6.6 Wave-filtered steering control

The estimator was implemented on the USV onboard navigation software DUNE [97] and tested during open ocean operations. The observer ran at regular time intervals with initial frequency  $\hat{\omega}_e^{init}$  obtained from the previous run. Once estimation stabilized to a range of values, the estimated WEF was used to filter the rudder angle signal computed by the course autopilot as shown in Figure 6.1. The course-keeping autopilot used in this mission is a PI controller with gains

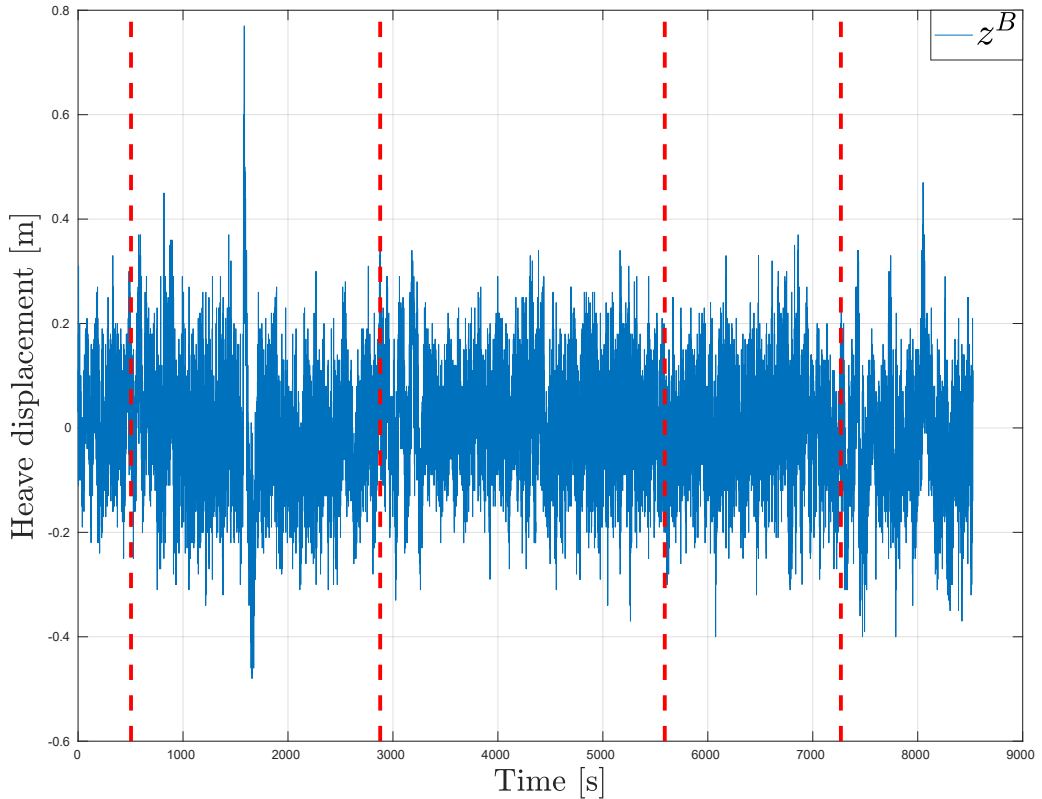


Figure 6.6: Heave displacement in body frame ( $z^B$ ); red dashed lines indicate change in desired course.

$K_p = 1$  and  $K_i = 0.1$ . Wave filtering is achieved with a first-order low-pass filter with cut-off frequency  $\omega_{LP} = n\hat{\omega}_e$  where  $n = 1.2$  is chosen in order to remove only high-frequency components. The filter cut-off frequency is computed from an estimated WEF  $\hat{\omega}_e = 1.12$  rad/s. Figure 6.9 compares magnitude and phase of the closed-loop transfer functions (from course reference to course) with and without the filter,  $H_{LP}(s)$  and  $H(s)$  respectively. This analysis assumes that the USV's steering dynamics is represented by a first-order Nomoto model [72] with parameters identified in [96]. It can be observed that the systems show the same response at high frequencies and a negligible difference up to 2 dB in magnitude and  $4^\circ$  in phase at low frequencies.

Figure 6.10 shows the rudder response when the low-pass filter is applied at time  $t = 265$  s (red dashed line). The suppression of high frequencies is clear, despite the amplitude of rudder oscillations (bounded to approximately  $10^\circ$ ) is not affected. This indicates that the control bandwidth of the system was not significantly re-

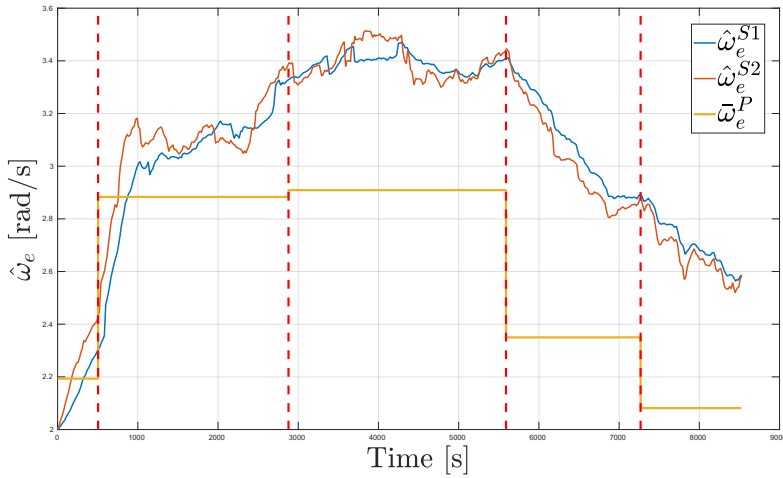


Figure 6.7: Estimated WEF with different gains sets ( $\hat{\omega}_e^{S1}$ ,  $\hat{\omega}_e^{S2}$ ), as compared to average frequency computed from heave peaks ( $\bar{\omega}_e^P$ ). Red dashed lines indicate change in desired course

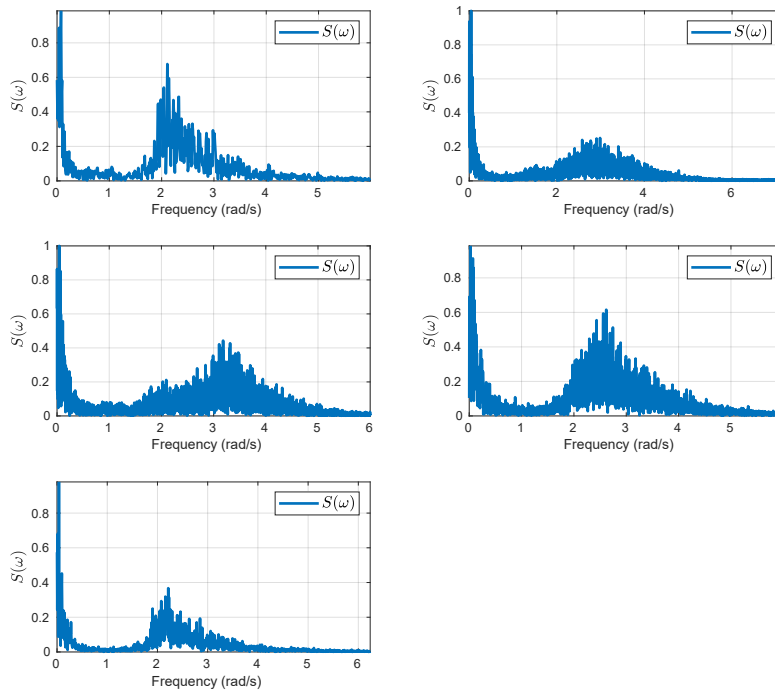


Figure 6.8: FFT spectral analysis indicates the range of frequencies present in the heave signal  $z^B$ , for each trajectory section.

duced (as the Bode plot confirms) and that despite the suppression of undesired wave-induced frequencies the autopilot is still able to command large oscillations to adjust the USV's course. While the rudder angle ( $\delta$ ) is logged onboard the USV, angular velocity ( $\dot{\delta}$ ) and acceleration ( $\ddot{\delta}$ ) are obtained offline. Figure 6.10 shows that the amplitude of the rudder angle velocity oscillations reduces of approximately 61% after the application of the filter. This increases the mechanism lifetime since prolonged use of the rudder at higher angular velocities is what wears the servo mechanism the most. Angular acceleration oscillations are instead damped by 89% of their average value when the filter is introduced, also limiting rudder jerks and therefore the stress on the mechanism. From a course-control

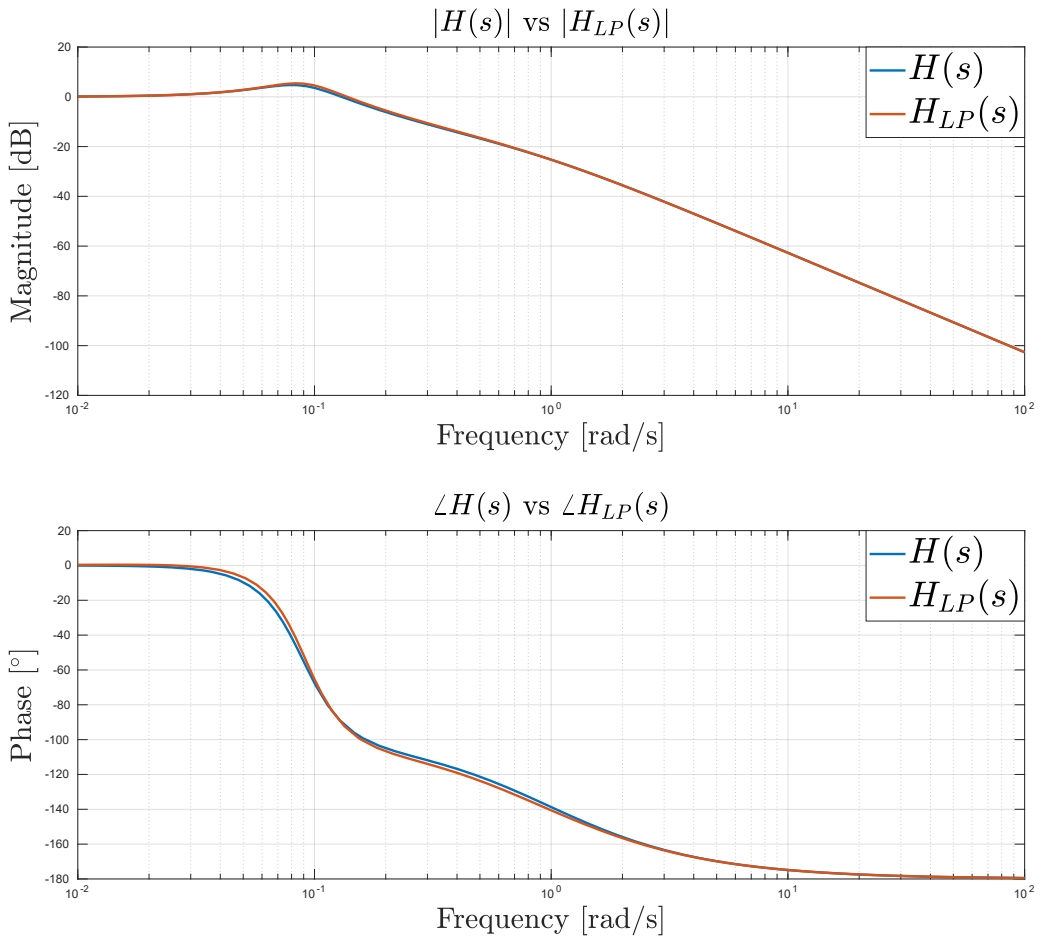


Figure 6.9: Bode plots of the closed loop transfer functions with ( $H_{LP}(s)$ ) and without ( $H(s)$ ) low-pass filter.

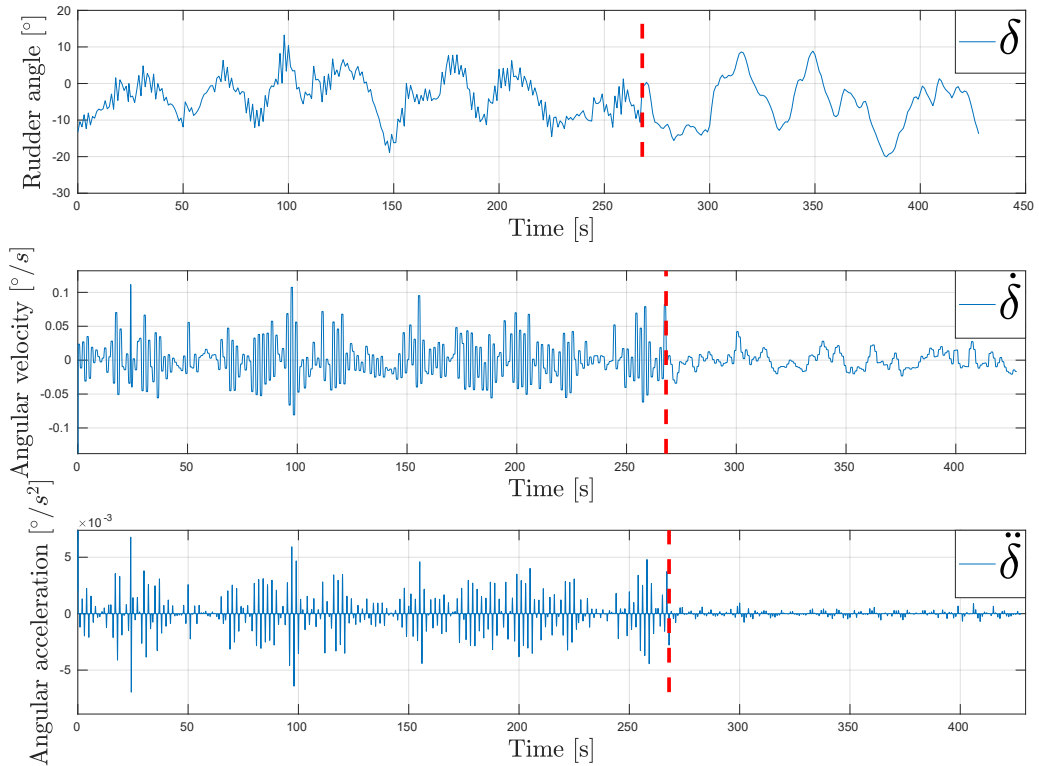


Figure 6.10: Commanded rudder angle  $\delta$  (top) and its derivatives  $\dot{\delta}$  (middle) and  $\ddot{\delta}$  (bottom). Red dashed lines indicate when filtering is activated.

perspective, Figure 6.11 shows that course-keeping performance is not impacted once the filter is introduced in the control loop, since similar course oscillations (with amplitude within  $15^\circ$ ) are observed before and after the application of the rudder signal filter at time  $t = 265$  s.

## 6.7 Discussion

This chapter discussed the validation of a nonlinear WEF estimator, which is tested on experimental data collected by a 5 meters long wave-propelled USV during field campaigns in the fjord and in the ocean. The estimated WEF is compared to the dominant frequency obtained with FFT, used as ground truth, and to the average frequency observed in the USV's heave measurement. Offline experimental results prove the ability of the observer to identify the dominant frequency in different waves spectra (ocean and fjord). Online use of the estimator onboard the USV is shown and experimental results clearly indicate the benefits of using the discussed

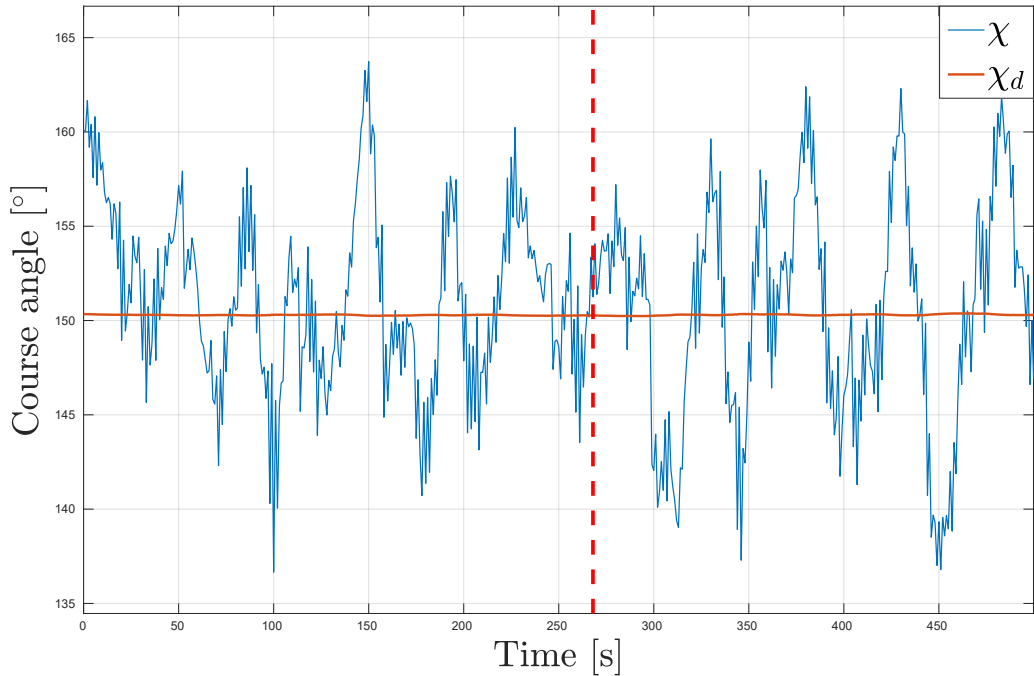


Figure 6.11: Measured ( $\chi$ ) and desired ( $\chi_d$ ) course over ground, before and after filtering (red dashed line).

algorithm for wave filtering of the rudder command from the course-keeping autopilot.

The obtained results show the benefits of using the WEF estimator for the computation of the dominant frequency of wave encounters, due to its lower computational needs as compared to FFT and search for local maxima in the heave measurement. Moreover, the use of the estimated WEF for wave filtering of the rudder command implies a significant suppression of the USV's rudder motions at higher frequencies. However, this does not involve an amplitude reduction in the rudder's commanded angles, allowing the onboard controller to maintain course-keeping performance. On the other hand, significant reduction of wave-induced motions of the servo reduces wear and stress while increasing the mechanism lifetime.

Sustained autonomous control is still an open challenge and even more so under the highly dynamic environmental changes experienced by an USV. Commanded and generated plans would likely be invalid during sustained exploration, relying on shore-based operators for support with new or modified mission goals. This, together with the fact that communication with shore could be sporadic and costly over expensive satellite links, motivates the need for the system to be self aware, robust to operational risks and failures, and therefore capable to generate its own

goals. In this chapter we indicate how the estimated WEF can additionally be used onboard a small USV to increase its situational awareness about the environment, by merging this knowledge with onboard sensors measurements and eventually re-planning the USV's intended route.





## Chapter 7

# Anti-Collision and anti-grounding system

### *Design and experimental validation of a ENC-based approach*

This chapter is based on the accepted conference article [136].

The unpredictability of the environment, the low speed and the limited maneuverability that characterizes wave-propelled USVs motivate the need of monitoring continuously both static and dynamic obstacles at sea. Detailed knowledge of the surrounding environment and vessels is important in order to maximize safety and ensure risk-free operations in both the near and distant future. While the knowledge of surrounding vehicles can be acquired with the automatic identification system (AIS) and radars, marine vessels usually rely on Electronic Navigational Charts (ENC) [137] to locate themselves with respect to land and static objects present at sea.

Anti-collision with other vessels is a well-investigated topic in the field of marine robotics [138, 139]. Typical collision avoidance systems are however developed for motored vehicles, for which course over ground and speed over ground are controllable in most of the sea states. For wave-propelled vehicles, the risk of colliding with other vessels or with static obstacles increases with the magnitude of environmental forces and the literature currently lacks of works that discuss the implementation of anti-collision and anti-grounding systems for wave-propelled vehicles.

This chapter presents an anti-grounding and anti-collision system that integrates the information contained in digital charts and AIS messages received onboard, to enhance the situational awareness as perceived by the AutoNaut, and enable

## 7. *Anti-Collision and anti-grounding system: Design and experimental validation of a ENC-based approach*

---

evasive maneuvers to avoid grounding and collisions with static and dynamic obstacles. Part of the work presented in this chapter is inspired by a collaboration between the author of this thesis and a master student at NTNU [140].

The proposed architecture merges two distinct functionalities that cooperate to ensure risk-free navigation at sea: anti-collision and anti-grounding. The first relies on the marine traffic information acquired over AIS, which is used in a scenario-based model predictive control (SB-MPC) algorithm [100] that computes optimal behaviors in order to minimize the risk of collision, grounding and damage. The employed algorithm is based on [100] and its implementations [141], [142]. Anti-grounding functionalities are instead achieved by consulting digital charts that are stored onboard the USV in the form of point clouds. Information about land and static obstacles at sea are compressed into a SQL database that contains precise indication of their location. Moreover, the databases contain depth contours (e.g., 10 meters depth contour) that are used to keep the adequate clearance from obstacles and avoid damage of the underwater propulsion system and sensors. The advantages of storing the information in databases are that fast SQL queries enable information retrieval in the order of milliseconds and that the onboard storage space required is minimal (e.g.,  $\approx 1\text{GB}$  for an area of  $12.000\text{ km}^2$ ).

Unlike the simulations and field experiments performed in [141] and [142], in this work there is additional focus on the environmental conditions and the implications that rough weather can have during scenarios with potential collisions and grounding. In particular, we focus on the effects that winds, waves, surface currents and coastal bathymetry have on the choice of an optimal control behaviour during a hazardous scenario. This is already partially investigated in [143], where the effects of wind are introduced in the cost function and increase the grounding risk if land is found in the wind direction. In our work, additional environmental terms (e.g., currents and surface waves) are also included in the optimization process of the SB-MPC algorithm, resulting in a pure anti-grounding system when the USV is close to land or to static objects but no vessels are in the surroundings.

This chapter describes the interaction between the two functionalities from a theoretical point of view. Limitations and benefits are described with a set of simulations and field experiments that validate experimentally the theoretical considerations.

## 7.1 MPC strategy for anti-collision & anti-grounding

A wide range of control algorithms for ship collision avoidance are nowadays found in the literature [144, 145]. Despite many of them implement compliance with the main rules of COLREGS, they generally do not scale very well to handle a high number of obstacles in dense traffic and accurately take into consideration the dynamics of the ship, steering and propulsion system, as well as environmental disturbances such as winds and ocean currents.

Model Predictive Control (MPC) is a powerful control method that can be used to compute an optimal trajectory based on predictions of the obstacles' motion, and account for their uncertainty. It is demonstrated that this method supports both the employment of a nonlinear dynamic vehicle model including environmental forces, but also a formalization of risk, hazard and operational constraints and objectives as a cost function and constraints in an optimization problem [100]. MPC has in fact been extensively employed for collision avoidance in automotive vehicles [146], underwater and ground vehicles [147, 148], and aircraft traffic control [149].

While numerical optimization methods can be used to compute optimal trajectories, the main challenges are related to the convergence and computational complexity of the optimization itself. In fact, complex scenarios may lead to non-convex optimization formulations which may be affected by local minima. This, and the fact that real-time implementation requires low latencies, makes it challenging to implement MPC algorithms for collision avoidance. For this reason, the formulation of models, trajectory parameterization, constraints, and numerical algorithms need to be carefully designed.

Higher performances and low software complexity can be achieved by limiting the optimization process of MPC over a finite number of control behaviors, based on a comparison of the cost, feasibility and risk that they involve [150, 151].

This work makes use of a MPC algorithm that considers a relatively small number of control behaviors that are parameterized as course over ground offsets. Since numerical optimization and the associated computation of gradients that is inherent in conventional MPC are avoided, the degrees of freedom available for control are reduced. This means that the set of alternative control behaviors must be carefully designed in order to achieve the required control performance of the collision avoidance system and COLREGS compliance. The main objective of the original implementation of the scenario-based MPC (SB-MPC) is to compute modifications to the desired course ( $\chi_d$ ) and speed ( $u_d$ ) that lead to a COLREGS-compliant USV trajectory. Since the AutoNaut's speed cannot be controlled, this work only considers course offsets. While the obstacle's future motion is predicted as a straight-line trajectory, this formulation focuses on a hazard minimization criterion (i.e., a cost function) that considers dynamic obstacles and COLREGS compliance. Un-

like previous works that make use of the same optimization principles [138, 139], this analysis integrates anti-grounding functionalities. To this purpose, the original algorithm is extended to include knowledge about land and static obstacles (e.g., buoys, beacons, islands, permanent or temporary installations). It is demonstrated that the extended algorithm provides efficient anti-collision and anti-grounding functionalities, that can operate at the same time and result in evasive maneuvers to avoid both static and moving obstacles. Finally, the integration of environmental factors allows the algorithm to choose the best control behavior that keeps the USV far from ground in case of high sea states, minimizing the risk of damaging the vehicle.

The proposed system is designed in way that allows anti-collision and anti-grounding functionalities to operate together or independently. This choice is motivated by the fact that, for example, operations in the open ocean might not require computational efforts to retrieve bathymetry. However, fjords can be congested and their coastlines are usually jagged.

As previously mentioned, the main objective of the SB-MPC algorithm considered in this work is to compute modifications to the desired course ( $\chi_d$ ) that lead to a safe, COLREGS-compliant USV trajectory. In this case, safety is not only related to risk-free navigation with respect to other vessels, but also with respect to grounding and static obstacles at sea.

A scenario in the MPC is defined by the current state of the USV, the trajectories of obstacles, and a candidate control behavior [100]. As already found in previous related works [141], the following course offsets are evaluated and assumed to be fixed on the prediction horizon:  $\chi_{ca} \in [-90, -75, -60, -45, -30, -15, 0, 15, 30, 45, 60, 75, 90]$ . The course modification is in turn applied to the desired course ( $\chi_d$ ) from the guidance system to obtain a course command (i.e.,  $\chi_d = \chi_d + \chi_{ca}$ ). This parametrization leads to a total of 13 possible scenarios to be simulated and evaluated. Since the obstacles' trajectories must also be predicted, the computational complexity depends on the number of scenarios, of obstacles and on the chosen prediction horizon.

### 7.1.1 Own USV model

A model of the USV is necessary to generate the trajectories to be evaluated by the cost function. At the time of the experiments, the full nonlinear dynamic model of Chapter 4 was not available yet. For this reason, this analysis assumes that the trajectory computed with the kinematic equations only is accurate enough. The kinematic model

$$\dot{\eta} = R(\chi)v \tag{7.1}$$

is therefore employed [72], where  $\eta = (x, y, \chi)$  denotes the position and course over ground in the earth-fixed frame,  $R(\chi)$  is the rotation matrix from body-fixed to earth-fixed frame and  $v = (v_x, v_y, r)$  denotes the velocities in surge, sway and yaw decomposed to BODY-fixed frame. The prediction of the trajectory in a scenario  $k$  is obtained by inserting the desired values into Equation 7.1. This model is however very simplistic, since it assumes no drift due to winds and currents (i.e.,  $\chi = \psi$ ). As discussed in Chapter 4, the steering performances of the USV are very much affected by the environmental forces, making this model not suited to represent the true dynamics of the USV in some cases. Nevertheless, the applicability of this model is confirmed by [101], in which both the kinematic equation and the full 3-DOF model were tested and produced only minor differences in the simulation results.

## 7.2 Environmental factors for collision avoidance scenarios

Typical scenarios encountered by the AutoNaut are in coastal environments including fjords and archipelagos that may involve multiple dynamic and static obstacles. Most importantly, situations with reduced maneuverability of the USV might occur depending on the sea state, wind and ocean currents. For this reason, the collision avoidance system needs to be aware of the prevailing environmental conditions. In order to safely navigate in these situations, informed and well-balanced decisions are needed in order to minimize the hazard and, thus, potential damage to the own vehicle and others.

### 7.2.1 Balancing operational risk with intent

The optimal solution in such complex scenarios is often dependent on the environmental conditions. If the sea is calm, there is no significant wind, waves, or current, and the seabed in the USV's surrounding coasts mainly consists of sandbanks, then cost and hazard associated to the scenario is not proportional to the perceived danger (i.e., distance to land). Therefore, in this situation, the main concern is to avoid colliding with dynamic obstacles with a clear margin and comply with the rules of COLREGS.

However, if the sea is rough, the wind and currents strong, the waves high, and there are mainly rocky shores around, navigating close to land is far more dangerous and the consequences of a grounding and damaging the vehicle are higher. In this case, avoiding ground should be a higher priority than complying with COLREGS, and in some cases, even higher than avoiding collisions with other vessels.

In order to differentiate between these situations, the following environmental factors are modeled.

### 7.2.2 Bathymetry

The bathymetry factor represents the amount of damage that is expected if the USV hits ground. The bathymetric features might differ greatly between fjords, archipelagos and other coastal areas. In this work, it is assumed that it is associated a higher cost to a steep rocky shelf than a flat sandbank because the USV would most likely suffer greater damage by colliding with the former. Information about the bathymetry and the seabed can be extracted from the ENCs. The ENCs contain the object Seabed Area (SBDARE), which contains the attribute Nature of Surface (NATSUR). NATSUR describes the surface material of the seabed and categorizes it into one or several categories, including mud, silt, sand, stone, rock, coral, and boulder. Although this information can be quite sparse, it gives an indication of the seabed conditions.

In areas with little information about the bathymetry, it is possible to use ENCs to compute the slope of the coastal shelf based on depth information and horizontal distance between the depth queries. The ENCs contain a Sounding object (SOUNDG), which are depth measurements that can be used to calculate the steepness of the underwater terrain slope towards the coastline. Despite the lack of accurate information, it is possible to assume that steep shelves are likely to be made of rocks and stony materials. The full bathymetric information will give an idea of what the underwater terrain looks like and how dangerous it would be for the AutoNaut to crash into it.

In the algorithm implementation, the bathymetry is treated as a binary term that indicates whether the shore is safe (sandy) or not (rocky).

### 7.2.3 Heave displacement

For the AutoNaut, the heave displacement and the wave height are very similar in amplitude. A large displacement in heave is associated to a higher environmental hazard because it indicates rough sea and increases the danger of damage if grounding. The heave displacement and wave height are measured directly in the onboard GNSS and/or IMU. Alternatively, the USV's pitch angle can be used.

Similarly, high waves correspond to higher environmental hazards because they make the sea shallower in the troughs, than it is indicated in the ENCs, and increase landing force to grounding. Alternatively, the wave height can also be obtained from weather forecasts. In the proposed implementation, the average heave displacement is named  $H$ .

### 7.2.4 Wind

Similarly to [143], for a scenario  $k$  the wind cost for the static obstacle  $i$  is defined as:

$$W_i^k(t) = \frac{V_w(t)^k}{d_{0,i}(t)^k} \max(0, \chi_{ca}^k \cdot \beta_w(t)^k), \quad (7.2)$$

where  $V_w^k$  and  $\beta_w^k$  are the wind speed and direction defined according to [72] and  $d_{0,i}^k$  is the distance between the USV. The dot product scales the wind force contribution toward the static obstacles in any orientation around the USV. This means that the risk increases for an obstacle to the east of the vehicle if the wind is coming from the west, etc. The dot product is positive when the angle between the USV-obstacle vector and the wind direction vector is less than  $90^\circ$ . Negative dot products are however set to zero, disregarding favorable winds with respect to perceived risks.

### 7.2.5 Sea current

Similarly, the sea current cost  $C$  is defined as:

$$C_i^k(t) = \frac{U_c(t)^k}{d_{0,i}(t)^k} \max(0, \chi_{ca}^k \cdot \beta_c(t)^k), \quad (7.3)$$

where  $U_c$  and  $\beta_c$  are the Earth-fixed current velocity and direction.

## 7.3 Risk factors & collision costs

Essentially, the algorithm computes the best control behavior associated to the worst-case hazard for each scenario, where the latter is a combination of own vehicle and predicted dynamic obstacle trajectories. The cost function indicates the hazard evaluation criterion used in the anti-collision strategy. This works adopts the main components proposed in [100] and [141].

### 7.3.1 Collision avoidance with dynamic obstacles

According to [100], the risk factor for collision with obstacle  $i$  can be defined as

$$R_i^k(t) = \begin{cases} \frac{1}{|t-t_0|^p} \left( \frac{d_i^{safe}}{d_{0,i}^k(t)} \right)^q, & \text{if } d_{0,i}^k(t) \leq d_i^{safe} \\ 0, & \text{otherwise} \end{cases} \quad (7.4)$$

where  $t_0$  is the current time and  $t > t_0$  is the time of prediction. The index  $k$  denotes a scenario associated with a single course offset belonging to  $\chi_{ca}^k \in$



## 7. Anti-Collision and anti-grounding system: Design and experimental validation of a ENC-based approach

$[-90^\circ, +90^\circ]$  leading to a trajectory with distance  $d_{0,i}^k(t)$  to obstacle  $i$  at time  $t$  under scenario  $k$ . The distance  $d_i^{safe}$  and the exponent  $q \geq 1$  must be selected large enough to follow COLREGS rules (e.g., COLREGS rule 16 that demands early and substantial give-way actions). In order to prioritize avoiding collisions that are close in time over those that are further into the future, the exponent  $p \geq 1/2$  indicates the inverse proportionality to time until occurrence of the event. Thus, the collision risk factor is higher for events close in time than for events in the more distant future.

The cost associated with collision with an obstacle  $i$  is chosen to be

$$C_i^k(t) = K_i^{coll} |\vec{v}_0^k(t) - \vec{v}_i^k(t)|^2 \quad (7.5)$$

where  $K_i^{coll}$  is the cost of collision parameter. The relative velocity of the obstacle is included, in order to minimize the consequences of a collision if a complicated situation would occur, where a collision is unavoidable.  $\vec{v}_0^k$  is the predicted velocity of the own vehicle and  $\vec{v}_i$  is the predicted velocity of the obstacle with index  $i$  in scenario  $k$ . We observe that since the own vehicle's ground speed is typically less than 3 knots, the cost associated to a collision is mostly proportional to the obstacle's speed.

### 7.3.2 Collision avoidance with grounding and static obstacles

The risk factor for grounding and collision with static obstacles, associated with each course offset  $k$  is defined as

$$R_g^k(t) = \begin{cases} \frac{1}{|t-t_0|^m} (r^k(t))^q, & \text{if } d_c^k(t) \leq d_k^{safe_G} \vee d_{\pm}^k(t) \leq d_k^{safe_G} \\ 0, & \text{otherwise,} \end{cases} \quad (7.6)$$

where  $r^k(t) = r_c^k(t) + r_+^k(t) + r_-^k(t)$  and

$$\begin{aligned} r_c^k(t) &= \frac{d^{safe_G}}{d_c^k(t)}, \\ r_+^k(t) &= \frac{d^{safe_G}}{d_+^k(t)}, \\ r_-^k(t) &= \frac{d^{safe_G}}{d_-^k(t)}. \end{aligned} \quad (7.7)$$

The distance  $d_c^k(t)$  is the distance between the own vehicle and the grounding obstacle at time  $t$  when own-ship follows the center direction  $\chi_{LOS} + \chi_{ca}^k$ , which is in the direction of the course offset that is currently being evaluated in scenario  $k$ . The terms  $d_-^k$  and  $d_+^k$  correspond the distances between the own-ship and land

locations found in the  $-15^\circ$  and  $+15^\circ$  directions, i.e.,  $\chi_{LOS} + \chi_{ca}^k \pm 15^\circ$ , and their projection onto the desired course path as defined in Figure 7.1. This is done to ensure safe navigation through narrow passages, keeping enough distance to land on the sides. Here,  $-15^\circ$  and  $+15^\circ$  are used, since this grounding data already is available for these courses. However, this can be tuned to include a wider range of directions to ensure that the distance to land in the range  $-90^\circ$  to  $+90^\circ$  is being kept larger than the safe distance to land. For collision avoidance with dynamic obstacles, the exponent factor  $p$  is used to prioritize events that are close in time over those that are further in the future and because there is an uncertainty of where the dynamic obstacle will be located in the future. For anti-grounding instead, since the obstacles and their locations are static the last argument is no longer valid. On the other hand, the USV will have more time to maneuver when looking further ahead. Nevertheless, the exponent  $m$  should have a smaller value for anti-grounding than for collision avoidance.

The cost associated with grounding is chosen to be

$$C_g^k(t) = K_g + K_{env} E^k(t) \quad (7.8)$$

where  $K_g$  is the cost of grounding parameter,  $K_{env} = [k_1, k_2, k_3, k_4]$  is a vector containing the weights for each environmental factor. The environmental factors

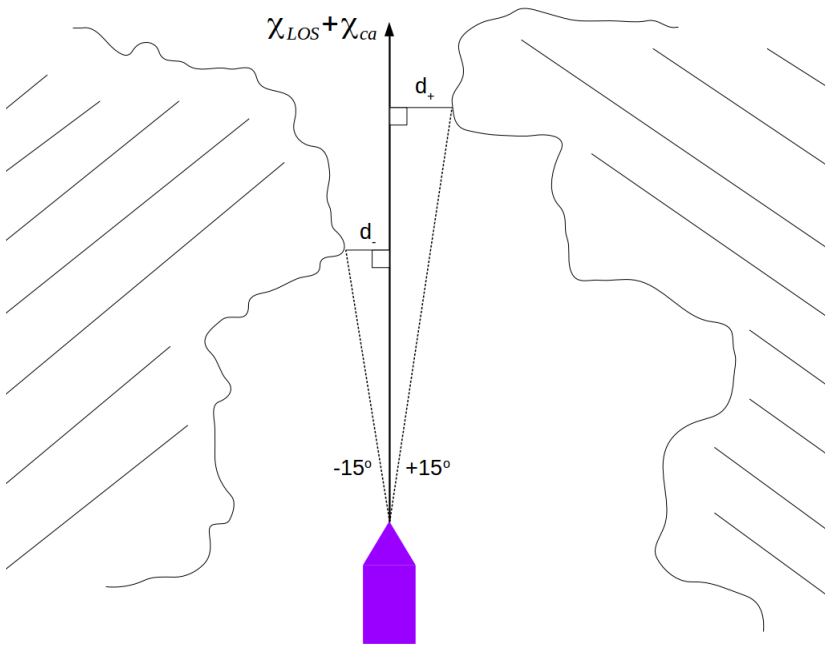


Figure 7.1: Definition of the distances used in the anti-grounding risk function.

## 7. Anti-Collision and anti-grounding system: Design and experimental validation of a ENC-based approach

---

are contained in the vector  $E^k(t) = [B, H, W(\chi_{ca}^k), C(\chi_{ca}^k)]^T$ . The velocities of the obstacle and of the own USV are not included, since static obstacles do not move and the ground speed of the USV is low.

### 7.3.3 Total environmental cost

The total environmental cost for a course offset  $\chi_{ca}^k$  is finally defined as:

$$K_{env}E^k = k_1B^2 + k_2H + k_3W(\chi_{ca}^k) + k_4C_O(\chi_{ca}^k). \quad (7.9)$$

The weights in  $K_{env}$  are tuned in simulations with a trial and error approach. Moreover, the weights can be adjusted to make some terms have a greater impact on the total cost than others, mostly depending on the current scenario and onboard measurements. The impact of large values of the bathymetry term and the heave displacement factor is emphasized by adding an exponent. The bathymetry, heave displacement, and wave height factor will give a constant cost for each course offset and will therefore only affect the trade-off between collision or grounding. The wind and current term, on the other hand, are functions of the course offset and will give different costs for different course offsets, depending on the direction of the wind and the current. For this reason, these terms will also affect the choice of the optimal course offset during pure anti-grounding situations (i.e., no surrounding vessels).

The total environmental cost of Equation 7.9 is added to the grounding cost function (Equation 7.8), and will only have an impact on the total hazard if the grounding risk for the given course offset is nonzero, i.e., there are grounding obstacles close by in the direction of the course offset.

### 7.3.4 Hazard evaluation criterion

In summary, the total hazard associated with scenario  $k$  at time  $t_0$  is

$$H^k(t_0) = \max_i \max_{t \in D(t_0)} \left( C_i^k(t)R_i^k(t) + C_g^k(t)R_g^k(t) + \kappa_i\mu_i^k(t) \right) + \lambda_i\tau_i^k(t) + f(\chi_{ca}^k), \quad (7.10)$$

where the first and second terms of the cost function are the collision hazard and the grounding hazard, respectively. As described in [100], the term  $\kappa_i\mu_i^k(t)$  is the cost of not complying with COLREGS, where  $\kappa_i$  is the tuning parameter and  $\mu_i^k \in (0, 1)$  is a binary denoting violations of COLREGS rule 14 or 15. The term  $\lambda_i\tau_i^k(t)$  is a COLREGS-transitional cost, where  $\lambda_i$  is a tuning parameter and  $\tau_i^k(t) \in (0, 1)$  is described in [141]. Finally, the fifth term is the cost of deviating from the nominal course respectively. We observe that the grounding hazard term  $C_g^k(t)R_g^k(t)$  is representing the term  $g(\cdot)$  used in [100].

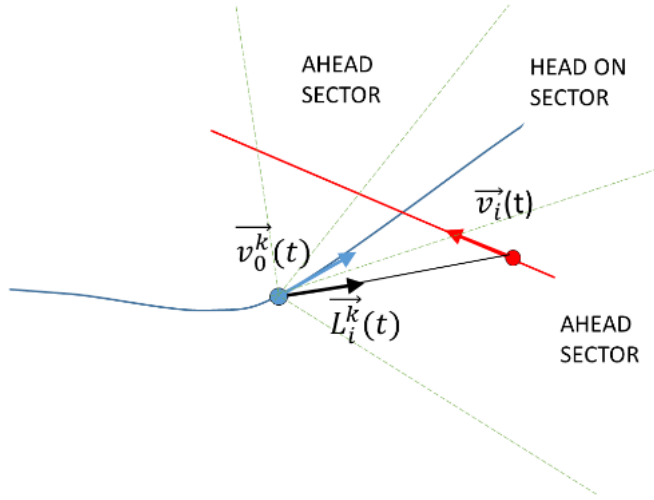


Figure 7.2: The key information used for hazard evaluation at a given future time  $t$  in scenario  $k$ . The blue and red dots indicate the predicted position of the own vehicle and of an obstacle with index  $i$ , respectively.

The selected control behavior at time  $t_0$  among the scenarios  $k \in 1, 2, \dots, N$  is the one with minimal hazard  $H^k(t_0)$

$$k^*(t_0) = \arg \min_k H^k(t_0). \quad (7.11)$$

During a potential collision scenario, this minimization is done at regular intervals of 5 seconds. In [100] it is emphasized that this optimization is “brute-force” deterministic and guarantees that the global minimum is found after a pre-defined number of cost function evaluations.

## 7.4 Scenario definitions

As in agreement with [100], four different scenarios are defined depending on the obstacle’s position relative to the own USV (the AutoNaut in this case). According to Figure 7.2, a scenario is named:

- **CLOSE:** if obstacle  $d_{0,i}^k(t) \leq d_i^{cl}$ , where  $d_{0,i}^k(t)$  is the distance between AutoNaut and obstacle  $i$  for scenario  $k$ . This distance  $d_i^{cl}$  is the largest distance where the COLREGS rules will apply.

## 7. Anti-Collision and anti-grounding system: Design and experimental validation of a ENC-based approach

---

- **OVERTAKEN:** the AutoNaut is overtaken by the obstacle if the obstacle has higher speed, is CLOSE to the AutoNaut and

$$\vec{v}_0^k(t) \cdot \vec{v}_i(t) > \cos(\phi_{ahead})|\vec{v}_0^k(t)||\vec{v}_i(t)|, \quad (7.12)$$

where  $\vec{v}_0^k$  is the predicted velocity of the AutoNaut and  $\vec{v}_i$  is the predicted velocity of the obstacle with index  $i$  in scenario  $k$ .

- **STARBOARD:** the obstacle is starboard of the AutoNaut if the bearing angle of  $\vec{L}_i^k(t)$  is larger than the heading angle of the vessel.  $\vec{L}_i^k$  is a unit vector in the LOS direction from the AutoNaut to the obstacle with index  $i$  in scenario  $k$ .

- **HEAD-ON:** the obstacle is head-on if it is CLOSE to the AutoNaut, and the obstacle's speed  $|\vec{v}_i(t)|$  is not close to zero and

$$\begin{aligned} \vec{v}_0^k(t) \cdot \vec{v}_i(t) &< -\cos(22.5^\circ)|\vec{v}_0^k(t)||\vec{v}_i(t)| \\ \vec{v}_0^k(t) \cdot \vec{L}_i^k(t) &> \cos(\phi_{ahead})|\vec{v}_0^k(t)| \end{aligned} \quad (7.13)$$

- **CROSSED:** the obstacle is crossed if it is CLOSE to the AutoNaut and

$$\vec{v}_0^k(t) \cdot \vec{v}_i(t) < \cos(\phi_{ahead})|\vec{v}_0^k(t)||\vec{v}_i(t)|, \quad (7.14)$$

where the value of the angle  $\phi_{ahead} = 68.5^\circ$  is selected to define where an obstacle is said to be ahead of the AutoNaut.

## 7.5 Hydrographic data extraction & transformation

The anti-grounding system developed in this work is based on digital charts (ENCs), which are vector-based electronic maps that contain all information necessary to conduct safe navigation at sea. The employed S-57 digital charts is provided by the Norwegian national hydrographic offices [152] for the International Hydrographic Organization (IHO). The provided maps follow the IHO standard S-57 for transfer of digital hydrographic data.

To store and use the *a priori* geographic information on the USV, a local SQLite [104] database was created. The SQLite database was chosen because it does not require connection to a server, and because DUNE already contains the necessary libraries. Another benefit is that it's a very light-weight database, since it stores the entire amount of information in a single file. As the SQLite is a relational database (see Chapter 3), it was decided to structure the information in a way

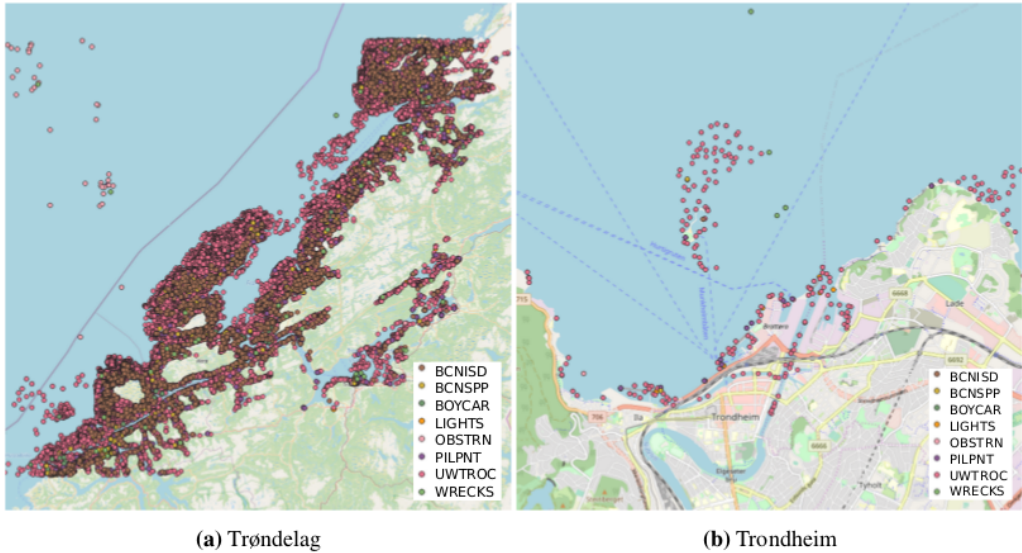


Figure 7.3: Features of interest extracted using FME. Figure obtained from [153].

that would allow easy categorization of i) static objects at sea (e.g., buoys, beacons, peers, etc) and ii) areas. Whereas the first category is represented by pairs of (latitude,longitude) locations, the second category is represented by polygons that are stored as 2-D grids or as a collection of vertices locations.

### 7.5.1 Extracting locations of interest from S-57 ENC

Treating the data contained in S-57 ENCs can be done in several ways. In this work, the FME suite<sup>1</sup> was used, given its simple interface and the SQLite3 support already integrated. The ENCs contain multiple features<sup>2</sup> (e.g., BOYCAR, BCNSPP, BCNISD) as point data that are of interest for an autonomous vehicle (see an example in Figure 7.3).

In the S-57 ENC, there is an object (DEPARE) representing the depth of the queried area. This is the most useful feature for navigational use, since from that one could infer the coastline and the depth of shallow waters. The DEPARE object represents the depth between an upper and lower bound, namely DRVAL2 and DRVAL1. For navigational use, DRVAL1 can be assumed to be the shallowest depth expected at a certain location. FME was used to create two-dimensional grids with the desired attributes from polygons in the DEPARE ENC object. The result was saved as a table in a SQLite database. FME also allows to change the resolution for certain

<sup>1</sup><https://www.safe.com/fme/>

<sup>2</sup><http://www.s-57.com/>

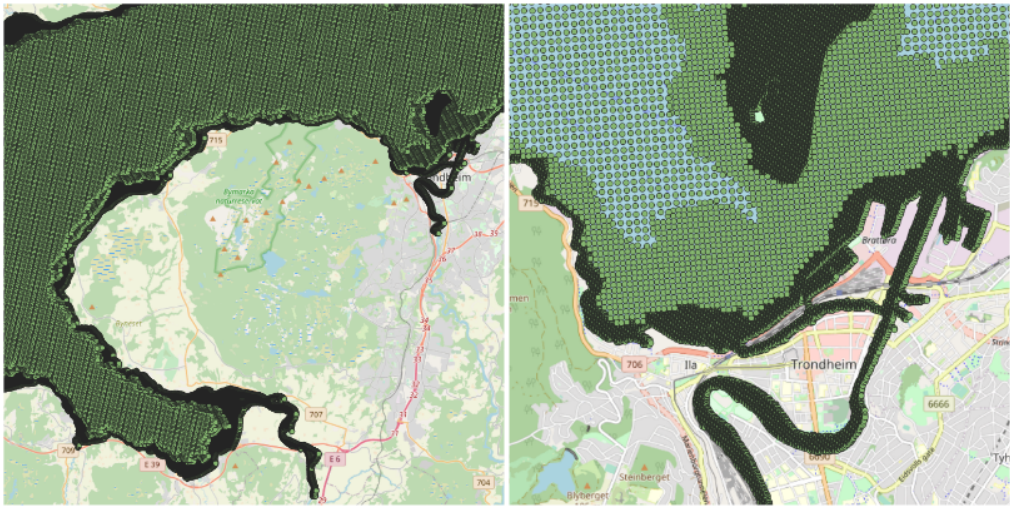


Figure 7.4: Two-dimensional grids with different resolutions. Figure obtained from [153].

depth intervals. For example, it is possible to have a higher resolution in these areas close to the coastline than in the open sea, where there is less danger of grounding. An example shown in Figure 7.4, where a 10 meters spatial resolution between queried locations is obtained in areas with  $DRVAL1 \leq 20$  m, and a 50 meters resolution is obtained for the locations with  $100 \text{ m} > DRVAL1 > 20$  m. Areas with  $DRVAL1 \geq 100$  m have a resolution of 75 meters.

### 7.5.2 Extracting the vertices of S-57 polygons

The two-dimensional grids uses a lot of storage, and searching for the desired area in the data also becomes computationally expensive. The approach of extracting only the vertices of the polygons is explored. This means that the vehicle only gets to know the boundaries of static obstacles or areas present at sea. For the DEPART object, this means that the software onboard the USV can only observe the depth contours as it explores an area with different depths. This is considered to be enough for implementing anti-grounding functionalities. For further reducing the amount of data handled with this method, just including the depth ranges that are interesting can be done. For the purpose of anti-grounding, depths above a certain threshold can be ignored, because the USV is only interested to know if it is heading towards a shallow area.

For both the two dimensional grids and for the DEPART vertices, finding the bal-



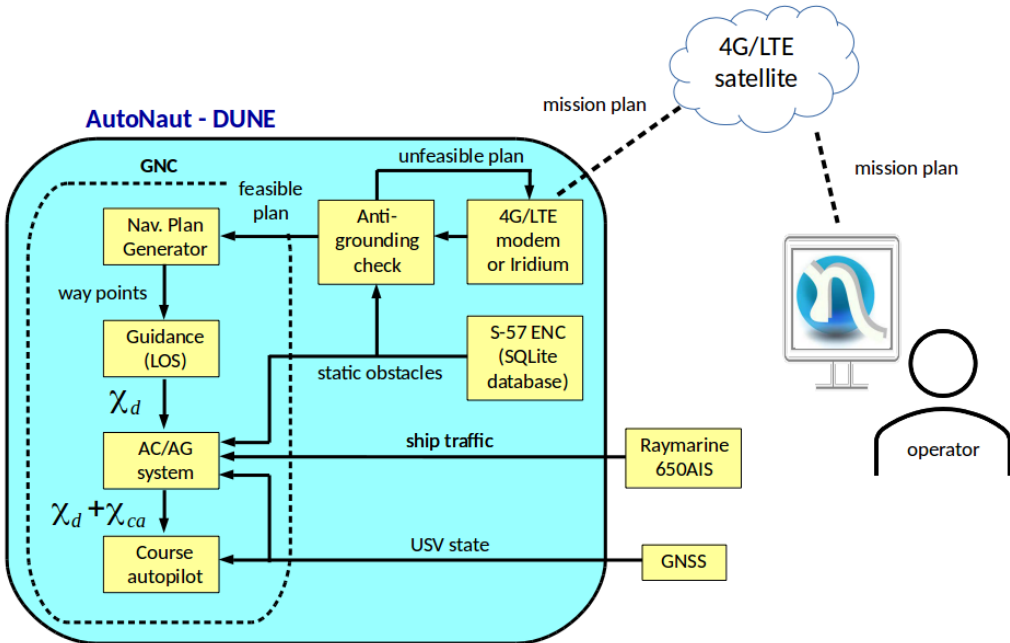


Figure 7.5: Designed software architecture including anti-collision (AC) and anti-grounding (AG) functionalities.

ance between spatial resolution and the amount of data is an important topic. On the one hand, better resolution will lead to smaller features such as narrow portions of the navigable area being detected. On the other hand, higher resolutions will make searching the data slower, and for motion planning on the two-dimensional grid, path planning is made more computationally expensive. The master thesis [153] contains more considerations about the performances of the employed method.

## 7.6 Architecture design

The method employed in this research is based on the second approach, i.e., the digital bathymetric information stored in the database uses the vertices extraction method presented above. The information contained in the database is queried with SQL queries implemented in DUNE's C++ environment.

Figure 7.5 shows the designed software architecture. A navigation plan is commanded from shore based on the available communication link. The plan is received onboard the USV and a dedicated software digests it. A preliminary evaluation of the commanded plan is performed, and each plan is categorized as feasible



## 7. Anti-Collision and anti-grounding system: Design and experimental validation of a ENC-based approach

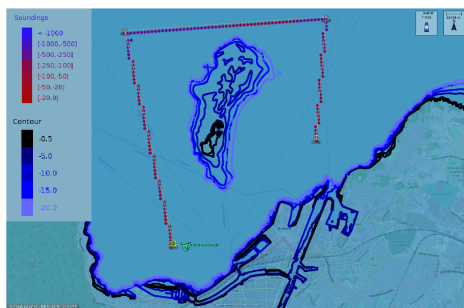


Figure 7.6: Trondheim's coastline, depth contours around Munkholmen.

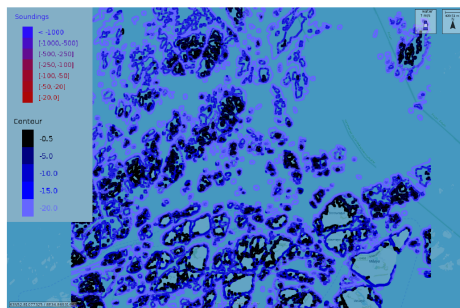


Figure 7.7: Islands and rocks surrounding Mausund.

or infeasible. A plan is infeasible if, for example, the path that connects multiple desired locations crosses land, islands, or static obstacles contained in the database. Also, a navigation plan is considered infeasible if the commanded path makes the USV navigate too close to static obstacles. A set of parameters have been established for determining when a plan is considered unsafe. In that case, the software replies with a warning, that is sent back to the operators. A plan that is considered safe is instead forwarded to the GNC unit and the vehicle can start executing the plan. As it navigates, the software will periodically assess the mission safety, by computing the USV's position with respect to the queried digital information. The periodical queries extract database information in a surrounding of the USV, so new information is provided as the USV moves. This is essential, since the navigation performances of the AutoNaut are highly dependent on the sea state and, environmental forces may cause the USV to drift from the original path which was initially considered safe. This means that a mission can initially be evaluated as safe and, during its execution dangers appear and the plan is not safe anymore. Also in this case the operators are notified through the available communication link. Figures 7.6 shows the initial evaluation of mission plan commanded from shore. The plan involves three way points around the Munkholmen island, starting from the initial USV's location. The figure represents the knowledge that the USV has about land and depth contours. The same situational awareness might not be available to the operators on shore, which motivates the importance of the developed system. Bathymetric information is displayed in the form of point clouds, whose color is defined based on the depth of the seafloor in the considered location. Moreover, Figure 7.6 also shows how the software evaluates the safety and feasibility of a commanded navigation plan: the path connecting the target locations is queried and the depth along it is retrieved. By checking the depth

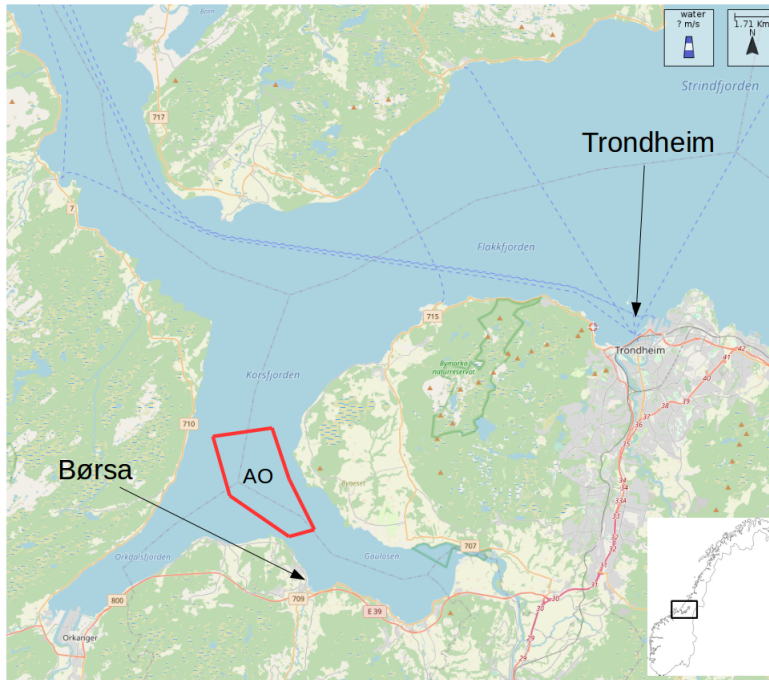


Figure 7.8: Area of operation of the field tests in December 2019.

soundings along a commanded path, the software becomes aware of the obstacles that it may be in its proximity. In this way, it is able to halt the execution of a mission in which the target destinations or the paths that connect them are not in safe, navigable waters.

Figure 7.7 confirms the importance of the proposed tool. The area considered in the figure is surrounding Mausund, an island part of the Froan archipelago, a few kilometers north of Frøya (Central Norway). The archipelago contains a myriad of small islands reefs and rocks that can reach the sea surface depending on the tide. As presented in other chapters of this thesis, some operations were based on the Mausund islands and the USV had to navigate in the dangerous waters depicted in Figure 7.7. Knowledge of the precise location of each island was important, especially if one considers the low maneuverability of the AutoNaut.

## 7.7 Results

The results presented in this chapter are a combination of field tests and simulations. In the first section below, pure anti-collision functionalities are presented and discussed. Then, the anti-grounding system is evaluated with a set of simula-

## 7. *Anti-Collision and anti-grounding system: Design and experimental validation of a ENC-based approach*

---

tions. Finally, anti-collision and anti-grounding functionalities are tested together and the results are discussed. Eventually, the onboard control architecture of the USV will benefit of both systems in order to ensure safe navigation when other vessels, land and/or islands are in the surroundings of the AutoNaut. Furthermore, the simulations indicate that it is possible to include the state of the environment in the algorithm's optimization process in order to enhance the mission's safety.

### 7.7.1 **Anti-collision with dynamic obstacles**

The collision avoidance algorithm was tested for the first time on the field in December 2019 in Børsla, 20 km south-west of Trondheim. Børsla is a small town situated in a branch of the Trondheim Fjord, as depicted in Figure 7.8. This area was chosen mainly because of the available infrastructure at the Marina of Børsla and because of the very little marine traffic in the area. In this first experiment, the tested collision avoidance involved only dynamic obstacles at sea, i.e., other vessels. At the time, no vehicles with AIS were available to be used as obstacles and a hybrid solution had to be found in order to create collision scenarios and test the implemented algorithm. The experiment lasted two consecutive days. On the first day, some virtual obstacle vessels were simulated on the operator's laptop onshore and the local network created on the laptop was shared with the USV. Doing so, the AutoNaut was perceiving the virtual obstacles as if they were actually real vehicles navigation at sea. This concept is shown in Figure 7.9. An instance of DUNE is run on the operators' laptop, where vehicles acting as obstacles for the collision scenarios are simulated. The operators are in this way capable of simulating motored vessels and deciding their speed and direction. The simulated vessels are set to transmit a fake AIS message (IMC::AIS) over the closed network at regular intervals, in way that emulates actual vehicles at sea. The AutoNaut transmits its telemetry back, so that the operators can observed the mission in Neptus. The simulated message contains both their static and dynamic information, usually encapsulated in AIS messages 1, 2, 3 and 5<sup>3</sup>. While AIS messages of type 1, 2 and 3 contain navigational information (e.g., location, ground speed, heading, navigation status, etc), type 5 messages contain static information about the ship as ship's length, width, draught, as well as the ship's intended destination. Whereas dynamic information (types 1, 2, 3 messages) is used by the collision avoidance algorithm to predict the ship's state and trajectory, the notion of its size (type 5 messages) is used to let the AutoNaut keep the appropriate clearance.

The onboard software monitors the vessels transmitting AIS messages in the 5000 meters surrounding the AutoNaut. When a potential collision scenario is identified, the collision avoidance algorithm runs at an interval of 5 seconds. This is

---

<sup>3</sup>[https://en.wikipedia.org/wiki/Automatic\\_identification\\_system](https://en.wikipedia.org/wiki/Automatic_identification_system)

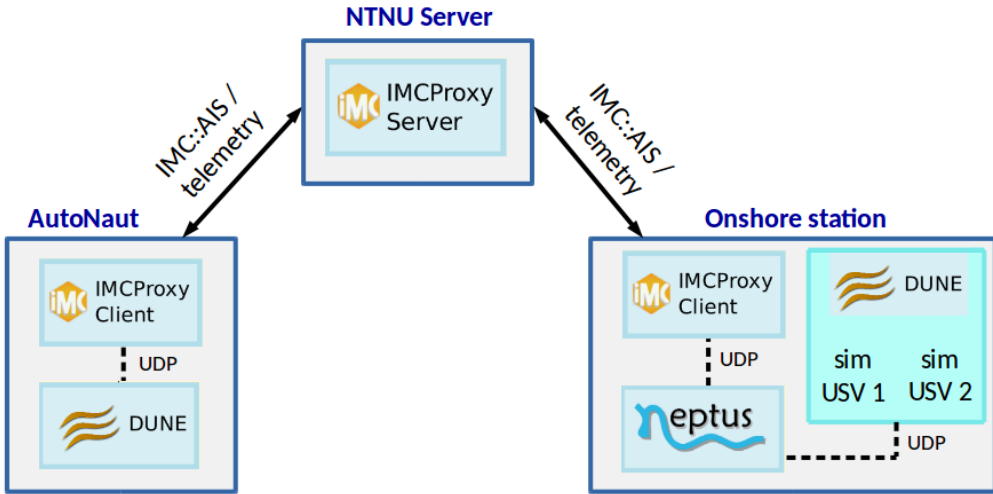


Figure 7.9: Hybrid testing: virtual obstacles are simulated on the onshore computer and shared with the AutoNaut via the IMCProxy while it operates in the field.

	Symbol	Value
Prediction horizon	$H$	600 s
Time step	$T$	5 s
Max. obstacle surveillance range	$d^{max}$	5000 m
Disappeared obstacle	$T_{max}$	240 s
SB-MPC surveillance range	$d^{sbmpc}$	700 m
Minimal safe distance to vessels	$d^{safe}$	300 m

Table 7.1: Collision avoidance algorithm parameters.

considered enough, given the slow dynamics of the USV. However, if the distance between the AutoNaut and one or more obstacles drops below a defined safety threshold, this interval is reduced.

Table 7.1 contains the parameters that are used in this initial test, which happened on 12th of December 2019. The obstacle's and AutoNaut's states are evaluated with a time step  $T = 5$  s over a prediction horizon  $H$  of 600 seconds. The software

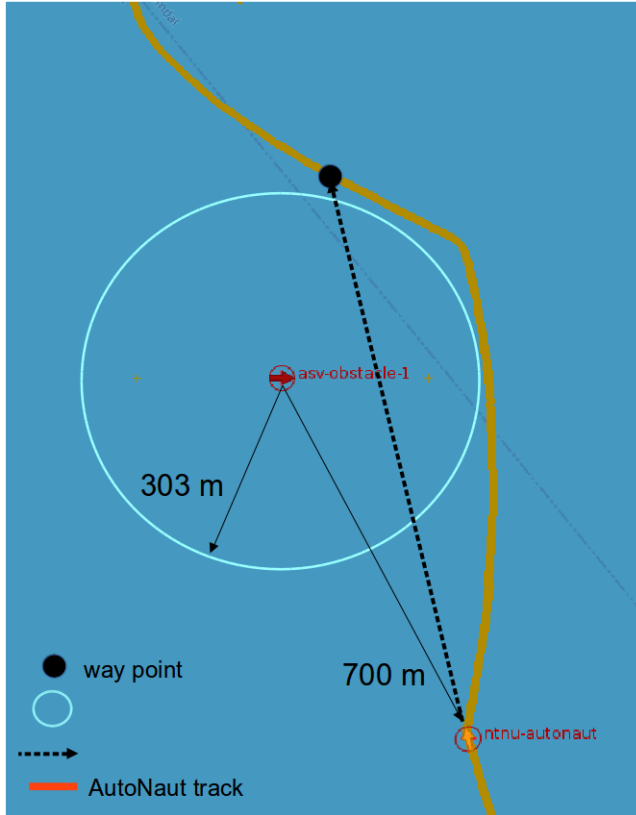


Figure 7.10: Head-on scenario with a static obstacle.

remembers the vessels in the  $d^{max}$  range up to  $T_{max} = 240$  s, period after which the potential obstacles which do not update their state via AIS are discarded from the monitored list. The algorithm actually considers an obstacle as a potential threat when its distance to the AutoNaut drops below  $d^{sbmpc} = 700$  m, meaning that action will be taken within this range if a potential collision is predicted. This range was chosen given the limited width of the fjord in the test area. A larger range should be used when the USV operates autonomously in open waters: given its slow dynamics it is desirable to perform safety maneuvers well in advance. The algorithm classifies the scenario according to the definitions in Section 7.4.

The first presented field test is a simple head-on scenario in which the obstacle is not moving. This is the simplest possible head-on scenario, since the obstacle speed is zero. The USV navigates from South to North with a desired course  $\chi_d = 355^\circ$  towards a desired way point, as shown in Figure 7.10. When the distance between the USV and the obstacle reaches 700 meters the SB-MPC algorithm decides to apply an offset  $\chi_{ca} = +30^\circ$  so that the new desired course used as reference for

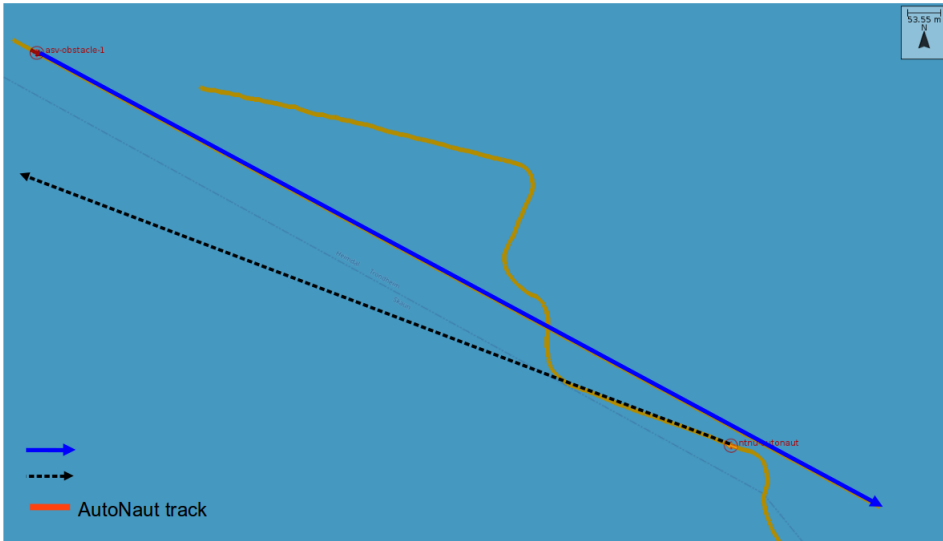


Figure 7.11: Head-on scenario with a moving obstacle.

the control becomes  $\chi_d = 25^\circ$ . This offset is re-evaluated at each algorithm iteration until the offset becomes  $\chi_{ca} = 0^\circ$  again. This can be clearly noticed as the USV takes a port turn and heads straight to the desired location. During the evasive maneuver, it can be observed that the minimum distance between the AutoNaut and the obstacle is approximately the desired one ( $D_{min} = 303$  m). The same result would be achieved if the static obstacle was a buoy, a beacon or, for example, a permanent or temporary installation at sea as long as its information is contained in digital S-57 charts.

The second tested scenario is a head-on scenario in which the obstacle is moving towards the AutoNaut. In this experiment, the simulated obstacle has a ground speed of approximately 1.3 m/s and a course of  $118^\circ$ , as depicted in Figure 7.11. Similarly to the previous experiment, when the distance between the two vehicles drops below 700 meters, the collision avoidance algorithm commands a positive course offset  $\chi_{ca} = +60^\circ$ . The new desired course becomes  $\chi_d = -2^\circ$ . It can be noticed that a larger course offset is commanded, since COLREGS rule 14 state that in a head-on scenario a vehicle is expected to turn starboard in order to avoid the other one. Once the AutoNaut is located on the port side of the obstacle the offset is set to  $\chi_{ca} = 0^\circ$  since the algorithm expects that also the other vessel is taking the necessary action. However, the obstacle does not comply with the COLREGS regulations and keeps a constant speed and course. The algorithm computes therefore a  $0^\circ$  course offset in order to avoid the collision and try keeping the desired minimal safety clearance to the obstacle. The minimal distance between the

## 7. Anti-Collision and anti-grounding system: Design and experimental validation of a ENC-based approach

---

USV and the obstacle is approximately 200 meters. Once the obstacle has passed, the AutoNaut resumes nominal navigation towards the desired destination. In the third experiment, the obstacle is in the port ahead sector (see Figure 7.2 and Figure 7.12), i.e., the obstacle see the AutoNaut on its starboard side. COLREGS rule 15 states that in a crossing situation with risk of collision, if one vessel can see another vessel on its starboard side, the former has to give way. In same situation, the vessel that has the other one on its port side is the stand on vessel. In other words, the simulated obstacle is expected to take a starboard turn in order to avoid colliding with the AutoNaut. In the test, this does not happen, and when the distance between the two vehicles drops below  $d^{sbmpc}$ , the algorithm opts for a course offset  $\chi_{ca} = +45^\circ$  as shown in Figure 7.12. While the AutoNaut keeps navigating with the new course  $\chi_d = 20^\circ$ , the obstacle does not take any action to avoid collision and the collision avoidance algorithm is forced to keep the same course offset in order to avoid collision and respect the desired minimal distance. When the obstacle has passed the AutoNaut, the offset is zeroed and the USV resumes line-of-sight navigation towards the desired location. The minimum distance between the two vehicles is 330 meters.

On the second day of field trials the operational setup was further modified. In this occasion, a small motorboat named Buster was employed to act as an obstacle (see Figure 7.13). Since this boat is not equipped with a AIS system, it was decided to create again a fake message and run this in the laptop's DUNE instance. Unlike the previous experiments, this time the telemetry of the simulated obstacles was obtained by the laptop's GPS and, the operator with the laptop was passenger on the motorboat. In this way, as the boat was moving on the sea, the laptop's GPS was providing telemetry data to DUNE, which was emulating the AIS on a vessel and sharing that with the AutoNaut over the closed network. In other words, the AIS of the motorboat was emulated through DUNE and the motorboat itself was acting as a vessel transmitting AIS messages. The advantage of using this setup is that the scenario can be more flexible, i.e., it is possible to steer the Buster in order to change the scenario. The first tested scenario involves two head-on situations, in which the Buster heads towards the AutoNaut. Figure 7.14 shows the first situation. Again, the obstacle does not comply with COLREGS regulations and keeps a constant course of approximately  $115^\circ$  and speed of 3.5 m/s. This time the algorithm decides to disregard COLREGS rules as a starboard turn is likely to lead to a collision. The decided offset is therefore  $\chi_{ca} = -90^\circ$ . The minimal distance between the vehicles during this scenario is approximately 200 meters, which is the maximum clearance that the AutoNaut can impose between the two vehicles given their velocities and the provided course offsets. Once the obstacle has passed over, the USV resumes its straight-line navigation towards the desired destination. Few minutes after, the Buster was driven back to its initial location and a new head-on scenario was initiated. Figure 7.15 shows the second consecutive head-on situa-

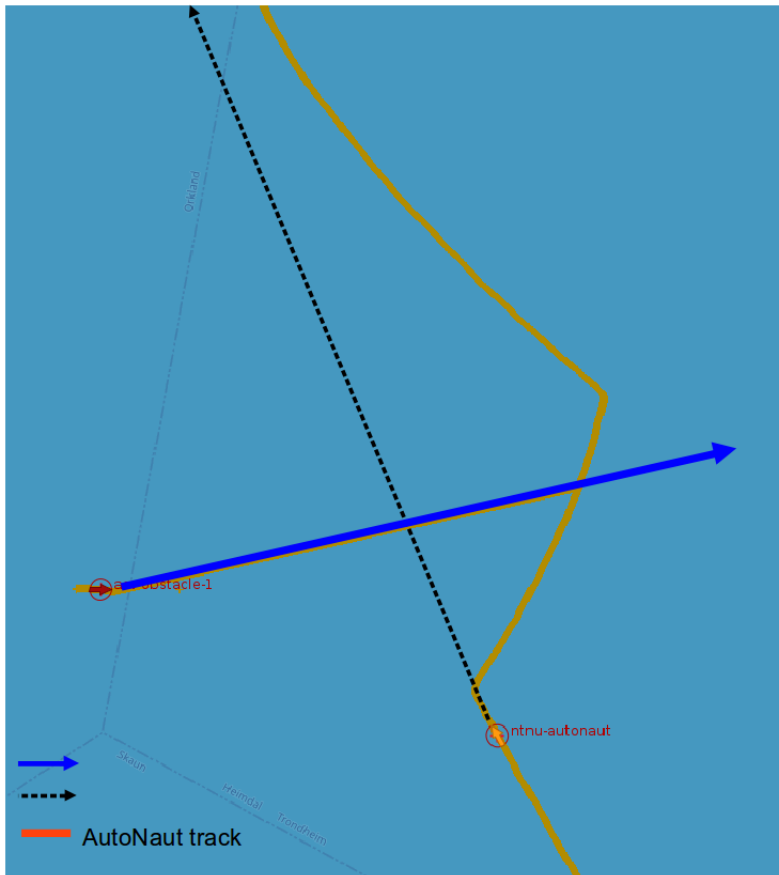


Figure 7.12: Crossing from starboard scenario with a moving obstacle.

tion. This time the AutoNaut finds itself on the port side of the obstacle’s frame, making it easier for the algorithm to choose a positive course offset.

In the last tested scenario the obstacle overtakes the AutoNaut without taking the precautions indicated by the COLREGS rule 13, which states that “any vessel overtaking any other shall keep out of the way of the vessel being overtaken”. The obstacle maintains instead its course and speed and, hence, the AutoNaut is forced to move out of its way with a starboard turn, as shown in Figure 7.16.

### 7.7.2 ENC-based anti-grounding

In this section, the results of the anti-grounding system are presented. To date, anti-grounding functionalities are only tested in simulation whose objective is to assess the feasibility and limitations of the proposed method.



7. Anti-Collision and anti-grounding system: Design and experimental validation of a ENC-based approach

---



Figure 7.13: The Buster motorboat.

	Symbol	Value
Time step	$T_g$	60 s
Max. surveillance range	$d^{max}$	5000 m
Minimum safe depth	$H^{safe}$	5 m
Minimum safe distance to land	$d_g^{safe}$	100 m
Grounding cost	$K_g$	100

Table 7.2: Anti-grounding algorithm parameters.

The anti-grounding system checks for land or static obstacles every  $T_g = 60$  s, given the low speed of the USV. In this implementation, the S-57 object DEPART (depth area) is the only object considered since from this it is possible to retrieve

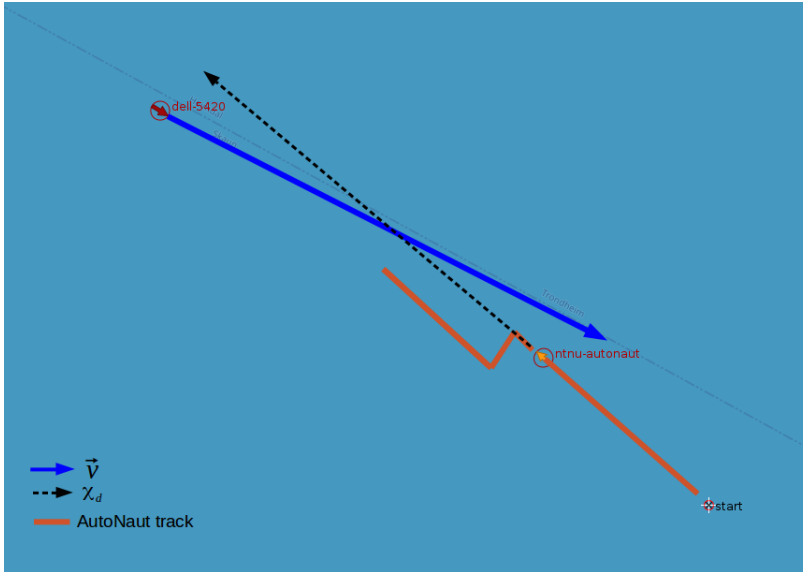


Figure 7.14: Head-on scenario involving the Buster.

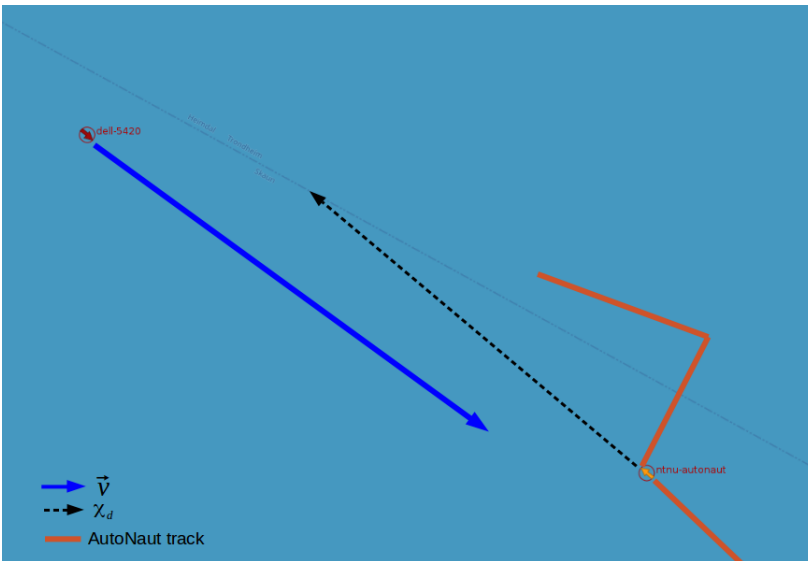


Figure 7.15: Head-on scenario involving the Buster.

the coastline as well as areas with shallow waters. Despite the database discussed previously also contains information about other static objects at sea, in this analysis the main focus is the depth contours. When the system scans the USV's sur-

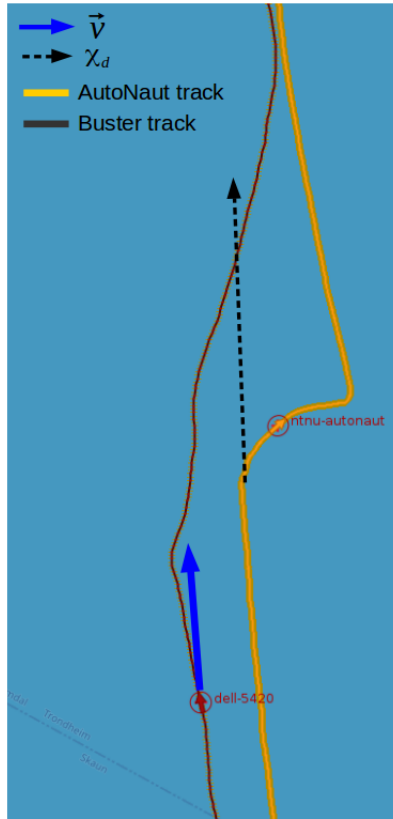


Figure 7.16: The AutoNaut being overtaken by the obstacle.

roundings, a query is made to the database containing the ENC data point clouds, asking for the depth of all the data points located within a distance of  $d^{max} = 5000$  meters from the AutoNaut, whose depth is within a specified range. For this reason, a minimum safe depth value parameter ( $H^{safe}$ ) is defined (see Table 7.2). Then, the algorithm iterates through the retrieved information in order to find the point that is the closest to the AutoNaut for each of the directions corresponding to the course offsets. This results in a new vector containing the closest data point in each course offset direction, shown as red points in Figure 7.17. Each point retrieved from the point-cloud database contains the geographic location and depth of the seafloor.

In this implementation, the SB-MPC algorithm is used for anti-grounding functionalities only, treating the land information as an obstacle that does not move. The optimization is then run as if the obstacles were moving. In other words, exactly as before, the algorithm iterates through all the possible course offsets and chooses the one corresponding to the lowest hazard, based on the associated distance to

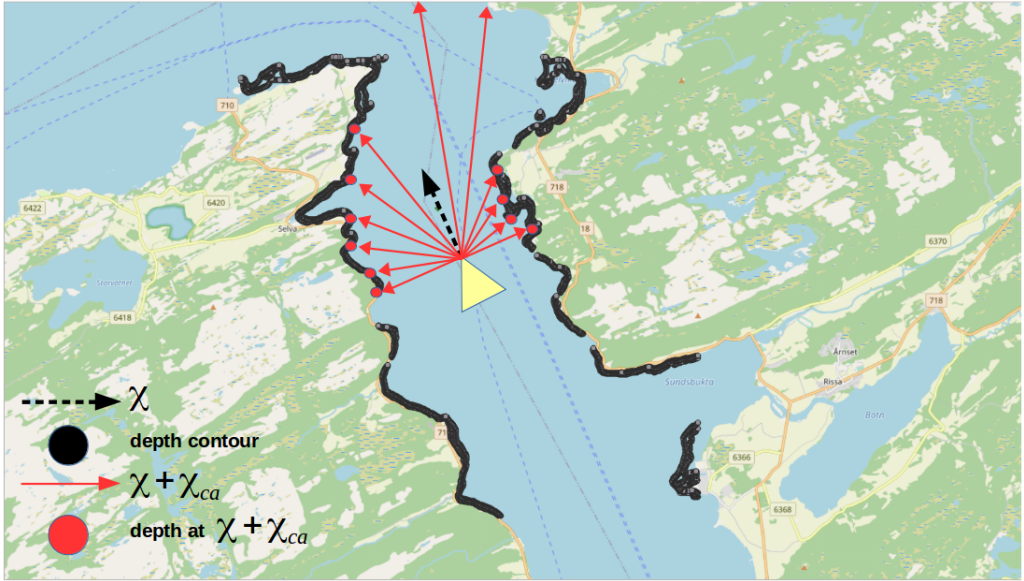


Figure 7.17: ENC data points (black) retrieved from the database in a square area around the AutoNaut. The red dots indicate the locations in the direction of the course offsets ( $\chi_{ca}$ ) relative to the USV's course ( $\chi$ ).

land along the considered offset. This is achieved by computing the risk and cost of grounding for each course offset. The chosen optimal course offset is added to the course angle from the LOS guidance law, and the modified course reference is sent to the autopilot.

From Equation 7.10 it can be deduced that the hazard in the case of anti-grounding only can be computed as

$$H_G(t_0) = \max_{t \in D(t_0)} (C_G(t)R_G(t)), \quad (7.15)$$

where  $C_G$  is the grounding cost function (see Equation 7.8) and  $R_G$  is the risk of grounding (see Equation 7.6).

In the first scenario, the AutoNaut moves straight towards the Munkholmen island (see Figure 7.18). Figure 7.19 shows how the grounding hazard evolves based on the distance between the USV and land, when environmental factors are not considered. This means that the risk evaluation is based on distance only. When the distance to land gets smaller, the magnitude of the hazard increases up to  $7 \times 10^4$ . Figures 7.20a-7.20d show the evolution of the hazard as a function of distance and of the environmental factors. Different values for wind and current velocity and direction are tested, while the remaining terms are set to constant values:

7. Anti-Collision and anti-grounding system: Design and experimental validation of a ENC-based approach

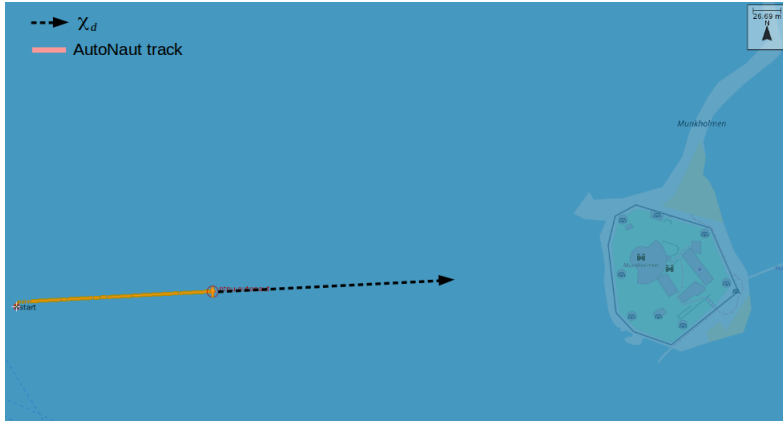


Figure 7.18: The AutoNaut moving straight towards the Munkholmen island.

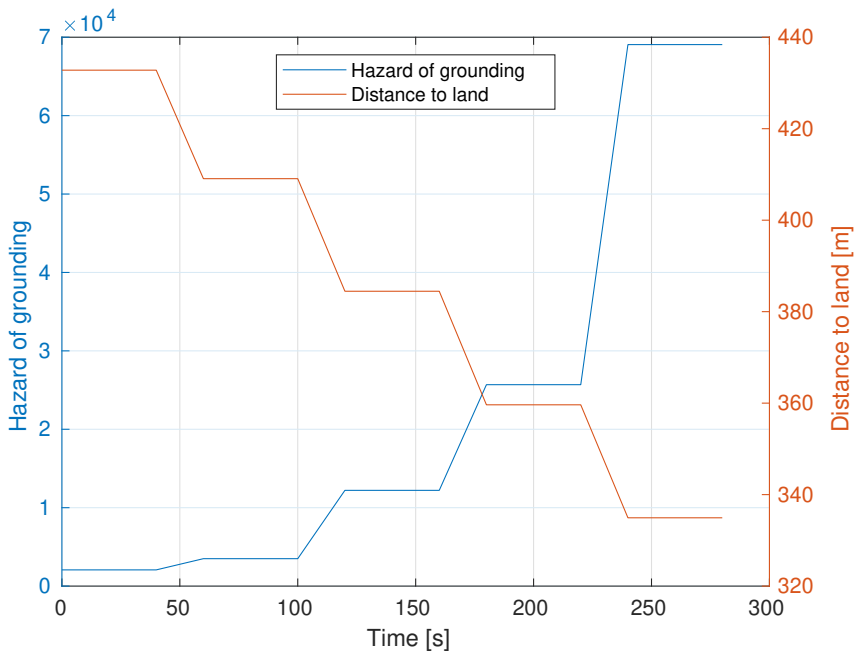


Figure 7.19: Grounding hazard and distance to land when environmental factors are not considered.

bathymetry  $B = 1.0$ , heave  $H = 2.0$  m. The given wind and current directions are the absolute directions, and the course of the AutoNaut is kept at  $87^\circ$  in all simulations. The plots in Figure 7.20a and 7.20b show that when the wind and

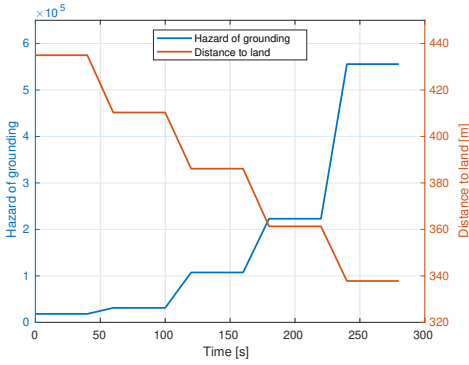
current are directed towards land, the hazard is higher. Figure 7.20b shows in fact that the hazard still increases, since the USV keeps moving towards the island, but it does not grow high since wind and sea current try to push the vehicle towards West. Similarly, in Figure 7.20c, the wind and current speeds are lower than in Figure 7.20b, but still the hazard is higher since the direction of wind and current push the AutoNaut towards Munkholmen. In Figure 7.20d, the wind and current come from the front sides of the vehicle, resulting in a smaller hazard than in Figure 7.20a, but a similar hazard as in Figure 7.20c, and higher than in Figure 7.20b. Note that the hazard has a magnitude in the size of  $10^5$  in all of the four plots shown here, which is considerably higher than in the plot without environmental cost (see Figure 7.19). This shows that the environmental factors can have a large impact on the perceived grounding hazard.

The behavior shown through these plots validates that the anti-grounding system behaves according to the theory presented. When the AutoNaut approaches land, the grounding hazard increases significantly. Adding the environmental factors results in a considerable increase in the grounding hazard, depending on the velocity and direction of wind and currents. A higher velocity leads to a larger hazard. Moreover, when the wind and current are directed towards land, the hazard increases.

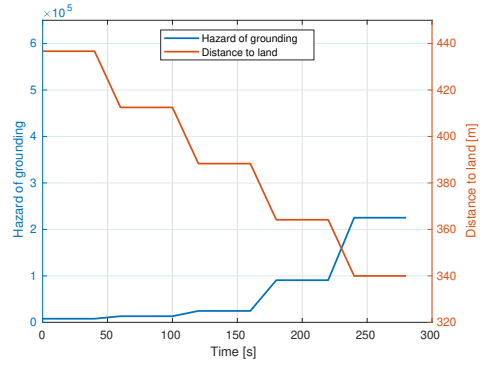
The anti-grounding system is tested in simulation. In the first simulation, the USV is commanded to a mission that involves crossing a portion of land in order to reach the target destination. If the anti-grounding system is not activated, the vehicle would just hit land (white dashed arrow in Figure 7.21). Figure 7.21 shows the depth information extracted by the algorithm. The distance to land in the direction of the course offsets ( $\chi + \chi_{ca}$ ) is provided to SB-MPC, which selects the appropriate offset needed to avoid grounding. The minimum safe distance to land is set to 100 meters, since the way point is located in a bay. The objective is that AutoNaut reaches it without getting closer to land than the minimum safe distance indicates. Instead, the minimum safe depth is set to 10 meters, meaning that the AutoNaut considers this depth as ground and wants to keep the minimum safe distance to this depth contour. The 10 meters depth contour is the dark blue contour shown in Figure 7.21.

It is important to emphasize that the anti-grounding system is a part of the reactive obstacle avoidance control system and is not intended to be used as a path planning system. Therefore, it does not aim at finding the optimal path to a way point. Even though the anti-grounding system manages to find a good solution in most of the situations, it cannot be guaranteed to work optimally. Because of its relatively short time horizon, it can get stuck in narrow passages and complex areas and not be able to find the optimal path for a longer mission.

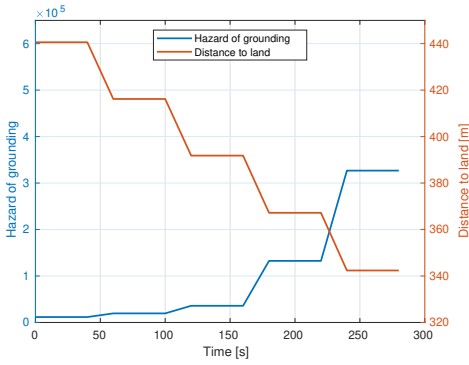
## 7. Anti-Collision and anti-grounding system: Design and experimental validation of a ENC-based approach



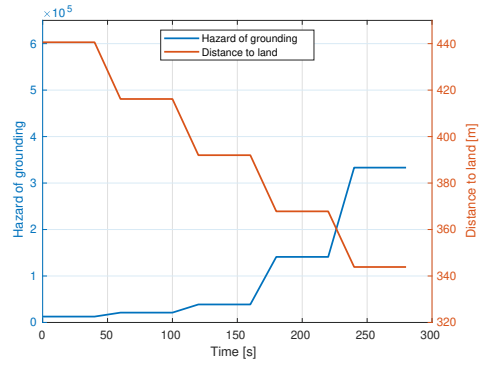
(a)  $V_w = 10.0 \text{ m/s}$ ,  $\beta_w = 90^\circ$ ,  
 $U_c = 0.3 \text{ m/s}$   $\beta_c = 90^\circ$



(b)  $V_w = 10.0 \text{ m/s}$ ,  $\beta_w = 270^\circ$ ,  
 $U_c = 0.3 \text{ m/s}$   $\beta_c = 270^\circ$



(c)  $V_w = 5.0 \text{ m/s}$ ,  $\beta_w = 90^\circ$ ,  
 $U_c = 0.1 \text{ m/s}$   $\beta_c = 90^\circ$



(d)  $V_w = 10.0 \text{ m/s}$ ,  $\beta_w = 60^\circ$ ,  
 $U_c = 0.3 \text{ m/s}$   $\beta_c = 120^\circ$

Figure 7.20: Plots of the grounding hazard and distance to land with environmental factors added, when the AutoNaut moves towards land. Different wind and current speeds and directions are tested.

### 7.7.3 Combined anti-collision and anti-grounding

In this last section, the combination of both systems is evaluated and discussed with simulations. The objective is to test the proposed system when the AutoNaut operates close to land, when environmental conditions are not favorable and other vessels are present in the vehicle's surroundings. In such situations, the algorithm should balance the risk of grounding with that of colliding with a moving vessel. The tuning of the costs are essential to guide the algorithm towards the desired behaviour. Additionally, the knowledge of sea state plays a main role in the

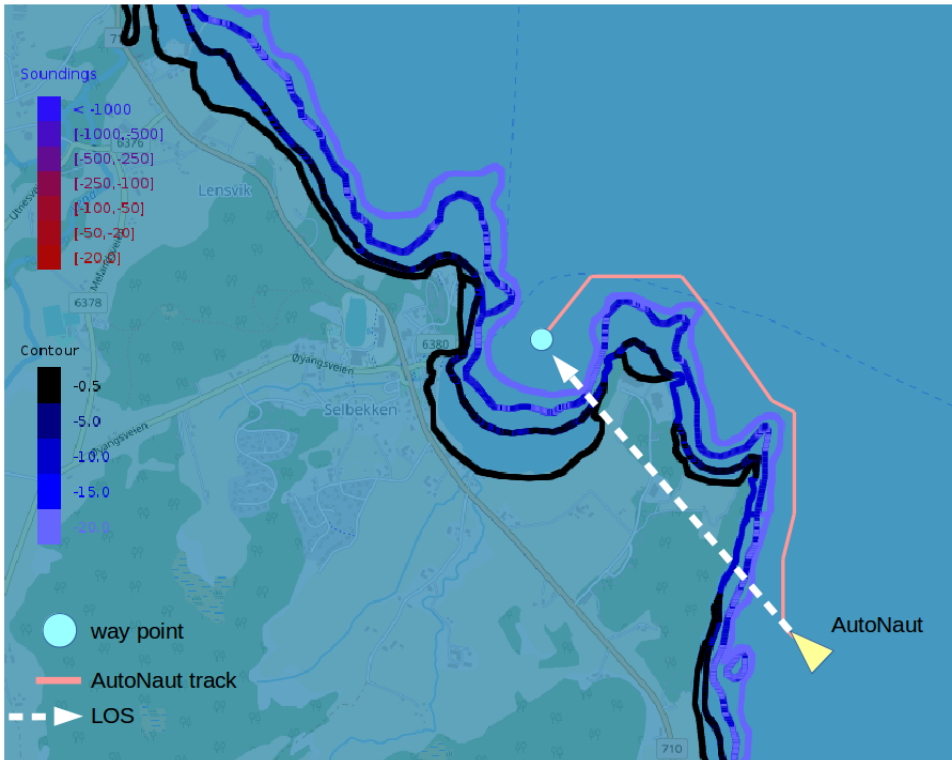


Figure 7.21: The AutoNaut avoids land by keeping a safety distance from the coastline.

control decision since grounding may be cause more or less damages depending on the state of the sea.

Figures 7.22 and 7.23 show a head-on scenario in which a simulated obstacle navigates towards the AutoNaut, without complying with COLREGS rules, at a constant speed of 13 m/s. When the anti-grounding system is deactivated (Figure 7.22), the algorithm chooses a 90° starboard turn, since this is the preferred COLREGS direction as stated in rule 14. The shortest distance between the two vehicles is 142 meters, while the shortest distance between land and the AutoNaut is about 65 meters. In this head-on scenario, the obstacle maintains a high speed and approaches the AutoNaut straight ahead, which means that the AutoNaut has too little time to react, and cannot manage to keep the minimal safety distance (300 meters), although it turns 90° starboard. When the anti-grounding system is enabled (Figure 7.23), the AutoNaut turns to port instead, to avoid getting closer to land, at the same time as it avoids collision with the obstacle. The shortest distance between the two vehicles this time is 202 meters, and the shortest distance



## 7. Anti-Collision and anti-grounding system: Design and experimental validation of a ENC-based approach



Figure 7.22: Head-on without anti-grounding activated.



Figure 7.23: Head-on with anti-grounding activated.

to land is about 240 meters, which explains why the AutoNaut does not choose to turn starboard. In this situation, the priority of avoiding grounding is considered more important than complying with COLREGS.

The same simulation was repeated with a lower obstacle speed of 6 m/s. Figure 7.24 shows the same exact head-on simulation with the only difference being the fact that the algorithm is aware of land. It can be observed that, knowing that land is very close on the USV's starboard side, the algorithm chooses a smaller offset ( $\chi_{ca} = +45^\circ$ ). Then in order to respect the minimal safety distance to the other vessel, the algorithm commands a  $+90^\circ$  offset for a short period, before the offset is zeroed and normal navigation is restored once the obstacle has passed.

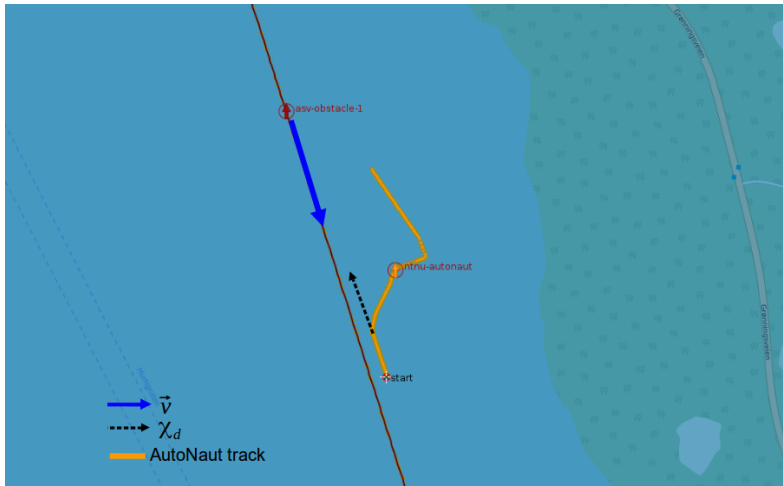


Figure 7.24: Head-on with anti-grounding activated.

Despite land is close to the USV, the algorithm chooses a starboard turn, since the obstacle's speed allows the AutoNaut to comply with COLREGS rules, while avoiding collision safely and navigate at a minimum desired distance from land. Despite the minimal distance between the two vehicles cannot be respected (approximately 150 meters), the minimum safety distance to land ( $d_g^{safe} = 100$  m) is respected since the measured minimum distance is 120 meters.

### Including the environmental state

In this section, the environmental factors and their additional cost  $K_{env}E^k$  are added in the simulations. The simulated scenario is the same as in the previous section and the speed of the obstacle is kept constant at 6 m/s. The environmental state is included, in order to understand if the environmental factors have an impact and, most importantly, the desired impact on the decisions of the collision avoidance and anti-grounding algorithm. In rough conditions, it is expected that the USV prioritizes avoiding grounding obstacles more than before and is careful about going close to land. In order to stress the importance of the sea state in the control decision, high environmental costs are considered. A change in behavior demands quite a high additional cost, which is desired since complying with COLREGS is important to ensure safe navigation at sea and should be the standard behavior. The total environmental cost can be tuned by adjusting the weights in the  $K_{env}$  factor. The values of the environmental factors, the grounding cost, and the weights used in this scenario are shown in Table 7.3. The values of the factors are set to create rough environmental conditions. The plot in Figure 7.25 shows

7. Anti-Collision and anti-grounding system: Design and experimental validation of a ENC-based approach

	Symbol	Value
Bathymetry	$B$	1.0
Heave displacement	$H$	2.0 m
Wind speed	$V_w$	10.0 m/s
Wind direction	$\beta_w$	30.0°
Current speed	$U_c$	0.3 m/s
Current direction	$\beta_c$	30.0°
Environmental weights	$K_{env}$	[10.0, 50.0, 50.0, 100.0]
Grounding cost	$K_g$	100.0

Table 7.3: Algorithm parameters.

the cost of each environmental term together with the resulting total environmental cost  $K_{env}E^k$  (in red) for each course offset. As intended by design, the cost is highest for the course offsets that coincide with the wind and current direction. The costs from the sea current and the bathymetry are quite low compared to the cost from wind and heave. This can be changed by adjusting the weights in the  $K_{env}$  vector.

Figure 7.26 shows that despite the obstacle speed is low enough to allow the USV to comply with COLREGS rule 14, the algorithm opts for a port maneuver. This is due to the wind and current that push the AutoNaut towards land on its starboard side. It can be noticed that the AutoNaut turns  $-90^\circ$  to port, instead of turning  $+45^\circ$  to starboard where it was considered safe to go in the previous simulation when the environmental state was not included in the optimization (see Figure 7.24). Because there is a quite strong wind and a current directed North-East, in addition to high waves, the total environmental cost is so high that keeping a safe distance to land is prioritized over choosing the COLREGS compliant behavior. Still, the AutoNaut manages to avoid collision with the obstacle and, at the same time, a safe distance from land is kept on its starboard side. The shortest distance to the obstacle is 118 meters, which is only a few meters shorter than before (Figure 7.24), while the shortest distance to land has increased to more than 200 meters. This result shows that in rough environmental conditions, the system will prioritize avoiding grounding obstacles, and that the environmental factors can have an impact on the decisions of the AutoNaut.

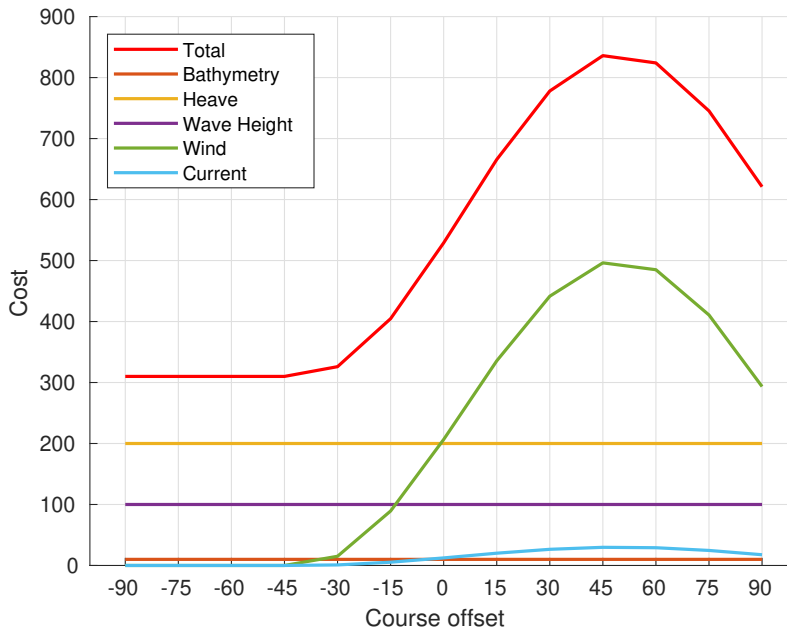


Figure 7.25: The evolution of each cost depending on the course offset.

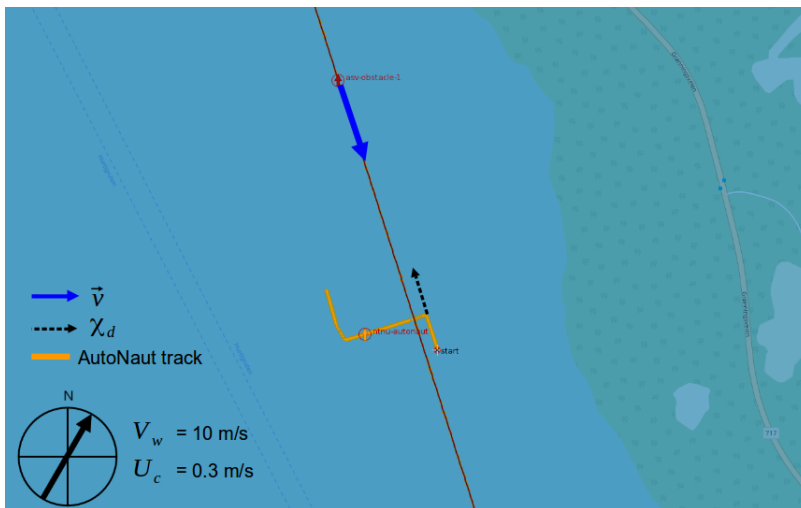


Figure 7.26: Head-on with anti-grounding activated and sea state included.

## 7.8 Discussion

The anti-collision and anti-grounding system presented in this chapter is a reactive obstacle avoidance control system intended to make the AutoNaut aware of, and avoid, the surrounding moving and static obstacles in situations where it has to diverge from its originally planned path. Anti-grounding situations will typically occur when the USV has to change its course to avoid collision with dynamic obstacles. Therefore, it is important that the existing collision avoidance system and the new grounding avoidance system work well together. The simulations and experimental results presented in this chapter show that the performance of the collision and grounding avoidance system is overall good and as desired. Further tuning of the weights might be explored, in order to achieve even more accurate results. Furthermore, the full system functionalities should be further tested in the field in order to assess the validity of the theoretical assumptions. As a first approach, simulations indicate that the two functionalities can co-exist.

The collision and grounding avoidance algorithms contain many tuning parameters which highly affect the control decisions and therefore the behavior of the USV. In this work, the tuning of the collision avoidance parameters is based on the values used in [101], which are adjusted to fit with the AutoNaut and the integrated anti-grounding system. The parameters related to anti-grounding and environmental terms are instead tuned through simulations. As pointed out in [101], tuning the the anti-collision algorithm is not straightforward because there are many parameters and some depend on each other as well as obstacle speed and size. The simulation study contains several different scenarios that demonstrate the most important mechanisms and functionalities of the system.

The minimum safe distance to land and to other vessels is set to 100 and 300 meters, respectively, in the simulations, but the USV is not always able to respect this distance. Tuning the SB-MPC surveillance distance parameter could improve the behavior, but note that these safe distances are not intended as absolute nor explicit constraints. Rather, the distances are set to make the USV aware of the high risk of keeping a distance shorter than the minimum safe distance. Although the optimal behavior is to keep the minimum distance to all obstacles, the system has not failed if it is not able to achieve that. In some situations where multiple obstacles are present, there are conflicting demands, making it impossible to meet all requirements. Then, the focus is to find a solution that will make the situation as safe as possible, considering all obstacles and finding a compromise. The results of the simulations show that the AutoNaut is able to do exactly that when scenarios involve both static and dynamic obstacles.

As mentioned earlier in this chapter, a natural future work is to include the non-linear dynamic model (presented in Chapter 4) of the USV and use that to update

the vehicle's state when winds and currents affect its navigation [105].



## Chapter 8

# Long-endurance operations in harsh weather conditions

### *Challenges and lessons learned*

This chapter is based on the article [154], presents operational experience of a long-duration operation in Norwegian coastal waters.

The system presented in this thesis was tested on a number of field trials. In the three years prior to the publication of this thesis, the control and communication architecture was tested over twenty times in Norwegian fjords, coastal and ocean waters.

The first long-duration deployment happened in May 2020, where the AutoNaut was employed in a week-long mission in Nordfjord (Central Norway). The objective of that mission was to monitor the annual migration of Salmon smolt in the fjord, by detecting the acoustic underwater signals emitted by tagged fish samples. This experiment is described in detail in Chapter 10.

The second long-duration mission took place some months after, in July 2020 from the Mausund island (close to Hitra and Frøya, Central Norway), where the USV operated continuously for two weeks in the open ocean, off the coasts of Central Norway. The purpose of this test was to test the long-term capabilities of the designed system, as well as the robustness of control and communication routines. Figure 8.1a shows the area covered by the USV in this long-duration mission. The designed communication and navigation system proved to be robust to rough environmental conditions, and reliable over time. On the last day of the mission, while the USV was coming back to the headquarters (Mausund Field Station), some strange behaviour was noticed. The speed suddenly dropped and the course could hardly be controlled. A rescue mission was initiated, while the USV was still at ap-



## 8. Long-endurance operations in harsh weather conditions: Challenges and lessons learned

---



(a) the track covered by the AutoNaut in July 2020.



(b) Side view of the strut extremity, where the hydrofoil was connected.

Figure 8.1: July 2020 offshore mission.

proximately 20 km from Mausund. The USV was towed back to shore and major damages to the underwater propulsion systems were discovered (see Figure 8.1b), i.e., the metal supports holding the foils were torn apart. The damages were due to the weakness of the struts that were holding the hydrofoils, and a system upgrade was requested to the manufacturer.

## 8.1 Cooperative monitoring of HABs

### 8.1.1 Mission overview

The most recent extensive field campaign took place in March and April 2021 in Frohavet, a semi-enclosed sea that separates the Trondheim Fjord to the Atlantic ocean (north-western coast of Central Norway). The deployment of the AutoNaut was planned as part of a larger mission that involved multiple robotic assets working together to monitor the birth and growth of harmful algal blooms (HABs) in the area. The AutoNaut's responsibility in the context of the mission was to monitor the levels of chlorophyll-a and of other parameters in the upper water layer. Other relevant parameters were sampled, in order to determine the actual appearance of an algal bloom, e.g., oxygen concentration, salinity, water temperature, sun radiation. The USV operated at sea for a total of 19 days, despite several challenges appeared during the mission, the harsh weather conditions being the most relevant. Safety procedure were put in place to ensure the safety of the people and equipment involved. The mission was executed according to plan for 19

days, until a system failure led the vehicle to grounding. Valuable experience on the vehicles situational awareness, abilities to navigate and communicate were obtained and can be used to further improve the autonomy of the vehicle and standard operational procedures.

This experiment involved several manned and unmanned robotic assets for a duration of over one month. The objective of the field campaign was to study the algal bloom at different space and time scales, from satellite observations of the whole Frohavet region down to the underwater sampling of the epipelagic (upper) water column. While satellite-based imagery was used to monitor the growth of the algal bloom and assist with mission planning, aerial and terrestrial robotic platforms were employed to gather in-situ measurements. Specifically, an airplane and a multi-rotor UAV were used to collect hyperspectral images of the targeted areas, the AutoNaut and an LAUV (AURLab, NTNU) were used to collect chlorophyll-a, salinity, oxygen measurements of the upper water column while the latter also recorded images with a silhouette camera. Additionally, vertical profiles were performed and samples were collected manually for further validation.

### 8.1.2 Scientific context

An algal bloom is a rapid increase in the density of algae in an aquatic system. A bloom is often triggered by the increase in temperature and sunlight during the spring. Fish farming is an important industry along the north-western coasts of Norway. The area surrounding Frøya (Central Norway) is populated with several fish farms. Algae can cause depletion of oxygen or be toxic for fish, thus being a threat to fish farms. It is uncertain exactly when and how a bloom evolves as it depends on a variety of factors. An important role is however played by photosynthetically active radiation (PAR), which is the amount of light available for photosynthesis. Algae will produce chlorophyll, thus an increase in chlorophyll-a can indicate that a bloom is in progress. The AutoNaut is equipped with the necessary instrumentation to measure both the level of chlorophyll-a and PAR, thus it is able to detect a bloom. In the described mission, the USV operates in Frohavet and takes periodical measurements of PAR and chlorophyll. The measurements collected by the AutoNaut are interpreted daily by a team of marine biologists, who are responsible for announce the actual appearance of a bloom or, alternatively, the need of additional measurements at different spatio-temporal scales.

## 8. Long-endurance operations in harsh weather conditions: Challenges and lessons learned

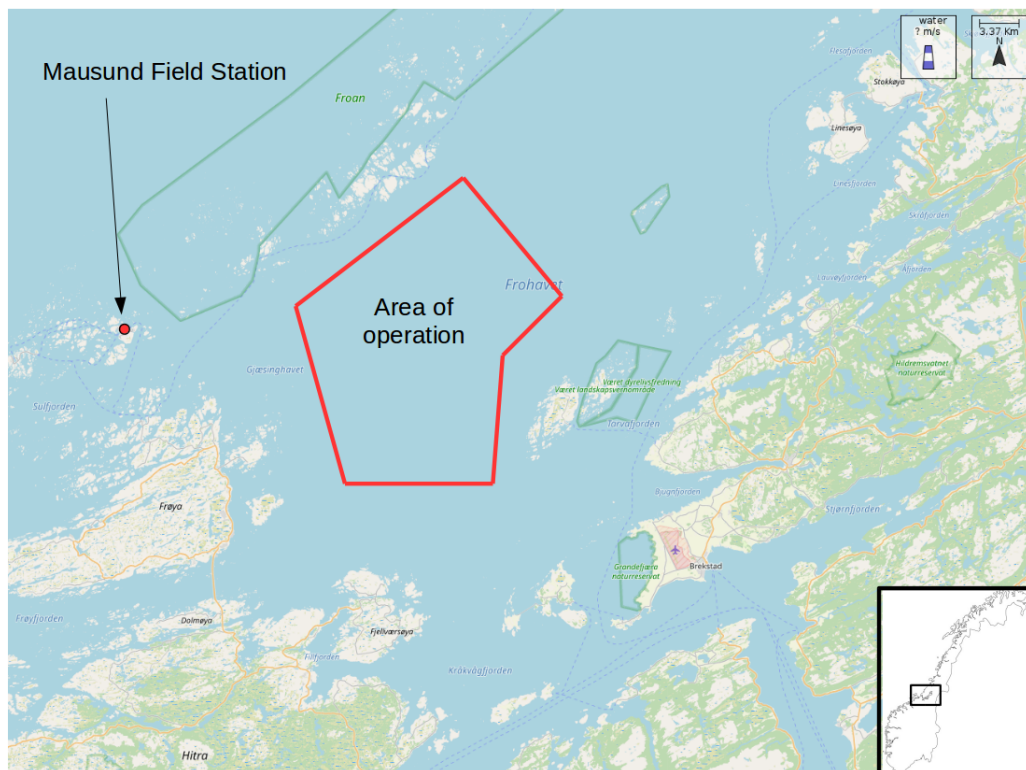


Figure 8.2: The area of operation in Frohavet and Mausund Field Station, operations headquarter.

## 8.2 Risk assessment & mitigation

### 8.2.1 Hazards

The area of operation (AO) for this mission is located along the Atlantic coast of Central Norway (see Figure 8.2). This area is usually characterized by strong winds and currents, high waves and significant ship traffic. Moreover, the North Atlantic Current, that hits the Norwegian continental shelf, brings a significant amount of floating debris. The USV autonomy is also impacted in this area since, in spring, strong rainfalls and cloudy sky are common, meaning low sun irradiance and hence limited onboard energy. The use of electronic navigational charts (ENC) plays a key role in this area, as the southern coasts of the Froan archipelago (upper part of Figure 8.2) is populated with several static obstacles as fish farms and beacons. Observing the bathymetric chart of the areas surrounding Frohavet, it is possible to notice a myriad of small islands and rocks awash. This suggests the necessity to define a safe operational area far enough from the archipelagos. Finally, the lack of

a good cellular network coverage might limit the operational flexibility and force the operators to rely on satellite communication. The mission requires the USV to stay in the AO and sample regularly the upper water column. To achieve this, a typical mission is defined in order to let the AutoNaut run in a loop within the AO. The vehicle executes autonomously the predefined mission, which involves way point navigation and data collection, storage and transmission to shore.

### **Collision**

A collision with another vessel poses a risk for both the AutoNaut and other vessels traveling in the AO. Small pleasure crafts are less likely to go into the AO at this time of year and the area is likely to be mainly populated by larger fishing vessels, cargo vessels, tankers and service vessels for the nearby fish farms. We therefore expect most vessels in the AO to have automatic identification system (AIS) and thus have the capability to detect the AutoNaut from a safe distance. As described in Chapter 7, the USV is equipped with an AIS-based COLREGS-compliant anti-collision system to prevent collisions with other vessels equipped with an AIS. Given its small size, a collision with another vessel may be fatal to the AutoNaut, but may result in only minor damages to any other vessel.

### **Loss of control**

At early spring the AO is prone to harsh weather conditions. Strong winds are to be expected and can regularly get as strong as 20-30 m/s at this time of year. Strong wind in combination with the proximity to the open ocean generates large waves as well. The proximity to islands and shallow waters is likely to generate strong and unpredictable currents at the surface. As discussed in Chapter 4, since the AutoNaut operates at low speed, low maneuverability and strong environmental forces can end up dominating the propulsion force and make the vehicle difficult to control, or in worst case completely uncontrollable.

### **Damage to external equipment**

The operational area is populated by floating debris and garbage. External equipment, like rudder, hydrofoils, sensors and antennas may be damaged by floating objects. Damages to any of the communication antennas will lead to a failure in communication which will limit or prevent any monitoring and control of the vehicle from land. Contingency plans can then not be executed from shore if a critical situation should arise, like a significant deviation from path caused by strong wind. A loss of communication will also mean that the position of the vehicle will be unknown, decreasing the chance of finding the vehicle if a rescue team is sent to recover it. A failure of any of the critical navigation sensors, rudder or hydrofoils,

## 8. Long-endurance operations in harsh weather conditions: Challenges and lessons learned

---

would result in a loss of navigation capabilities, which leaves the vehicle uncontrollable.

### Endangered recovery crew

The AutoNaut requires a support vessel to bring it between the deployment site and the AO by towing it. This is due to the presence of shallow waters with many reefs between the AO and deployment site. If a recovery of the vehicle is necessary, the support vessel has to approach the AutoNaut in order to connect a tow line. This operation can be very hazardous if the weather conditions are harsh (e.g., high waves, strong winds), as the recovery vessel may collide with the USV. Moreover, attempting a recovery of the USV in harsh weather conditions represents a hazard for the manned crew the support vessel.

### Onboard power depletion

Even though the vehicle requires no electricity to propel it self, it requires electricity to power the onboard computers, sensors and rudder. This power is provided by the battery bank, which is charged by the solar panels. Should the electric energy deplete, critical equipment such as the GNSS receiver and rudder will shut down and leave the vehicle uncontrollable. The vehicle is set to start powering down non-essential equipment if the battery voltage drops below a certain level. The scientific payload (*Level 3*) is defined as non-essential, thus if the battery voltage drops too low, the vehicle will no longer be able to achieve the goals of the assigned scientific mission. It will instead only focus on its survival and keep on navigating the route planned.

### 8.2.2 Risk assessment

The hazards are summarized in tables 8.1 and 8.2, while the risk matrix (see table 8.3) categorizes the various hazards into a red, yellow and green category. Red indicates an unacceptable risk and additional mitigating actions must be taken to reduce the risk. The yellow instead, is an evaluation area where further mitigating actions should be considered to reduce the risk. Green indicates an acceptable or negligible risk where no action is required.

### 8.2.3 Safety procedures

As outlined in the previous section a number of risks will be present during the mission. Safety procedures to reduce the risk associated with the hazards are discussed below.

Hazard	Consequence	Mitigation
Collision	A collision with either another vessel or stationary object may lead to damages to both parties involved. Serious damages to the USV may result in it sinking.	An AIS-based COLREG compliant automatic collision-avoidance system is implemented to avoid collisions with other vessels. In addition, a lantern and radar reflector are used to increase its visibility.
Grounding	Grounding may damage the external equipment or, in the worst case, the hull.	The AO is restricted to deeper waters to reduce the risk of grounding. The AutoNaut is towed to and from the AO.
Energy depletion	Onshore planning considers cloud forecasts. A loss of power will result in loss of critical sensors, actuators and communication units, thus the vehicle will be at risk of grounding or colliding.	The power levels are monitored and non-essential equipment may be turned off if power conservation is necessary. If a complete loss of power is expected, the vehicle may be retrieved by the rescue team.
Recovery in rough weather	Harsh weather conditions may cause injuries to the rescue team, damages to the rescue vessel or the AutoNaut	The rescue team would only be dispatched if the weather allows it and will only consist of highly experienced crew familiar with the AO.

Table 8.1: Summary of the hazards presented in this section and their corresponding consequences and mitigation.

### GPS satellite beacon

All sensors and actuators on the AutoNaut are powered by the onboard battery bank. In the event of a failure of the electric system, all sensors and actuators will stop working. This means the USV will be unable to navigate, but it also means that the onboard GNSS receiver will no longer transmit the vehicle's position to land. In the event of such failure, the position of the vehicle is necessary so that

8. Long-endurance operations in harsh weather conditions: Challenges and lessons learned

Hazard	Consequence	Mitigation
Control loss due to rough weather	If controlability is lost the vehicle can end up colliding or grounding.	Controlability can be regained by altering the original mission to align the vehicle better with the environmental forces. A set of contingency plans were made prior to the mission in case of extreme weather.
Leak	Significant leaks may fill the hull with water and result in electronics failure and vehicle sinking.	The hull is split in three separate compartments and each contains a bilge pump running at fixed intervals. Critical electronic components are placed in watertight boxes inside the hull, and are connected with watertight cable connectors.
Capsize	A capsize may lead to damages to external equipment (e.g., antennas) and cause short circuits and failure of electric components. Functionalities would be lost for the duration of the capsize.	The hull is designed to self-correct. All internal equipment are strapped in place to prevent them from moving in the event of a capsize.
Damage to external equipment	Damages to equipment critical for navigation or communication may lead to a loss of control or loss of communication with onshore operators.	The control architecture has navigation and communication redundancy, and an independent GNSS beacon.

Table 8.2: Summary of the hazards presented in this section and their corresponding consequences and mitigations.

the rescue team is able to locate it. Thus, a separate GPS satellite beacon <sup>1</sup> was installed on the vehicle. The beacon has built-in battery and can therefore transmit

<sup>1</sup>NOVATCH iSurface delivered by Metocean Telematics

Consequence	Likelihood				
	Minimal 1	Low 2	Medium 3	High 4	Very High 5
E Very Critical					
D Critical	1,4				
C Dangerous		2,5	3		
B Relatively Safe		7	8	6	
A Safe					

Table 8.3: Risk matrix identifying the risks associated with the mission.

its location independently of the main power system onboard the USV. This will reduce the risk of collision or grounding in the event of a loss of power.

### Around-the-clock monitoring

To reduce the risk of collision and grounding, a watch systems was implemented with around-the-clock watches. This ensured that a person always was available to asses the situation and take necessary action should the USV be in danger. During the day the operations were supervised more or less continuously, while during the nights it was watched every two hours. Given the vehicle's low velocity (even while drifting with the wind) and the distance to land in the AO, watches every second hour was considered sufficient. For this purpose, the Grafana API (see Chapter 3) provides a good overview of the USV and the mission status, and can is easily accessible to the public. This made it possible to recruit and train a larger team of watchers. If an undesirable event were to happen, the watchers would contact an operator with access to Neptus and the ability to control the AutoNaut.



### **Contingency plans**

In cooperation with the rescue team, contingency plans were made. Areas with more sheltered water were identified such that the AutoNaut could be moved there in case of faults or if the weather made it impossible to operate in the intended area. This reduces the risk of the vehicle losing controllability and as a result colliding or grounding.

### **Monitoring of metocean forecasts**

Several services providing tidal and metocean forecasts exist and were closely monitored to anticipate future problems with navigation due to the weather. A loss of controllability due to strong winds, waves, and currents may not be critical if it can be regained by altering the mission, e.g., moving the way points to increase the wind angle of attack on the vehicle. Persistently bad weather may increase the risk of the vehicle losing controllability for a long period of time and thereby grounding or colliding with other vessels. In that case contingency plans may be executed on the basis of forecasts.

### **Monitoring of ship traffic**

AIS online services give information about global marine traffic. This makes the operators able to predict future possible collisions and take necessary action. If necessary, AIS services can provide the operator with contact information to the vessel, such that the crew can be alerted of the presence of the AutoNaut.

### **Search and rescue team**

A search and rescue team was on standby at Mausund Field Station (see Figure 8.2). If the vehicle was in critical danger, the team could deploy on a short notice if the weather conditions permitted it. The assets available for the rescue team was the boat Hunter, a 11 × 3 meters aluminum vessel, as well as several smaller vessels. Hunter has a cruising speed of about 20 knots, which makes it able to reach any point in the entire AO in about one hour. Missions are planned such that the AutoNaut keeps a distance of at least 10 km to land. Assuming an average speed of 1.5 m/s for the AutoNaut, it will take the vehicle approximately 2 hours to move 10 km. This means the USV will at all times be approximately 2 hours from grounding, giving the rescue team a maximum response time of 1 hour in the worst case.

### Software upgrades

Whenever the vehicle is within 4G cellular coverage the operators onshore have the ability to update the software running on the *Level 2* and *Level 3* computers. This means the navigation and control software can be altered or improved during the deployment should a problem occur.

### Data logging

Data is communicated back to the onshore operator at all times, either over 4G if the vehicle is within cellular coverage or over the Iridium satellite network if otherwise. However, all data is also stored on an onboard hard drive. When received onshore, data are automatically logged by the server at NTNU (see Chapter 3). Additionally, when the vehicle is retrieved, all measurements from the mission can be retrieved by accessing the onboard storage.

## 8.3 Case study

In this section challenging mission scenarios are described. The first five scenarios show situations where faults were detected or where the USV was unable to execute its plans. The safety procedure was triggered to maintain mission safety. The two final cases show challenging scenarios in which the vehicle was able to handle the situation autonomously without human intervention or any safety procedures being executed.

### 8.3.1 Case 1: unfeasible path due to strong wind

As expected, strong winds up to 15m/s and currents were present in the AO. When that happens, the passive wave-propulsion mechanism of the vehicle can be overpowered and the planned path became unfeasible, as already investigated in Chapter 4. An example of this can be seen in Figure 8.3. While maneuvering from the eastern-most to the southern-most way point, the USV struggles more and more to stay on track. While the absolute wind speed ( $V_W^P$ ) and direction ( $\beta_W^P$ ) are depicted in Figure 8.4, measured course ( $\chi$ ) and desired course ( $\chi_d$ ) are shown in Figure 8.5. It can be seen that the wind approaches 20 m/s with gusts up to 30 m/s towards the end, as measured by the onboard weather station. The significant wave height increased to about 3 meters, and course oscillations around the desired one appear. As the wind increases, it eventually overpowers the vehicle and it is no longer able to make any progress towards the way point. In this scenario the wind is directed from south-west towards north-east, hitting the vehicle from the front. While the AutoNaut is headed directly into the wind, the lateral force

## 8. Long-endurance operations in harsh weather conditions: Challenges and lessons learned

made by the wind is zero, but even a small deviation in heading will make the lateral wind forces substantial and create a moment to turn the vehicle around. This can clearly be seen in Figure 8.5, where large course oscillations can be observed during the last part of the considered period. In this scenario the vehicle is not able to reach the target location. In order to allow the USV to make progress on the mission, a new way point was set manually by the onshore operators such that the wind angle of attack is larger.

### 8.3.2 Case 2: re-routing due to forecasted strong wind

As stated in the safety procedures, the operators onshore should monitor the weather forecast continuously to predict any hazardous situations. In this example the USV was executing a circular navigation plan in the AO under moderate weather conditions (see Figure 8.6), while the battery voltage started to approach the critical level. At the same time the weather forecast showed an upcoming increase in wind and waves. The forecast showed an increase in the winds towards 20 m/s and an increase in significant wave height from 2 to 3 meters. Low battery

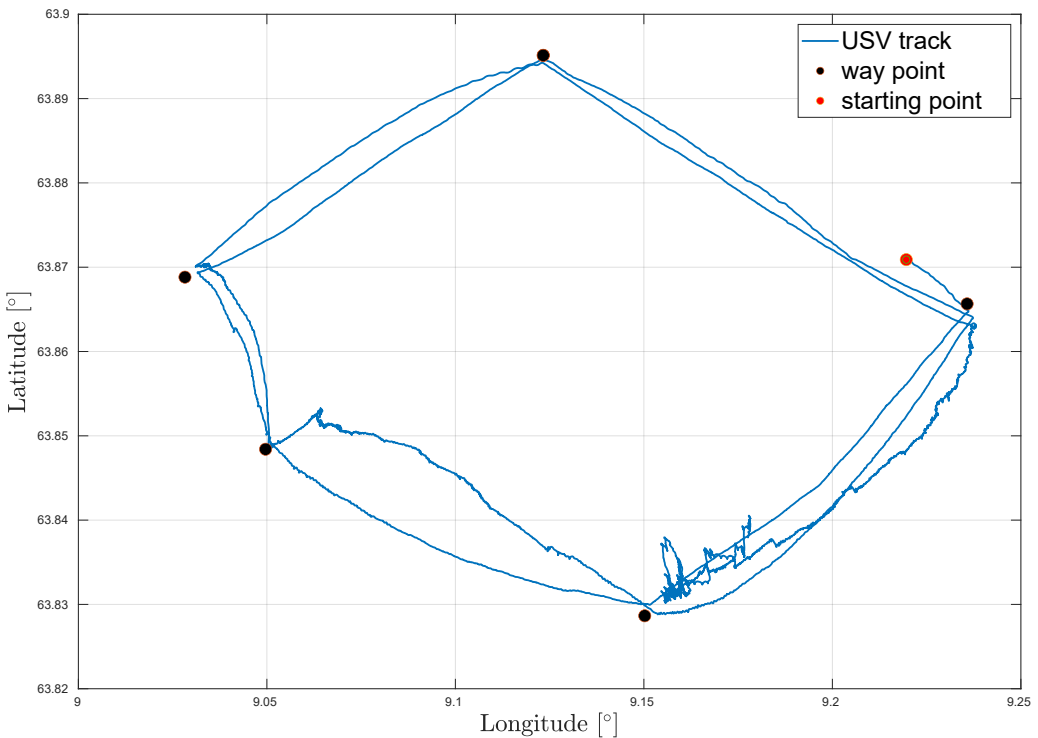


Figure 8.3: AutoNaut's location during a 42 hour period during the deployment.

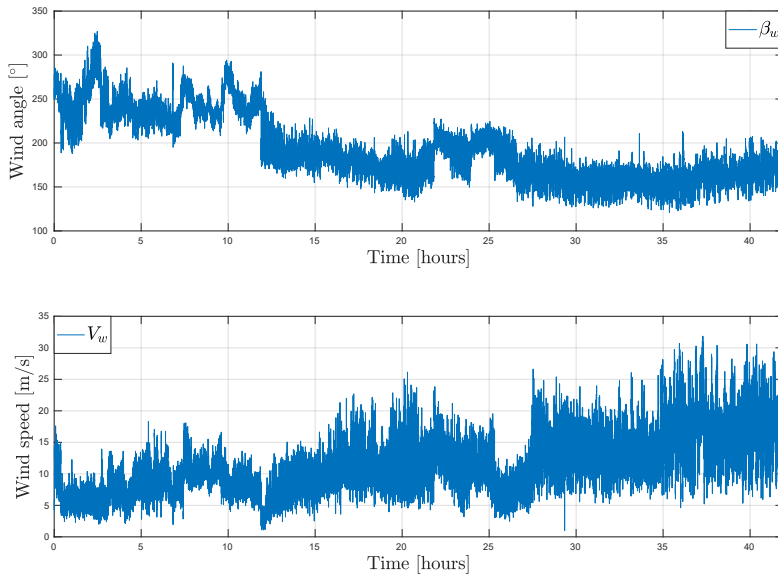


Figure 8.4: Absolute wind direction (top,  $\beta_w^P$ ), absolute wind speed (bottom,  $V_w^P$ ).

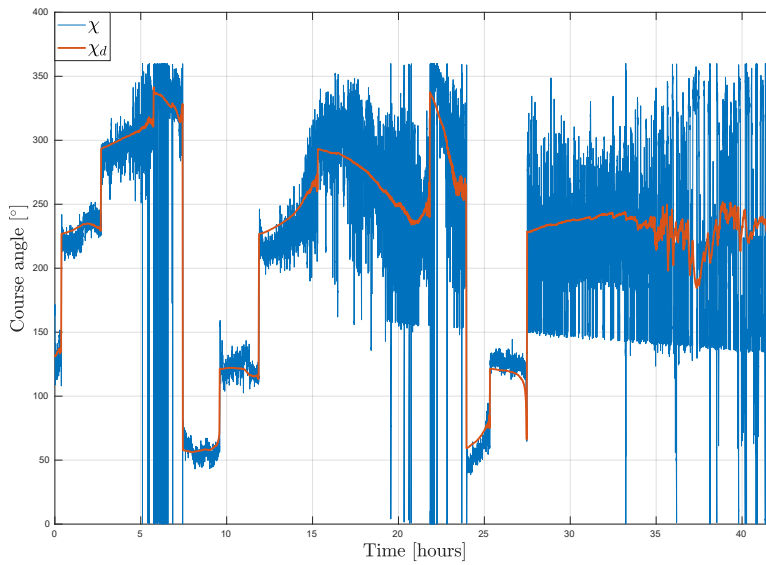


Figure 8.5: Measured ( $\chi$ ) and desired ( $\chi_d$ ) course for a 42 hour period during the deployment.

voltage would normally trigger a rescue mission, but it was uncertain if the rescue team would manage to retrieve the vehicle before the weather conditions wors-



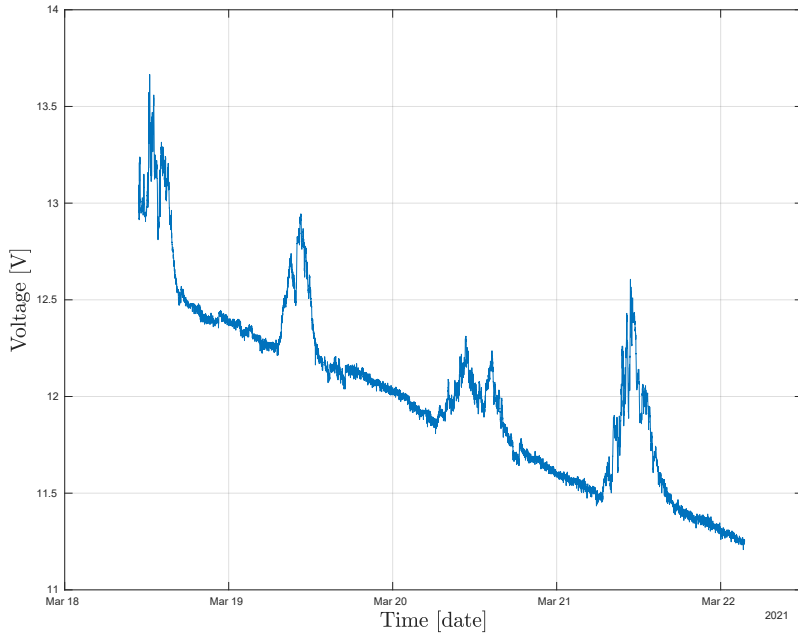


Figure 8.7: Onboard battery voltage.

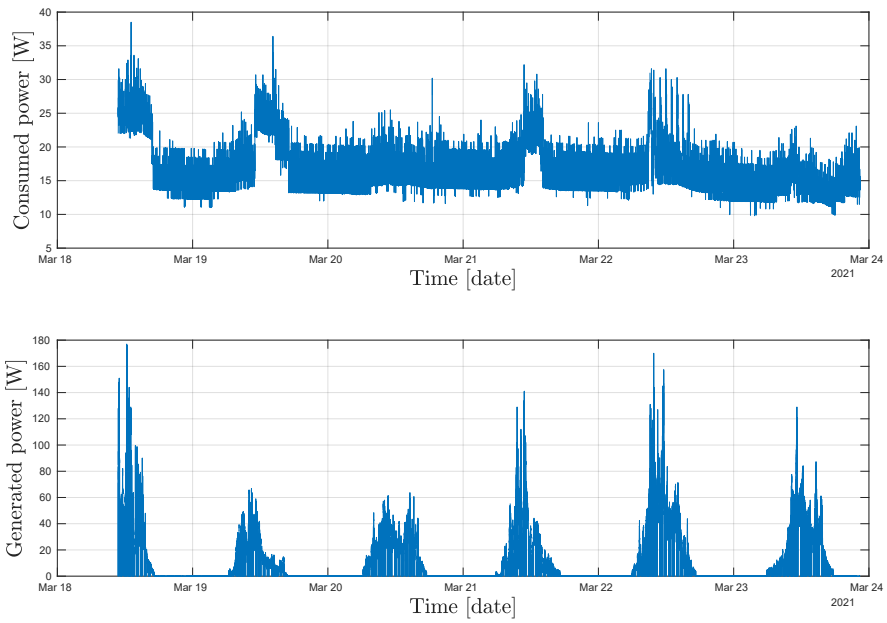


Figure 8.8: Power consumed onboard.

## 8. Long-endurance operations in harsh weather conditions: Challenges and lessons learned

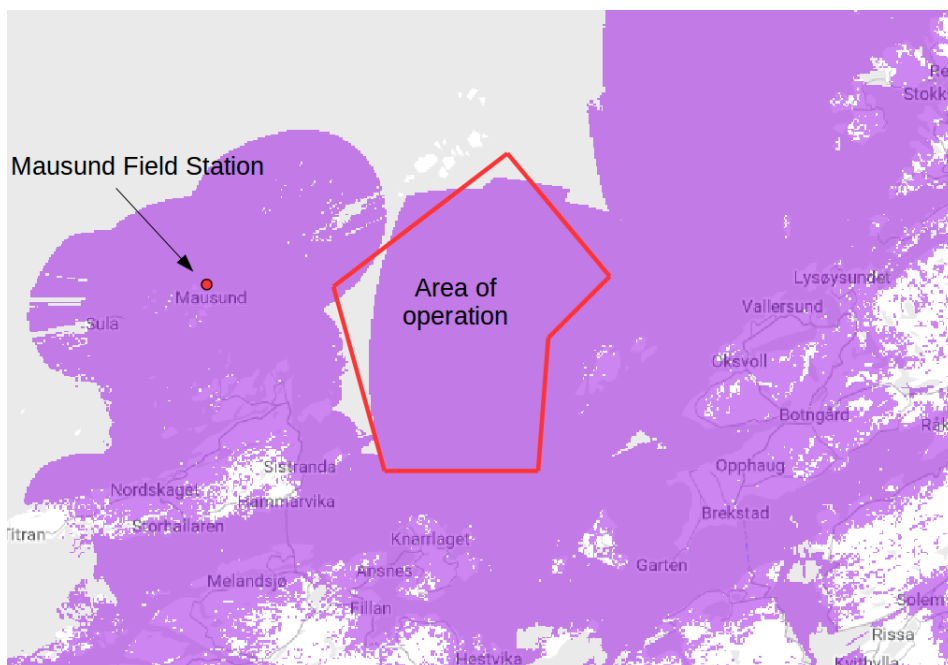


Figure 8.9: 4G coverage map from Telia (<https://www.telia.no/>).

weather during the mission caused the solar panels to generate only small amounts of power. Figures 8.7 and 8.8 shows the evolution of the battery voltage over a 6-day period as well as the consumed and generated power. It can be noticed that the battery voltage is consistently decreasing day by day. During the day the voltage increases as the batteries are mildly charged despite the cloud coverage, but the generated power is not enough to make up for the consumption during the night. At the end of this period the voltage dropped below the critical level of 11V, triggering the safety procedures. The recovery team was dispatched from Mausund Field Station to recover the vehicle. The vehicle was still capable of navigation and was sent to meet the recovery team, that could monitor in real-time the location of the USV on Grafana.

### 8.3.4 Case 4: loss of communication

The 4G/LTE connection is claimed to be quite good in Norwegian fjords and in coastal area, as shown in Figure 8.9. However, the proximity of the onboard 4G/LTE antenna to the water surface causes the signal to deteriorate significantly, especially when in high sea states. This was expected and frequent losses of 4G/LTE signal occurred. In the event of a connection loss, the vehicle continues operating

as planned, but switches to the Iridium satellite network as its main source of communication with the operators on shore. The bandwidth is decreased significantly and thus the amount of information transmitted from the USV is decreased. This results in reduced situational awareness for the operators. Since the VHF communication link was not used in this mission, if the Iridium communication channel fails, the USV would lose all means of communication, which is a critical situation. Due to water leaking into the Iridium antenna connector, the Iridium antenna suffered a failure during the mission. The fault was immediately detected by an operator onshore. Without any means of communicating with the onboard computers, the decision was made to recover the vehicle and the safety procedure was immediately initiated. Although the GNSS device was functioning, the lack of communication made it impossible to transmit the vehicle's location to the operators. By using the location broadcast from the independent GPS beacon, the crew were successful in finding and recovering the USV. The failure of the Iridium antenna was due to a leak in the antenna connector on the vehicle deck, resulting in a temporary short circuit. The antenna and connector were both replaced. In addition, dielectric grease was added to all connectors to limit corrosion before the vehicle was towed back to the AO and resumed its mission.

### 8.3.5 Case 5: transitioning from 4G/LTE to Iridium satellite communication

As previously mentioned, the AO was affected by unreliable 4G/LTE connection and at several times during the mission the connection was lost. Figures 8.10 and 8.11 show a situation where the onboard communication software switches from using its primary communication link to its secondary. The vehicle broadcasts a report at a fixed interval set by the operators. This message contains the most crucial information regarding the status of the vehicle, such as location, battery voltage, speed-over-ground (SOG), course-over-ground (COG), mode (i.e., if the vehicle is in standby or maneuvering) and information on what equipment is turned on. The time interval of the reports was initially set to 60 minutes, but was decreased to 30 minutes by the operators once the vehicle lost cellular connection. Figures 8.10 and 8.11 show the COG, SOG and battery voltage and the USV's track. The high-rate measurements were retrieved from the local storage on the vehicle and can be observed in comparison to the values transmitted over the Iridium network. As the figures show, the mission progress and vehicle's status can still be monitored despite the reduced bandwidth.

As documented in Chapter 3 (Section 3.7.2), more detailed information on the navigation performance of the vehicle exists. Some messages are not sent regularly, but are instead transmitted by the vehicle when queried by the operator. For



## 8. Long-endurance operations in harsh weather conditions: Challenges and lessons learned

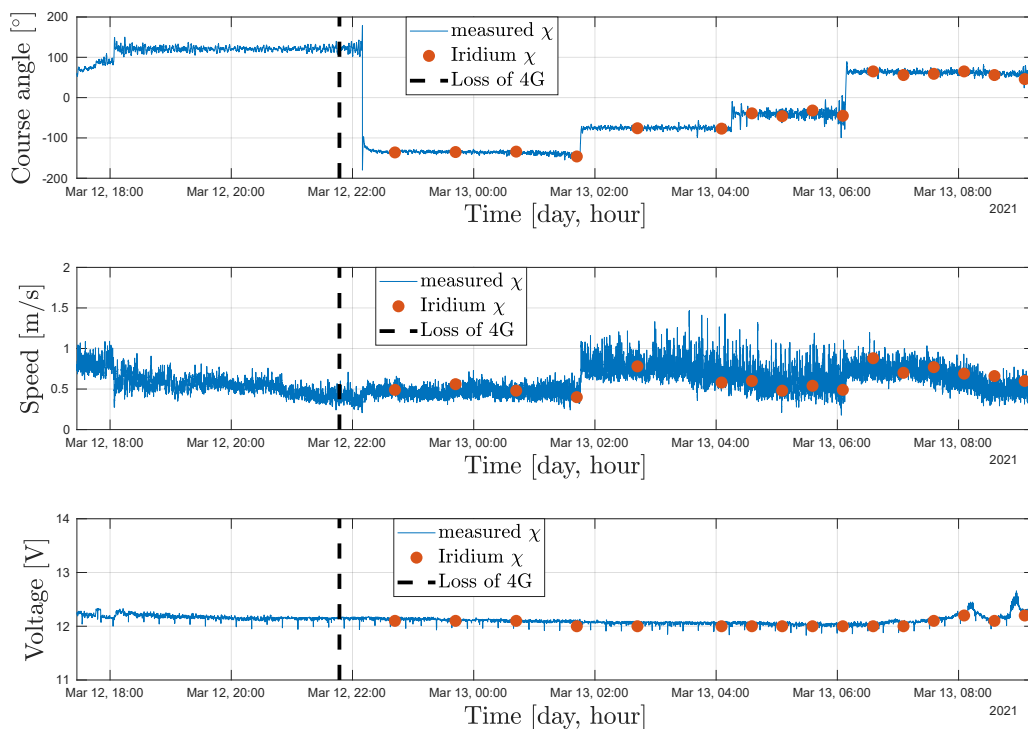


Figure 8.10: Measured wind, course and battery level broadcast from the USV via Iridium satellite communication compared to the logged measurements.

example, the message `navstat` contains information about course, desired course, ground speed, wind speed and direction, thruster and rudder usage. When the USV navigates in harsh environmental conditions, the message can be queried regularly to ensure the vehicle is navigating as intended, i.e., the course error is small. It is also helpful in ensuring that critical equipment, like the rudder, is functioning properly.

### 8.3.6 Case 6: capsizing and GNSS failure

After 19 days of operations, strong winds from the Atlantic Ocean and high waves appeared in the AO. The wind speed was measured to over 20 m/s with gusts reaching 30 m/s and directed towards west, eventually turning towards southwest. The strong winds combined with high waves caused the AutoNaut capsizing. The vehicle is designed to withstand a capsize and after approximately 10 minutes it self-corrected, according to the data logged onboard. During the capsizing all external antennas and sensors were completely submerged. This resulted in a complete loss of communication and navigation capabilities. The weather station

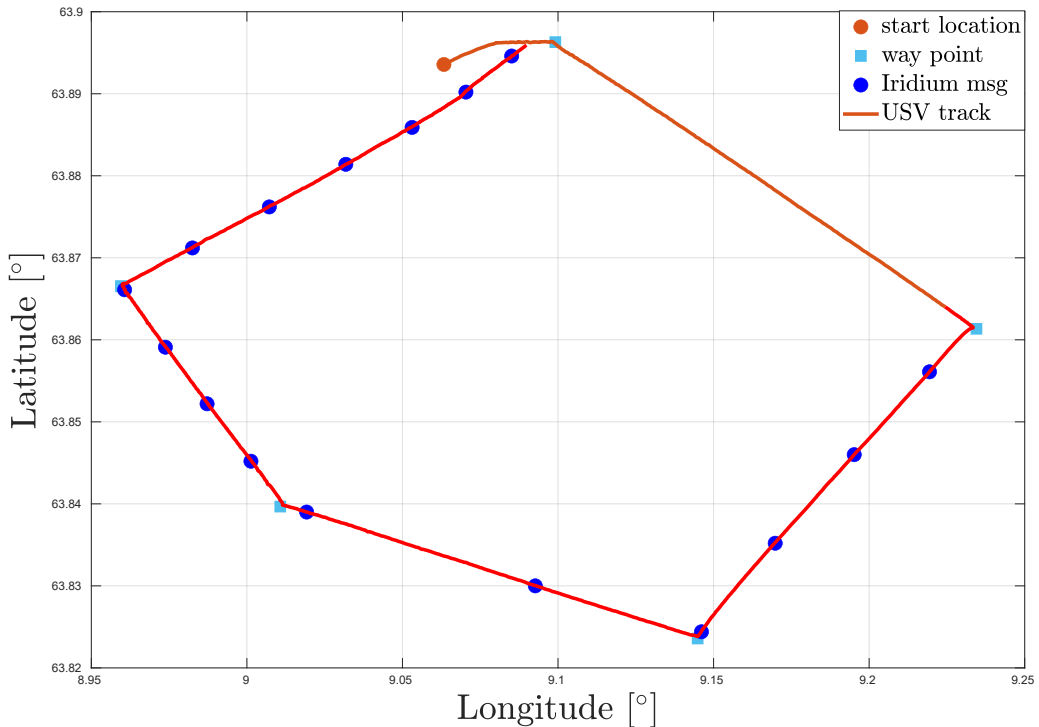


Figure 8.11: The observed vehicle's location sent via satellite, compared to the logged measurement.

was not rated to withstand a full submersion and its failure was immediately noticed when the USV rolled back. The weather station is not considered critical to the mission and therefore no action were taken and the mission continued.

Approximately 9 hours after the capsizing, the AutoNaut once again capsized for another 10 minutes. This time the GNSS receiver failed. The vehicle is equipped with a second GNSS receiver, however, this receiver was in a closed circuit with the AIS and not set up to provide measurements to the navigation system. Without a GNSS receiver signal for navigation the vehicle lost its navigation capabilities and started drifting subject to winds and tidal currents. This is a critical failure and safety procedures were initiated. The recovery team was alerted, but due to the harsh weather condition with waves up to 6 meters and winds with gusts up to 30 m/s a rescue operation was not possible without unacceptable risk to the team.

After the second capsizing, the vehicle drifted approximately 24 km south-east, passing through a narrow strait between two islands into more shallow waters. Here it took a turn towards west, most likely due to local variations in the tidal current, and grounded on a beach at the island Storfosna. The track of the vehicle

## 8. Long-endurance operations in harsh weather conditions: Challenges and lessons learned

---

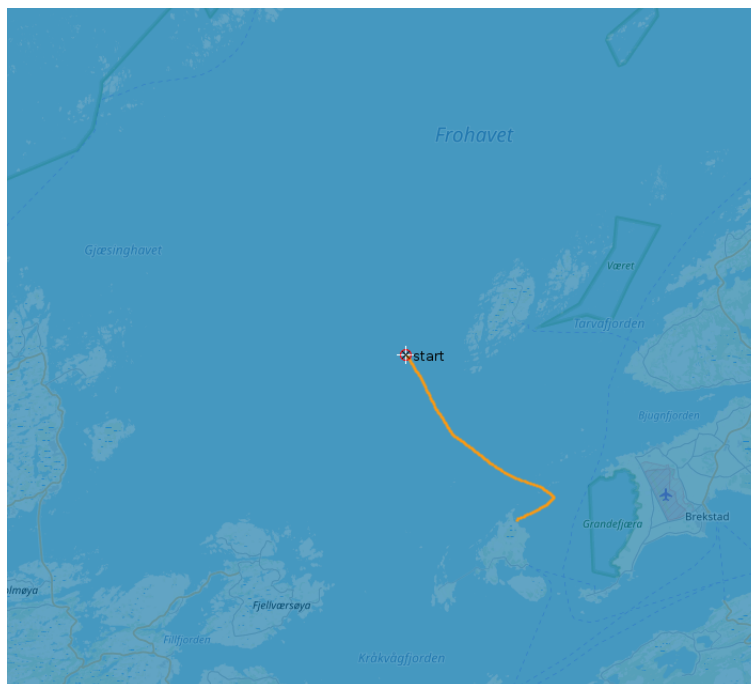


Figure 8.12: USV's track in the hours following up to the capsizing and grounding.

in the time leading up to the first capsize and until it hit land can be seen in Figure 8.12. As the tides were going out the vehicle was left on dry land where locals were contacted and they were able to recover it, as shown in Figure 8.13. The grounding had caused only small damages to the foils. The GPS beacon was operational during these events and provided some situational awareness to the onshore operators.

### 8.3.7 Case 7: collision avoidance

As described in Chapter 7, the onboard software runs a collision avoidance system. During the mission, a situation occurred where a vessel approached the AutoNaut on a collision course from north-east towards south-west. The speed of the approaching vessel was approximately 4 m/s while the AutoNaut had a speed of approximately 0.9 m/s. Figure 8.14 shows the track of the USV and the approaching vessel. The track indicates that the AutoNaut performs an evasive maneuver when the approaching vessel gets too close. The anti-collision system is tuned to monitor obstacles within a range of 5000 meters, but no action is taken before the obstacle is within 2000 meters. A fault in the software was detected during the evasive maneuver performed by the USV, causing the chosen maneuver to be sub-



Figure 8.13: How the AutoNaut was found on the beach of Storfosna.

optimal. As can be seen from the track, the AutoNaut acts overly cautious as the obstacle moves fast enough to never pose any real danger. This is however desirable, as it is desired that the USV always operates with a considerable clearance to other vessels. The cautiousness of the AutoNaut will ensure safe operations even if the approaching vessel should start maneuvering more unpredictably, e.g., stop or make a U-turn.

## 8.4 Discussion

The cases presented previously are evidence of the challenges associated to autonomous operations of a long-endurance wave-propelled unmanned surface vehicle. It is clear that the main challenge is the harsh weather conditions, an underlying factor in almost all the presented cases. Several technical weaknesses became apparent as a result of the weather conditions and revealed hidden problems not observed previously.

The combination of reduced solar exposure and strong winds made it difficult for the USV to operate autonomously over a long period of time. The lack of solar

## 8. Long-endurance operations in harsh weather conditions: Challenges and lessons learned

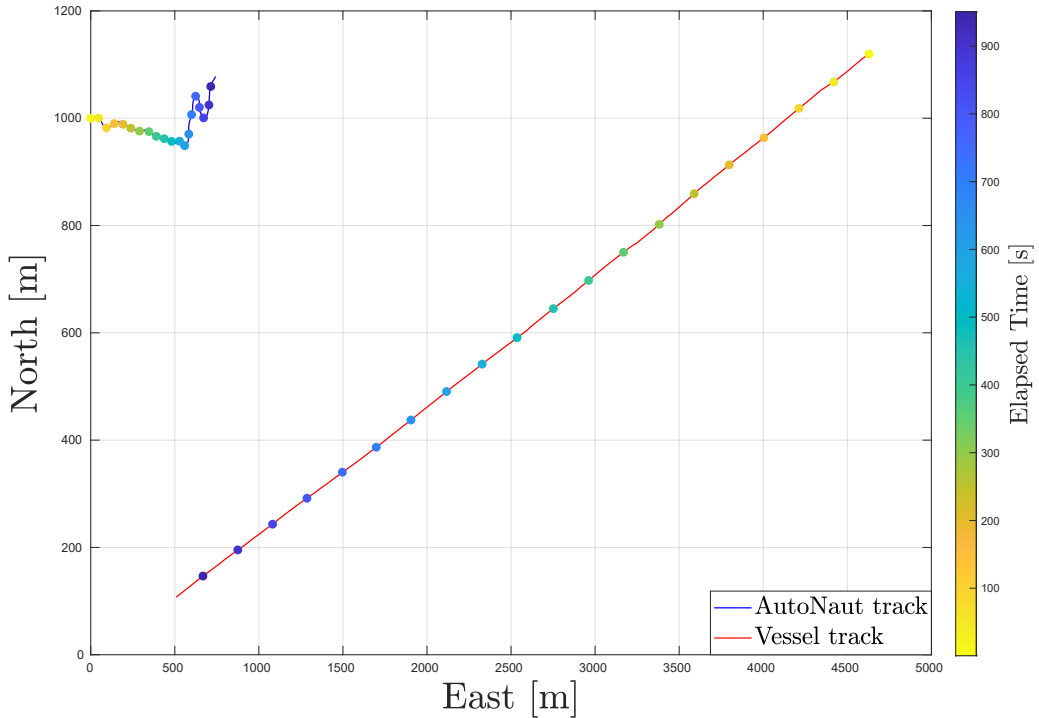


Figure 8.14: The track of the AutoNaut and the approaching a vessel.

energy harvesting triggered in total two rescue mission so that the vehicle could be recharged on land. Having a recovery team on standby proved to be essential in maintaining the integrity of the mission. In total, the vehicle was successfully recovered by the team three times. Two times for charging and once for replacing the damaged Iridium antenna. The weather conditions also proved to be a limiting factor for the recovery team as they were unable to go out during the situation that eventually lead to the vehicle grounding.

Despite having to recover the AutoNaut several times, the vehicle stayed on the water and executed its mission for a total of 19 days, providing measurements with scientific relevance. A significant algal bloom was not detected in the surface during the mission, however, the measurements provided by the AutoNaut show an increase in the chlorophyll-a and may be used to validate other measurements obtained during the mission, e.g., from satellites and mathematical ocean models (SINMOD) that were run in real-time during the mission. Water samples were collected by scientists shortly after the grounding of the USV and the data is currently being analysed. Once ready, the data can be compared to the data collected by the AutoNaut to validate its measurements.

The AutoNaut is designed to handle a capsizing. The vehicle is fully enclosed and it eventually self-corrects. However, when the antennas are submerged in water they lose signal. That means it is impossible to communicate with it. Moreover, the rudder will not be useful and maneuvering will be impossible. Most of the equipment on the vehicle's deck is waterproof, however, the weather station was not rated to withstand a full submerging and therefore it failed. In the second capsizing, also the primary GNSS receiver used for navigation failed. It is still not fully understood what caused this failure, as the GNSS is rated to withstand being submerged. The weather station was not protected by a fuse and it is hence believed the failure in the weather station may have affected the GNSS receiver since they are connected to the same power source and controlled by the same computer. After the recovery of the vehicle the GNSS receiver was tested and showed to be fully functional without any repair necessary. The vehicle in itself only suffered minor damages after the stranding. Two of the foils and a bracket holding the antennas to the mast broke. The hull was completely intact and only suffered small scratches. Navigating in the conditions on the day of the capsizing is a challenge. However, based on previous experience, the vehicle is able to maintain a degree of controllability by aligning the heading with the environmental forces. Without the failure of the GNSS receiver a grounding could likely have been avoided.

Several times strong winds and currents proved to make navigation hard or impossible in certain directions. This required an operator to re-assign way points in order to make progress on the mission. A future work involve a more autonomous high-level mission planner, able to choose such new locations on its own. Due to the wave propulsion mechanism the dynamics of the vehicle are strongly dependent on the ocean environment as the speed will vary with the waves. Strong environmental forces can make the nonlinearities in the vehicle dynamics stronger. Several times during the considered deployment the USV experienced loss in the 4G/LTE cellular connection. The Iridium satellite connection proved to provide sufficient information to monitor the status of the vehicle. However, several times the onshore operators were required to manage the missions due to the harsh weather and the possibility of infeasible paths when the wind and currents increased in strength, as described in Case 1 (Section 8.3). The onboard software supports changing way points using satellite communication. New missions consisting of a single go-to command can be uploaded to the vehicle via satellite communication, but more complex mission require a 4G/LTE cellular connection. This means that whenever the USV is using satellite communication as its primary communication channel, the onshore operators have limited ability to alter missions. A mission planner aware of the environmental conditions and forecasts may make plans which prevents unfeasible paths and thereby make the AutoNaut capable of preventing unfeasible paths by it self.

This chapter concludes the first part of the thesis. In the second part of the thesis, the designed system is involved in two applications related to oceanography and marine biology.

In the first one (Chapter 9), a satellite-USV system is proposed to enhance persistent observation of mesoscale oceanographic phenomena. The benefits and limitations of the modeled architecture, supported with simulations and experimental data, indicate the possibility to use the AutoNaut to complement satellite imagery for the study of harmful algal blooms (HAB) (as previously discussed in this chapter).

The second application (Chapter 10) concerns the study of Atlantic salmon (smolt) migration in a 90 km long fjord in Western Norway. This research shows and discusses the benefits of employing the wave-propelled USV to extend the grid of static acoustic receivers typically employed to detect tagged fish in fjords and rivers, and therefore to study their migratory behaviour.

## Chapter 9

# Persistent observation of mesoscale oceanographic phenomena

### *Modelling and simulations of a satellite-USV system*

#### 9.1 Introduction

This chapter is based on the article [39] and it describes a system designed to enhance the study of oceanographic phenomena. In the proposed architecture, satellites cooperate with in-situ marine assets, as compared to using each platform independently. The proposed architecture is composed of a space segment with a mission-specific small satellite and “traditional” Earth observation (EO) satellite data, a ground mission control center and a long-endurance wave-propelled USV, as shown in Figure 1.7 of the thesis Introduction. The satellite offers an overview of an area where the sea glider collects detailed in-situ measurements and transmits them to shore. In one variant of the system architecture, EO-data from existing satellites were used, whereas in the two other variants it is modeled how the architecture would benefit from using a dedicated small satellite, such as the HYPerspectral small Satellite for Oceanographic observations (HYPSO-1) satellite developed at NTNU.

To best exploit the capabilities of each asset, a method for optimizing the information flow between the nodes of the architecture is proposed. This involves a System-of-Systems (SoS) approach [155] for modeling and development and the solution presented can be classified as an *acknowledged SoS*. The use of an SoS approach has already been applied to other studies involving unmanned vehicles [156–158]. In particular, [159] describes the application of an SoS approach



for the detection and monitoring of forest fires involving forest-based infrared sensors, CubeSats providing early warning and communication services, and UAVs for high-resolution mapping.

The proposed architectures indicate that tight cooperation between satellites and surface marine vehicles can improve the observation of oceanographic mesoscale phenomena and contribute to increasing the data available on harmful algal bloom (HAB) phenomena, both qualitatively and quantitatively, and provide data of a higher value and timeliness to end-users. The analysis shows that while integrating existing systems will provide added information with little effort, making use of new tailor-made assets such as small satellites will improve the timeliness and the adaptivity of the observational system since the users can select the Areas of Interest (AoIs) to a greater extent than currently possible.

## **9.2 Motivation**

The oceans are continuously surveyed on a global scale by remote sensing satellite systems like Copernicus [160, 161], and even systems like Landsat provide data products, including monitoring of inland waters [162]. In addition, oceans are populated with measurement buoys (drifters) that continuously sample their surrounding environment and transmit collected data to shore for further analysis and processing [23]. As already described in the Introduction of this thesis, the network created by remote sensing buoys is expanded by remotely controlled platforms able to exploit the environment to achieve an intended navigational behavior [21, 22, 25, 27], which are not constrained by fixed position, short sensor range, lagrangian motion or limited payload energy.

As presented and discussed in Chapter 4 and 5, the control of such robotic systems is challenging task due to the unpredictability of the environment. Moreover, communication challenges such as the limited bandwidth of satellite links influence the ability to provide valuable data to shore.

In [33], a Wave Glider is used to persistently collect chlorophyll-a data for several months and validate satellite measurements. This work demonstrates that in-situ measurements provided by long-endurance marine systems can be used, in combination with satellite observations, to provide a better understanding of the natural phenomena and climate changes of the planet. The Wave Glider was also used to validate winds measured by satellites that use microwave sensors to observe the sea surface backscatter [34].

Despite the important contributions of these works, their main objective was to validate quantitatively and qualitatively the existing satellite-based ocean monitoring methods. In [35], a HAB detection system is proposed using existing satellites

(MODIS Aqua and Terra, NASA) and gives some indications on how predictions of HAB can be carried out. Moreover, the 2021 IOCCG report [36] provides more examples of HAB warning systems and how the data can be collected.

This work addresses the observation of mesoscale phenomena in the short time range, i.e., phenomena detection from satellite images and its in-situ observation using marine assets within the time scale of the phenomenon itself. Communication latency is assessed with simulations that provide insight on the spatial and temporal coordination that is needed among the involved assets. This coordination can increase the quality and amount of collected data, and contribute to our understanding of the targeted phenomena.

## 9.3 System & scenario description

One of the current limitations in space-based remote sensing is that several maritime areas of scientific and economic interests are not well covered. Examples are the Norwegian sea and Arctic areas, the coast of Chile, Canadian waters, and areas in Scotland because of aquaculture installations [36].

Small satellites in Low Earth Orbit (LEO) equipped with instruments selected for each mission and use-case can target specific AoIs with greater spectral and spatial resolution than large EO satellites at higher altitudes. The temporal resolution can also be determined by the user to a greater extent, by scheduling observations on-demand and by selecting an orbit suitable for the AoI, such as polar orbits for Arctic areas.

The following sections describe the constituent systems in the presented SoS shown in Figure 1.7 and the scenarios foreseen to support the collection of HAB data and other oceanographic data.

The system consists of a space segment and a ground segment. The ground segment includes the wave-propelled USV AutoNaut, ground stations to communicate with the satellite, and a Coordinated Mission Control Center (CMCC). Note that there is a clear distinction between the ground stations and the CMCC. While the ground stations encompass the antenna and infrastructure needed to establish the radio link to the satellite, the CMCC is where the operator is located at.

### 9.3.1 The HYPSONO satellite and ground segment

The small satellite HYPSONO is a 6U CubeSat equipped with a HyperSpectral Imager (HSI) payload featuring onboard processing of hyperspectral data based on a push-broom acquisition of data to support coordinated missions with unmanned vehicles [163]. The HSI telescope uses a Commercial-Off-The-Shelf (COTS) image sensor, COTS optical components, and in-house designed machined interfaces [164].

The design results in an unbinned signal-to-noise ratio (SNR) of 180, detects wavelengths between 400 – 800 nm with a Full-Width at Half-Maximum (FWHM) of approximately 4 nm. The onboard processing unit is built on a Zynq-7030 Xilinx PicoZed System-on-a-Chip with a Field Programmable Gate Array (FPGA) and a two-core ARM processor. This processing unit provides a configurable platform for onboard processing and software, which can be tailored to suit the mission’s needs while in orbit. The FPGA enables rapid processing of large datasets, such as the hyperspectral data, and utilizes CCSDS-123 lossless compression for image processing [165]. The configurable onboard processing of images can provide target detection and classification services to direct unmanned asset data collection. In addition, the HYPPO-1 CubeSat features an S-band radio link, a UHF radio link, and an Attitude Determination and Control System (ADCS) that allows for slew maneuvers to increase the SNR and improve the ground sampling distance [163]. While HYPPO-1 features a high spectral resolution, its spectral range and observations are limited by cloud coverage, and payload operating time is limited by energy constraints.

The space segment also includes commercially available communication systems that may be compatible with those onboard the AutoNaut. The ground segment supporting the HYPPO-1 spacecraft consists of commercially available ground communication services and an in-house ground station that communicates with HYPPO-1 and can be configured for other asset communication. These systems are interconnected through a CMCC and cooperate to deliver the requested data to the end-users.

When operational, the HYPPO-1 satellite can deliver two types of data products: “raw” HSI data and “operational” data. The former can be downloaded to the CMCC for further processing (see Figure 1.7). However, transmitting raw data to the CMCC involves some challenges. The large data volume each observation generates, combined with a limited downlink capacity, leads to a time needed for data download spanning several Ground Station (GS) passes. Thus, the resulting age of data will add up to hours and may limit the operational utility of the data itself. Instead, operational data derived by onboard processing can be tailored to different uses, such as information about the location and characteristics of a current or future phenomenon. The data budget for HYPPO-1 can be found in [163], and the assumptions and constraints for the communication links are discussed in sections 9.3.2 and 9.3.2.

### 9.3.2 Operational concept

To illustrate how satellite observations can aid in-situ observations from unmanned vehicles like the AutoNaut, three scenarios that model the information flow between the assets are explored. Scenario 1 makes use of data from existing EO-

sources, while Scenario 2 and 3 rely on a dedicated satellite, represented by HYPSON-1. Furthermore, Scenarios 1 and 2 involve the CMCC as a coordinating entity, whereas Scenario 3 does not.

In Scenarios 2 and 3, HYPSON-1 monitors an area and uses the onboard detection algorithms to determine whether the observation is a natural phenomenon of interest or not. If the retrieved information is classified as such, the satellite forwards directives to the USV. Depending on the scenario and communication mode, the information may be either relayed through an existing ground segment to the CMCC (Scenario 2), or directly transmitted to the AutoNaut employing a dedicated communication system (Scenario 3).

Despite that direct communication between the satellite and the USV could decrease latency and enable faster in-situ response, it comes with challenges related to employing a communication link and the amount of data transmitted. Moreover, the downlink capabilities onboard the USV might depend on the sea state and the amount of data to be downlinked.

Those limitations are negligible if data are first downlinked to ground, post-processed, and then transmitted to the USV in the form of a navigation and data collection (mission) plan. This process means that the data forwarded to the AutoNaut by the satellite in the second scenario must be processed operational data including a navigational plan. Once data are received onboard the AutoNaut, the onboard software modifies the goals of its current mission to steer the vehicle towards the desired location and sample the targeted phenomenon.

The three different scenarios, shown in Figure 9.1, describe how the information flow above can be achieved:

- **Scenario 1:** the CMCC retrieves data from existing space assets, like Copernicus Sentinels and other EO-satellites, and processes them to detect phenomena that should be investigated in-situ. The age of data and the predicted behavior of the phenomena must be included in the processing. In case of detection, the CMCC creates a navigation and sensors usage plan and forwards it to the AutoNaut.
- **Scenario 2:** a dedicated satellite such as HYPSON-1 monitors a selected AoI and forwards (processed) data to the CMCC. If processed data indicate an ongoing or potential phenomenon of interest, a dedicated mission is built and dispatched to the USV from the CMCC.
- **Scenario 3:** following an observation from the AoI, a dedicated satellite like HYPSON-1 processes the acquired data onboard and communicates a mission plan directly to the AutoNaut.

Physical events in the oceans are dynamic and constantly changing, and the timeliness of information delivery and data latency are important metrics to consider

## 9. Persistent observation of mesoscale oceanographic phenomena: Modelling and simulations of a satellite-USV system

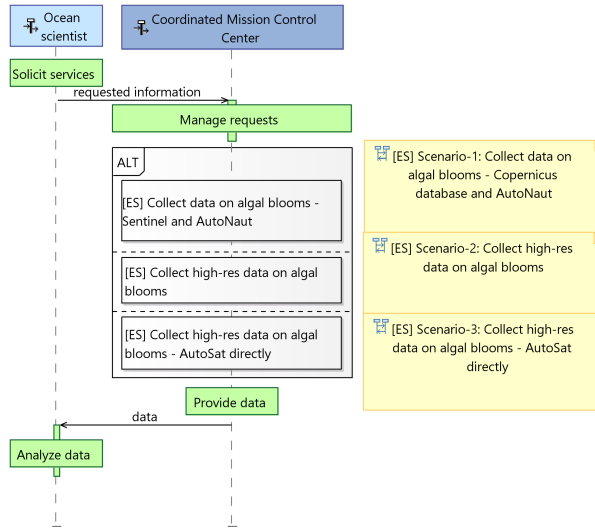


Figure 9.1: Exchange scenario (ES) overview in a lifeline format. The dashed lines indicate the lifeline of the actor, and the solid lines indicate a functional exchange between a source and a target actor. A green box indicates a function, the grey box with [ALT] indicates choices between different ES. The yellow sticky notes are there for linking between diagrams for the user.

to assess the utility of the system.

The lowest data latency and age is achieved through scenarios where onboard processing extracts the important information from the data at an early stage to minimize the data volume to downlink, and hence the time for this data transfer. Scenario 3 has the potential of providing data with virtually no delay between the satellite and the AutoNaut, given some assumptions that are discussed in detail in Section 9.3.2.

The three data distribution strategies are explored, compared and discussed in the following sections.

### Scenario 1: satellite imagery from existing infrastructures

In the first scenario, the architecture exploits existing technologies and infrastructures to gather satellite imagery of a selection of AoIs and commands in-situ assets for data collection, as shown in the top path of Figure 9.2. As discussed in Chapter 8, in the spring of 2021, the Sentinel database [166] was used to retrieve processed imagery of Frohavet (Central Norway) and coordinate in-situ observation and sampling of coastal areas typically affected by HAB. This is further discussed in Section 9.5.

Based on information from the available satellite observations, a user or a data processing tool selects an area of interest for the AutoNaut to investigate. The latency of satellite data can vary between 3 and 24 hours, depending on the chosen infrastructure (e.g., Copernicus Sentinels or other). The data spectral and spatial resolution may vary depending on the satellite source used.

This scenario requires a processing pipeline to be available. The data latency will be the sum of the age of satellite data products, the processing and commanding time, and the time needed for data collection and communication to shore from the sampling site. Whereas the time periods for information retrieval using existing infrastructures is usually known, the time required to retrieve to shore data collected in-situ depends on several factors as described in Section 9.3.3.

**Assumptions** For Scenario 1, information about the AoI is made available to the AutoNaut based on the EO data processing at the CMCC. This means that the data age is determined by the service level of the data provider,  $t_{\text{dataage}}$ . Assuming a well-programmed processing pipeline, the time for processing selected data,  $t_{\text{processing}}$ , will be very short compared with the data age. Furthermore, since this scenario uses existing infrastructure the communication delay,  $t_{\text{transmit}}$ , can be approximated to zero, since the communication delay through a 4G network or Iridium is negligible if compared to the time scale of the USV navigation capabilities (the distance covered in time) and to the time scale of the observed phenomenon. Hence, the only factor determining the freshness of the data product is the age and availability of EO data. A typical value for this parameter is in the range of 6 to 24 hours.

### Scenario 2: dedicated small satellite – CMCC – AutoNaut

Small EO satellites, such as the HYPSON-1 satellite [163], enable more agile and customized operations. The use of such systems enhances the flexibility of the operations, such as the choice of the area to be monitored and use of reconfigurable and adaptive algorithms for compression and processing of the data to be downlinked. The satellite can transmit processed information directly to the CMCC obtained from single or multiple observations. The CMCC is responsible for the definition of the mission plan that should be communicated to the AutoNaut, and hence their communication to the USV, as shown in the middle path of Figure 9.2. After making an observation, the satellite must transit from the AoI to the next available ground station until it can transmit data to the CMCC. Similar to the previous scenario, the data product latency is a sum of response time needed for image processing, downlink, ground data processing and the time relaying the connected data and mission plan to the AutoNaut.

## 9. Persistent observation of mesoscale oceanographic phenomena: Modelling and simulations of a satellite-USV system

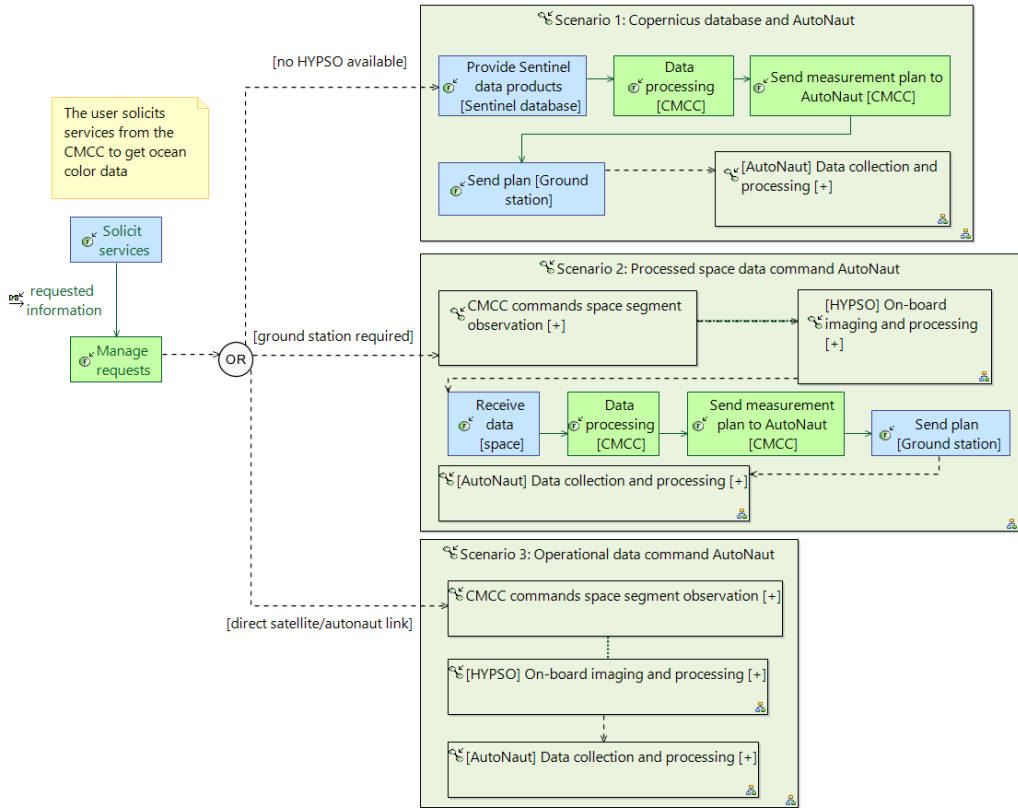


Figure 9.2: Information flow in the different scenarios is shown as functional chains. Dashed lines signify sequenced exchanges, while solid lines signify functional exchanges. The blue boxes represent functions allocated to actors, and green boxes allocated to the system-of-interest (here, the CMCC). The [+] indicates that an element can be expanded but was not in this diagram to maintain the high-level perspective and clarity.

The response time of the image processing includes uplinking to the satellite, the time it takes for the target to become observable and processed onboard.

**Assumptions** For Scenario 2, a model simulated in Python with the *PyOrbital* library is used for propagating the satellite that is set to observe a selection of AoIs. For each AoI pass, the time until the satellite passes over a ground station is computed and used as an estimate for when processed data can be delivered to the AutoNaut. The AoIs are defined by their center location to simplify simulations. Also In this case,  $t_{\text{transmit}}$  can be neglected as the navigational plan data is assumed to be around 100 bytes transmitted over either 4G or Iridium, with a minimum bitrate of 1200 bytes per second for Iridium.

Moreover, some other important considerations are:

1. Since the HYPSON-1 is not launched yet, LUME-1 is used as a representative model. Two Line Element (TLEs) are automatically obtained from Celestrak<sup>1</sup>.
2. Minimum elevation for optical target observation: 20°.
3. Minimum elevation for radio communication to ground station: 0°.
4. Only daylight passes are considered: from 8:00 to 19:00 local time.
5. Only onboard processed data are considered to reduce the data size needed for downlinking.
6. Ground station locations from the KSAT Lite network are considered, see Figure 9.4. Two simulations are compared; either using one station only, or the full network.
7. The downlink is based on S-band with 1 Mbps raw data rate.

The impact of assumption 2 is that the most extreme slant range passes are ignored, so every target is only observable one to three times a day. If assumption 5 is omitted, when transmitting raw data from the satellite, multiple passes would be needed to download the relevant data, which may take hours or days to complete [163, Table VII], heavily affecting the  $t_{\text{dataage}}$ . The total time to download data will depend on the length of the observation. Transmitting onboard processed data, such as a target position, will take only seconds under the same conditions. The satellite used for simulations is LUME-1, built for the European project Fire RS from the joint efforts of the University of Porto (Portugal), LAAS-CNRS (France), Universidade de Vigo (Spain), and Alén Space (Spain) [159].

This satellite is in a representative orbit for HYPSON-1, thus simulation results are expected to be similar to what HYPSON-1 will experience.

---

<sup>1</sup><https://celestrak.com/>



For some target areas, the satellite will see both the target and a ground station simultaneously. The simulations take this into account. Cases where the ground station contact ends at least four minutes after the observation ends to allow for processing time and downlinking are included in the simulation results. For these occurrences, both maximum, minimum and mean delays are set to zero. This also assumes that booking and scheduling of ground station passes are available so that the satellite can transmit data to the first ground station it passes over.

### **Scenario 3: dedicated small satellite – AutoNaut**

In the third and last scenario (see the bottom path of Figure 9.2), a flow of information that makes no use of ground communication infrastructure is envisaged. After a small satellite, such as the HYPSON-1, makes an observation, data is processed onboard and instructions and a navigation plan are communicated to the terrestrial assets such as the AutoNaut directly. For example, target detection can be used to create a map showing the most likely locations of a particular spectral signature [167, 168]. Either the map can directly inform the path planning or be expressed in a simpler form, such as the most probable location of a bloom.

The response time and data latency will, in this case, be the sum of the response time for imaging of the selected area, the processing time, the downlinking time, and sampled data transmission to shore.

A central topic in this scenario is how to enable the communication infrastructure between the assets. This brings forth challenges with both the physical infrastructure needed (radios and antennas) and network management.

This scenario requires that both assets know their location and the location of the other so that communication can be scheduled accordingly.

**Assumptions** The same target list and simulations as for Scenario 2 are considered. In addition, the satellite must contact the AutoNaut within a time-window that allows transmission of the navigation plan, before the AutoNaut is out of view. The data preparation (satellite onboard processing) time after observations is assumed to be less than one minute. Furthermore, the resulting data volume is assumed small enough to be transmitted over a 10 – 100 kbps link for less than one minute. The size of the navigational plan and other needed information is assumed to be similar to what is the case today, which is around 100 bytes (see the assumptions for Scenario 2). The complete specification of this link is the topic of future work. This requires the AutoNaut to be in the AoI and within satellite coverage for at least one minute after data preparation for downlinking.

### 9.3.3 Constraints

Optical sensors operating in the visible range are affected by cloud coverage and, therefore, may have limited detection capabilities. The AutoNaut capabilities of observing oceanographic phenomena can instead be impacted by storms or other weather conditions that can degrade the quality of data it provides, its maneuverability and response time (i.e., the travel time to the survey site). The encompassing system and services must consider constituent systems (CS) constraints when defining the SoS operational scenarios and CS requirements.

This section describes the high-level constraints that affect all architectural variants of the proposed system. Namely, general constraints that affect the execution of the information flow and that are common to all scenarios.

#### Wave-propelled USV constraints

As discussed in previous chapters, the AutoNaut capabilities depend on the sea state. The velocity of such vehicles is not controllable and therefore, to predict future locations, one must rely on estimates based on present and forecasted sea state. Situational awareness is achieved via onboard sensors that sample physical environmental properties and provide the vehicle control system an estimated present sea state used to adapt the navigation control parameters.

As shown in Chapter 4 and 5, stable course control can also be a challenge whenever the forces exerted by the environment dominate on steering and propulsion mechanisms, preventing the vehicle from following an intended path. The USV's speed and course are affected by waves direction, height, and frequency, and by surface currents and winds.

This has a considerable impact on the AutoNaut capability to monitor oceanographic phenomena that occur far from its current location, as the time needed to reach a destination depends on the surrounding environments.

A second major limitation is the onboard energy available (as discussed in Chapter 8). The onboard battery bank is constantly harvesting solar energy produced by deck-mounted solar panels providing the necessary power to sensors and electric steering. Significant power limitations are experienced in winter at high latitudes, where light is not sufficient to recharge the batteries, and the time span of the mission may be reduced. This impacts the possibility of observing specific phenomena as too little energy might prevent the activation of a specific sensor. Moreover, power should not only suffice for sampling specific features but also to allow data transmission to shore (e.g., via Iridium, 4G or VHF) and navigation control.

Communication is the third constraint that affects operational flexibility (also dis-

cussed in Chapter 8). The USV is equipped with three communication links that are used depending on the type and amount of information to be transmitted and the location of the vehicle. Satellite communication (for example, through Iridium) constitutes a reliable link proven to work in most areas of the globe. However, this is costly and limited by the amount of data that can be transmitted. 4G/LTE communication allows transmitting a much larger amount of data even though it is limited by distance to shore.

Data acquired onboard can be stored and transmitted over the mentioned links depending on the type of data and the vehicle location. For example, sea current information for the whole upper water column involves a large amount of data that can be easily transferred over Internet or WiFi, but cannot be sent over satellite. It is thus possible to transfer only key information over Iridium or, alternatively, let the USV navigate close to shore within 4G/LTE coverage. For example, key information about a specific water property could be the temporal average of the collected numeric values over predefined time periods.

Based on field experience, it is observed that the USV speed in the ocean fluctuates between 0 and 3 knots, depending on the sea state. Therefore it can safely assumed that the vehicle is capable of traveling in average 30 *km* per day.

Based on the time period of the phenomenon to be observed, the vehicle proximity to the targeted area is a constraint that must be considered during the mission planning phase.

### **Constraints for small satellites**

Small satellites can be an agile tool since they are relatively cheap and have a short development time [169]. As satellites such as HYPSON-1 are small, they are influenced by physical constraints leading to system constraints impacting the power/energy availability due to a limited solar array area. Moreover, the size of the satellite may restrict antenna sizes, especially in the VHF and UHF-bands.

The power constraint comes into play in the sense that only a limited part of the Earth can be actively covered at the time because there is limited energy for payload operation and data downlink.

A dedicated small satellite has the agility to accept any area of interest defined by the mission operators on short notice. Additionally, in EO missions that generate a large volume of data, both energy for operating the downlink radio leading to a time limitation, and data rates are constrained by physical antenna sizes and the availability of ground stations limits the amount of data possible to download every day.

The challenge of data volume is mitigated by performing onboard payload processing, thus compressing the data and effectively reducing the data volume by

several orders of magnitude. The limitations in coverage, the revisit time over a given area, is a function of the number of satellites in the network and can be mitigated by increasing the number of satellites and orbital planes.

For single satellites, there are some limitations in coverage and agility. The coverage area and accessibility at a given time of day are constrained but well known and defined by the satellite orbit. This can be mitigated by adding more satellites, for example, in different orbital planes. The selection of the AoI must also be done in due time before the satellite passes over a ground station prior to a target pass, so the satellite can prepare for the observation. Initially, operators will determine the AoI by selecting a coordinate for the center of the image, but the development of more sophisticated AoI geometries is a topic of future research. Moreover, adding more ground stations at suitable locations will improve agility.

The integration of autonomous sensor agents into heterogeneous networks together with satellites either as independent sensors or communication relays has been studied in several surveys and proposals [170–174]. Networking principles enabling the network integration encompassing a multitude of agents, by employing standard toolchains and efficient network protocols as well as location-aware smart routing principles are discussed in [175–177].

#### **Communication technologies and analysis**

Scenario 1 will only make use of existing communication infrastructure; both between the EO-satellites and ground systems, as well as between the CMCC and the AutoNaut.

For Scenario 2, existing radio links between the satellite and the ground stations can be employed. Correspondingly, the existing infrastructure for command and control for the AutoNaut can be used. To bind these two constituent systems together, a middleware layer with a messaging protocol must be developed and implemented.

For Scenario 3, the direct communication between the satellite and the AutoNaut must be based on new infrastructure. This is a research topic that should be further explored. It should be mentioned that the recent years have seen an increase in deployments of new satellite-based communication infrastructure, such as Internet-of-Things IoT-constellations [178] and megaconstellations such as Starlink, OneWeb or Kupier. However, the use of the megaconstellations is considered not relevant for the scenarios, as their ground terminals will be too big for the AutoNaut.

Moreover, the available IoT solutions may still not fill the gap created by low throughput, one-way data traffic, and their method of dealing with multiple access, like providing channel access for users at random time intervals. A limited

number of communication channels suitable for each proposed scenario exists.

### 9.3.4 Other architecture variants

In addition to the suggested architectures discussed as Scenario 1 and Scenario 2; there are options for how the satellite and robotic agents such as the AutoNaut can be interconnected. The satellite could be equipped with equipment creating an Inter-Satellite-Link (ISL) between the small satellite and other space-based infrastructure instead of transmitting its observations to a GS. Possible options include “traditional” satellite phone/Machine-to-Machine communication (M2M) systems such as Iridium, Globalstar and OrbComm, “traditional” broad-band satellite systems as Inmarsat and Intelsat based on Geostationary Orbit (GEO) satellites, in addition to the new megaconstellations as well as new IoT-satellite constellations. The work behind this chapter does not aim to evaluate and compare these options in full, but a brief discussion on the alternatives follows.

Previous studies encompassing mostly Iridium and Globalstar options have shown that such methods will allow for the transmission of a small amount of data, most likely to be adequate to direct the AutoNaut to an area of interest. Rodriguez et al. [179] have summarized several studies in their paper. Several activities are supported by NASA, for example, through their PhoneSat series. In [180] instead, results from an on-orbit experiment shows that an LEO satellite equipped with an Iridium transmitter is able to deliver low volumes of telemetry within a 30-minute delay, for about 90% of the time. This result is comparable to the results for sparse ground stations, described in Section 9.5.2.

Making use of networks meant for terrestrial use on-orbit, also means that there are similar constraints for parameters as Doppler shift and maximum usable range, limiting the usable service area from, i.e., the Iridium satellites [180]. In addition, more constraints follow from the combination of orbits, where the inclination has the largest effect. This leads to the case that ISL to low-inclined services (such as OrbComm, Globalstar) are not ideal for polar-orbiting satellites. The same will be the case for crosslinking from LEO to GEO for Inmarsat services, for example.

## 9.4 Methods

### 9.4.1 Description of workflow

A simple workflow shown in Figure 9.3 was followed for the research provided in this chapter. In the *Modelling and developing operational concept* phase, a combination of a whiteboard, virtual meetings and drawings, and discussions to develop

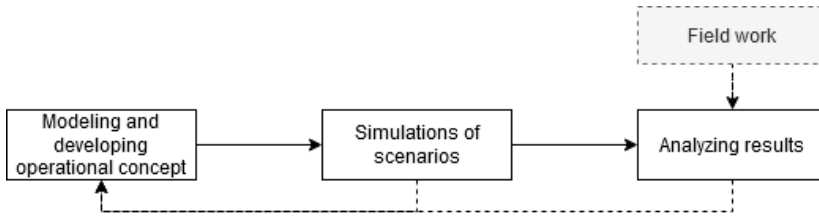


Figure 9.3: The workflow applied in this work.

the operational concepts was used, along with a literature survey to identify relevant AoIs. These operational concepts were modeled in the Capella<sup>2</sup> software and iterated on through discussions. In the *Simulations of scenarios* phase, the scenarios were set up for the simulations with the assumptions given for each scenario in Section 9.3.2. In the phase *analysing results*, the objective was to improve the simulations, the scenarios and ensure that the assumptions were valid. Moreover, the AutoNaut experimental data were used to validate the results, and to provide feedback to the assumptions and simulations.

### 9.4.2 Tools used

In this analysis, the Arcadia method [181] with the open-source Capella software tool were used to support the Model-Based Systems Engineering (MBSE) effort and provide an operational and logical architecture of the SoS [64].

The system model enables the representation of the architecture with different viewpoints, such as “exchange scenarios”, “context diagrams”, and “architecture diagrams”. There are also possibilities for integration with domain-specific tools such as System Tool Kit (STK), that can be used to demonstrate the quantitative performances of the proposed SoS.

Additional simulations have been performed using Python, in particular using the *pyorbital* library. This library calculates orbital parameters and computes other astronomical parameters from satellites’ TLEs. The TLEs are collected from Celestrak.

### 9.4.3 Selection of Areas of Interest

The objective of the SoS is to detect but also sample in-situ oceanographic phenomena remotely. It was chosen to observe areas that have historically been affected by phenomena such as HAB. Since HAB can result in the death of farmed fish; the targets selected for the simulations are areas where fish farming is common. The selected targets are popular areas for fish farming, and where HAB may occur

<sup>2</sup><https://www.eclipse.org/capella/>.

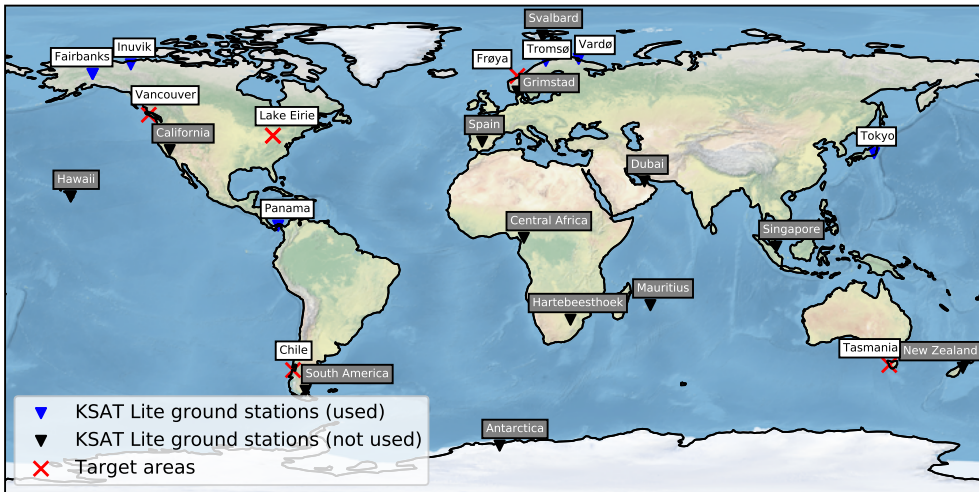


Figure 9.4: Areas of Interest and considered ground stations. The ground stations with blue symbols and white labels were selected by the simulator, the stations with black symbols and grey labels were available but not used. The areas of interest are indicated with a red cross.

(see [182] for an overview). These are the Norwegian Atlantic coast near Frøya, the coast of Chile south of Puerto Montt, the coast of Canada near Vancouver Island, the coast of Tasmania in Australia and Lake Erie [183], a fresh-water lake in the US where HAB are common. These locations and the considered ground stations are shown in Figure 9.4.

#### 9.4.4 Communication delay estimation

One of the key metrics for evaluating the performance of the data flow and utility of the SoS is the data delay, meaning the time from observation to the data is available for the AutoNaut. In this case, the “data” is the navigational plan and all information needed for the AutoNaut to perform its operations. The time for returning samples and analysis from the AutoNaut will be the same for all three scenarios, so this duration is omitted in further discussions.

Equation 9.1 shows how estimate the total delay in time ( $t_{total}$ ) is estimated, between the time an oceanographic event of an AoI is observed, and the time the AutoNaut is notified and commanded to investigate this event in-situ.  $t_{dataage}$  is the age of the observation data until it is processed either on ground or in-orbit,  $t_{processing}$  is the time spent for data processing and  $t_{transmit}$  is the time it takes to transmit a set of commands to the AutoNaut.



For Scenarios 1 and 2,  $t_{\text{transmit}}$  is assumed to be equal since both cases rely on using the same communication infrastructure from the CMCC to the AutoNaut. The value for this delay is in the range of hundreds of milliseconds to a few seconds, based upon 4G or Iridium. The range for the processing time,  $t_{\text{processing}}$ , is from seconds to a few minutes. The value for  $t_{\text{transmit}}$  is assumed to be less than two minutes. This is based upon the assumptions for the communication links listed above and the size of the navigational plan, which is about 100 bytes.

$$t_{\text{total}} = t_{\text{dataage}} + t_{\text{processing}} + t_{\text{transmit}} \quad (9.1)$$

### 9.4.5 Simulations

Based on the above assumptions, a Python program was implemented to generate a set of times for when the satellite can observe the targets, and deliver the observational data either to the CMCC through a ground infrastructure (Scenario 2), or directly to the AutoNaut (Scenario 3). For Scenario 2, two different simulations were performed, one with only one ground station, and one with all the ground stations of the KSAT Lite network available.

The function called `get_next_passes`<sup>3</sup> from `pyOrbital` library was used to estimate when the satellite was over the ground stations and the target areas. The main parameters specified for the simulations are: start date [exact date and time to start the simulations], number of hours to simulate, coordinates of observation location [longitude and latitude], altitude above sea level and minimum elevation for contact between location and satellite [minimum elevation for a pass]. The simulation start date was set to 2021-06-09 16:00 UTC and the time to simulate for a week. First, all possible passes over the targets and the ground stations are computed. The passes over the targets are limited to those during daylight [between 8:00 and 19:00 local time]. For each target pass, the delay is estimated as the difference between the start time of each ground station pass and the end time of the target pass. When the difference between the end of a ground station pass and the end of a target pass is longer than a minimum communication window, the delay is saved. The ground station whose pass offers the minimum delay after an observation of a target is considered the first ground station used. The maximum delay and the mean delay are calculated for each target pass. The simulations are performed both for a sparse ground station network [just one ground station] and dense ground station network [where six ground stations are used].

## 9.5 Results

In this section, the different scenarios and their utility are explored.

<sup>3</sup><https://github.com/pytroll/pyorbital/issues/22>



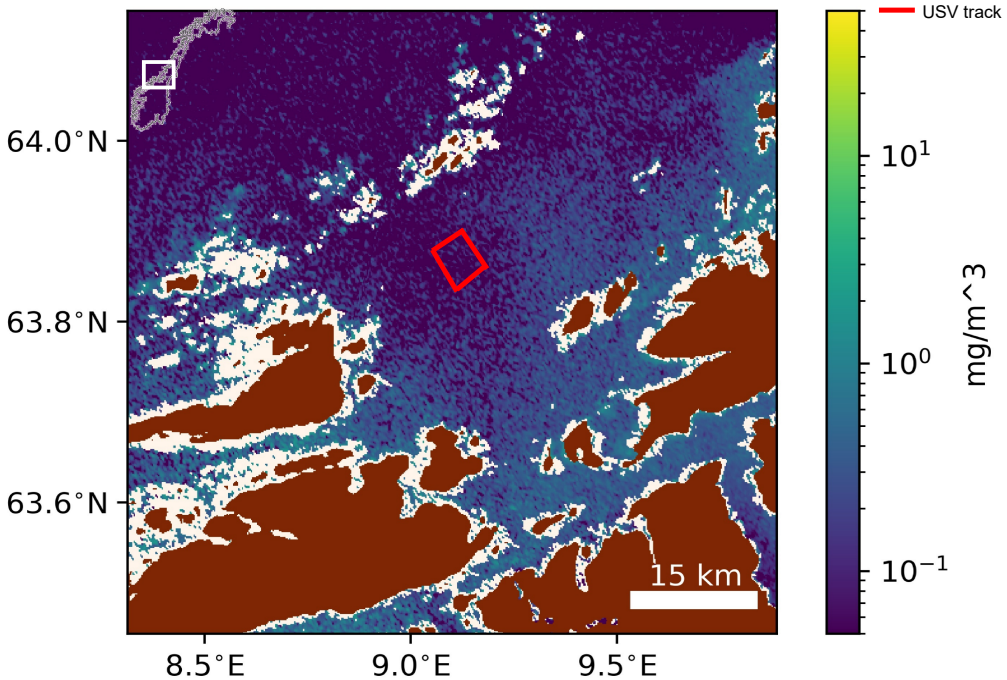


Figure 9.5: Sentinel-3 imagery of chlorophyll-a concentration in Frohavet (Central Norway) on March 14, 2021. The AutoNaut track in Frohavet is shown in red. In the top left corner the location of Frohavet in Norway is depicted.

### 9.5.1 Scenario 1: coordinated observation of HABs

The information flow described in Scenario 1 was tested in the field in spring 2021, in the context of HAB coordinated observation involving both aerial and terrestrial platforms (see Chapter 8). This experiment involved several manned and unmanned robotic assets for a duration of over one month and the objective of the field campaign was to study the algal bloom at different space and time scales, from satellite observations of the whole Frohavet region down to the underwater sampling of the epipelagic (upper) water column. In particular, satellite-based imagery was acquired from Sentinel-3, Terra and Aqua (MODIS data) and PRISMA<sup>4</sup> when available. The imagery, see Figure 9.5, recorded on March 14th was used to monitor the growth of the algal bloom in the operational area and assist with high-level mission planning and coordination of the involved robotic platforms gathering in-situ measurements.

<sup>4</sup><https://www.asi.it/en/earth-science/prisma/>

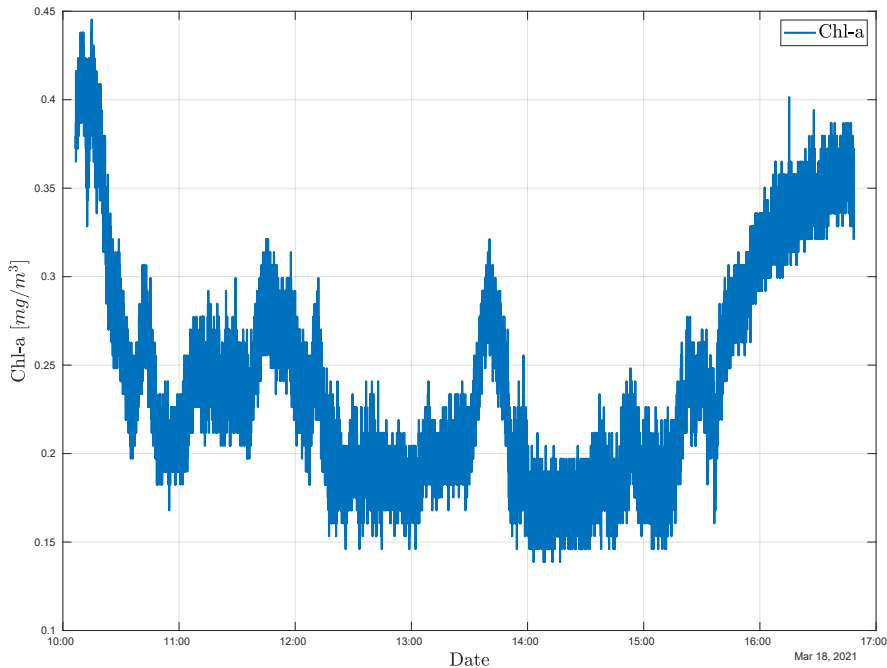


Figure 9.6: In-situ chlorophyll-a measurements collected by the AutoNaut in Frohavet.

Among the assets, the AutoNaut was the first deployed, and it provided the overall mission insight into how algae grew and multiplied in the period leading up to the bloom. As described in Chapter 8, the AutoNaut was at sea for a total of 24 days, collecting and transmitting data continuously over 4G and Iridium. In addition to providing additional long-term insight into the algal bloom dynamics itself, the USV collected data to be used to validate hyperspectral cameras carried by the UAV and airplane involved in the mission.

Figures 9.5 and 9.6 also show the track covered by the AutoNaut in Frohavet on March 14th and the surface chlorophyll-a data collected in-situ. It can be observed that the surface chlorophyll-a measurements performed by AutoNaut validate the Sentinel-3 observations in the same area.

### 9.5.2 Scenario 2: satellite – CMCC – AutoNaut

The delay from an observation to the CMCC was simulated for two different sub-cases; one with only one ground station available. Svalbard is selected as it is seen by all revolutions by a polar orbiting satellite. This is called a *sparse* ground station distribution. The second run, where all the ground stations of KSAT Lite network

9. Persistent observation of mesoscale oceanographic phenomena: Modelling and simulations of a satellite-USV system

	Delay stats for single GS			Delay stats for GS network		
	min	max	mean	min	max	mean
Lake Erie (USA)	06:38	07:59	06:59	01:53	03:34	02:31
Western coast of Chile	29:58	31:08	31:08	05:56	10:40	07:42
Tasmania (Australia)	27:46	28:28	28:09	12:25	15:01	12:22
Vancouver (Canada)	05:40	06:59	06:08	00:00	00:00	00:00
Frøya (Norway)	00:00	00:00	00:00	00:00	00:00	00:00

Table 9.1: Statistics for dense and sparse ground station coverage (mm:ss) for one week, showing the delay from end of an observation to the first available ground station.

were available, is called *dense* ground station coverage. This delay will give an estimate for the  $t_{\text{dataage}}$  for this scenario.

The simulation is run for one week starting from the 9th of June 2021. The satellite orbit is based on TLEs for the LUME-1 satellite, received from Celestrak. LUME-1 moves south-to-north over Western Europe during daylight hours. In both cases it is assumed that the AutoNaut is within 30 km of the center of the AoI, as this is the range the AutoNaut may navigate during the day.

### Sparse ground station coverage

For Scenario 2, the satellite will acquire and process the data, before it needs to reach a GS to forward the data to the CMCC for final processing and forwarding to the AutoNaut.

With  $t_{\text{transmit}}$  in this case being similar to Scenario 1,  $t_{\text{processing}}$  is similar to Scenario 3, it is again  $t_{\text{dataage}}$  that will be the driving factor for  $t_{\text{total}}$ .

From the column named *Delay stats for single GS* in Table 9.1, it can be noticed that for a single ground station, the delay (meaning the duration after an observation until the satellite can reach the ground station at Svalbard) varies from about 0 minutes for the Frøya target to about a half hour for Chile and Tasmania targets. This duration/delay corresponds to the value for the parameter  $t_{\text{dataage}}$  in Equation 9.1.

### Dense ground station coverage

Column *Delay stats for GS network* in Table 9.1 shows the results for the minimum time after an observation until the satellite reaches a ground station, given the

	<i>Inuvik</i>	<i>Panama</i>	<i>Tokyo</i>	<i>Fairbanks</i>	<i>Vardø</i>	<i>Tromsø</i>
<b>Lake Erie</b>	7	0	0	0	0	0
<b>Chile</b>	0	8	0	0	0	0
<b>Tasmania</b>	0	0	7	0	0	0
<b>Vancouver</b>	3	0	0	6	0	0
<b>Frøya</b>	0	0	0	0	4	10

Table 9.2: Count of first ground station used after each target for the simulated period.

availability of the full KSAT Lite ground station network. From the simulations, it can be observed that the mean time to reach a ground station varies between 0 and less than 13 minutes, depending on the target location. For all targets with a delay larger than 0, there is a reduction compared to the sparse ground station setup. Tasmania and Chile targets get their mean delays more than halved.

The number of instances for when a ground station was the closest after a target observation is shown in Table 9.2. Such mapping can also be used to derive and plan which stations should be utilized, and which stations can be removed to reduce cost, for example. Since the satellite is in an Sun-Synchronous Orbit (SSO) type orbit, where focus is on daylight passes only, the same ground stations will be utilized every time. From the table, it can be noticed that maximum two stations are needed for each target. In this particular case, it is observed that Inuvik is the station that may collect data from the highest number of targets.

### 9.5.3 Scenario 3: direct communication between satellite and USV

For Scenario 3, the observation time (including onboard processing) represents the value for  $t_{\text{dataage}}$ , and is in the range of one to two minutes [163].

The short onboard processing time,  $t_{\text{processing}}$ , (about one minute) allows for transmission of a short message to the AutoNaut immediately after an observation is made, given that the AutoNaut is in the vicinity of the AoI. The observation time is set to 2 minutes for all occasions, starting when the satellite is at Acquisition of Signal (AOS). This is following the operational concept of the HYPSON-1-mission [163] plus a one-minute margin. This numeric results (hh:mm:ss) are depicted in Table 9.3. In this case, the value for  $t_{\text{transmit}}$  will be in the order of seconds for trans-

9. Persistent observation of mesoscale oceanographic phenomena: Modelling and simulations of a satellite-USV system

Target	Target AOS	Target LOS	Target max duration	Target obs. end	Autonaut LOS	Avail. time for comms
Lake Erie	15:16:35	15:21:15	00:04:40	15:18:35	15:24:34	00:05:59
Chile	13:20:37	13:23:01	00:02:24	13:22:37	13:27:14	00:04:37
Chile	14:53:50	14:56:43	00:02:53	14:55:50	15:00:42	00:04:52
Tasmania	00:44:48	00:48:53	00:04:05	00:46:48	00:52:29	00:05:41
Vancouver	18:50:53	18:55:16	00:04:23	18:52:53	18:58:42	00:05:49
Frøya	07:32:35	07:34:46	00:02:11	07:34:35	07:38:54	00:04:19
Frøya	09:04:29	09:09:19	00:04:50	09:06:29	09:12:35	00:06:06

Table 9.3: Simulations of target observations and communication windows (UTC hh:mm:ss) to the AutoNaut.

mission of navigation coordinates and instructions. The total delay  $t_{\text{total}}$  is within two to three minutes, proving that near real-time operations can be achieved.

Table 9.3 shows all daylight passes for the 16th of April 2021. The columns indicate when the target is visible which is the time between *Target AOS* and *Target LOS*. This gives a total possible observation time. Furthermore, 2 minutes was chosen as the actual observation time, leaving a given duration available for processing and communication between the observation end and the AOS-event for the AutoNaut.

## 9.6 Discussion

In this chapter, three different architecture variants are considered and evaluated through simulations. The main results focus on the HAB use-case. The architecture variants are generic but are exemplified and evaluated through simulations employing properties of the HYPSON-1 satellite and the AutoNaut as example implementations.

The main advantage of the proposed solution is that the multi-asset and multi-sensor approach can enable near real-time coordinated oceanographic observations of HAB, which are challenging to detect and classify.

### Main results:

- In Scenario 1, the  $t_{\text{total}}$  is expected to be 3–24 hours, based on the “publishing time” for traditional EO-data. This limits the operational real-time use of this

type of data. In addition, the AoIs cannot be selected by the end-user.

- In Scenario 2, the mean value of  $t_{\text{total}}$  is less than 16 minutes for a dense ground stations network, and less than 30 minutes for all selected targets if only a single ground station is used.
- In Scenario 3, the  $t_{\text{total}}$  is estimated to be on the order of 1–3 minutes, given the assumptions.

Even without direct contact between a satellite and a USV, it is possible to transmit fresh EO-data from a remote sensing satellite to an in-situ vessel as the AutoNaut within 30 minutes for most cases. The use of onboard processing and existing infrastructure will make this scenario possible with little cost and effort. Depending on resources and delay requirements, one or more GSs from a commercial ground station supplier can be used to achieve this. Which GS to use can be decided based on simulations, as shown in this chapter. A CMCC must be in place, integrating the communication satellite and the USV(s) through a common middleware layer.

### 9.6.1 Scenario evaluation

The three scenarios are analysed and discussed in the following.

#### Scenario 1

In Scenario 1, no efforts are needed to ensure periodical delivery of the required imagery. Moreover, several EO data sources are accessible for no cost. Despite these advantages, the chosen services and infrastructures are not configurable, so the end-user cannot select the AoI the EO-satellites will observe and have instead to rely on historical data and a “best-effort” revisit time. Moreover, the age of the observational data is arbitrary and near “real-time” operation with a data age requirement of less than 6 – 24 hours cannot be supported. This would affect the in-situ observation and sampling of targeted phenomena which are commonly defined in a limited time frame.

A processing pipeline for selecting/filtering and processing of the EO data must be created, and can be based on existing frameworks and technologies. In addition, a middleware layer integrating the processing pipeline and the commanding software for the AutoNaut must be developed, but no other infrastructure will have to be developed. An example of this scenario is provided in Section 9.5.1, where satellite imagery from existing infrastructure is used to command marine and aerial assets with the purpose of observing a HAB.

## **Scenario 2**

In Scenario 2, the time between a dedicated satellite observation until this data can be for instructions and navigation plans for the AutoNaut is estimated. Similar to Scenario 1, this scenario also relies on existing infrastructure, except for the need of an CMCC with a processing pipeline and middleware layer able to integrate messages between the satellite and the AutoNaut.

A dedicated satellite that can be commanded to observe selected AoIs may deliver information to the AutoNaut 30 minutes later (depending on the target locations), even if only one ground station is used. If a full GS network is used, this time can be further reduced, down to about 15 minutes. As shown, targets within Arctic/sub-Arctic areas are close to existing GSs; thus the time between an observation and a downlink pass may be close to zero.

Even with using only one ground station, it can be observed that for the case of Frøya (Central Norway) the satellite will see both the target area (Frøya) and the ground station (Svalbard) at the same time for part of the observation pass. This means that the data can be downloaded immediately after processing. For the simulation, useful communication passes must end at least 4 minutes after the observation ended, in order to have time to do both processing (limited to one minute, similar to Scenario 3) and perform downlinking in a reasonable time. All passes in this simulation leave more than 5 minutes for downlinking.

When making the full GS-network available for the simulation, the simulator will choose the closest usable ground station in each case. For example, the assumed best station (Svalbard, as it is seen from all satellite orbital passes) is not used since other stations can pick up the signal from the satellite earlier. In addition to utilizing existing infrastructure, the main advantage of Scenario 2 is that satellite data can be requested and retrieved on-demand. Onboard data processing will reduce the size of data to be transmitted to ground, thus reducing energy for operation of the radio system as well as the time to download the data. Selecting the number and locations of GSs will impact the response time of the system, and possibly also influence the cost of ground station lease, depending on the commercial model of the ground station provider (if accessing more than one GS costs more than one, or if it only is the time of access that determines the cost.)

## **Scenario 3**

The main advantage of Scenario 3 is that, depending on the communication delays between the satellite and the USV, the closed-loop from space observation to in-situ sampling and data analysis onshore observation of an oceanographic phe-

nomenon can be achieved with lower data latency and time responses compared to Scenario 1 and Scenario 2. Despite such benefits, this implementation comes with some limitations concerning the data processing capabilities onboard both assets, the need of resilient algorithms for human supervision/intervention and a robust communication link between the assets. The possibility of adding onshore processing and data from other sources in Scenario 2, as the CMCC can make use of larger computational capabilities to run complex metocean models on the base of satellite observations, may outweigh the gain of a faster response in Scenario 3. This could help to optimize the missions commanded to terrestrial assets and thus the quality of data retrieved to shore.

The analysis indicates that an architecture like the SoS presented in this chapter can be used for tailored and adaptive observation systems, adapted to their specific target areas. The commonality of a generic architecture consisting of satellite(s), a CMCC, and in-situ agents can be utilized to observe a variety of oceanographic properties and geographic regions. The specific satellite and in-situ platform and instrument can be adapted to season or other properties.

The specific properties of the different architecture variants can be exploited to match different purposes, and they come with different costs for implementation and resources for realization. Scenario 1 is available today, as demonstrated in the field experiment of Section 9.5.1. The real-time constraints of this scenario as well as the limitation in an active selection of AoIs, motivates the exploration and development of Scenario 2 and Scenario 3.

Like Scenario 1, Scenario 2 is available with existing technology, or technology available in the near future. Scenario 2 can provide fresh data, both for a dense and sparse ground station topology. The cost of using more ground stations has to be traded against the gain of getting data up to 1 to 20 minutes earlier. Optimal ground stations can be chosen based on target selection and similar simulations, as shown in this chapter. Even though the difference in data delivery times between those scenarios is on the order of 30 minutes in favor of Scenario 3, the architecture variant of Scenario 3 represents the possibility of tighter integration between sensor agents, without the need of a CMCC.





## Chapter 10

# A persistent sea-going platform for robotic fish telemetry

### *Technical solutions and proof-of-concept*

Over the last few decades, sea-going unmanned surface and underwater vehicles (USVs and UUVs) have found widespread use as flexible, persistent and cost-effective platforms for ocean observation [184]. The idea of equipping such robotic vehicles with fish telemetry receivers represents an emerging approach with the potential to significantly advance the current operational limits of fish movement studies [185]. Such mobile receiver platforms may operate independently or as additional resources to mitigate coverage issues and the consolidation of passive receiver systems. Moreover, the ability to dynamically relocate receiver resources to areas of particular interest or high activity will make adaptive sampling strategies possible, which could in turn optimise coverage and increase data yield [186]. Adaptive sampling requires (near) real-time availability of detection data in a networked system of stationary and mobile receivers, and although not common in passive acoustic telemetry yet, real-time solutions for these systems have been demonstrated and used in several studies [187, 188]. USVs and UUVs will usually include one or more long-range telecommunication links for remote monitoring and control purposes, either through satellite, cellular or other proprietary services. Using these communication capabilities during fish tracking experiments will increase situational awareness and facilitate a more agile approach to the planning and management of such experiments. Robotic ocean observing platforms also come with the additional benefit of producing simultaneous high-resolution measurements of the proximal ocean environment. These platforms typically carry with them a range of sensors for essential ocean variables, such as sea temperature, water quality parameters, water currents, chlorophyll, plankton and fish aggrega-

tions [184]. These data would otherwise require dedicated resources and can be hard to obtain with sufficient temporal and spatial resolution when fish actually reside within a particular area, despite being key information for interpreting and understanding the movement patterns of fish.

An increasing number of studies have been reported over the last few years where unmanned marine vehicles have been employed in acoustic fish telemetry studies. With their ability to dive directly into the fish habitat and survey deeper waters, underwater vehicles of various designs appear so far to be the most commonly used vehicle type for carrying acoustic receivers [189–193]. Autonomous underwater vehicles (AUVs) with electric thrusters are relatively fast and have field-proven capabilities of detecting and localising acoustically tagged fish [185, 194, 195], but onboard energy resources strictly constrain mission times for these platforms, and they often require proximity to ship or shore for communication and navigational assistance. However, the integration of acoustic receivers into underwater gliders that feature an energy-efficient buoyancy-driven propulsion mechanism mitigates this energy limitation to a large extent and enables long-term unassisted fish tracking missions even in remote oceanic regions [196–198]. On the other hand, underwater gliders are relatively slow and can experience large offsets in position due to sea currents, which can cause challenges with manoeuvring in shallower and more confined waters. Like underwater gliders, surface gliders are less constrained by onboard energy limitations with respect to propulsion, but can, in addition, carry a more extensive sensor suite, harvest solar and wind energy for powering of payload and auxiliary propulsion, and can, unlike underwater vehicles, keep telecommunication links operational and uninterrupted throughout missions due to their continuous surface access. These properties make surface gliders an interesting option as mobile long-endurance robotic receiver platforms in acoustic telemetry studies, and the utility and performance of such platforms have been explored and demonstrated in several recent studies using the Liquid Robotics Wave Glider [199–201].

This chapter is based on the manuscript [62], submitted to the *Frontiers in Marine Science* journal, which presents a technical solution where a contemporary acoustic receiver is integrated as a system-level payload on the AutoNaut, essentially creating an energy autonomous robotic fish telemetry platform. The deep integration of the receiver with the control and telecommunication system of the USV provides real-time transmission of fish detections to an operator for remote piloting of the vehicle, and prepares the vehicle itself for increased situational awareness and autonomous control during vehicle-fish encounters. The vehicle's capacity to detect a small acoustic fish tag at different ranges and propulsion modes is investigated through a field trial, and the resulting detection probability for different

vehicle-fish "sail-by" scenarios is estimated through simulations. Finally, a proof-of-concept study where the AutoNaut was deployed in a Norwegian fjord during the seaward migration of Atlantic salmon smolts and demonstrate that the vehicle was able to detect a tagged smolt at the fringe of the open ocean beyond the reach of the fjord's stationary receiver grid.

## 10.1 Methods

This section discusses the integration of the TBLive, a real-time acoustic fish telemetry receiver, into the instrument payload onboard the AutoNaut. During normal operations when waves propel the vehicle, the AutoNaut is a silent platform. This makes it well-suited for the application considered in this chapter where acoustic noise levels need to be kept low in order to optimise hydrophone performance and fish detection capabilities. Moreover, the USV's autonomy and long-endurance capabilities make its employment suited for the study of slowly evolving, yet spatially and temporally extensive processes such as the migration of salmon post-smolts and other fish of moderate size, as demonstrated in this chapter of the thesis.

### 10.1.1 Integration of acoustic receiver

#### Receiver properties

The acoustic fish telemetry receiver used in this work is the TBLive<sup>1</sup> (Thelma Biotel AS<sup>2</sup>, Trondheim, Norway), a digital multi-channel receiver for detection of acoustic tags in the frequency range 63 - 77 kHz. The unit features a cabled RS-485 real-time communication interface and a time pulse input from a GNSS source for precise high-resolution time-stamping of tag detections. The TBLive runs a proprietary software on an advanced digital signal processing unit. The processing algorithm dynamically tries to maintain high acoustic performance even in noisy environments and further reduces signal collision events by singling out the strongest when multiple signals are present.

In addition to its main task of decoding R-coded acoustic tag detections [50] and sending these in real-time over its communication interface, the receiver provides measurements of background noise level and water temperature. The receiver consumes less than 45 mW of power depending on the number of channels monitored.

---

<sup>1</sup><https://www.thelmabiotel.com/wp-content/uploads/tb-live-datasheet-1.pdf>

<sup>2</sup><https://www.thelmabiotel.com>

Field N°	Sample	Description
0	\$	Start of String
1	1000041	TBLive serial number
2	1589557002	Timestamp in UNIX time
3	615	Timestamp in milliseconds
4	S64K	Transmitter Protocol
5	1234	Transmitter ID number
6	0	Transmitter Data Value
7	21	Detection Signal-to-Noise Ratio (SNR)
8	65	Detection Frequency in kHz
9	19	Number of strings sent since power up
10	\r	End of String

Table 10.1: Acoustic detection sample

### Acoustic detections

When a coded acoustic signal has been detected and recognized by TBLive a CSV-formatted ASCII-string is printed on the serial line. The string leads with \$ and terminates with \r, as described in Table 10.1 for the ASCII message \$1000042,1589557202,615,S64K,1285,0,24,69,11.

The hydrophone automatically relays acoustic detections using the versatile industrial standard RS-485. The sensor output is picked up by DUNE, that stores it and broadcasts it in the onboard local network.

### Hydrophone performance

The hydrophone listening capabilities are observed through log messages periodically outputted by the sensor, whose format is shown in Table 10.2. The information contained in this messages is useful to characterize the environment in which the sensor operates and indicates the presence of acoustic noise, that limits the hydrophone ability to detect acoustic messages.

Field N°	Sample	Description
0	\$	Start of String
1	1000041	TBLive serial number
2	1589557002	Timestamp in UNIX time
3	TBR Sensor	Identifier for Log Messages
4	297	Temperature in Kelvin
5	11	Average background noise
6	39	Peak background noise
7	61	Detection Signal-to-Noise Ratio (SNR)
8	19	Number of strings sent since power up
9	\r	End of String

Table 10.2: Sensor log sample

### Physical integration

As described in Chapter 3, the vehicle carries a heterogeneous scientific payload that collects information about a wide range of environmental variables. The receiver is installed on the 27 cm long vertical keel near the longitudinal centre of the vehicle in order to maximise the distance between the sensor and the sea surface and hence decrease the potential noise effects due to proximity to the boundary layer (see Figure 10.1). The keel also hosts an Optode4835 oxygen sensor<sup>3</sup> and an ECO Puck Triplet<sup>4</sup>. Whereas the latter measures light scattering and fluorescence to determine primary production features of the upper water column, the former provides information about the oxygen concentration based on fluorescence quenching. Both are optical instruments and are therefore not expected to interfere with the hydrophone measurements, despite being tightly integrated at the end of the instrument keel. The TBLive also protrudes 6 cm deeper than the other two sensors to ensure an unobstructed acoustic path to the hydrophone. The TBLive power and communication cable is terminated to a wet-mateable SubConn bulkhead connector that penetrates the hull inside the base of the instrument

<sup>3</sup>[https://www.aanderaa.com/media/pdfs/d385\\_aanderaa\\_oxygen\\_sensor\\_4835.pdf](https://www.aanderaa.com/media/pdfs/d385_aanderaa_oxygen_sensor_4835.pdf)

<sup>4</sup><https://www.seabird.com/eco-triplet-w/product?id=60762467721>

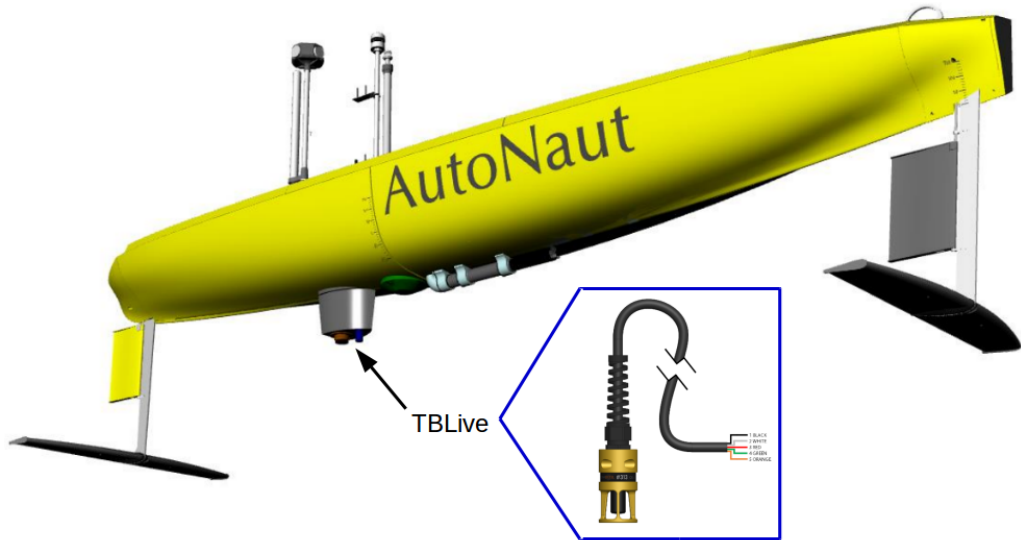


Figure 10.1: 3D model of the AutoNaut USV showing the underwater wave foil propulsion system and the sensor payload connected to the hull and the keel. The acoustic receiver TBLive (inset) is mounted to the end of the protruded instrument keel at 50 cm depth.

keel and provides connection to the AutoNaut’s scientific payload control unit, as depicted in Figure 10.2.

### Software integration

Onboard the AutoNaut, the receiver is controlled by a dedicated software module running in DUNE, a software framework designed with strong emphasis on flexibility in the configuration of sensors and on data collection and transmission over different communication interfaces [175]. The TBLive talks through an NMEA0183 inspired protocol over an RS-485 serial line to the Level 3 computer, which interprets and converts receiver tag detections and sensor readings (noise level, water temperature) to DUNE IMC messages and shares them with other onboard computers for transmission to shore over Internet or Iridium Satellite upon request. As shown in Figure 10.2, a 4G/LTE modem onboard the USV allows continuous, two-way communication to shore over the Internet. This enables a continuous real-time monitoring of fish detections and receiver performance via two different user interfaces.

As described in previous chapters, the vehicle operators make use of the graphical command and control user interface Neptus [98], which is also a part of the

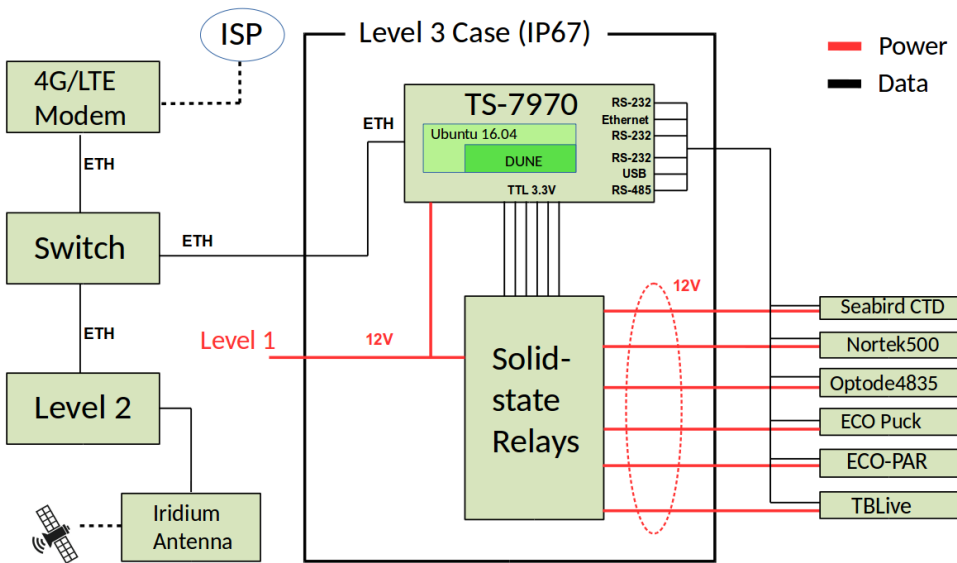


Figure 10.2: Hardware architecture of the AutoNaut control, communication and payload management system. Sensor data collected by the *Level 3* scientific payload control unit include fish detections from the TBLive and are shared in real-time to the *Level 2* vehicle control computer over Ethernet, where they are available for the USV control and navigation system.

LSTS Toolchain [175]. Since the Neptus interface is mainly intended for vehicle control and management, an ancillary GUI was developed to provide scientific personnel such as biologists and oceanographers with real-time sensor data related to fish detections and the ocean environment. Again, the scientific data GUI was implemented using the public Grafana HTTP API (see Chapter 3), which displays timestamped data from all sensors and georeferenced fish detections on a scalable map in terms of an interactive Grafana dashboard (see Figure 10.3). The Grafana dashboard permits inspection and comparison of environmental properties (e.g., water temperature, salinity, oxygen concentration, sea current profiles, weather data) both at the time of detection and for subsequent offline analysis to facilitate studies migration processes and fish behavior within an environmental context.

### 10.1.2 Tag detection performance

#### Detection range model and test

The underlying physical mechanisms determining whether the moving USV will detect (or not detect) an acoustic tag transmission are notoriously complex and



## 10. A persistent sea-going platform for robotic fish telemetry: Technical solutions and proof-of-concept

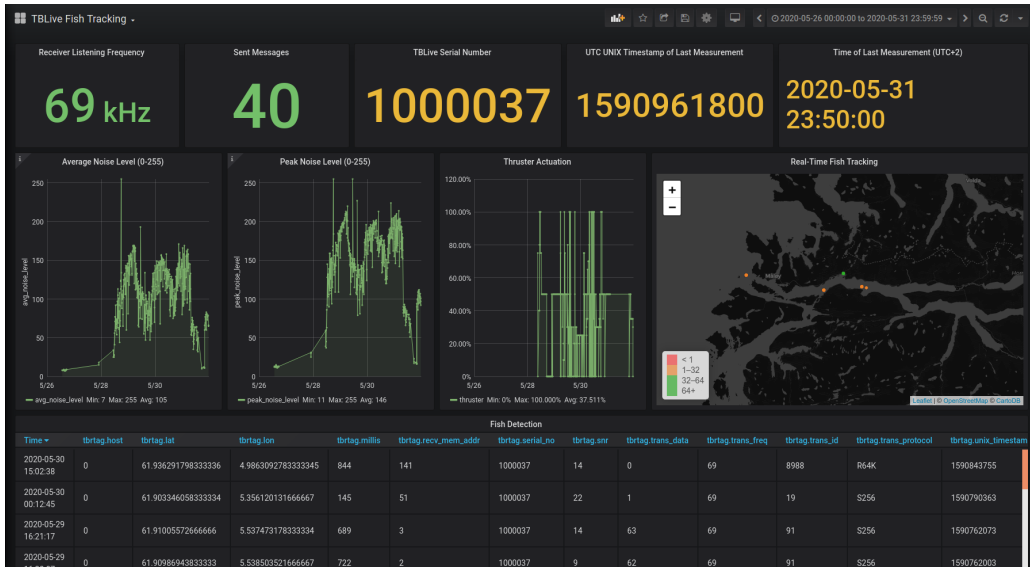


Figure 10.3: The fish tracking dashboard of the Grafana real-time monitoring interface. Information is constantly updated as the USV navigates in areas with 4G/LTE coverage.

depend on the properties of the highly dynamic acoustic channel as well as characteristics intrinsic to the receiver, the transmitter and the vehicle itself. However, as shown by e.g., [202], detection probability as a function of range and other conditions can be modelled using a logistic relation as a simple, but feasible approach. A tag transmission may be regarded as a Bernoulli trial [203] represented by a binary random variable  $Y$  with outcomes “detected” ( $Y = 1$ ) or “not detected” ( $Y = 0$ ). Using the distance to the tag  $x$  as the predictor, the probability  $p$  of making a detection can be modelled as a logistic function by assuming that the logarithm of the detection odds  $p/(1-p)$  is linearly dependent on distance:

$$\ln\left(\frac{p}{1-p}\right) = \hat{\beta}_0 + \hat{\beta}_1 x. \quad (10.1)$$

Solving for  $p$  gives the detection probability:

$$p = P(Y = 1|x) = \frac{1}{1 + e^{-(\hat{\beta}_0 + \hat{\beta}_1 x)}}, \quad (10.2)$$

which predicts a sigmoid relationship between the detection probability and the distance to the tag, where  $\hat{\beta}_0$  and  $\hat{\beta}_1$  are regression coefficients.

The regression coefficients were estimated from data collected by conducting a controlled field experiment in the Trondheim Fjord (Central Norway). An acoustic

transmitter with size and power output specifications (diameter 7.3 mm, length 17 mm, 139 dB re  $1\mu Pa$ ) similar to those used for tagging of Atlantic salmon post-smolts [204] was selected for the experiment in order to preserve the relevance of the results with respect to the Nordfjord full-scale trial described below. The tag (R-LP7, Thelma Biotel AS, Trondheim, Norway) was, however, programmed as a range test transmitter with a short and fixed transmission interval (10 s) and with a monotonously increasing transmission sequence number as data payload to facilitate rapid data collection and straightforward assessment of the number of received and lost messages. The range test transmitter was kept at a fixed location by attaching it to a buoy mooring at 2 m depth, while the AutoNaut with the integrated receiver was navigated at different distances from the buoy. The experiment was divided into two trials where only the passive wave-foils were used to propel the AutoNaut during the first trial, whereas the second trial also involved activation of the ancillary electric thruster. During both trials, all tag transmissions were registered and for each transmission the AutoNaut's position and range to the buoy were noted together with the event of whether the signal was detected or not. The background noise in the acoustic channel was recorded continuously from the receiver, and if a signal was detected, the signal-to-noise ratio (SNR) was registered as well.

### Sail-by scenarios

The detection probability model permits simulation of simple “sail-by” scenarios and estimation of the expectancy of making one or more fish detections as the USV and a tagged fish pass each other at different distances. The purpose of the simulation was to provide some initial predictions on the “sweeping efficiency” of the USV as it moves through an area populated with tagged fish, although several assumptions and simplifications were made to make the calculations more tractable and the results easier to interpret. Here it was assumed that the fish remained near the surface at a fixed position relative to the USV and that the USV followed a linear path at constant speed and passed the fish at some minimum distance. It was also assumed that the tag emitted acoustic messages that were repeated with a uniformly distributed random delay within a fixed time interval, which is a common feature of acoustic fish tags. This means that a sail-by may result in a variable number of transmissions where the probability of detection is greater than zero, depending on the transmission interval, the relative speed between vehicle and fish, and the sail-by distance. In these simulations, the number of detections can be viewed as a random variable consisting of a sequence of independent Bernoulli trials where each trial (transmission)  $i$  is associated with a varying probability of success (detection)  $p_i$ , given by the actual range and the logistic model described the previous section. The random variable can therefore be characterized as hav-

ing a Poisson binomial distribution [205]. The expected value of a random variable having this distribution is simply the sum of the detection probabilities  $\sum_i p_i$  over all transmissions during a sail-by. This fact was used to find an estimate of the maximum passing distance where at least one detection can be expected.

### 10.1.3 Full-scale trial

A full-scale trial with the AutoNaut was planned and conducted over a period of three days in May 2020 in Nordfjord, Norway (N61°54', E5°14'). Nordfjord is with its 106 km the sixth longest fjord in Norway (see Figure 10.4). Several of the rivers entering the fjord sustain significant populations of Atlantic salmon (*Salmo salar*) and anadromous brown trout (*Salmo trutta*), where the Stryn and Eid rivers constitute two of the main salmonid habitats. The trial was aligned with an already ongoing acoustic telemetry experiment in these two rivers, where the fjord and seaward migration of these species were studied. The trial therefore gave a reasonable chance of experiencing vehicle-fish encounters in the setting of a genuine fish migration study and served as a realistic test of the AutoNaut as a mobile robotic telemetry platform.

Following the procedure described in [204], 100 salmon pre-smolts and 85 sea trout had been captured by electrofishing, implanted with an acoustic transmitter, and released at their respective capture sites in the Stryn and Eid rivers between the 10<sup>th</sup> and 16<sup>th</sup> of April 2020. Two different types of acoustic transmitters were used; the D-LP6 and the ID-LP7 (Thelma Biotel AS, Trondheim, Norway). While the D-LP6 transmits swimming depth as sensor data payload in addition to a unique ID code, the ID-LP7 is a pure ID transmitter and acoustically identical to the R-LP7 employed in the range test with the AutoNaut. Both transmitter types had a battery life of roughly 150 days and were programmed with a uniformly distributed random delay/transmit interval of 30–90 seconds to permit time-division multiplexing, giving an average sending rate of 60 IDs per hour.

As part of the fish telemetry experiment reported in [204], a system of 74 VR2W passive acoustic receivers (Innovasea Systems Inc., Halifax, Canada) had been deployed at fixed stations distributed from the rivers to the outer rim of the fjord, as shown in Figure 10.4. The full record of detection data from the passive receivers was downloaded in the summer after the smolt migration season had ended and provided ground-truth data for the subsequent analysis of the trial. In addition to the full data record, fish detections registered during the three days of the trial at stations within or in the vicinity of the area covered by the AutoNaut were extracted and used to establish an overview of the evolving migration situation and potential detection targets. As a simple approximation, the migration route of fish that had been detected at more than one station was estimated by using the

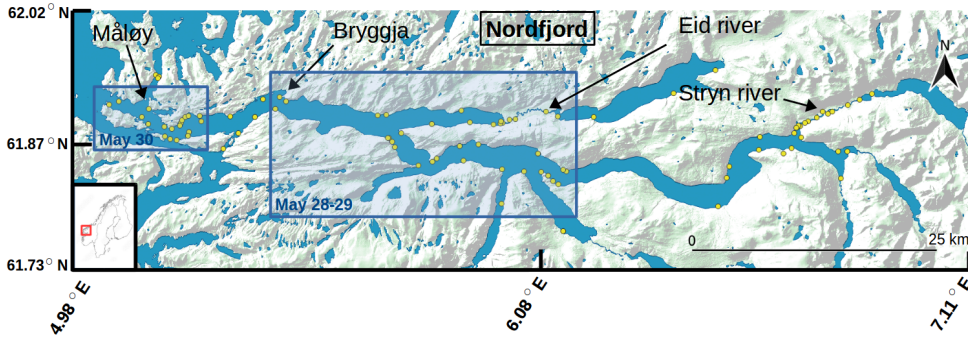


Figure 10.4: Map showing Nordfjord in western Norway, from river Stryn in the east to the fjord outlet and the North Atlantic Ocean in the west, which was site of the field trial with the fish telemetry-enabled AutoNaut. A system of 74 passive receivers were deployed at fixed locations over the full length of the fjord (yellow circles). Blue rectangles indicate the two areas that were analysed in detail, in which the AutoNaut navigated between the 28<sup>th</sup> and 30<sup>th</sup> May 2020 and where the receiver grid provided ground-truth fish detection data.

recorded detection times along with the shortest linear path through the fjord connecting the respective receiver positions. The migration routes were then used to calculate the fish's distance to the river mouth as a function of time and compared to the corresponding position of the AutoNaut, which was logged continuously using the onboard GNSS receiver.

The timing of the trial was decided based on experience from earlier migration studies in the same area [204], and the route of the AutoNaut was nominally planned to the outer 40 km section of the fjord and consisted of shoreline and mid-fjord traverses as well as a short excursion to the open sea. Still, the vehicle's route was under real-time control and prepared for adjustments at any time to adapt to situations caused by, e.g., weather conditions, sea currents or opposing ship traffic. Fish detections from the receiver grid were not used actively for vehicle guidance during the trial since they were not readily available in real-time. It was also desirable to retain the scope of the trial as a baseline test of the unbiased detection capacity of the mobile receiver platform.

## 10.2 Results

### 10.2.1 Technical integration

The full-scale trial in Nordfjord and the range test in the Trondheim Fjord provided five days of technical performance testing and validation of the AutoNaut and

TBLive receiver integration. The mechanical installation of the receiver was observed to have no perceivable effect on the vehicle's drag or navigational performance, which was expected due to the receiver's small size and tight integration on the vehicle's streamlined instrument keel. Potential issues related to air exposure or bubble entrainment around the relatively shallow hydrophone can not be ruled out since weather conditions were generally calm and wave height never exceeded 1 m, although no indications of such effects were observed during the trials. Integration of the TBLive with the AutoNaut payload control software showed immediate availability of accurately timestamped tag detection data, background noise level, and water temperature both locally in the vehicle guidance computer and on the remote user interfaces. With the 4G/LTE cellular link active, the latency time of receiver data to the Neptus and Grafana GUIs was typically less than 2 seconds. Tag detections were georeferenced by the payload computer by adding the vehicle GNSS position to the detection record before they were broadcast as DUNE IMC messages, and it was confirmed that they appeared on the map panel of the Grafana dashboard in real-time (see Figure 10.3). All receiver data were successfully logged to the vehicle database along with all other sensor data for post-mission analysis.

The TBLive receiver experienced an elevated and fluctuating noise level during the full-scale trial that was not present during the range test. This most likely caused a reduction in the AutoNaut's effective detection range. The noise figure reported by the receiver is an accumulated measure of the noise observed in the frequency band averaged over 5-minute intervals. In a moving platform, noise will be affected by a variety of naturally fluctuating noise sources such as environmental noise, turbulent flow, thruster usage, and inherent electrical properties of the hydrophone sensor itself. However, the source of the elevated noise level was subsequently identified simply as a case of electrical interference between the Seabird CTD sensor and the receiver, and was eliminated by a rewiring of the sensors' ground connections and installation of a line filter on the receiver's power supply. The specific reduction of detection range during the Nordfjord trial was not quantified, but the fact that both tagged fish and test transmitters deployed from a boat were detected suggests that the vehicle receiver was still functional despite the noise issue.

### **10.2.2 Detection range and sail-by simulations**

The range test was conducted in the Trondheim Fjord under calm conditions. The small acoustic transmitter (R-LP7, 7.3 mm, 69 kHz) was deployed at 2 m depth by attaching it with a thin metal string to the mooring line of a surface buoy that was held taut and in a fixed position by a heavy anchor. The string served to offset the tag a few centimetres from the thick mooring line and keep it in a horizontal orientation similar to that of a tag implanted in a fish. The buoy was installed

approximately 100 m from the shore at 10 m water depth, with the seafloor sloping moderately to about 50 m depth outside the buoy at the far end of the test range. The position of the tag (buoy) was determined using a GPS with accuracy better than 2 m. The wave height was low during the test, ranging from ripples to small waves (< 25 cm), which caused the AutoNaut to move at relatively low speed (below 0.4 m/s) when driven only by wave propulsion.

The range test was divided into two trials and provided 298 tag detections out of a total of 468 transmissions. The first trial, with the AutoNaut driven by the wave-foils only, lasted approximately 35 minutes and gave 129 detections out of 210 transmissions. The second trial, where the AutoNaut also had the ancillary thruster engaged, lasted approximately 43 minutes and gave 169 detections out of 258 transmissions. The distance between the tag and the AutoNaut was calculated for all detected and lost transmissions using the vehicle's measured GNSS position (logged at 1 s intervals) at the time of reception and was further organised into 25 m range bins in the interval 0-300 m (0-25, 25-50, ..., 275-300). The maximum detection range recorded for the first and the second trial was 256 m and 135 m, respectively.

The detection ratio (detections/transmissions) for all range bins were then calculated and processed by the MATLAB<sup>®</sup> function *glmfit* (The Math Works Inc., Natick, MA, USA) to estimate the coefficients of the logistic regression model given in Equation 10.2. The regression results are shown in Figure 10.5 and summarised in Table 10.3. It was estimated that the AutoNaut would have a 50% efficient detection radius (detecting transmissions with probability 0.5, or  $R_{0.5}$ ) of 207 m or 95 m depending on whether the vehicle was passively or actively propelled, respectively. The corresponding  $R_{0.9}$  detection radii were estimated to 117 m and 46 m.

The detection range model fitted to the wave-propulsion case was used subsequently to simulate sail-by scenarios for the vehicle and an acoustically tagged

Table 10.3: Regression results for range test trials using the model in Equation 10.2.

Propulsion	Regression coefficients		Detection radius (m)	
	$\hat{\beta}_0$	$\hat{\beta}_1$	$R_{0.5}$	$R_{0.9}$
Wave-foils	5.021	-0.024	207	117
Wave-foils + thruster	4.294	-0.045	95	46

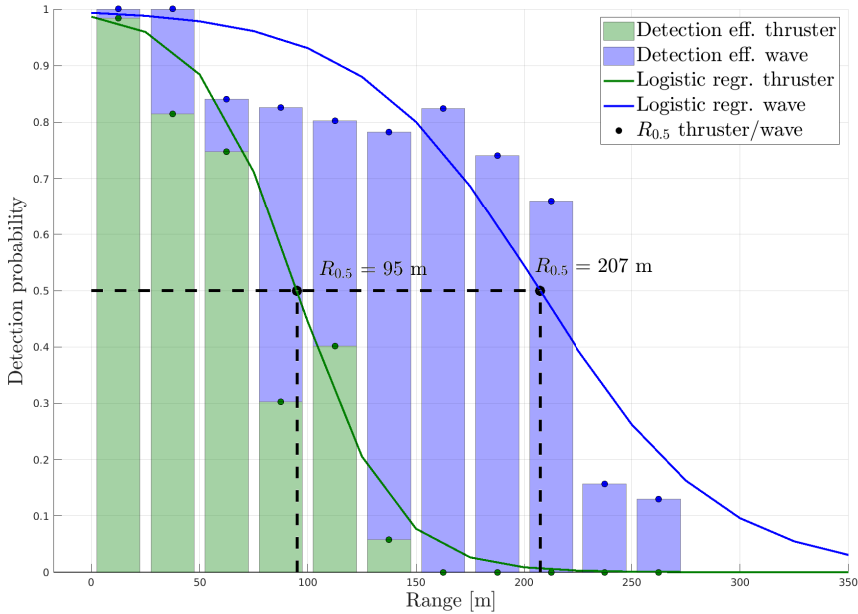


Figure 10.5: Logistic regression applied to the range test data where the vehicle was propelled by the wave-foils only (blue) or with both wave-foils and electric thruster (green). Dashed lines indicate ranges corresponding to 50% chance of detection, reaching 207 and 95 meters respectively.

fish in order to estimate the effective range where at least one detection can be expected. In these simulations, it was assumed for the sake of simplicity that the vehicle and fish followed straight and parallel paths with a constant relative speed difference between them. It was also assumed that the receiver’s sensitivity is constant with respect to vehicle speed, that the fish stays near the surface, and that the tag emits energy omni-directionally and features a sending schedule similar to the tags used in the full-scale trial with a 30-90 s uniformly distributed random delay/sending interval. The simulations were set up with 1 km vehicle transects with minimum sail-by distances in the range 0-500 m (10 m steps), and relative speed between vehicle and fish in the range 0.1-1.5 m/s (0.1 m/s steps). An example of a sail-by simulation is shown in Figure 10.6 (only sail-by distances in steps of 50 m retained for clarity), where the surface colour contour indicates the tag detection probability and stem plots indicate tag transmissions along the straight vehicle transects.

The expected number of detections along all transects for all relative speeds were



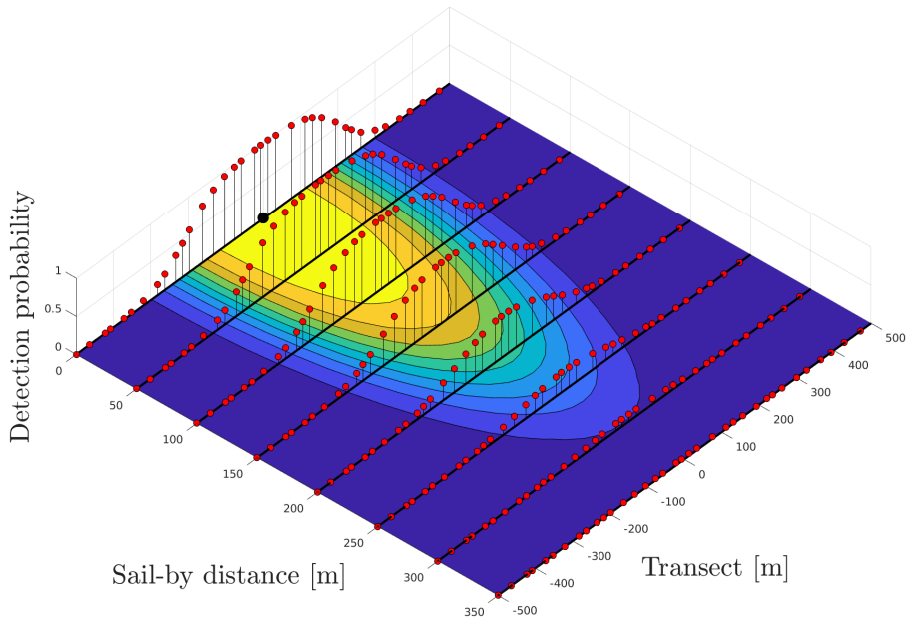


Figure 10.6: Example of sail-by simulation scenarios with the acoustic transmitter located in the origin and the vehicle moving at 0.5 m/s in straight 1 km transects (heavy black lines) at eight passing distances (0-350 m). The coloured surface contour indicates the detection probability (yellow  $> 0.9$ , dark blue  $< 0.1$ ) at a given coordinate. Tag transmissions with semi-random delay/transmit interval 30-90 seconds are shown with their associated detection probability as stem plots along the vehicle transects.

calculated as the expectancy value of the associated Poisson binomial distribution (see Section 10.1.2). For the different relative speeds, the sail-by distances that gave exactly one detection were determined numerically by fitting high-order polynomials to the detection expectancy curves using MATLAB<sup>®</sup> functions *polyfit* and *fzero*, as shown in Figure 10.7 and 10.8. In Figure 10.7, each curve (blue) represents a constant relative speed between vehicle and fish in the interval 0.1-1.5 m/s (speed gradient indicated by arrow). Moreover, Figure 10.8 shows that a single detection of the tag can be expected at a sail-by distance of 371 m for the lowest speed (0.1 m/s), while the distance is reduced to 241 m for the highest speed (1.5 m/s). On the other hand, the area efficiently swept by the AutoNaut will be almost ten times higher for the latter case due to the speed difference.



## 10. A persistent sea-going platform for robotic fish telemetry: Technical solutions and proof-of-concept

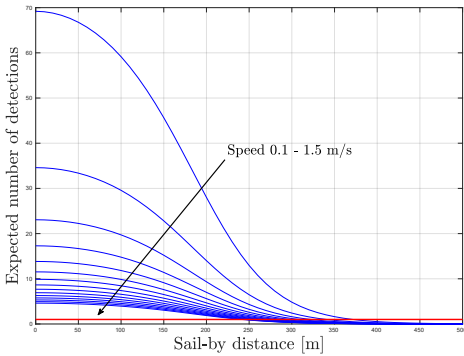


Figure 10.7: Expected number of detections as a function of sail-by distance. Expectancy of one detection indicated with a red line.

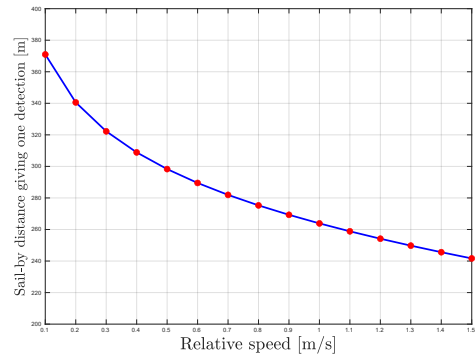


Figure 10.8: Sail-by distances giving exactly one detection as a function of relative speed.

### 10.2.3 Nordfjord field trial

The AutoNaut was launched 28<sup>th</sup> May 2020 at Bryggja on the north side of Nordfjord, 25 km east of the fjord outlet and 70 km west of the Stryn river (see Figure 10.4), and was recovered four days later at the same location. Weather conditions were sunny/clear with the sea state ranging from flat calm to small waves (<0.5 m) as well as some swell at the open ocean. The generally calm conditions required partial activation of the ancillary thruster to assist wave propulsion, which gave an overall average speed over ground of 0.4 m/s. External recharging of the batteries was not required as the solar panels proved sufficient for powering the vehicle's electrical subsystems throughout the mission, including the thruster. Surface temperature and salinity were measured every two minutes by the onboard sensors and showed average values (mean  $\pm$  SD.)  $11.2 \pm 1.5^\circ\text{C}$ ;  $16.2 \pm 6.7\text{ppt}$  and  $12.5 \pm 0.6^\circ\text{C}$ ;  $26.9 \pm 1.7\text{ppt}$  for the fjord sections east and west of Måløy, respectively. The results presented here concern the 54-hour period from the launch up to the point when a fish was detected at an offshore location west-northwest of the fjord in the afternoon 30<sup>th</sup> May, after the AutoNaut had travelled a distance of 80 km. Inspection of the detection record from the passive receiver system confirmed that the timing of the trial coincided with the migration of salmon post-smolts from the Stryn river. Due to hydrological differences between the two rivers, tagged salmon from the Eid river migrated earlier (median 13<sup>th</sup> May) and were not detected in the fjord at the time of the trial. As shown in Figure 10.9, a total of 27 migrating salmon were detected on receivers in the Stryn estuary that spring, and the detection record verified that at least three of these fish migrated through the outer half of the fjord at the time of the trial. The further analysis will focus on these three

individuals whose detection records are shown in Tables 10.4 and 10.5 and in the lower panel of Figure 10.9, where the blue area indicates the period when the AutoNaut was operating in the target area. Two of the fish carried ID-LP7 tags with ID 8988 and 8996, while the third one carried a D-LP6 with ID 252. The fork lengths of the fish were measured in April during tag implantation to 13.6, 13.7 and 13.4 cm, respectively. In general, the detection records show that the three individuals exhibited a distinct and directed seaward migration behaviour during the time of the trial. Although hypothetical, the proximity of the fish detections in space and time, with all fish detected at the fjord outlet in an interval of just three hours after swimming 100 km from the estuary, suggests that the post-smolts may have migrated as part of a larger group. It can also be observed that the migration route included at least one fjord crossing for all fish. Using the detection times shown in Tables 10.4 and 10.5 and the shortest straight fjord-path between the receiver positions, the average rate of movement through the outer half of the fjord for the three fish were 3.7, 3.2 and 3.4 BL/s (Body Lengths per second, using the April measurements). In the remaining part of this chapter, the three individuals will be identified by their tag ID number, or with letters A, B and C, respectively. Figures 10.10 and 10.11 illustrate how the situation evolved in space and time in terms of the location of the fish detections and the corresponding position and track of the AutoNaut in two distinct sections of the fjord during 28-29<sup>th</sup> and 30<sup>th</sup> May. All fish were detected on passive receivers located a few kilometres further inside the fjord relative to the vehicle's position on the 28-29<sup>th</sup> May, with fish 8996 detected at one point (A4) only 2.3 km to the south-east behind the AutoNaut. About 17 hours later, the same fish was detected again by a passive receiver located 28 km further out (A5), still with the AutoNaut only 2.4 km apart, suggesting that the fish and the vehicle had moved at similar speeds over this stretch of the fjord. The vehicle's average ground speed was measured to 0.52 m/s, while the fish had maintained a speed of at least 3.8 BL/s. The fish was not detected by the AutoNaut, which may be explained by the fact that the vehicle was commanded to stay more in the middle of the fjord over this stretch (typically 500-1300 m from shore), as opposed to the day before, when the AutoNaut traversed relatively close to the northern shore of the fjord (see Figure 10.10). The passive receivers on which the fish was detected were both located close to the shore, suggesting a more shore-oriented migration route. In addition, the relative positions of the vehicle and the detection points indicated that the vehicle may have been some distance ahead of the fish. This interpretation, however, should be regarded as hypothetical since the fish' exact migration route and speed between the detection points can not be known. Fish 8986 was finally detected at the westernmost receiver at the fjord outlet (A6) and had at that point increased its average movement speed to at least 4.6 BL/s and overtaken the AutoNaut by 7.4 km after the vehicle had been commanded to execute a temporary excursion to the northern shore of the fjord

## 10. A persistent sea-going platform for robotic fish telemetry: Technical solutions and proof-of-concept

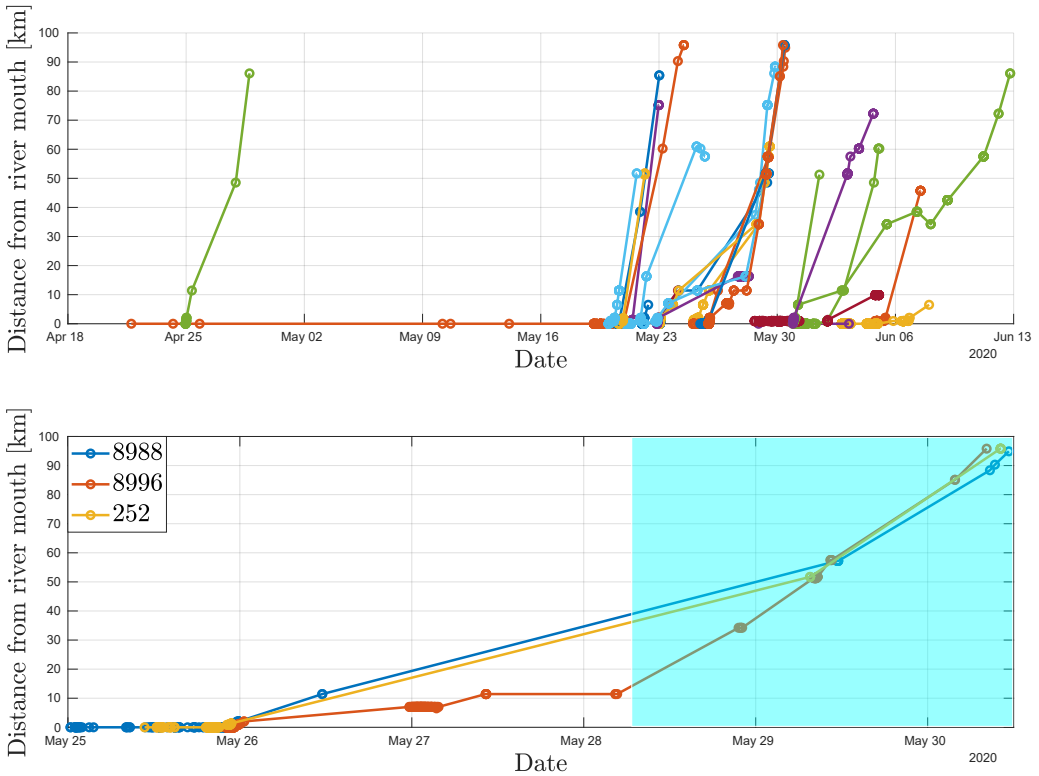


Figure 10.9: Top: Migration pattern of tagged salmon post-smolts from Stryn river spring 2020. Bottom: Detail of migration pattern for IDs 8988, 8996 and 252. The light blue area indicates the period in which the AutoNaut was operating in the fjord.

(see Figure 10.11). This example, with the eventual separation of the vehicle and fish, clearly demonstrates the transient nature of fish migrations and the challenge of sampling such processes as they evolve in space and time.

Fish 8988 and 252 were also detected by passive receivers on 29<sup>th</sup> May around 50 km from the fjord outlet (see Figure 10.10, label B1 and C1). They were observed to behave in a similar manner as 8996, with the fish and the AutoNaut moving approximately at the same average speed through the outer half of the fjord. Twenty-one hours later, 8988 was detected again on three passive receivers distributed over the outer 8 km stretch of the fjord with the AutoNaut (“unknowingly”) moving in the same direction 1.5-2.5 km ahead of the fish, as can be seen from Figure 10.11 (label B2-B4) and Figure 10.12. Here, the AutoNaut maintained an average speed of 0.82 m/s, and the fish a minimum of 6 BL/s, showing an increase in migration speed similar to that observed for fish 8996 towards the outer

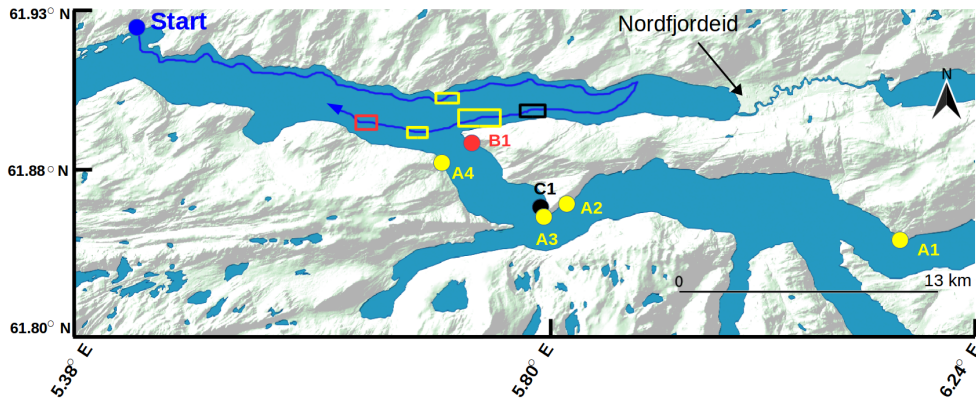


Figure 10.10: Section of the fjord navigated by the AutoNaut on 28<sup>th</sup> and 29<sup>th</sup> May (blue track), fish detections on passive receivers (coloured circles), and the AutoNaut's position at the detection times (correspondingly coloured rectangles). Numerical order of detection labels correspond to rectangle positions in chronological order. See Tables 10.4 and 10.5 for colour and label coding, and Figure 10.4 for geographical reference.

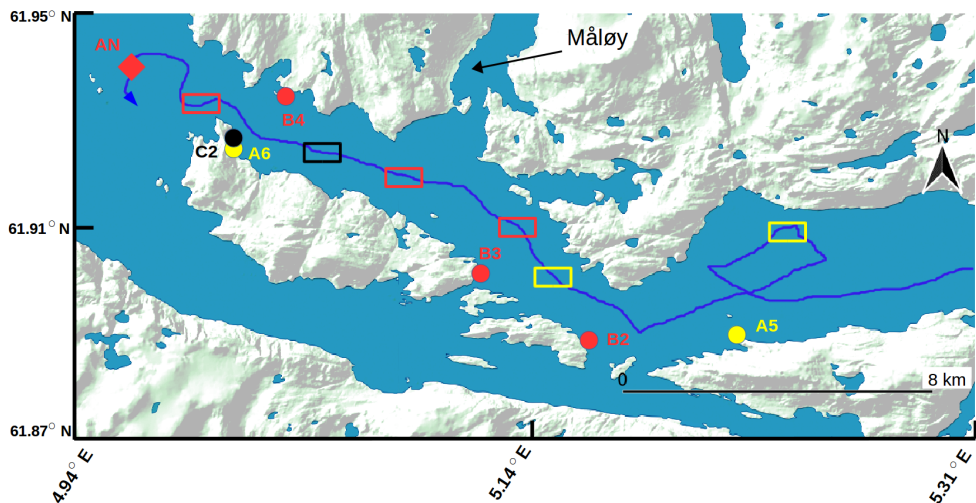


Figure 10.11: Section of the fjord navigated by the AutoNaut on 30<sup>th</sup> May (blue track), fish detections on passive receivers (coloured circles), and the AutoNaut's own detection (red diamond). Numerical order of detection labels correspond to rectangle positions in chronological order. See Tables 10.4 and 10.5 for colour and label coding, and Figure 10.4 for geographical reference.

10. A persistent sea-going platform for robotic fish telemetry: Technical solutions and proof-of-concept

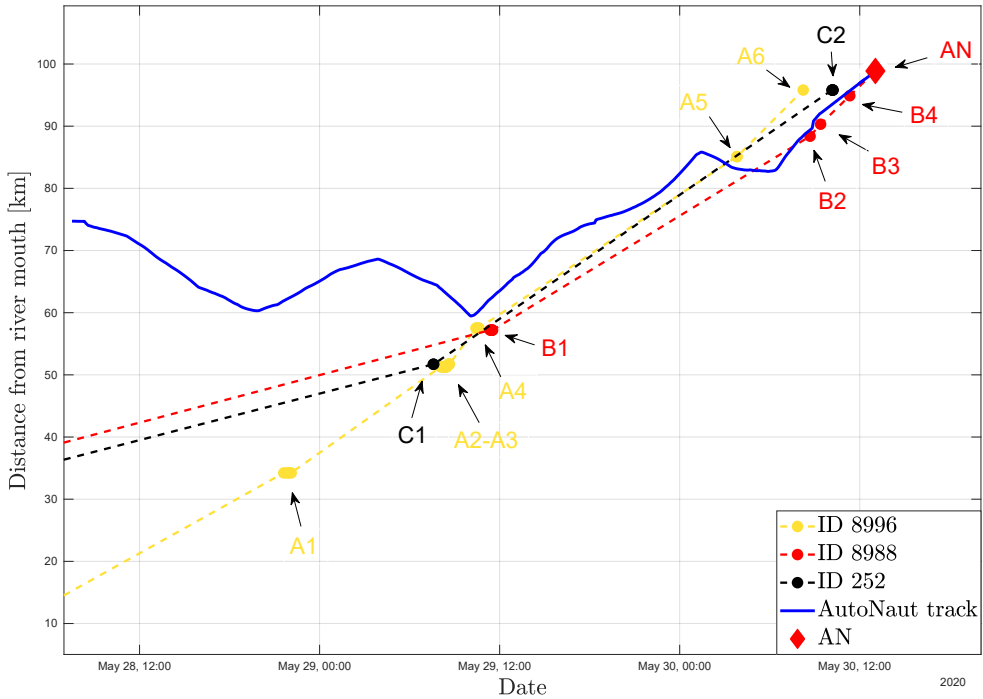


Figure 10.12: The distance from the Stryn estuary to the AutoNaut and the three fish. Coloured circles indicate detections on passive receivers (see Tables 10.4 and 10.5), while the red diamond indicates the AutoNaut’s detection of fish 8988 in the open sea. Dashed lines represent interpolated fish positions based on the shortest straight path between receivers.

part of the fjord. Using depth transmitters, previous telemetry studies of salmon post-smolts in Nordfjord have shown that the fish typically stay in the upper three meters of the water column during the fjord migration [204]. It is therefore reasonable to assume that the fish’ net movement speed will include components of advective transport in addition to active swimming. The outer part of Nordfjord can sustain significant tidal currents in the surface layer [206], but their actual contribution to the movement speed observed in this study were not quantified.

Finally, in the afternoon of May 30<sup>th</sup>, after having navigated around 3 km off the fjord into the open ocean, the AutoNaut system conveyed a successful detection of fish 8988, as indicated in Figure 10.11 (label AN). The salmon post-smolt had at that point migrated a (minimum) distance of around 100 km from the Stryn river estuary over a period of 4.5 days. Assuming that the speed and direction of movement in the hours up until the AutoNaut detection can be used to project the fish’ continued migration into the open ocean, the post-smolt would be 60-70 km

offshore west of the Stad peninsula (N62.18°, E5.12°) the following day and arrive at the continental shelf in the Norwegian Sea about 6-7 days after leaving its natal river Stryn.

### 10.3 Discussion

Surface gliders have found widespread use as persistent, flexible and cost-effective ocean observation platforms in a variety of applications of ocean observation [184, 207] and are also emerging as an interesting option as mobile and remotely operated sensing assets in fish movement studies [199–201]. In this study I have introduced an energy-autonomous robotic fish telemetry platform that was realised through the integration of a real-time acoustic receiver into a sea-going wave- and solar-powered USV. The open architecture presented in Chapter 3 permitted system-level integration of the acoustic receiver making fish detections along with other sensor data available in real-time to the vehicle’s onboard GNC (guidance, navigation and control) system, as well as to remote user interfaces and databases through cellular Internet connection.

The detection performance of the system was investigated by fitting a logistic regression model to range test data obtained from a controlled experiment using a small acoustic transmitter with physical specifications consistent with those used for tagging of salmon post-smolt and other small-sized fish. When the vehicle was passively driven by waves, the 50% detection probability radius was estimated from the model to 207 m, which is comparable to detection ranges observed using sentinel tags with similar specifications in long term deployments in stationary receiver arrays at sea (see e.g., [208]). Theoretical “sail-by” simulations based on the regression model predicted that a single detection can be expected at ranges up to around 350 m for very low passing speeds, while the corresponding range would be just above 300 m for the average vehicle speed (0.4 m/s) maintained during the Nordfjord full-scale trial. Assuming stationary transmitters, complete coverage of the 28 km<sup>2</sup> fjord section traversed by the AutoNaut in Figure 10.10 would under these conditions be achieved in about 32 hours. These results are based on idealised assumptions and must be regarded as highly hypothetical, but may serve as ballpark figures for the sweeping efficiency of the vehicle system.

It should be noted that the range test was limited in time and conducted under relatively mild conditions in small waves and the result therefore reflects detection performance that could be expected in a situation with low levels of environmental noise and low to moderate vehicle motion. It is likely that the detection radius will decrease with an increasing sea state due to both added noise and the receiver’s proximity to the surface layer. However, [209] found that the noise generated by a comparable wave-driven surface vehicle (Wave Glider, Liquid Robotics) was low



## *10. A persistent sea-going platform for robotic fish telemetry: Technical solutions and proof-of-concept*

---

both around the glider/sinker and surface float and that sea state did not have a strong influence on the vehicle's emitted noise at least up to 2.8 m significant wave height. It was also shown that noise dropped off considerably towards higher frequencies and was lowest at the highest frequency measured (60 kHz), which is close to the frequency spectrum normally utilized for acoustic fish tags in marine applications. An extensive range test spanning a wider range of sea states will nevertheless be required for a more complete characterisation of the AutoNaut's detection performance under passive wave propulsion.

Although the AutoNaut is primarily a wave-driven vehicle, the auxiliary electric thruster serves as backup propulsion in flat calm conditions and to increase rudder force during tight manoeuvres or to counter drift forces when waves are insufficient to keep an acceptable forward speed. With its high rotational speed and proximity to the receiver (approx. 2 m from the receiver at the AutoNaut's stern strut), it was considered important to quantify the thruster's impact on detection performance. The range test confirmed that activation of the thruster increases ambient noise level in the relevant frequency bands and causes a more than 50% reduction in detection radius (to 95 m) as compared to pure wave propulsion. While the result clearly suggests that thruster activation should be minimized during fish tracking operations, it should be noted that measurements were obtained using one of the smallest and least powerful acoustic transmitters available (139 dB). The loss of detection performance is not complete even with a weak transmitter and could be acceptable in situations where the alternative is a dead drifting vehicle or in studies where more powerful transmitters are applied. Nevertheless, a towed solution that separates the receiver by a greater distance from both the thruster and surface layer should be investigated and considered for future deployments. Technically, this can readily be achieved by suspending the receiver directly from the instrument keel by a properly arranged cable extension, which in principle can be several tens of meters without causing problems for the receiver's RS-485 communication interface. The feasibility of using the AutoNaut with a towed acoustic sensor array was shown by [210], although issues like increased drag, entanglement risk and sub-optimal receiver orientation must be considered against the convenience of a clean keel-mounted solution.

The basic functionality of the vehicle concept as an energy-autonomous and remotely piloted mobile fish telemetry platform with real-time connectivity was demonstrated during a three-day trial in the outer regions of a fjord in western Norway. The trial provided an opportunity to experience genuine encounters between the vehicle and tagged fish since it was conducted in parallel with an already ongoing acoustic telemetry experiment targeting the seaward migration of Atlantic salmon post-smolts from rivers in the Nordfjord area. The early marine migration represents a critical life stage of salmon with an urgent need of improved scientific understanding [211], but insight is limited and precluded by the technical and

practical difficulties of obtaining relevant observations beyond estuaries and confined coastal areas [212, 213]. Having a primary conceptual and technical focus, rigorous biological inference on post-smolt behaviour was not the aim of our study and it should neither be regarded as an integral part of the original biologically focused experiment, which will be reported elsewhere (see [204]). Nevertheless, along with the preceding detections recorded by the passive receivers, the fish detection made by the AutoNaut provides an interesting and rare observation of the pathway of an actively migrating salmon post-smolt extending beyond the fjord environment, at least in a Norwegian context. The author therefore believes that the main contribution of this study relates to the manifestation of the AutoNaut's ability to observe even small free-ranging fish in the ocean environment, and the associated prospects of evolving the concept into a powerful mobile autonomous fish telemetry tool with capacity to complement and extend the reach of traditional receiver setups and experimental designs. Considering that fish detection was possible despite the relatively short duration of the trial, and the fact that optimal system performance was impeded by the initial electrical noise interference problem as well as the thruster usage necessitated by the unusually calm weather conditions, suggest that performance will improve as the system evolves from its prototypical state and more operational experience is gained.



10. *A persistent sea-going platform for robotic fish telemetry: Technical solutions and proof-of-concept*

Table 10.4: Detection record for fish ID 8996. See Figures 10.10 and 10.11 for map references.

Fish tag ID	Map label	UTC Date/Time	Distance to USV (km)
8996	A1	2020-05-28 21:36:41	21.8
		2020-05-28 21:52:56	21.4
		2020-05-28 21:54:12	21.4
		2020-05-28 22:06:19	21.2
	A2	2020-05-29 08:04:08	5.1
		2020-05-29 08:10:28	5.2
		2020-05-29 08:13:25	5.2
		2020-05-29 08:15:51	5.2
		2020-05-29 08:18:38	5.3
		2020-05-29 08:20:49	5.3
		2020-05-29 08:22:09	5.3
		2020-05-29 08:24:47	5.3
	A3	2020-05-29 08:29:10	5.4
		2020-05-29 08:35:10	5.5
		2020-05-29 08:35:47	5.5
		2020-05-29 08:36:21	5.6
		2020-05-29 08:37:35	5.6
	A4	2020-05-29 08:38:58	5.6
		2020-05-29 10:25:06	2.3
		2020-05-29 10:28:19	2.4
2020-05-29 10:31:01		2.4	
2020-05-29 10:34:56		2.5	
		2020-05-29 10:37:09	2.6

Table 10.5: Detection record for fish ID 8996, 8988 and 252. See Figures 10.10 and 10.11 for map references.

Fish tag ID	Map label	UTC Date/Time	Distance to USV (km)
8996	A5	2020-05-30 03:48:05	2.4
		2020-05-30 03:49:32	2.5
	A6	2020-05-30 08:13:51	7.4
8988	B1	2020-05-29 11:21:46	4.7
		2020-05-29 11:25:28	4.9
		2020-05-29 11:29:10	5.0
		2020-05-29 11:30:33	5.1
		2020-05-29 11:31:39	5.2
	B2	2020-05-30 08:41:22	2.5
	B3	2020-05-30 09:23:22	2.0
	B4	2020-05-30 11:20:05	1.5
AN	2020-05-30 13:02:39	< 0.3	
252	C1	2020-05-29 07:34:28	5.6
		2020-05-29 07:36:25	5.5
	C2	2020-05-30 10:09:02	1.9
		2020-05-30 10:10:12	1.9
		2020-05-30 10:11:34	1.9
		2020-05-30 10:12:08	1.8
		2020-05-30 10:13:22	1.7



# Chapter 11

## Conclusions

As we come to the conclusion of this thesis, it is adequate to discuss how the presented results contribute to the fields of hardware and software integration, control engineering, collision avoidance and acoustic fish telemetry.

Traditional ocean observation methods based on point measurements are limited in space and time, and their operational scales are constrained by a number of factors that prevent continuous sampling of natural phenomena.

Among the major limitations we find technological development, high costs related to field campaigns and logistics. Also, human exposure to harsh environments and environmental pollution need to be considered as constraining factors. Nowadays, the lack of persistent mobile data collection systems is a well-known limitation in ocean related studies. Despite several valuable efforts show that robots, remotely operated or autonomous, can be employed in environmental studies, most of the employed systems feature limited onboard energy and scientific payload. This constrains the operational flexibility and temporal scope, since robots need proximity to shore or to support ships. As discussed in the introduction of this thesis, robotic underwater and surface gliders are more suitable platforms when persistence and endurance are requirements set by the scientific objectives.

This overall main intent of this thesis is to propose a robotic, wave-propelled, surface, autonomous marine platform meant to replace humans at sea. Among the key features of the presented system we find endurance and navigation autonomy. This thesis delves into the architectural design solution of the control and communication system onboard the USV, which motivated by a set of operational requirements defined based on the idea that the robot is meant to serve, and improve the quality of ocean observation methods.

Since the propulsion is generated by sea forces, wave-propelled USVs involve sev-

eral challenges related to control and navigation. The literature lacks of detailed models and solutions that explain how these limitations can be addressed. The research proposed in this thesis makes use of numerical model to highlight the main elements that lead to situations in which the vehicle is not maneuverable or, eventually, not controllable at all. The theoretical considerations introduced in Chapter 4 and Chapter 5 are further studied in the frequency domains, where the major nonlinearities are isolated and quantified. The design of a linear heading/course and of a gain-scheduled course controller is made possible based on the previous theoretical considerations. Simulating the involved environmental and USV state dynamics is not an easy task, especially without a detail hydrodynamic model of the vehicle. For this reason, several field campaigns were organized and executed in fjords and oceanic coastal waters. Experimental results are indeed a key component of this research.

### 11.1 Summary of the main contributions

Long-duration autonomous operations can be achieved once the necessary confidence with the USV and with the designed architecture is obtained. This motivates the works presented in the first part of the thesis, namely the system design, integration and testing is presented. Since little information can be found in the literature on how to control wave-propelled USVs, the experimental results gathered in numerous field experience is crucial in this research.

The reliability of the integrated communication and control systems are essential elements in order to perform enduring missions. The research campaigns conducted on the field, and presented in the second part of this thesis, assume in fact that the system is controllable, communication is possible according to the operational area and to the available link.

#### 11.1.1 System design and integration

In Chapter 3 (**Paper A**), the development and integration of a control and communication architecture is described. The design choices are motivated by a set of system operational requirements (Section 3.1), that envision autonomous, long-duration operations in Norwegian, Atlantic and Arctic waters. Unlike similar systems available on the market, the architecture presented in this thesis is entirely developed in academic environment using COTS components, and therefore publicly available.

## **Real-time monitoring platform**

An important contribution of this thesis is the design and implementation of a communication architecture that allows continuous, near real-time monitoring of oceanographic variables. The data relayed during a mission are made available to operators for control, planning and monitoring reasons, and to scientists, who are given the opportunity to observe the trend of sampled variables while the mission is executed. This enhances the flexibility of a mission, since their opinion supports mission planning and control from shore. The transmitted data are not, however, publicly available, as Grafana's dashboard require logging in with username and password. Moreover, the designed data monitoring interface is modular and scalable, as it allows easy integration of additional sensors and communication links at the software level. As of today, 4G/LTE and Iridium satellite communications are integrated, as discussed previously.

The implemented data observation system was tested in a number of field campaigns, and proved itself of uttermost utility both in fjords and ocean missions.

### **11.1.2 Control system: design and experimental validation**

In Chapter 4 (**Paper B**), the control system design is presented. Detailed mathematical models are derived and supported by extensive analysis in the frequency domain. Based on the discussed theoretical assumptions, methods from classical linear control theory are applied to control the heading and course of the USV. The main novelty in this chapter concerns the accurate modeling of the effects introduced by sea currents in the USV's steering dynamics.

Chapter 5 (**Paper C**) is a natural continuation of the previous chapter. The theoretical advantages of a gain-scheduled control system, explored in Chapter 4, are further investigated. Again, detailed mathematical modeling and analysis precede extensive simulation and experimental results showing the benefits of scheduling the gains of the course-keeping autopilot.

## **Wave-filtered steering control**

The possibility to improve navigation and increase situational awareness of the environment is further explored in Chapter 6 (**Paper D**), where the role of the wave encounter frequency is explained in the context of sea state estimation and wave filtering of the rudder command. This chapter presents the first closed-loop field experiments employing the WEF estimator in a course-control architecture. The results show that wave filtering of the rudder command is important to preserve the rudder mechanism, and at the same time to attenuate unnecessary high-frequency wave-induced oscillations without impacting course-keeping performances.

### **Collision avoidance and anti-grounding**

Safe navigation in trafficked and jagged coastal areas is of extreme importance. The design and implementation of collision avoidance and anti-grounding functionalities are described in Chapter 7 (**Paper E**). The simulation and experimental results show that the SB-MPC algorithm, adapted and tuned for the AutoNaut USV, enhances collision-free navigation with respect to dynamic (ship) obstacles and to static (e.g., land) obstacles. Two main novelties result from this research. The first is the integration of sea state variables (i.e, wind, current, waves, bathymetry) in the COLREGS-compliant SB-MPC algorithm used to control the USV's path. The second is the tight interaction between the onboard navigation (path planning) system and electronic charts. Information retrieval for anti-grounding purposes relies on a DBMS which stores and represents static obstacles as point clouds. The advantages of this implementation are the possibility to execute very fast SQL queries and to store large amount of information in little disc space.

### **Operational field experience**

Chapter 8 (**Paper F**) concludes the experimental validation of the presented platform and discusses the challenges associated to autonomous operations of a long-endurance wave-propelled USV. This chapter presents the risk assessment of a long-duration mission in Norwegian coastal waters (March-April 2021, Frohavet). The experience gathered during long-duration field experiences is discussed and analysed, by presenting and motivating the mission monitoring routines and the safety procedures that were put in place.

#### **11.1.3 USV employment in ocean studies**

##### **Persistent observation of oceanographic phenomena**

In Chapter 9 (**Paper G**), the employment of the AutoNaut in coordinated oceanographic studies is discussed. Specifically, a satellite-USV system is modeled in three different variants. The modelling challenges and the feasibility of observing oceanographic mesoscale phenomena with the proposed architecture is investigated. This research discusses the feasibility and the limitations related to the cooperation of space and marine assets.

##### **Fish telemetry**

Chapter 10 (**Paper H**) presents and discusses the deep integration of an acoustic receiver within the control and communication system of the USV, which provides real-time transmission of fish detections. The passive propulsion system and

the extended operational capabilities make the AutoNaut an ideal mobile long-endurance robotic receiver platform in acoustic telemetry studies. Mathematical modelling and model fitting, using experimental data, is proposed and discussed. Finally, a proof-of-concept study where the platform was deployed in a Norwegian fjord during the seaward migration of Atlantic salmon smolts is presented.

## 11.2 Future works

The AutoNaut's hardware and software architectures are entirely designed in an academic environment, making use of COTS components and parts designed and crafted at the mechanical workshop of the Department of Engineering Cybernetics (NTNU). Some design improvements have already been discussed. For example, the architecture could be simplified by reducing the number of involved hardware components. This would also reduce the redundancy, and appropriate precautions should be considered at the software level.

### 11.2.1 Speed estimation

A research topic that is not addressed in this thesis, and that is crucial to enhance mission planning functionalities, is the estimation of the USV's speed. As discussed in thesis, the USV's velocity depend on winds, currents and waves. The complex dynamics of natural forces affect significantly the motion of the vehicle, making it hard to predict the travel time to a destination. Ideally, the onboard software should be able to use current sensor measurements (from, for example, wind station, ADCP and IMU) to reconstruct the complete sea state, and merge this with weather forecasts downloaded from meteorological services or fed from shore (see Figure 11.1) in order to synthesize predictions of the sea state.

An accurate speed estimation would play a key role in path and mission planning methods. For example, based on the knowledge of the future USV's velocity, the decision-making onboard system would command a different path or, eventually, redefine the whole mission objectives. Moreover, the research work on anti-collision and anti-grounding presented in Chapter 7 would be improved significantly by a speed estimation algorithm. If a speed estimate is available to the SB-MPC algorithm, more reliable predictions of the USV's state can be computed, based on current a future sea states. This would increase the accuracy of the simulated scenario, but also operational safety with respect to land and other obstacles, independently of the environmental conditions.

The work presented in [63] contains the first attempt to predict the speed of the AutoNaut using linear and Gaussian process regression methods. The models are trained using onboard measurements from field operations, while the predictions are performed using Metocean (wind, wave and current) forecasts.



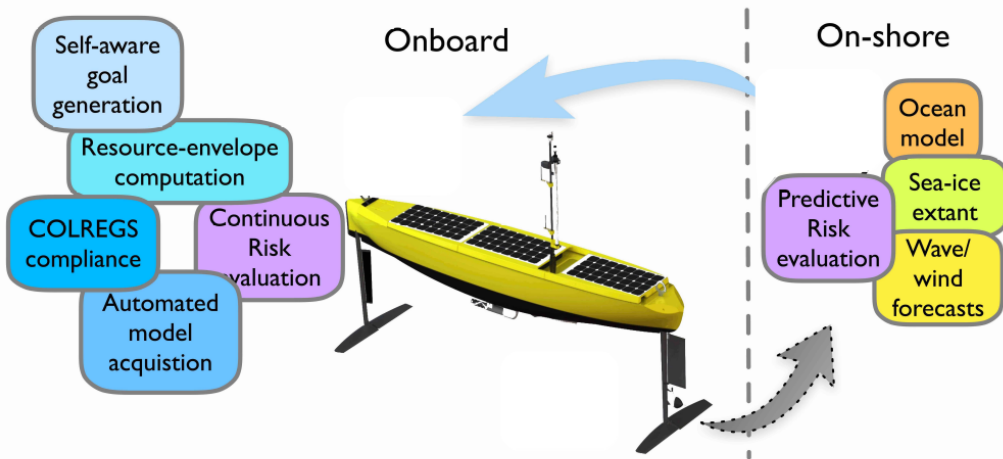


Figure 11.1: Decision-support systems on ship and shore provide oceanographers real-time data with the capability of command/control of assets in the field, which is currently not possible. Credits: Kanna Rajan.

### 11.2.2 Enhanced mission planning & risk modelling

Increasing the autonomy of the USV is of primary interest. Our goal is to change a platform designed for human-in-the-loop control for surface observations, to a vehicle which can take high level human intent, and computationally break it down into actionable tasks, while being critically aware of operational risks related to shallow bathymetry, surface traffic, low solar irradiance or overly calm waters (see Figure 11.1). Doing so will require novel ways to encode models onboard, imbibe low-bandwidth ocean model predictions, enable in-situ data interpretation and enforce the ability to monitor itself to circumvent future failures included in risk models by tasking itself with new goals without human intervention.

Persistent monitoring capabilities involve several challenges principally to deal with a high degree of robustness and endurance in hardware and software. The control of robotic systems and the communication with them are challenging tasks due to the variation and unpredictability of the environments. These amount to the following:

- Environmental factors: the propulsive power of the AutoNaut is heavily dependent on surface waves. Goal driven intent for scientific measurements will require careful balancing of value of information with the ability to be at the *right place at the right time*.
- Balancing goal-driven opportunism with intent: data and sample collection

will be driven not only by the form and content of the information collected, but the urgency of returning that data (samples) to shore. Water samplers onboard the AutoNaut for example can only be considered “fresh” enough for analysis within specific time windows. The conundrum of *exploration* vs. *exploitation* will then need to be worked out within the context of the value of information by trading (for instance) the cost of gathering and enabling sample return versus exploring “interesting” regions elsewhere.

- Balancing operational risks with remote intent: while the vehicle is in-situ and has a well-defined situational awareness of its environment, the onboard goal-driven autonomy has to trade operational risk in the ‘here and now’ with the desire and intent shaped by humans on shore who might not have full situational awareness or worse, issue command directives in error.
- Communication challenges: deciding what and when to transmit collected data to shore will be a significant challenge especially in northern latitudes where satellite communication coverage is sparse.

Balancing predictions from shore-side simulations, with data collected in-situ is challenging while tying closely to long and short-term task planning, since the time horizon may impact which factors are relevant. Discrepancies between planning models and reality are often handled ad-hoc. Thus, formalizing the notion of model “robustness” such that it provides guarantees against specified risks is a crucial step forward in the use of autonomous goal driven operations. Uncertainty concerning plan execution might lead to delays, or significant loss in mission achievement. Planning and plan execution, therefore, have to adhere to a risk model that provides a formal description of undesired scenarios that might occur with sufficient time for vehicle response. The risk model has to provide conservative assumptions of how a given phenomena can affect plan execution. For example, it is observed that strong currents or winds can prevent motion in certain directions within a useful time window or consume more energy than planned (see Chapter 4 and Chapter 5). Similarly, a cloudy sky might make energy generation challenging and defeat the purpose of data collection (see Chapter 8). The risk model can be generated and updated according to periodic observations of the environment driven by shore-side models and assimilated by onboard sensors. The data from the risk model can then be propagated to the planner and consequently, plans might often change and some goals might even become unachievable. Conversely, at heightened risk-awareness levels, it might be more beneficial to either disregard certain goals or even synthesize entirely new expected outcomes. This can only occur by introspection of the existing goal, evaluating with known exogenous (e.g., model predictions, very low or very high sea states) information, with those generated by onboard sensors endogenously (e.g., IMU state indicating a disparity of sea-surface height with an expected predict, or an occasional detection of

high chlorophyll levels). Introspection for goal generation, requires the USV to be “self-aware” and recognize substantial deviations in the present or near future, to take an actionable step towards mitigating such conditions; this could pose either risk, or an opportunity. A typical source of operational risk is in the failure and degraded performance of critical systems on the vehicle. For mitigation, the control architecture of the AutoNaut has a 3-level structure where the lowest level has been designed to be highly robust in order to alleviate risk due to loss of control functionality (see Chapter 3).

# Appendices



# Appendix A

## A.1 AutoNaut USV model parameters

We define ship and steering model parameters in Tables A.1 and A.2 accordingly. Computation of the system matrices  $M$ ,  $C$  and  $D$  is explained in section A.1.1.

	Symbol	Value
Mass	$m$	250 (kg)
Length at waterline	$L_{pp}$	4.6 (m)
Beam	$B$	0.7 (m)
Draught	$T$	0.15 (m)
Block coefficient	$C_b$	0.51
Radius of gyration	$R_{66}$	$0.25L_{pp}$ (m)
CG long. displacement	$x_g$	0 (m)

Table A.1: Vehicle's parameters.

### A.1.1 System matrices

We employ the method presented by [109] to compute the system matrices  $M$ . The inertia matrix  $M$  is assumed to be constant,

$$M = \begin{pmatrix} 277.7 & 0 & 0 \\ 0 & 462.9 & 0 \\ 0 & 0 & 593.35 \end{pmatrix}. \quad (\text{A.1})$$

	Symbol	Value
Rudder area	$A_R$	0.11 ( $m^2$ )
Aspect ratio	$\Lambda$	1.68
Rudder coefficient	$C_N$	1.56
Drag coefficient	$t_R$	0.3
Force factor	$a_H$	0.2
Interaction coefficient	$x'_H$	-1.8
Lateral force coordinate	$x_H$	-0.4
Longitudinal rudder position coordinate	$x_R$	-2.3

Table A.2: Steering model's parameters.

The off-diagonal terms in  $M$  are less than 5% of the diagonal terms and are therefore neglected in this model. The Coriolis and centripetal matrix  $C$  depend on the relative speed and therefore its coefficients will be recomputed during the simulations.

The damping matrix  $D$  is obtained by choosing  $D_{11} = M_{11}/T_{surge}$  with  $T_{surge} = 2$  s,  $D_{22} = M_{22}/T_{sway}$  with  $T_{sway} = 4$  s and  $D_{66} = M_{33}/T_{yaw}$  with  $T_{yaw} = 3$  s. Consequently,

$$D = \begin{pmatrix} 138.85 & 0 & 0 \\ 0 & 115.73 & 0 \\ 0 & 0 & 197.8 \end{pmatrix} \quad (\text{A.2})$$

The remaining coefficients are computed as:  $A_{11} = M(1,1) - m = 27.73$ ,  $A_{22} = M(2,2) - m = 212.9$ ,  $A_{66} = M(3,3) - J_z = 262.72$  where  $J_z = mR_{66}^2 + mx_g^2 = 330.62$ .

### A.1.2 Wind model

Wind creates forces in surge  $F_{Xw}$  and sway  $F_{Yw}$ , and a moment in yaw  $N_{Zw}$ . According to [72], surge and sway forces generated by the wind are computed as

$$F_{Xw} = \frac{1}{2} \rho_a V_{rw}^2 |C_X(\gamma_{rw}) A_{Fw}| \quad (\text{A.3})$$

$$F_{Yw} = \frac{1}{2} \rho_a V_{rw}^2 |C_Y(\gamma_{rw}) A_{Lw}|, \quad (\text{A.4})$$

	Symbol	Value
Wind coefficient	$[c_x, c_y, c_z]$	[0.5,0.7,0.05]
Frontal projected area	$A_{Fw}$	0.195 (m <sup>2</sup> )
Lateral projected area	$A_{Lw}$	1.5 (m <sup>2</sup> )
Length overall	$L_{oa}$	5 (m)

Table A.3: Wind model's parameters.

whereas yaw wind-generated moment is expressed as

$$N_{Zw} = \frac{1}{2} \rho_a V_{rw}^2 |C_N(\gamma_{rw}) A_{Lw} L_{oa}|, \quad (\text{A.5})$$

where the non dimensional wind coefficients  $C_X$ ,  $C_Y$  and  $C_N$  are usually computed using  $h = 10m$  as reference height,  $\gamma_{rw}$  is the wind angle of attack relative to the bow and  $\rho_a$  is the air density. For vehicles that are symmetrical with respect to the xz and yz planes, the wind coefficients for horizontal plane motions can be approximated by

$$C_X \approx -c_x \cos(\gamma_{rw}) \quad (\text{A.6})$$

$$C_Y \approx c_y \sin(\gamma_{rw}) \quad (\text{A.7})$$

$$C_N \approx c_n \sin(2\gamma_{rw}), \quad (\text{A.8})$$

where  $c_x \in [0.50, 0.90]$ ,  $c_y \in [0.70, 0.95]$ ,  $c_n \in [0.05, 0.20]$ .

$A_{Fw}$ ,  $A_{Lw}$  and  $L_{oa}$  are frontal, lateral areas and length overall respectively. Relative speed  $V_{rw}$  between vehicle and wind is computed as

$$V_{rw} = \sqrt{u_{rw}^2 + v_{rw}^2} \quad (\text{A.9})$$

where  $u_{rw} = u - u_w$  and  $v_{rw} = v - v_w$ , while the components of  $V_w$  in the x and y directions are

$$u_w = V_w \cos(\beta_w - \psi) \quad (\text{A.10})$$

$$v_w = V_w \sin(\beta_w - \psi). \quad (\text{A.11})$$

with  $V_w$  and  $\beta_w$  being the wind speed and direction relative to the vehicle (measured onboard), as shown in Figure A.2, and is  $\psi$  the vehicle's heading. The wind model parameters are reported in Table A.3.



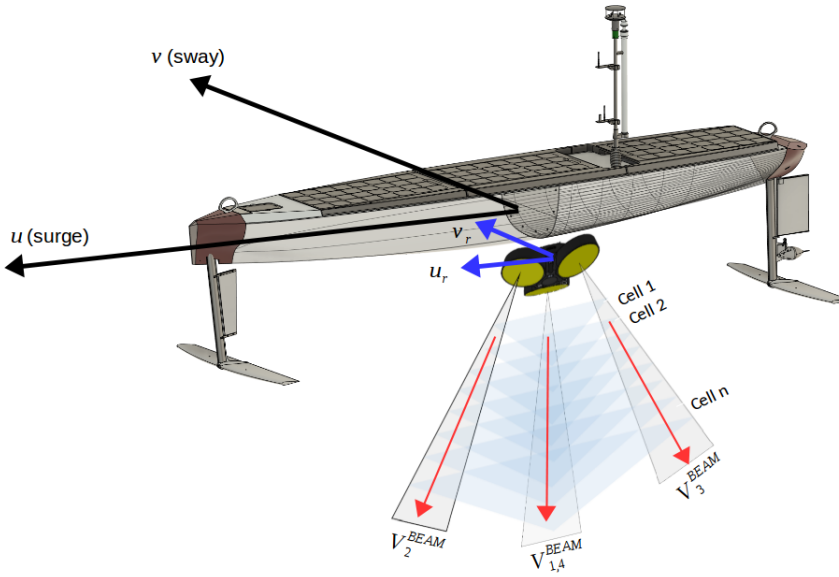


Figure A.1: ADCP sampling principle.

## A.2 ADCP & ocean currents transformations

Figure A.1 shows the ADCP operating principles. The current is initially computed in the beam frame ( $V_n^{BEAM}$ ). Knowing the orientation of the beams, the ADCP computes internally the Cartesian components associated to its frame. We note that, since the USV is not stationary, the measured current is not the earth-fixed stream velocity but instead the relative velocity between the USV and the flow ( $U_r = \sqrt{u_r^2 + v_r^2}$ ). The longitudinal and lateral ( $u_r$  and  $v_r$  respectively) components of the relative speed can be used to compute the flow velocity components  $u_c = u - u_r$  and  $v_c = v - v_r$ .

For purposes related to oceanography and marine biology, it is often useful to know the Earth-fixed direction and velocity of the planar (XY) current. These can be computed, knowing the North-East-Down (NED) components of the current, as  $[N_c, E_c]^T = R[u, v]^T$ , where  $R$  is the 2D rotation matrix from BODY to NED frame:

$$R = \begin{pmatrix} \cos \psi \cos \theta & \cos \psi \sin \theta \sin \phi - \sin \psi \cos \phi \\ \sin \psi \cos \theta & \cos \psi \cos \phi + \sin \psi \sin \theta \sin \phi \end{pmatrix}, \quad (\text{A.12})$$

where  $\psi$ ,  $\theta$  and  $\phi$  are the heading, pitch and roll angles respectively. The Earth-fixed current direction and velocity can then be computed as  $\beta_c = \arctan(E_c/N_c)$  and  $U_c = \sqrt{N_c^2 + E_c^2}$  respectively.

### A.2.1 Sea current from Earth-fixed to BODY frame

We assume the sea current velocity in the Earth-fixed frame is denoted by  $U_c$ , while  $\beta_c$  is its direction relative to North (see Figure A.2). The North-East-Down (NED) components of the current are obtained as

$$N_c = U_c \cos \beta_c \quad (\text{A.13})$$

$$E_c = U_c \sin \beta_c. \quad (\text{A.14})$$

The current longitudinal and lateral components in the USV's BODY frame are then obtained as

$$\begin{pmatrix} u_c \\ v_c \end{pmatrix} = \begin{pmatrix} \cos \psi & -\sin \psi \\ \sin \psi & \cos \psi \end{pmatrix} \begin{pmatrix} N_c \\ E_c \end{pmatrix}. \quad (\text{A.15})$$

## A.3 Wind transformations

Figure A.2 shows the definition of wind and sea current angles in the USV's BODY frame. The onboard weather station measures the wind velocity ( $V_w^B$ ) and direction ( $\beta_w^B$ ) relative to the USV's BODY frame. Using the measured ground velocity ( $U$ ) of the vehicle we can compute the theoretical wind speed ( $V_w^T$ ), which is the wind speed the USV would perceive if it was stationary:

$$V_w^T = \sqrt{V_w^{B2} + U^2 - 2V_w^B U \cos \beta_w^B}. \quad (\text{A.16})$$

Given the low ground speed of the USV, relative and theoretical winds have often similar values. Additionally, we note that the theoretical wind speed is already the absolute (true) wind speed:  $V_w^T = V_w$ .

Using the measured vehicle's heading ( $\psi$ ), the absolute (true) wind direction ( $\beta_w$ ) is simply computed as:

$$\beta_w = \psi + \beta_w^B. \quad (\text{A.17})$$

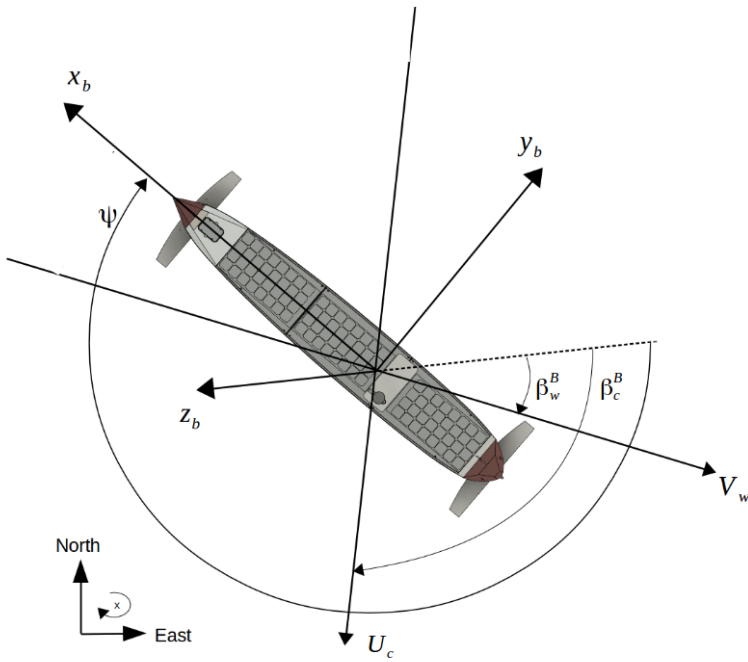


Figure A.2: Wind and sea current angles definitions in BODY frame.

# References

- [1] P. McGillivray, J. Borges de Sousa, R. Martins, K. Rajan, and F. Leroy, “Integrating autonomous underwater vessels, surface vessels and aircraft as persistent surveillance components of ocean observing studies,” in *2012 IEEE/OES Autonomous Underwater Vehicles (AUV)*, Sep. 2012, pp. 1–5.
- [2] NOAA, “How much of the ocean have we explored?,” 2021.
- [3] R. Davis, *Oceanography: An Introduction to the Marine Environment*, W.C. Brown Publishers, 1991.
- [4] F. Nansen, *The Norwegian North polar expedition, 1893-1896; scientific results*, vol. v.1 (1900), London, Longmans, Green and co., 1900, <https://www.biodiversitylibrary.org/bibliography/14631>.
- [5] W. H. Munk, C. I. Wunsch, H. Charnock, and A. M. Adye, “Observing the ocean in the 1990s,” *Philosophical Transactions of the Royal Society of London. Series A, Mathematical and Physical Sciences*, vol. 307, no. 1499, pp. 439–464, 1982.
- [6] F. P. Bretherton, R. E. Davis, and C. Fandry, “A technique for objective analysis and design of oceanographic experiments applied to MODE-73,” *Deep Sea Research and Oceanographic Abstracts*, vol. 23, no. 7, pp. 559–582, 1976.
- [7] P. Minnett, A. Alvera-Azcárate, T. Chin, G. Corlett, C. Gentemann, I. Karagali, X. Li, A. Marsouin, S. Marullo, E. Maturi, R. Santoleri, S. Saux Picart, M. Steele, and J. Vazquez-Cuervo, “Half a century of satellite remote sensing of sea-surface temperature,” *Remote Sensing of Environment*, vol. 233, pp. 111366, 2019.
- [8] J. C. McWilliams, “Modeling the Oceanic General Circulation,” *Annual Review of Fluid Mechanics*, vol. 28, no. 1, pp. 215–248, 1996.

- [9] W. HANSEN, “Hydrodynamical methods applied to oceanographic problems,” *Proc. Symp. Math.-hydrodyn. Meth. Phys. Oceanogr.*, 1962, 1962.
- [10] E. Kalnay, *Atmospheric Modeling, Data Assimilation and Predictability*, Cambridge University Press, 2002.
- [11] W. Lahoz and P. Schneider, “Data Assimilation: Making Sense of Earth Observation,” *Frontiers in Environmental Science*, vol. 2, 05 2014.
- [12] T. D. Dickey, “Emerging ocean observations for interdisciplinary data assimilation systems,” *Journal of Marine Systems*, vol. 40, pp. 5–48, 2003.
- [13] T. Curtin, J. Bellingham, J. Catipovic, and D. Webb, “Autonomous Oceanographic Sampling Network,” *Oceanography*, vol. 6, 01 1993.
- [14] J. Pinto, M. Faria, J. Fortuna, R. Martins, J. Sousa, N. Queiroz, F. Py, and K. Rajan, “Chasing Fish: Tracking and control in a autonomous multi-vehicle real-world experiment,” in *MTS/IEEE Oceans*, San Diego, California, 2013.
- [15] L. L. Sousa, F. López-Castejón, J. Gilabert, P. Relvas, A. Couto, N. Queiroz, R. Caldas, P. S. Dias, H. Dias, M. Faria, F. Ferreira, A. S. Ferreira, J. Fortuna, R. J. Gomes, B. Loureiro, R. Martins, L. Madureira, J. Neiva, M. Oliveira, J. Pereira, J. Pinto, F. Py, H. Queiró, D. Silva, P. B. Sujit, A. Zolich, T. A. Johansen, J. Sousa, and K. Rajan, “Integrated monitoring of Mola mola behaviour in space and time,” *PLOS one*, vol. 11, no. 8, August 2016.
- [16] A. S. Ferreira, M. Costa, F. Py, J. Pinto, M. A. Silva, A. Nimmo-Smith, T. A. Johansen, J. B. de Sousa, and K. Rajan, “Advancing multi-vehicle deployments in oceanographic field experiments,” *Autonomous Robots*, Oct 2018.
- [17] M. J. Costa, J. Pinto, P. S. Dias, J. Pereira, K. Lima, M. Ribeiro, J. B. Sousa, T. Lukaczyk, R. Mendes, M. P. Tomasino, C. Magalhães, I. Belkin, F. Lopez-Castejon, J. Gilabert, K. Skarpnes, M. Ludvigsen, K. Rajan, Z. Mirmalek, and A. Chekalyuk, “Field Report: Exploring Fronts with Multiple Robots,” in *2018 IEEE/OES Autonomous Underwater Vehicle Workshop (AUV)*, 2018, pp. 1–7.
- [18] D. Glickson, R. Kiss, R. Pittenger, F. Chavez, M. Edwards, R. Fine, N. Rabalais, E. Saltzman, J. Swift, W. Wilcock, and D. Yoerger, “Science at Sea: Meeting Future Oceanographic Goals with a Robust Academic Research Fleet,” *AGU Fall Meeting Abstracts*, 12 2009.
- [19] O. Schofield, S. Glenn, and M. Moline, “The Robot Ocean Network,” *American Scientist*, vol. 101, pp. 434, 11 2013.

- 
- [20] L. R. Haury, J. A. McGowan, and P. H. Wiebe, "Patterns and Processes in the Time-Space Scales of Plankton Distributions," in *Spatial Pattern in Plankton Communities*, J. H. Steele, Ed., pp. 277–327. Springer US, Boston, MA, 1978.
- [21] I. Fer and D. Peddie, "Near surface oceanographic measurements using the SailBuoy," in *2013 MTS/IEEE OCEANS - Bergen*, June 2013, pp. 1–15.
- [22] R. Hine, S. Willcox, G. Hine, and T. Richardson, "The Wave Glider: A Wave-Powered autonomous marine vehicle," in *OCEANS 2009*, Oct 2009, pp. 1–6.
- [23] CLS Group, "ARGOS (webpage)," 2014, Accessed March 2014.
- [24] J. Manley and S. Willcox, "The Wave Glider: A New Concept for Deploying Ocean Instrumentation," *IEEE Instrumentation Measurement Magazine*, vol. 13, no. 6, pp. 8–13, December 2010.
- [25] P. Johnston and M. Poole, "Marine surveillance capabilities of the AutoNaut wave-propelled unmanned surface vessel (USV)," in *OCEANS 2017 - Aberdeen*, June 2017, pp. 1–46.
- [26] A. M. Chiodi, C. Zhang, E. D. Cokelet, Q. Yang, C. W. Mordy, C. L. Gentemann, J. N. Cross, N. Lawrence-Slavas, C. Meinig, M. Steele, D. E. Harrison, P. J. Stabeno, H. M. Tabisola, D. Zhang, E. F. Burger, K. M. O'Brien, and M. Wang, "Exploring the Pacific Arctic Seasonal Ice Zone With Saildrone USVs," *Frontiers in Marine Science*, vol. 8, pp. 481, 2021.
- [27] L. Technologies, "C-Enduro Long Endurance ASV," 2019.
- [28] A. Dallolio, B. Agdal, A. Zolich, J. A. Alfredsen, and T. A. Johansen, "Long-Endurance Green Energy Autonomous Surface Vehicle Control Architecture," 2019, *OCEANS 2019*, Seattle, Washington.
- [29] R. Jha, "Wave Measurement Methodology and Validation from Wave Glider Unmanned Surface Vehicles," in *2018 OCEANS - MTS/IEEE Kobe Techno-Oceans (OTO)*, 2018, pp. 1–7.
- [30] Y. Zhang, B. Kieft, C. Rueda, T. O'Reilly, J. Ryan, T. Maughan, C. Wahl, and F. Chavez, "Autonomous front tracking by a Wave Glider," in *OCEANS 2016 MTS/IEEE Monterey*, 2016, pp. 1–4.
- [31] Y. Zhang, B. Kieft, B. W. Hobson, B.-Y. Raanan, S. S. Urmy, K. J. Pitz, C. M. Preston, B. Roman, K. J. Benoit-Bird, J. M. Birch, F. P. Chavez, and C. A. Scholin, "Persistent Sampling of Vertically Migrating Biological Layers by

- an Autonomous Underwater Vehicle Within the Beam of a Seabed-Mounted Echosounder,” *IEEE Journal of Oceanic Engineering*, vol. 46, no. 2, pp. 497–508, 2021.
- [32] H. Cheyne, C. Key, M. Satter, M. Ornee, and C. Clark, “Multi-channel acoustic data acquisition and telemetry on an autonomous vehicle for marine mammal monitoring,” in *2013 OCEANS - San Diego*, 2013, pp. 1–5.
- [33] N. Goebel, S. Frolov, and C. Edwards, “Complementary use of Wave Glider and satellite measurements: Description of spatial decorrelation scales in Chl-a fluorescence across the Pacific basin,” *Methods in Oceanography*, vol. 10, 08 2014.
- [34] K. M. Schmidt, S. Swart, C. Reason, and S.-A. Nicholson, “Evaluation of Satellite and Reanalysis Wind Products with In Situ Wave Glider Wind Observations in the Southern Ocean,” *Journal of Atmospheric and Oceanic Technology*, vol. 34, no. 12, pp. 2551–2568, 12 2017.
- [35] P. R. Hill, A. Kumar, M. Temimi, and D. R. Bull, “HABNet: Machine Learning, Remote Sensing-Based Detection of Harmful Algal Blooms,” *IEEE Journal of Selected Topics in Applied Earth Observations and Remote Sensing*, vol. 13, pp. 3229–3239, 2020.
- [36] IOCCG, *Observation of Harmful Algal Blooms with Ocean Colour Radiometry*, vol. 20 of *Reports of the International Ocean-Colour Coordinating Group*, IOCCG, Dartmouth, Canada, 2021.
- [37] IOCCG, *Remote Sensing of Ocean Colour in Coastal, and Other Optically-Complex, Waters*, vol. 3 of *Reports of the International Ocean Colour Coordinating Group*, IOCCG, Dartmouth, Canada, 2000.
- [38] IOCCG, *Uncertainties in Ocean Colour Remote Sensing*, vol. 18 of *Reports of the International Ocean-Colour Coordinating Group*, IOCCG, Dartmouth, Canada, 2019.
- [39] A. Dallolio, G. Quintana-Diaz, E. Honoré-Livermore, J. L. Garrett, R. Birke-land, and T. A. Johansen, “A Satellite-USV System for Persistent Observation of Mesoscale Oceanographic Phenomena,” *Remote Sensing*, vol. 13, no. 16, 2021.
- [40] C. Albouy, P. Archambault, W. Appeltans, M. B. Araújo, D. Beauchesne, K. Cazelles, A. R. Cirtwill, M.-J. Fortin, N. Galiana, S. J. Leroux, L. Pellissier, T. Poisot, D. B. Stouffer, S. A. Wood, and D. Gravel, “The marine fish food web is globally connected,” *Nature Ecology & Evolution*, vol. 3, no. 8, pp. 1153–1161, Aug. 2019.

- [41] W. C. Leggett, "The Ecology of Fish Migrations," *Annual Review of Ecology and Systematics*, vol. 8, pp. 285–308, 1977, Publisher: Annual Reviews.
- [42] D. Secor, *Migration Ecology of Marine Fishes*, Johns Hopkins University Press, 2015.
- [43] P. Morais and F. Daverat, Eds., *An Introduction to Fish Migration*, CRC Press, 0 edition, Apr. 2016.
- [44] B. S. Halpern, M. Frazier, J. Potapenko, K. S. Casey, K. Koenig, C. Longo, J. S. Lowndes, R. C. Rockwood, E. R. Selig, K. A. Selkoe, and S. Walbridge, "Spatial and temporal changes in cumulative human impacts on the world's ocean," *Nature Communications*, vol. 6, no. 1, pp. 7615, July 2015.
- [45] R. Lewison, A. J. Hobday, S. Maxwell, E. Hazen, J. R. Hartog, D. C. Dunn, D. Briscoe, S. Fossette, C. E. O'Keefe, M. Barnes, M. Abecassis, S. Bograd, N. D. Bethoney, H. Bailey, D. Wiley, S. Andrews, L. Hazen, and L. B. Crowder, "Dynamic Ocean Management: Identifying the Critical Ingredients of Dynamic Approaches to Ocean Resource Management," *BioScience*, vol. 65, no. 5, pp. 486–498, May 2015.
- [46] A. M. Allen and N. J. Singh, "Linking Movement Ecology with Wildlife Management and Conservation," *Frontiers in Ecology and Evolution*, vol. 3, pp. 155, 2016.
- [47] M. R. Donaldson, S. G. Hinch, C. D. Suski, A. T. Fisk, M. R. Heupel, and S. J. Cooke, "Making connections in aquatic ecosystems with acoustic telemetry monitoring," *Frontiers in Ecology and the Environment*, vol. 12, no. 10, pp. 565–573, Dec. 2014, Publisher: John Wiley & Sons, Ltd.
- [48] N. E. Hussey, S. T. Kessel, K. Aarestrup, S. J. Cooke, P. D. Cowley, A. T. Fisk, R. G. Harcourt, K. N. Holland, S. J. Iverson, J. F. Kocik, J. E. Mills Flemming, and F. G. Whoriskey, "Aquatic animal telemetry: A panoramic window into the underwater world," *Science*, vol. 348, no. 6240, 2015.
- [49] R. J. Lennox, K. Aarestrup, S. J. Cooke, P. D. Cowley, Z. D. Deng, A. T. Fisk, R. G. Harcourt, M. Heupel, S. G. Hinch, K. N. Holland, N. E. Hussey, S. J. Iverson, S. T. Kessel, J. F. Kocik, M. C. Lucas, J. M. Flemming, V. M. Nguyen, M. J. Stokesbury, S. Vagle, D. L. VanderZwaag, F. G. Whoriskey, and N. Young, "Envisioning the Future of Aquatic Animal Tracking: Technology, Science, and Application," *BioScience*, vol. 67, no. 10, pp. 884–896, Oct. 2017.



- [50] D. G. Pincock and S. V. Johnston, "Acoustic Telemetry Overview," in *Telemetry techniques: A user guide for fisheries research*, N. S. Adams, J. W. Beeman, and J. H. Eiler, Eds. American Fisheries Society, Sept. 2012.
- [51] C. C. Wilmers, B. Nickel, C. M. Bryce, J. A. Smith, R. E. Wheat, and V. Yovovich, "The golden age of bio-logging: how animal-borne sensors are advancing the frontiers of ecology," *Ecology*, vol. 96, no. 7, pp. 1741–1753, July 2015, Publisher: John Wiley & Sons, Ltd.
- [52] H. Baktoft, K. O. Gjelland, F. Okland, and U. H. Thygesen, "Positioning of aquatic animals based on time-of-arrival and random walk models using YAPS (Yet Another Positioning Solver)," *Scientific Reports*, vol. 7, no. 1, pp. 14294, Oct. 2017.
- [53] H. Mitamura, E. Thorstad, I. Uglem, and F. Økland, "In situ measurement of salinity during seaward migration of Atlantic salmon post-smolts using acoustic transmitters with data-storage capabilities and conventional acoustic transmitters," *Animal Biotelemetry*, vol. 5, 12 2017.
- [54] G. Jackson, "The Development of the Pacific Ocean Shelf Tracking Project within the Decade Long Census of Marine Life," *PloS one*, vol. 6, pp. e18999, 04 2011.
- [55] G. Chaput, J. Carr, J. Daniels, S. Tinker, I. Jonsen, and F. Whoriskey, "Atlantic salmon (*Salmo salar*) smolt and early post-smolt migration and survival inferred from multi-year and multi-stock acoustic telemetry studies in the Gulf of St. Lawrence, northwest Atlantic," *ICES Journal of Marine Science*, vol. 76, no. 4, pp. 1107–1121, Dec. 2018, \_eprint: <https://academic.oup.com/icesjms/article-pdf/76/4/1107/31238675/fsy156.pdf>.
- [56] C. Simpfendorfer, M. Heupel, and R. Hueter, "Estimation of short-term centers of activity from an array of omnidirectional hydrophones and its use in studying animal movements," *Canadian Journal of Fisheries and Aquatic Sciences*, vol. 59, pp. 23–32, 01 2002.
- [57] R. Hedger, F. Martin, J. Dodson, D. Hatin, F. Caron, and F. Whoriskey, "Optimized interpolation of fish positions and speeds in an array of fixed acoustic receivers," *ICES Journal of Marine Science*, vol. 65, 06 2008.
- [58] R. Kraus, C. Holbrook, C. Vandergoot, T. Stewart, M. Faust, D. Watkinson, C. Charles, M. Pegg, E. Enders, and C. Krueger, "Evaluation of Acoustic Telemetry Grids for Determining Aquatic Animal Movement and Survival," *Methods in Ecology and Evolution*, 03 2018.

- 
- [59] H. A. Urke, T. Kristensen, J. B. Ulvund, and J. A. Alfredsen, "Riverine and fjord migration of wild and hatchery-reared Atlantic salmon smolts," *Fisheries Management and Ecology*, vol. 20, no. 6, pp. 544–552, 2013.
- [60] D. Welch, G. Boehlert, and B. Ward, "POST-the Pacific Ocean salmon tracking project," *Oceanologica Acta*, vol. 5, 09 2002.
- [61] A. Steckenreuter, X. Hoenner, C. Huveneers, C. Simpfendorfer, M. J. Buscot, K. Tattersall, R. Babcock, M. Heupel, M. Meekan, J. van den Broek, P. McDowall, V. Peddemors, and R. Harcourt, "Optimising the design of large-scale acoustic telemetry curtains," *Marine and Freshwater Research*, vol. 68, no. 8, pp. 1403–1413, 2017.
- [62] A. Dallolio, H. B. Bjerck, H. A. Urke, and J. A. Alfredsen, "Enhancing a passive acoustic fish telemetry system with a wave-propelled USV: technical solution and proof-of-concept," *Frontiers in Marine Science* (in preparation), 2021.
- [63] A. Heggernes, H. Øveraas, A. Dallolio, T. H. Bryne, and T. A. Johansen, "Predicting the Speed of a Wave-Propelled Autonomous Surface Vehicle Using Metocean Forecasts," *OCEANS 2022, Chennai, India* (accepted).
- [64] E. Honoré-Livermore, A. Dallolio, R. Birkeland, D. D. Langer, C. Haskins, and T. A. Johansen, "MBSE modeling of a SoS with a small satellite and autonomous surface vessels for persistent coastal monitoring," in *16th Annual Conference on System of Systems Engineering*, Virtual, 2021.
- [65] S.-P. Hong, J.-W. Jeong, C.-W. Lee, H.-S. Lee, H.-W. Choi, and I.-H. Park, "A Study on the Environment of USV Wireless Communication," *Journal of Ocean Engineering and Technology*, vol. 23, 01 2009.
- [66] Z. Liu, Y. Zhang, X. Yu, and C. Yuan, "Unmanned surface vehicles: An overview of developments and challenges," *Annual Reviews in Control*, vol. 41, 05 2016.
- [67] G. N. Roberts, Ed., *Advances in Unmanned Marine Vehicles*, Institution of Engineering and Technology, 2006.
- [68] H. Huang, Y. Li, Y. Zhuang, M. Gong, S. Sharma, and D. Xu, "Line-of-Sight Path Following of an Underactuated USV Exposed to Ocean Currents using Cascaded Theorem," in *2018 WRC Symposium on Advanced Robotics and Automation (WRC SARA)*, 2018, pp. 326–333.

- [69] Z. Dong, L. Wan, Y. Li, T. Liu, and G. Zhang, "Trajectory tracking control of underactuated USV based on modified backstepping approach," *International Journal of Naval Architecture and Ocean Engineering*, vol. 7, no. 5, pp. 817–832, 2015.
- [70] Y. Zhao, X. Qi, Y. Ma, Z. Li, R. Malekian, and M. A. Sotelo, "Path Following Optimization for an Underactuated USV Using Smoothly-Convergent Deep Reinforcement Learning," *IEEE Transactions on Intelligent Transportation Systems*, pp. 1–13, 2020.
- [71] M. Breivik, *Topics in Guided Motion Control of Marine Vehicles*, Ph.D. thesis, NTNU, 06 2010.
- [72] T. Fossen, *Handbook of Marine Craft Hydrodynamics and Motion Control, 2nd Edition*, Wiley, 2021.
- [73] T. I. Fossen, K. Y. Pettersen, and R. Galeazzi, "Line-of-Sight Path Following for Dubins Paths With Adaptive Sideslip Compensation of Drift Forces," *IEEE Transactions on Control Systems Technology*, vol. 23, no. 2, pp. 820–827, 2015.
- [74] E. Fredriksen and K. Pettersen, "Global  $\lambda$ -exponential way-point maneuvering of ships: Theory and experiments," *Automatica*, vol. 42, pp. 677–687, 04 2006.
- [75] S. Sharma, R. Sutton, A. Motwani, and A. Annamalai, "Non-linear control algorithms for an unmanned surface vehicle," *Proceedings of the Institution of Mechanical Engineers, Part M: Journal of Engineering for the Maritime Environment*, vol. 228, pp. 146–155, 05 2013.
- [76] L. Liu, D. Wang, and Z. Peng, "ESO-Based Line-of-Sight Guidance Law for Path Following of Underactuated Marine Surface Vehicles With Exact Sideslip Compensation," *IEEE Journal of Oceanic Engineering*, vol. 42, no. 2, pp. 477–487, 2017.
- [77] Y. Deng, X. Zhang, and G. Zhang, "Line-of-Sight-Based Guidance and Adaptive Neural Path-Following Control for Sailboats," *IEEE Journal of Oceanic Engineering*, vol. 45, no. 4, pp. 1177–1189, 2020.
- [78] M. Breivik and T. I. Fossen, "Guidance Laws for Autonomous Underwater Vehicles," in *Underwater Vehicles*, A. V. Inzartsev, Ed., chapter 4. IntechOpen, Rijeka, 2009.

- 
- [79] F. A. Papoulias, “Bifurcation analysis of line of sight vehicle guidance using sliding modes,” *International Journal of Bifurcation and Chaos*, vol. 01, pp. 849–865, 1991.
- [80] R. Polvara, S. Sharma, J. Wan, A. Manning, and R. Sutton, “Obstacle Avoidance Approaches for Autonomous Navigation of Unmanned Surface Vehicles,” *Journal of Navigation*, vol. 71, no. 1, pp. 241–256, 2018.
- [81] O. Souissi, R. Benatitallah, D. Duviervier, A. Artiba, N. Bélanger, and P. Feyzeau, “Path planning: A 2013 survey,” *Proceedings of 2013 International Conference on Industrial Engineering and Systems Management (IESM)*, pp. 1–8, 2013.
- [82] J. Farrell, *Aided Navigation: GPS with High Rate Sensors*, McGraw-Hill, Inc., USA, 1 edition, 2008.
- [83] T. I. Fossen and J. P. Strand, “Passive nonlinear observer design for ships using lyapunov methods: full-scale experiments with a supply vessel,” *Automatica*, vol. 35, no. 1, pp. 3–16, 1999.
- [84] R. E. Kalman, “A New Approach to Linear Filtering and Prediction Problems,” *Transactions of the ASME—Journal of Basic Engineering*, vol. 82, no. Series D, pp. 35–45, 1960.
- [85] P. D. Groves, “Principles of GNSS, inertial, and multisensor integrated navigation systems, 2nd edition [Book review],” *IEEE Aerospace and Electronic Systems Magazine*, vol. 30, pp. 26–27, 2015.
- [86] M. Caccia, M. Bibuli, R. Bono, and G. Bruzzone, “Basic navigation, guidance and control of an Unmanned Surface Vehicle,” *Auton. Robots*, vol. 25, pp. 349–365, 11 2008.
- [87] Y. Peng, J. Han, and Q. Huang, “Adaptive UKF based tracking control for Unmanned Trimaran Vehicles,” *International Journal of Innovative Computing, Information and Control*, vol. 5, pp. 3505–3515, 10 2009.
- [88] S. Campbell, W. Naeem, and G. Irwin, “A review on improving the autonomy of unmanned surface vehicles through intelligent collision avoidance manoeuvres,” *Annual Reviews in Control*, vol. 36, no. 2, pp. 267–283, 2012.
- [89] C. R. Sonnenburg and C. A. Woolsey, “Modeling, Identification, and Control of an Unmanned Surface Vehicle,” *Journal of Field Robotics*, vol. 30, no. 3, pp. 371–398, 2013.

- [90] A. S. Gadre, C. Sonnenburg, S. Du, D. J. Stilwell, and C. Woolsey, “Guidance and control of an unmanned surface vehicle exhibiting sternward motion,” in *2012 Oceans*, 2012, pp. 1–9.
- [91] E. Børhaug, A. Pavlov, E. Panteley, and K. Y. Pettersen, “Straight Line Path Following for Formations of Underactuated Marine Surface Vessels,” *IEEE Transactions on Control Systems Technology*, vol. 19, no. 3, pp. 493–506, 2011.
- [92] K. Nomoto, “On the steering qualities of ships,” *International shipbuilding progress*, vol. 4, pp. 354–370, 1957.
- [93] M. Ludvigsen et al., “Network of heterogeneous autonomous vehicles for marine research and management,” in *OCEANS 2016 MTS/IEEE Monterey*. IEEE, 2016, pp. 1–7.
- [94] A. Zolich, A. Sægrov, E. Vågsholm, V. Hovstein, and T. A. Johansen, “Coordinated maritime missions of unmanned vehicles — Network architecture and performance analysis,” in *2017 IEEE International Conference on Communications (ICC)*, May 2017, pp. 1–7.
- [95] A. N. A. Ali, M. H. Saied, M. Z. Mostafa, and T. M. Abdel-Moneim, “A survey of maximum PPT techniques of PV systems,” in *2012 IEEE Energytech*, 2012, pp. 1–17.
- [96] B. O. Agdal, “Design and Implementation of Control System for Green Unmanned Surface Vehicle,” M.S. thesis, NTNU, 2018.
- [97] J. Pinto, P. Calado, J. Braga, P. Dias, R. Martins, E. Marques, and J. Sousa, “Implementation of a Control Architecture for Networked Vehicle Systems,” *IFAC Proceedings Volumes*, vol. 45, no. 5, pp. 100 – 105, 2012, 3rd IFAC Workshop on Navigation, Guidance and Control of Underwater Vehicles.
- [98] P. S. Dias, S. L. Fraga, R. M. Gomes, G. M. Goncalves, F. L. Pereira, J. Pinto, and J. B. Sousa, “NEPTUS- A framework to support multiple vehicle operation,” in *Proc Oceans MTS/IEEE Conference*, Brest, France, 2005, pp. 963–968.
- [99] R. Martins, P. Dias, E. Marques, J. Pinto, J. Sousa, and F. Pereira, “IMC: A communication protocol for networked vehicles and sensors,” in *OCEANS 2009 - EUROPE*, 2009, pp. 1–6.
- [100] T. A. Johansen, T. Perez, and A. Cristofaro, “Ship Collision Avoidance and COLREGS Compliance Using Simulation-Based Control Behavior Selection

- With Predictive Hazard Assessment,” *IEEE Transactions on Intelligent Transportation Systems*, vol. 17, no. 12, pp. 3407–3422, Dec 2016.
- [101] I. B. Hagen, “Collision avoidance for ASVs using model predictive control,” M.S. thesis, Trondheim, NTNU, 2017.
- [102] S. D. Sæter, “COLREGS compliant Collision Avoidance System for a Wave and Solar Powered USV,” M.S. thesis, Trondheim, NTNU, 2018.
- [103] R. Elmasri and S. B. Navathe, *Fundamentals of Database Systems, Global Edition*, Pearson, 7 edition, 8 2016.
- [104] C. Newman, *SQLite*, Developer’s library. Sams, 2005.
- [105] A. Dallolio, H. Øveraas, J. A. Alfredsen, T. I. Fossen, and T. A. Johansen, “Design and Validation of a Course Control System for a Wave-Propelled Unmanned Surface Vehicle,” *Field Robotics* (in press), 2021.
- [106] L. Wang, Y. Li, Y. Liao, K. Pan, and W. Zhang, “Course Control of Unmanned Wave Glider With Heading Information Fusion,” *IEEE Transactions on Industrial Electronics*, vol. 66, no. 10, pp. 7997–8007, 2019.
- [107] R. Smith, J. Das, G. Hine, W. Anderson, and G. Sukhatme, “Predicting Wave Glider Speed from Environmental Measurements,” 09 2011.
- [108] J. Bowker, M. Tan, and N. Townsend, “Forward Speed Prediction of a Free-Running Wave-Propelled Boat,” *IEEE Journal of Oceanic Engineering*, vol. PP, pp. 1–12, 06 2020.
- [109] D. Clarke, P. Gedling, and G. Hine, “The Application of Manoeuvring Criteria in Hull Design Using Linear Theory,” 1982.
- [110] K. Kijima, Y. Nakiri, Y. Tsutsui, and M. Matsunaga, “Prediction Method of Ship Manoeuvrability in Deep and Shallow Waters,” in *Proceedings MARSIM & ICSM 90 (1990)*, 1990.
- [111] H. Fujii and Tsuda, “Experimental Researches on Rudder Performance. (3),” *Journal of Zosen Kiokai*, vol. 1962, pp. 105–111, 1962.
- [112] K. Matsumoto and K. Suemitsu, “The prediction of manoeuvring performances by captive model tests,” in *J Kansai Soc Naval Archit Jpn (in Japanese)*, 1980.
- [113] H. K. Khalil, *Nonlinear systems; 3rd ed.*, Prentice-Hall, Upper Saddle River, NJ, 2002, The book can be consulted by contacting: PH-AID: Wallet, Lionel.

- [114] W. J. Rugh and J. S. Shamma, “Research on gain scheduling,” *Automatica*, vol. 36, no. 10, pp. 1401–1425, 2000.
- [115] A. Dallolio, H. Øveraas, and T. A. Johansen, “Gain-Scheduled Steering Control for a Wave-Propelled Unmanned Surface Vehicle,” *Ocean Engineering* (submitted), 2021.
- [116] D. Leith and W. Leithead, “Survey of gain-scheduling analysis and design,” *Int. J. Control*, vol. 73, pp. 1001–1025, 01 2000.
- [117] J. Shamma, *Analysis and design of gain scheduled control systems*, Ph.D. thesis, Massachusetts Institute of Technology, Department of Mechanical Engineering, 1988.
- [118] D. H. dos Santos and L. M. G. Goncalves, “A gain-scheduling control strategy and short-term path optimization with genetic algorithm for autonomous navigation of a sailboat robot,” *International Journal of Advanced Robotic Systems*, vol. 16, no. 1, pp. 1729881418821830, 2019.
- [119] D. Santos, A. Negreiros, J. Jacobo, L. Goncalves, A. Silva Junior, and J. M. Silva, “Gain-Scheduling PID Low-Level Control for Robotic Sailboats,” in *2018 Latin American Robotic Symposium, 2018 Brazilian Symposium on Robotics (SBR) and 2018 Workshop on Robotics in Education (WRE)*, 2018, pp. 147–152.
- [120] S. Kragelund, V. Dobrokhodov, A. Monarrez, M. Hurban, and C. Khol, “Adaptive speed control for autonomous surface vessels,” *OCEANS 2013 MTS/IEEE - San Diego: An Ocean in Common*, 01 2013.
- [121] Z. Peimin, Z. Huajun, and T. Xinchu, “The Design of Gain Scheduling PID Controller of the USV Course Control System,” in *2018 Chinese Automation Congress (CAC)*, 2018, pp. 1408–1413.
- [122] D. Kim and K. Yu, “Uncertainty Estimation of the ADCP Velocity Measurements from the Moving Vessel Method, (I) Development of the Framework,” *KSCE Journal of Civil Engineering*, vol. 14, pp. 797–801, 09 2010.
- [123] C. Rennie and M. Church, “Mapping spatial distributions of uncertainty of water and sediment flux in large gravel-bed river reach using an aDcp,” *Journal of Geophysical Research*, vol. 115, 09 2010.
- [124] R. L. Dinehart and J. R. Burau, “Averaged indicators of secondary flow in repeated acoustic Doppler current profiler crossings of bends,” *Water Resources Research*, vol. 41, pp. 09405, 2005.

- 
- [125] A. Dallolio, J. A. Alfredsen, T. I. Fossen, and T. A. Johansen, “Experimental Validation of a Nonlinear Wave Encounter Frequency Estimator Onboard a Wave-Propelled USV,” *IFAC-PapersOnLine*, vol. 54, no. 16, pp. 188–194, 2021, 13th IFAC Conference on Control Applications in Marine Systems, Robotics, and Vehicles CAMS 2021.
- [126] T. I. Fossen and T. Perez, “Kalman filtering for positioning and heading control of ships and offshore rigs,” *IEEE Control Systems Magazine*, vol. 29, no. 6, pp. 32–46, 2009.
- [127] J. Balchen, N. Jenssen, M. Eldar, and S. Saelid, “A Dynamic Positioning System Based on Kalman Filtering and Optimal Control,” *Modeling, Identification and Control*, vol. 1, 07 1980.
- [128] U. Nielsen, “Estimation of directional wave spectra from measured ship responses,” vol. 2, pp. 1103–1112, 01 2005.
- [129] E. Tannuri, J. V. Sparano, A. N. Simos, and J. J. Da Cruz, “Estimating directional wave spectrum based on stationary ship motion measurements,” *Applied Ocean Research*, vol. 25, pp. 243–261, 10 2003.
- [130] D. J. Belleter, D. A. Breu, T. I. Fossen, and H. Nijmeijer, “A Globally K-Exponentially Stable Nonlinear Observer for the Wave Encounter Frequency,” *IFAC Proceedings Volumes*, vol. 46, no. 33, pp. 209 – 214, 2013, 9th IFAC Conference on Control Applications in Marine Systems.
- [131] D. J. Belleter, R. Galeazzi, and T. I. Fossen, “Experimental verification of a global exponential stable nonlinear wave encounter frequency estimator,” *Ocean Engineering*, vol. 97, pp. 48 – 56, 2015.
- [132] C. Holden, R. Galeazzi, C. Rodríguez, T. Perez, T. I. Fossen, M. Blanke, M. de Almeida, and S. Neves, “Nonlinear Container Ship Model for the Study of Parametric Roll Resonance,” *Modeling, Identification and Control*, vol. 28, no. 4, pp. 87–103, 2007.
- [133] S. Aranovskiy and A. Bobtsov, “Output harmonic disturbance compensation for nonlinear plant,” in *2012 20th Mediterranean Conference on Control Automation (MED)*, 2012, pp. 386–391.
- [134] S. V. Aranovskii, A. A. Bobtsov, A. S. Kremlev, and G. V. Luk’yanova, “A robust algorithm for identification of the frequency of a sinusoidal signal,” *Journal of Computer and Systems Sciences International*, vol. 46, no. 3, pp. 371–376, Jun 2007.



- [135] T. Bryne, R. Rogne, T. Fossen, and T. Johansen, “A virtual vertical reference concept for aided inertial navigation at the sea surface,” *Control Engineering Practice*, vol. 70, pp. 1–14, 01 2018.
- [136] A. Dallolio, T. K. Berg, P. De La Torre, H. Øveraas, and T. A. Johansen, “ENC-based Anti-Grounding and Anti-Collision System for a Wave-Propelled USV,” OCEANS 2022, Chennai, India (accepted).
- [137] International Hydrographic Bureau Monaco, “IHO Transfer Standard for Digital Hydrographic Data - Special Publication No. 57. 3.1,” 11 2000.
- [138] B.-O. H. Eriksen, G. Bitar, M. Breivik, and A. Lekkas, “Hybrid Collision Avoidance for ASVs Compliant With COLREGs Rules 8 and 13–17,” *Frontiers in Robotics and AI*, vol. 7, 2020.
- [139] E. Brekke, E. Wilthil, B.-O. H. Eriksen, D. K. Kufoalor, Ø. K. Helgesen, I. B. Hagen, M. Breivik, and T. Johansen, “The Autosea project: Developing closed-loop target tracking and collision avoidance systems,” 2019.
- [140] T. K. Bergh, “ENC-based Collision and Grounding Avoidance System for a Green-Energy Autonomous Surface Vehicle,” M.S. thesis, NTNU, 2021.
- [141] I. B. Hagen, D. K. M. Kufoalor, E. F. Brekke, and T. A. Johansen, “MPC-based Collision Avoidance Strategy for Existing Marine Vessel Guidance Systems,” in *2018 IEEE International Conference on Robotics and Automation (ICRA)*, 2018, pp. 7618–7623.
- [142] D. K. M. Kufoalor, T. A. Johansen, E. F. Brekke, A. Hepsø, and K. Trnka, “Autonomous maritime collision avoidance: Field verification of autonomous surface vehicle behavior in challenging scenarios,” *Journal of Field Robotics*, vol. 37, no. 3, pp. 387–403, 2020.
- [143] S. Blindheim, S. Gros, and T. A. Johansen, “Risk-Based Model Predictive Control for Autonomous Ship Emergency Management,” *IFAC-PapersOnLine*, vol. 53, no. 2, pp. 14524–14531, 2020, 21th IFAC World Congress.
- [144] C. Tam and R. Bucknall, “Review of Collision Avoidance and Path Planning Methods for Ships in Close Range Encounters,” *Journal of Navigation*, vol. 62, pp. 455 – 476, 07 2009.
- [145] T. Statheros, G. Howells, and K. McDonald-Maier, “Autonomous Ship Collision Avoidance Navigation Concepts, Technologies and Techniques,” *Journal of Navigation*, vol. 61, pp. 129 – 142, 01 2008.

- [146] T. Shim, G. Adireddy, and H. Yuan, “Autonomous vehicle collision avoidance system using path planning and model-predictive-control-based active front steering and wheel torque control,” *Proceedings of the Institution of Mechanical Engineers, Part D: Journal of Automobile Engineering*, vol. 226, no. 6, pp. 767–778, 2012.
- [147] C. Caldwell, D. Dunlap, and E. Collins, “Motion planning for an autonomous Underwater Vehicle via Sampling Based Model Predictive Control,” 09 2010, pp. 1–6.
- [148] *The Role of Model Fidelity in Model Predictive Control Based Hazard Avoidance in Unmanned Ground Vehicles Using LIDAR Sensors*, vol. 3 of *Dynamic Systems and Control Conference*, 10 2013, V003T46A005.
- [149] K. Bousson, “Model predictive control approach to global air collision avoidance,” *Aircraft Engineering and Aerospace Technology*, vol. 80, pp. 605–612, 10 2008.
- [150] A. Bemporad and M. Morari, *Robust model predictive control: A survey*, vol. 245, pp. 207–226, 10 2007.
- [151] L. Chisci, J. Rossiter, and G. Zappa, “Systems with persistent disturbances: Predictive control with restricted constraints,” *Automatica*, vol. 37, pp. 1019–1028, 07 2001.
- [152] Kartverket, “Elektroniske sjøkart (ENC),” .
- [153] N. Låuvas, “Design and development of a robotic fish tracking vehicle,” M.S. thesis, NTNU, 2020.
- [154] H. Øveraas, A. Dallolio, P. De La Torre, and T. A. Johansen, “Field Report: Long-Endurance Operation of Wave-Propelled and Solar-Powered Autonomous Surface Vehicle,” *Field Robotics* (submitted), 2021.
- [155] A. M. Madni and M. Sievers, “System of Systems Integration: Fundamental Concepts, Challenges and Opportunities,” in *Advances in Systems Engineering*, J. Hsu and R. Curran, Eds., vol. 252, pp. 1–34. American Institute of Aeronautics and Astronautics, Reston, Virginia, USA, 2016.
- [156] R. Gomes, J. Straub, A. Jones, J. Morgan, S. Tipparach, A. Sletten, K. W. Kim, D. Loegering, N. Feikema, K. Dayananda, G. Miryala, A. Gass, K. Setterstrom, J. Mischel, D. Shipman, and C. Nazzaro, “An interconnected network of UAS as a system-of-systems,” in *2017 IEEE/AIAA 36th Digital Avionics Systems Conference (DASC)*, 2017, pp. 1–7.

- [157] R. Zhang, B. Song, Y. Pei, and Q. Yun, “Improved method for subsystems performance trade-off in system-of-systems oriented design of UAV swarms,” *Journal of Systems Engineering and Electronics*, vol. 30, pp. 720–737, 2019.
- [158] M. LaSorda, J. M. Borky, and R. M. Sega, “Model-based architecture and programmatic optimization for satellite system-of-systems architectures,” *System Engineering*, vol. 21, 2018.
- [159] F. Pérez-Lissi, F. Aguado-Agelet, A. Vázquez, P. Yañez, P. Izquierdo, S. Lacroix, R. Bailon-Ruiz, J. Tasso, A. Guerra, and M. Costa, “FIRE-RS: Integrating land sensors, cubesat communications, unmanned aerial vehicles and a situation assessment software for wildland fire characterization and mapping,” in *69th International Astronautical Congress*, 2018.
- [160] M. Berger, J. Moreno, J. A. Johannessen, P. F. Levelt, and R. F. Hanssen, “ESA’s sentinel missions in support of Earth system science,” *Remote Sensing of Environment*, vol. 120, pp. 84–90, 2012, The Sentinel Missions - New Opportunities for Science.
- [161] Z. Malenovský, H. Rott, J. Cihlar, M. E. Schaepman, G. García-Santos, R. Fernandes, and M. Berger, “Sentinels for science: Potential of Sentinel-1, -2, and -3 missions for scientific observations of ocean, cryosphere, and land,” *Remote Sensing of Environment*, vol. 120, pp. 91–101, 2012, The Sentinel Missions - New Opportunities for Science.
- [162] I. Ogashawara, L. Li, and M. J. Moreno-Madriñán, “Slope algorithm to map algal blooms in inland waters for Landsat 8/Operational Land Imager images,” *Journal of Applied Remote Sensing*, vol. 11, no. 1, pp. 1 – 18, 2016.
- [163] M. E. Grøtte, R. Birkeland, E. Honoré-Livermore, S. Bakken, J. L. Garrett, E. F. Prentice, F. Sigernes, M. Orlandić, J. T. Gravdahl, and T. A. Johansen, “Ocean Color Hyperspectral Remote Sensing With High Resolution and Low Latency—The HYPSON-1 CubeSat Mission,” *IEEE Transactions on Geoscience and Remote Sensing*, pp. 1–19, 2021.
- [164] E. F. Prentice, M. E. Grøtte, F. Sigernes, and T. A. Johansen, “Design of a Hyperspectral Imager Using COTS Optics for Small Satellite Applications,” in *International Conference on Space Optics*, 2021.
- [165] J. Fjeldtvedt, M. Orlandić, and T. A. Johansen, “An Efficient Real-Time FPGA Implementation of the CCSDS-123 Compression Standard for Hyperspectral Images,” *IEEE Journal of Selected Topics in Applied Earth Observations and Remote Sensing*, vol. 11, no. 10, pp. 3841–3852, 2018.

- [166] ESA and EUMETSAT, “S3 Product Notice - OLCI,” Tech. Rep., EUMETSAT, 2019.
- [167] D. Manolakis, M. Pieper, E. Truslow, T. Cooley, M. Brueggeman, and S. Lipson, “The remarkable success of adaptive cosine estimator in hyperspectral target detection,” in *Algorithms and Technologies for Multispectral, Hyperspectral, and Ultraspectral Imagery XIX*. International Society for Optics and Photonics, 2013, vol. 8743, p. 874302.
- [168] Đ. Bošković, M. Orlandić, and T. A. Johansen, “A reconfigurable multi-mode implementation of hyperspectral target detection algorithms,” *Microprocessors and Microsystems*, vol. 78, pp. 103258, 2020.
- [169] M. N. Sweeting, “Modern Small Satellites-Changing the Economics of Space,” *Proceedings of the IEEE*, vol. 106, no. 3, pp. 343–361, March 2018.
- [170] A. Zolich, D. Palma, K. Kansanen, K. Fjørtoft, J. Sousa, K. H. Johansson, Y. Jiang, H. Dong, and T. A. Johansen, “Survey on Communication and Networks for Autonomous Marine Systems,” *Journal of Intelligent & Robotic Systems volume*, vol. 95, pp. 789–813, 2019.
- [171] M. Ludvigsen, P. S. Dias, S. Ferreira, T. O. Fossum, V. Hovstein, T. A. Johansen, T. R. Krogstad, Ø. Midtgaard, J. S. P. Norgren, Ø. Sture, E. Vågsholm, and A. Zolich, “Autonomous Network of Heterogeneous Vehicles for Marine Research and Management,” in *IEEE Oceans 2016 – Monterey, CA*, September 2016.
- [172] A. G. Guerra, A. S. Ferreira, M. Costa, D. Nodar-López, and F. Aguado Agelet, “Integrating small satellite communication in an autonomous vehicle network: A case for oceanography,” *Acta Astronautica*, vol. 145, pp. 229 – 237, 2018.
- [173] A. G. C. Guerra, F. Francisco, J. Villate, F. A. Agelet, O. Bertolami, and K. Rajan, “On Small Satellites for Oceanography: A Survey,” *Acta Astronautica*, vol. 127, pp. 404 to 423, 2016.
- [174] R. Birkeland, D. Palma, and A. Zolich, “Integrated SmallSats and Unmanned Vehicles for Networking in Remote Locations,” in *Proceedings of The 68th International Astronautical Congress*, 2017.
- [175] J. Pinto, P. S. Dias, R. Martins, J. Fortuna, E. R. B. Marques, and J. B. de Sousa, “The LSTS toolchain for networked vehicle systems,” *2013 MT-S/IEEE OCEANS - Bergen*, p. 1–9, jun 2013.

- [176] I. Bekmezci, I. Sen, and E. Erkalkan, “Flying ad hoc networks (FANET) test bed implementation,” in *2015 7th International Conference on Recent Advances in Space Technologies (RAST)*, June 2015, pp. 665–668.
- [177] D. Palma and R. Birkeland, “Enabling the Internet of Arctic Things With Freely-Drifting Small-Satellite Swarms,” *IEEE Access*, vol. 6, pp. 71435–71443, 2018.
- [178] D. Mohny, “The 2018 summer of satellite IoT – 18 startups, over 1,600 satellites,” .
- [179] C. Rodriguez, H. Boiardt, and S. Bolooki, “CubeSat to Commercial Inter-satellite Communications: Past, present and Future,” in *IEEE Aerospace Conference*, 2016.
- [180] V. J. Riot, L. M. Simms, and D. Carter, “Lessons Learned Using Iridium to Communicate with a CubeSat in Low Earth Orbit,” *Journal of Small Satellites*, vol. 10, no. 1, 2 2021.
- [181] J.-L. Voirin, S. Bonnet, V. Normand, and D. Exertier, “From initial investigations up to large-scale rollout of an MBSE method and its supporting workbench: the Thales experience,” *INCOSE International Symposium*, vol. 25, no. 1, pp. 325–340, 2015.
- [182] G. Hallegraeff, H. Enevoldsen, and A. Zingone, “Global harmful algal bloom status reporting,” *Harmful Algae*, vol. 102, pp. 101992, 2021, Global Harmful Algal Bloom Status Reporting.
- [183] D. Scavia, J. David Allan, K. K. Arend, S. Bartell, D. Beletsky, N. S. Bosch, S. B. Brandt, R. D. Briland, I. Daloğlu, J. V. DePinto, D. M. Dolan, M. A. Evans, T. M. Farmer, D. Goto, H. Han, T. O. Höök, R. Knight, S. A. Ludsin, D. Mason, A. M. Michalak, R. Peter Richards, J. J. Roberts, D. K. Rucinski, E. Rutherford, D. J. Schwab, T. M. Sesterhenn, H. Zhang, and Y. Zhou, “Assessing and addressing the re-eutrophication of Lake Erie: Central basin hypoxia,” *Journal of Great Lakes Research*, vol. 40, no. 2, pp. 226–246, 2014.
- [184] C. Whitt, J. Pearlman, B. Polagye, F. Caimi, F. Muller-Karger, A. Coping, H. Spence, S. Madhusudhana, W. Kirkwood, L. Grosjean, B. M. Fiaz, S. Singh, S. Singh, D. Manalang, A. S. Gupta, A. Maguer, J. J. H. Buck, A. Marouchos, M. A. Atmanand, R. Venkatesan, V. Narayanaswamy, P. Testor, E. Douglas, S. de Halleux, and S. J. Khalsa, “Future Vision for Autonomous Ocean Observations,” *Frontiers in Marine Science*, vol. 7, pp. 697, 2020.

- 
- [185] J. H. Eiler, T. M. Grothues, J. A. Dobarro, and M. M. Masuda, “Comparing Autonomous Underwater Vehicle (AUV) and Vessel-based Tracking Performance for Locating Acoustically Tagged Fish,” *Marine Fisheries Review*, vol. 75, no. 4, 2013.
- [186] T. Fossum, *Adaptive Sampling for Marine Robotics*, Ph.D. thesis, NTNU, 07 2019.
- [187] Y. Yang, J. J. Martinez, J. Lu, H. Hou, and Z. D. Deng, “Design and implementation of a real-time underwater acoustic telemetry system for fish behavior study and environmental sensing,” in *OCEANS 2019 MTS/IEEE SEATTLE*, 2019, pp. 1–4.
- [188] W. Hassan, M. Føre, J. Ulvund, and J. Alfredsen, “Internet of Fish: Integration of acoustic telemetry with LPWAN for efficient real-time monitoring of fish in marine farms,” *Computers and Electronics in Agriculture*, vol. 163, 2019.
- [189] T. M. Grothues, J. Dobarro, J. Ladd, A. Higgs, G. Niezgoda, and D. Miller, “Use of a multi-sensored AUV to telemeter tagged Atlantic sturgeon and map their spawning habitat in the Hudson River, USA,” in *2008 IEEE/OES Autonomous Underwater Vehicles*, 2008, pp. 1–7.
- [190] M. J. Oliver, M. W. Breece, D. A. Fox, D. E. Haulsee, J. T. Kohut, J. Mander-son, and T. Savoy, “Shrinking the Haystack: Using an AUV in an Integrated Ocean Observatory to Map Atlantic Sturgeon in the Coastal Ocean,” *Fish-eries*, vol. 38, no. 5, pp. 210–216, May 2013, Publisher: John Wiley & Sons, Ltd.
- [191] Y. Lin, J. Hsiung, R. Piersall, C. White, C. G. Lowe, and C. M. Clark, “A Multi-Autonomous Underwater Vehicle System for Autonomous Tracking of Marine Life,” *Journal of Field Robotics*, vol. 34, no. 4, pp. 757–774, June 2017.
- [192] O. Ennasr, C. Holbrook, D. W. Hondorp, C. C. Krueger, D. Coleman, P. Solanki, J. Thon, and X. Tan, “Characterization of acoustic detection efficiency using a gliding robotic fish as a mobile receiver platform,” *Animal Biotelemetry*, 10 2020.
- [193] I. Masmitja, J. Navarro, S. Gomariz, J. Aguzzi, B. Kieft, T. O’Reilly, K. Katija, P. J. Bouvet, C. Fannjiang, M. Vigo, P. Puig, A. Alcocer, G. Vallicrosa, N. Palomeras, M. Carreras, J. del Rio, and J. B. Company, “Mobile robotic platforms for the acoustic tracking of deep-sea demersal fishery resources,”

- Science Robotics*, vol. 5, no. 48, pp. eabc3701, Nov. 2020, Number: 48 Publisher: American Association for the Advancement of Science.
- [194] C. M. Clark, C. Forney, E. Manii, D. Shinzaki, C. Gage, M. Farris, C. G. Lowe, and M. Moline, "Tracking and Following a Tagged Leopard Shark with an Autonomous Underwater Vehicle," *Journal of Field Robotics*, vol. 30, no. 3, pp. 309–322, 2013.
- [195] J. Eiler, T. Grothues, J. Dobarro, and R. Shome, "Tracking the Movements of Juvenile Chinook Salmon using an Autonomous Underwater Vehicle under Payload Control," *Applied Sciences*, vol. 9, pp. 2516, 06 2019.
- [196] M. Oliver, M. Breece, D. Haulsee, M. Cimino, J. Kohut, D. Aragon, and D. Fox, "Factors affecting detection efficiency of mobile telemetry Slocum gliders," *Animal Biotelemetry*, vol. 5, 12 2017.
- [197] D. Haulsee, M. Breece, D. Miller, B. Wetherbee, D. Fox, and M. Oliver, "Habitat selection of a coastal shark species estimated from an autonomous underwater vehicle," *Marine Ecology Progress Series*, vol. 528, pp. 277–288, 05 2015.
- [198] M. Oliver, M. Breece, D. Fox, D. Haulsee, J. Kohut, J. Manderson, and T. Savoy, "Shrinking the Haystack: Using an AUV in an Integrated Ocean Observatory to Map Atlantic Sturgeon in the Coastal Ocean," *Fisheries*, vol. 38, pp. 210–216, 05 2013.
- [199] R. Carlon, "Tracking tagged fish using a wave glider," 10 2015, pp. 1–5.
- [200] M. Cimino, M. Cassen, S. Merrifield, and E. Terrill, "Detection efficiency of acoustic biotelemetry sensors on Wave Gliders," *Animal Biotelemetry*, vol. 6, 12 2018.
- [201] D. Cote, J.-M. Nicolas, F. Whoriskey, A. M. Cook, J. Broome, P. M. Regular, and D. Baker, "Characterizing snow crab (*Chionoecetes opilio*) movements in the Sydney Bight (Nova Scotia, Canada): a collaborative approach using multiscale acoustic telemetry," *Canadian Journal of Fisheries and Aquatic Sciences*, vol. 76, no. 2, pp. 334–346, 2019.
- [202] C. Huveneers, C. A. Simpfendorfer, S. Kim, J. M. Semmens, A. J. Hobday, H. Pederson, T. Stieglitz, R. Vallee, D. Webber, M. R. Heupel, V. Peddemors, and R. G. Harcourt, "The influence of environmental parameters on the performance and detection range of acoustic receivers," *Methods in Ecology and Evolution*, vol. 7, no. 7, pp. 825–835, 2016.

- [203] A. Papoulis and S. Pillai, *Probability, Random Variables, and Stochastic Processes*, McGraw-Hill series in electrical engineering: Communications and signal processing. McGraw-Hill, 2002.
- [204] H. Bjerck, H. Urke, T. Haugen, J. A. Alfredsen, J. Ulvund, and T. Kristensen, “Synchrony and multimodality in the timing of Atlantic salmon smolt migration in two Norwegian fjords,” *Scientific Reports*, vol. 11, 03 2021.
- [205] S. K. Katti and A. V. Rao, “Handbook of The Poisson Distribution,” *Technometrics*, vol. 10, no. 2, pp. 412–412, 1968.
- [206] H. Urke, K. Daae, H. Viljugrein, I. Kandal, A. Staalstrøm, and P. Jansen, “Improvement of aquaculture management practice by integration of hydrodynamic modelling,” *Ocean & Coastal Management*, vol. 213, pp. 105849, 2021.
- [207] J. Thomson and J. Girton, “Sustained Measurements of Southern Ocean Air-Sea Coupling from a Wave Glider Autonomous Surface Vehicle,” *Oceanography*, vol. Vol. 30, pp. 104–109, 06 2017.
- [208] R. A. K. Main, “Migration of Atlantic salmon (*Salmo salar*) smolts and post-smolts from a Scottish east coast river,” M.S. thesis, University of Glasgow, 2021.
- [209] B. Bingham, N. Kraus, B. Howe, L. Freitag, K. Ball, P. Koski, and E. Galimire, “Passive and active acoustics using an autonomous wave glider,” *Journal of Field Robotics*, vol. 29, no. 6, pp. 911–923, apr 2012.
- [210] P. Johnston and C. Pierpoint, “Deployment of a passive acoustic monitoring (PAM) array from the AutoNaut wave-propelled unmanned surface vessel (USV),” in *OCEANS 2017 - Aberdeen*. jun 2017, IEEE.
- [211] E. B. Thorstad, F. Whoriskey, I. Uglem, A. Moore, A. H. Rikardsen, and B. Finstad, “A critical life stage of the Atlantic salmon *Salmo salar*: behaviour and survival during the smolt and initial post-smolt migration,” *Journal of Fish Biology*, vol. 81, no. 2, pp. 500–542, jul 2012.
- [212] J. Barry, R. J. Kennedy, R. Rosell, and W. K. Roche, “Atlantic salmon smolts in the Irish Sea: First evidence of a northerly migration trajectory,” *Fisheries Management and Ecology*, vol. 27, no. 5, pp. 517–522, 2020.
- [213] M. Newton, J. Barry, A. Lothian, R. Main, H. Honkanen, S. Mckelvey, P. Thompson, I. Davies, N. Brockie, A. Stephen, R. O. Murray, R. Gardiner, L. Campbell, P. Stainer, and C. Adams, “Counterintuitive active directional



## *References*

---

swimming behaviour by Atlantic salmon during seaward migration in the coastal zone,” *ICES Journal of Marine Science*, vol. 78, no. 5, pp. 1730–1743, may 2021.